ISSN 1349-113X
JAXA-SP-07-008E

JAXA Special Publication

Proceedings of Lectures and Workshop International -Recent Advances in Multidisciplinary Technology and Modeling-

February 2008

Japan Aerospace Exploration Agency

Preface

These Proceedings feature papers
presented at the International Workshop on
Recent Advances in Multidisciplinary Technology and Modeling
held in Tokyo at the University of Tokyo ,May 23 -25,2007.
As the title indicates,
it brought together a group of internationally known experts
in diverse area centered on Aircraft technology.
We wish to thank Dr. Jiro Nakamichi and J A X A
for their generous support in making the Workshop possible.

A V Balakrishnan , U C L A , Workshop Chair

Lectures and Workshop International
- Recent Advances in Multidisciplinary Technology and Modeling -

23-25 May 2007
University of Tokyo
Tokyo, Japan

Overview

The multidisciplinary technology is a common focus of aeronautic researchers, because an aircraft is a large and fine system which couples technologies of aerodynamics, structures, materials, control and guidance, and other intelligent equipments especially in the flight control systems. In order to satisfy this circumstance, the subjects of this "*Lectures and Workshop*" were exactly directed to this multidisciplinary technology and the constituting individual technologies.

As the organizers had intended, this meeting brought the valuable opportunity for the attendees to gain the cutting-edge information from the notable professors and researchers in these fields; the attendees were also able to have active discussions and exchanges between the lecturers.

Totally, six lecturers were invited to this meeting: four from the outside of Japan and two from Japan. And, during the period, almost seventy people attended at the meeting.

Cosponsored by

University of California, Los Angeles, UCLA, U.S.A.
University of Tokyo, Japan
Kyushu University, Japan
Japan Aerospace Exploration Agency, JAXA, Japan

General Chair

Prof. A.V.Balakrishnan, UCLA

Organizing Committee

Prof. A.V. Balakrishnan, UCLA
Prof. Y. Miyazawa, Kyushu University
Prof. S. Suzuki, University of Tokyo
Prof. M. Murozono, Kyushu University
Dr. J. Nakamichi, JAXA

Workshop Secretariat

Dr. M. Tamayama, JAXA
Dr. H. Arizono, JAXA
Mr. S. Machida, JAXA
Mr. K. Saitoh, JAXA

CONTENTS

<< LECTURES >>

<< WORKSHOP >>

Some papers were reorganized from the originally-presented ones to fit this post-conference publication and/or changed their paper titles.

Lectures and Workshop International- Recent Advances in Multidisciplinary Technology and Modeling- May 23-25, 2007

Efficient Time-Linearised TSD Computations Including the Effects of Shock-Generated Entropy, Vorticity and Shock Wave Motion

Eddie Ly
School of Mathematical & Geospatial Sciences
RMIT University
Melbourne, Australia

Jiro Nakamichi
Aviation Program Group
Japan Aerospace Exploration Agency
Tokyo, Japan

ABSTRACT

The effect of small perturbations on steady nonlinear transonic small disturbance flow-fields, in the context of two-dimensional flows governed by the general-frequency transonic small disturbance equation with nonreflecting far-field boundary conditions, is investigated. This paper presents a time-linearised time-domain solution method that includes effects due to the shock-generated entropy and vorticity and shock wave motions. The solution procedure correctly accounts for the small-amplitude shock wave motion due to small unsteady changes in the aerofoil boundary conditions, and correctly models a flow-field with embedded strong shock waves. Steady and first harmonic pressure distributions for the NACA 0003 aerofoil with a harmonically oscillating flap, and NACA 0012 aerofoil undergoing a sinusoidal pitching oscillation, are predicted and compared with the Euler results.

1.0 INTRODUCTION

Transonic flows are characterised by the presence of adjacent regions of subsonic and supersonic flow, usually accompanied by shock waves. In the past, there has been much activity in the development of computational methods for the analysis of time-linearised transonic flows. This activity was motivated by the need to supplement expensive and time consuming wind tunnel tests with an affordable and reliable alternative.

This paper presents a simple and fast scheme for computing time-linearised solutions to the general frequency transonic small disturbance (TSD) equation subject to nonreflecting far-field boundary conditions. The first author presented the time-linearised theory in Ly and Gear[1,2], and has shown the importance of proper modeling of shock wave motion if one wants to obtain accurate time-linearised transonic solutions. The purpose of this paper is to present the modifications that have been recently incorporated into the time-linearised theory and existing potential code,

TranFlow2D, of Ly and Gear[2] to enhance its capabilities to model flowfields with embedded strong shock waves, so that Euler-like solutions can be obtained. The resulting time-linearised theory will be referred to as the modified time-linearised TSD (MTL-TSD) theory throughout this paper.

First modification is the inclusion of the shock-generated entropy and vorticity effects (Hafez and Lovell[3], Whitlow *et al.*[4], Batina[5] and Dang and Chen[6]) to enhance the capability of *TranFlow2D* in simulating flowfields with embedded strong shock waves. The second modification involves a procedure, which we have referred to as the shock jump correction procedure (Ly and Gear[2]), that allows one to include the shock wave motion effects by correcting the solution values behind the shock wave, such that the time-linearised form of the shock jump condition will be satisfied.

We treat the unsteady flow as a small perturbation about a steady (mean) state. This results in a coupled flow problem for the steady and first-order unsteady reduced velocity potentials. The steady flow problem is governed by the usual nonlinear steady TSD equation (Ly and Gear[2], Traci *et al.*[7,8], Fung *et al.*[12] and Ly *et al.*[13]) and shock-generated entropy and vorticity effects are incorporated. The governing equation for the first-order unsteady reduced potential is linear, locally of mixed elliptic/hyperbolic type depending upon the nature of the steady-state solution, and solved in conjunction with the shock jump correction procedure. This will effectively correct the solution values behind the shock wave, which in turn introduces the shock wave motion effects into the time-linearised solution. In the closure, the validity of the present theory is verified by comparing the predicted results for the NACA 0003 aerofoil with a harmonically oscillating flap, and NACA 0012 aerofoil undergoing a sinusoidal pitching oscillation about quarter chord point, with those obtained from the NAL's Euler code. The comparisons show that the MTL-TSD theory has the capabilities to capture the flow characteristics shown in the Euler results.

2.0 GENERAL-FREQUENCY TSD EQUATION AND BOUNDARY CONDITIONS

The unsteady, isentropic and inviscid flow over a thin aerofoil is assumed to be governed by the general-frequency TSD equation,

which may be written in a convenient form as

$$M_\infty^2 \frac{\partial}{\partial t}(\phi_t + 2\phi_x) + \frac{\beta^2}{2\bar{u}} \frac{\partial}{\partial x} W^2 - \frac{\partial}{\partial z}\phi_z = 0 \qquad (1)$$

where

$$W = \bar{u} - \phi_x \qquad (2),(3)\ (4)$$

and $\phi_x = \partial\phi/\partial x$, etc.

$\beta^2 = 1 - M_\infty^2$

The spatial coordinates (x, z), t and ϕ have been nondimensionalised by c, c/U_∞ and cU_∞, respectively. In nondimensional terms, the fluid velocity vector is given by $\mathbf{v}=(u,w) = grad(x+\phi)$. Here u denotes the value of ϕ_x at sonic condition, that is, where local Mach number is one.

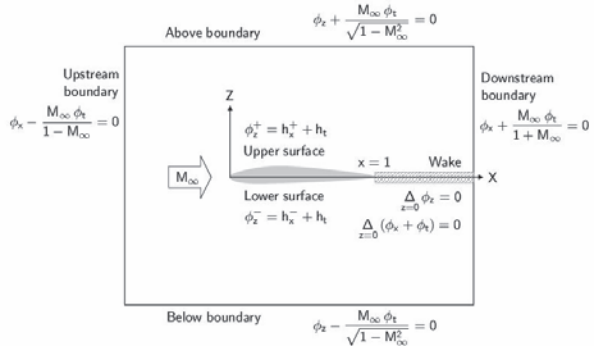

Figure 1. Boundary conditions.

Nonreflecting boundary conditions (Gear *et al.*[1] and Kwak[17]), derived from the theory of wave propagation, are employed at the far-field computational boundaries, and Kutta condition is satisfied at the trailing edge and pressure continuity condition ia also satisfied in the wake region behind the aerofoil. The flow tangency boundary condition is imposed on a flat mean surface (approximation to the aerofoil) in terms of aerofoil slopes as depicted in Figure 1. The aerofoil lies on the z = 0 plane with the leading and trailing edges located at x = 0 (also the origin of the Cartesian coordinate system) and x = 1, respectively. Nonreflecting far-field boundary conditions are imposed at some finite distances and serve to simulate the disturbances that propagate outward from the aerofoil to infinity. Consequently, the far-field boundaries can be moved closer to the aerofoil. Any shock wave that exists in the flowfield must satisfy the shock jump condition (Fung *et al.*[12] and Ly *et al.*[13]) derived from the conservation law form of Equation (1), namely,

$$M_\infty^2 \langle \phi_t + 2\phi_x \rangle \langle \phi_x \rangle \frac{d\Lambda}{dt} + \frac{\beta^2}{\bar{u}} \overline{W} \langle \phi_x \rangle^2 + \langle \phi_z \rangle^2 = 0 \qquad (5)$$

together with the condition derived from the assumption of irrotationality,

$$\theta = -\frac{\langle \phi_z \rangle}{\langle \phi_x \rangle} \qquad (6)$$

3.0 MODIFIED TIME-LINEARISED TSD THEORY

This section describes the time-linearisation process of the general-frequency TSD equation in time domain and the two modifications introduced into the inviscid theory.

3.1 Time-linearised time-domain formulation

In the time-linearisation process, we assume unsteady disturbances are small relative to a fixed mean state. This mean state is presumeably represented by the nonlinear steady flowfield (Ly and Gear[2], Traci *et al.*[7,8] and Ly *et al.*[13]), and result in a coupled flow problem for the steady (ϕ_s) and first-order unsteady (ϕ_u) reduced potentials. The main dimensionless parameter governing unsteady flow is the reduced frequency number, k. The disturbance is assumed small, so that the aerofoil motion and reduced potential can be time-linearised as, to first-order approximations

$$\begin{aligned} h^\pm(x,t) &= h_s^\pm(x) + h_u(x,t) \\ \phi(x,z,t) &= \phi_s(x,z) + \phi_u(x,z,t) \end{aligned} \qquad (7) \text{ and } (8)$$

We define the mean potential by the steady-state potential obtained at the mean position of the aerofoil motion. This restriction ensures that the calculation of the first harmonics potential is accurate.

There are two advantages of time-linearising the reduced potential of the form shown in Equation (8):

1. Shock wave motion effects can be included in the time-linearised calculation, so that the solution within the shock trajectory will be correctly predicted.
2. There are no restrictions imposed on the mode of aerofoil motion that can be simulated, comparing to the harmonic decomposition of the following form

$$\begin{aligned} h^\pm(x,t) &= h_s^\pm(x) + \Re\left\{h_o(x)\, e^{ikt}\right\} \\ \phi(x,z,t) &= \phi_s(x,z) + \phi_o(x,z)\, e^{ikt} \end{aligned} \qquad (9), (10)$$

where ϕ_o is a complex-valued oscillatory component of the reduced potential. To facilitate the use of high density of grid points surrounding the aerofoil, a smooth non-uniform computational mesh is constructed via an algebraic mapping process. In general terms, the mapping functions

can be represented by

$$\xi = \xi(x) \qquad (11)$$

$$\zeta = \zeta(z) \qquad (12)$$

Substituting approximations (7) and (8) into Equation (1) with the boundary conditions shown in Figure 1, and separating the steady and unsteady components, we find that ϕ_s satisfies the usual nonlinear steady TSD equation,

$$\frac{\beta^2}{2\bar{u}} \xi_x \frac{\partial}{\partial \xi} W_s^2 - \zeta_z \frac{\partial}{\partial \zeta} \zeta_z \frac{\partial \phi_s}{\partial \zeta} = 0 \qquad (13)$$

where

$$W_s = \bar{u} - \xi_x \frac{\partial \phi_s}{\partial \xi} \qquad (14)$$

Equation (13) is locally of elliptic/hyperbolic type representing subsonic/supersonic flow when W_s is positive/negative, and its solution contains discontinuous jumps that approximate steady shock waves. The required steady boundary conditions are those depicted in Figure 1 without the time-dependent terms and with ϕ_s replacing ϕ. While ϕ_u satisfies

$$M_\infty^2 \frac{\partial^2 \phi_u}{\partial t^2} + 2M_\infty^2 \frac{\partial}{\partial t}\xi_x \frac{\partial \phi_u}{\partial \xi} = \frac{\beta^2}{\bar{u}}\xi_x \frac{\partial}{\partial \xi} W_s \xi_x \frac{\partial \phi_u}{\partial \xi} + \zeta_z \frac{\partial}{\partial \zeta}\zeta_z \frac{\partial \phi_u}{\partial \zeta} \quad (15)$$

subject to the same far-field and wake boundary conditions of Figure 1, but with ϕ_u replacing ϕ and the following aerofoil boundary condition

$$\zeta_z^{\pm} \frac{\partial \phi_u^{\pm}}{\partial \zeta} = \xi_x \frac{\partial h_u}{\partial \xi} + \frac{\partial h_u}{\partial t} \quad (16)$$

Equation (15) is linear with respect to ϕ_u, and it is locally of the same mixed elliptic/hyperbolic type as Equation (13), depending upon the nature of the steady-state solution. The linearity of Equation (15) makes the computational effort required to obtain a solution much less than the effort required to obtain a solution of the full nonlinear TSD equation [Equation (1)].

The required solution for ϕ_s, which does not depend on ϕ_u, is solved independently, and is then used in the unsteady solution process to determine ϕ_u. This approach has the benefit that ϕ_s need not be regenerated for each unsteady boundary disturbance or reduced frequency of interest. Once ϕ is determined, the isentropic pressure coefficient can be determined from

$$\begin{aligned} C_p &= C_{ps} + C_{pu} \\ &= -2\xi_x \frac{\partial \phi_s}{\partial \xi} - 2\left[\xi_x \frac{\partial \phi_u}{\partial \xi} + \frac{\partial \phi_u}{\partial t}\right] \end{aligned} \quad (17)$$

On the right side of Equation (17), the first term and terms inside the brackets correspond to C_{ps} and C_{pu}, respectively, and the critical pressure coefficient is defined by

$$C_p^* = -2\bar{u} \quad (18)$$

3.2 Inclusion of shock-generated entropy and vorticity effects

The shock-generated entropy and vorticity effects, similiar to those reported by Hafez and Lovell[3], Whitlow *et al.*[4], Batina[5] and Dang and Chen(6), are incorporated into the steady analysis, so that flowfields with embedded strong shock waves can be simulated accurately. Rotational effects become influential when strong shock waves exist in the flowfield, since vorticity is generated due to the entropy changes along the shock. Such effects were not included in the conventional inviscid TSD theory, see Gear *et al.*[1], Ly and Gear[2] and Ly *et al.*[13], because of the irrotationality assumption necessary for the existence of a velocity potential. Therefore, when modelling such flowfield it is essential to include the shock-generated entropy and vorticiy effects. We replace the streamwise flux of Equation (13) by an alternative flux, and rewrite the new steady governing equation with an artificial time derivative appended, so that the method of false transients can be applied (see Ly *et al.*[13,18], Ly[14] and Catherall[19] for more details),

$$\frac{\partial \phi_s}{\partial \tau} = \frac{\beta^2}{2\bar{u}}\xi_x \frac{\partial}{\partial \xi}\hat{W}_s^2 - \zeta_z \frac{\partial}{\partial \zeta}\zeta_z \frac{\partial \phi_s}{\partial \zeta} \quad (19)$$

$$\hat{W}_s = \frac{\bar{u}}{\mu} - \frac{\mu(1+\mu^2)\xi_x \dfrac{\partial \phi_s}{\partial \xi}}{1+\mu^2+\xi_x \dfrac{\partial \phi_s}{\partial \xi}} \quad (20), (21)$$

$$\mu = \left(1+2\bar{u}\right)^{1/4}$$

In the modification to include vorticity effects, $\boldsymbol{v}$ is treated as a sum of potential and rotational components, and the rotational component assumed to exist only in the region downstream of the shock wave. Since entropy is constant in steady flow, and assuming small shock curvature, the steady streamwise component of $\boldsymbol{v}$, namely u_s, for grid points behind the shock wave is modified to

$$u_s = 1 + \xi_x \frac{\partial \phi_s}{\partial \xi} - \ln\left[\frac{2\gamma M_n^2 - \gamma + 1}{\gamma + 1}\right]^{\frac{1}{\gamma(\gamma-1)M_\infty^2}} + \ln\left[\frac{(\gamma+1)M_n^2}{2+(\gamma-1)M_n^2}\right]^{\frac{1}{(\gamma-1)M_\infty^2}} \quad (22)$$

The first two terms on the right side of Equation (22) represent the contribution from the inviscid model, and the last two terms are related to the production of shock-generated entropy. The entropy jump is a function of the normal Mach number upstream of the shock wave (Rankine-Hugoniot shock jump relation), and the shock wave location must be determined before the entropy jump can be computed. The present finite difference scheme uses a type-dependent finite differencing strategy (see Gear *et al.*[1], Engquist and Osher[20], Murman[21] and Subsection 4.2) to capture shock waves and to properly treat the local subsonic and supersonic regions, thus the shock wave can easily be located. Consequently, the modified TSD theory will have a new steady governing equation given by Equation (19).

3.3 Inclusion of shock wave motion effects

In two-dimensional small-disturbance transonic flowfields, the shock waves that usually occur are nearly normal to the flow direction (Tijdeman(16)). Therefore, we can assume that if the steady flowfield has a shock wave, then this shock may be approximated by a normal shock wave. We computed the shock wave motion in conjunction with the solution to Equation (15). The shock wave motion effects are incorporated into the solution procedure by correcting the solution values behind the shock wave, such that the time-linearised form of the shock jump condition [Equation (5)] is satisfied. The shock wave motion is time-linearised (Ly and Gear[2] and Fung *et al.*[12]) as, to first-order approximation and,

$$\Lambda(t) = \Lambda_s + \Lambda_u(t) \quad (23)$$

where Λ_u is the magnitude of the time-linearised shock motion. The reduced velocity potential at the shock wave is expanded via a Taylor series expansion about $\xi = \xi(\Lambda_s)$,

$$\phi(\Lambda(t),\zeta,t) = \phi(\Lambda_s,\zeta,t) + \Lambda_u \xi_x \frac{\partial \phi}{\partial \xi} + \frac{\Lambda_u^2}{2}\xi_x \frac{\partial}{\partial \xi}\xi_x \frac{\partial \phi}{\partial \xi} + \frac{\Lambda_u^3}{6}\xi_x \frac{\partial}{\partial \xi}\xi_x \frac{\partial}{\partial \xi}\xi_x \frac{\partial \phi}{\partial \xi} + \ldots$$

(24)

threading the shock front and neglecting higher order terms in Λ_u, provides

$$\langle \phi_s(\Lambda_s, \zeta) \rangle = 0 \qquad (25), (26)$$
$$\langle \phi_u(\Lambda_s, \zeta, t) \rangle = \tfrac{1}{2}\Lambda_u \langle C_{ps} \rangle$$

In addition to the above relations, the shock wave speed relation is required, so that Λ_u can be computed once ϕ_u is known. Simplifying Equation (5) for normal shock waves, and making use of Equations (8) and (23) leads to $W_s = 0$ and the following time-linearised shock jump condition relations,

$$\frac{d\Lambda_u}{dt} = \frac{\beta^2}{2\bar{u}M_\infty^2}\overline{\xi_x \frac{\partial \phi_u}{\partial \xi}} \qquad (27), (28)$$
$$\theta = 0$$

Equation (27) is integrated at the shock foot at each time level of the solution process.

4.0 NUMERICAL IMPLEMENTATION

4.1 Steady and unsteady finite difference based algorithms

The numerical solution procedure involves applying the method of false transients (Ly *et al.*[13,18], Ly[14] and Catherall[19]) to solve Equation (19) for ϕ_s, and noniterative alternating directional implicit (ADI) method in conjunction with the shock jump correction procedure to solve Equation (15) for ϕ_u.

The ADI method computes the solution by marching forward in time from its initial steady-state to subsequent time levels in a two-step process from time-level t_n to t_{n+1}. Intermediate values, $\psi(\xi, \zeta, t)$, are computed at the midpoint of each time interval. We first write Equation (15) and all associated unsteady boundary conditions at time-level $t_{n+1/2}$, which is the midpoint of time levels t_n and t_{n+1}, and evaluate ψ_t by the trapezoidal rule and ψ_{tt} by a second-order accurate nonstandard forward difference rule involving solution values from time-level t_{n-2} to t_{n+1}. The vertical derivative is averaged between the values at time-level tn and $tn+1$. Equation (15) is then split into two half equations with ψ computed along the ζ = constant lines of the computational grid in the first half step, and then along the ξ = constant lines in the second half step for $\phi^{n+1}{}_u$. It is necessary to introduce boundary values for ψ, which we will not discuss here, that are compatible with the interior algorithms corresponding to the two half equations, so that a global truncation error of second-order in time can be attained. Equation (26) is differentiated with respect to time at time-level $t_{n+1/2}$, and replacing the time-linearised shock wave speed term with Equation (27). The final finite difference scheme being globally second-order accurate in the spatial and time dimensions, except in the flow regions where shock wave motion occurs, in which case the time dimension is reduced to first-order accuracy. In the first half-step we solve for ψ along ζ = constant lines using

$$\frac{2M_\infty^2}{\Delta t}\xi_x\frac{\partial \psi}{\partial \xi} - \frac{\beta^2}{\bar{u}}\xi_x\frac{\partial}{\partial \xi}W_s\xi_x\frac{\partial \psi}{\partial \xi} = \frac{2M_\infty^2}{\Delta t}\xi_x\frac{\partial \phi_u^n}{\partial \xi} + \zeta_z\frac{\partial}{\partial \zeta}\zeta_z\frac{\partial \phi_u^n}{\partial \zeta} \qquad (29)$$

in conjunction with the computation of new ψ value behind the shock wave,

$$\langle \psi \rangle = \langle \phi_u^n \rangle + \frac{\Delta t\,\beta^2}{4\bar{u}M_\infty^2}\overline{\xi_x\frac{\partial \phi_u^n}{\partial \xi}}\langle C_{ps} \rangle \qquad (30)$$

With ψ determined, the second half-step follows, computing ϕ_{n+1} u along ξ = constant lines using

$$\frac{3M_\infty^2}{2(\Delta t)^2}\phi_u^{n+1} + \frac{2M_\infty^2}{\Delta t}\xi_x\frac{\partial \phi_u^{n+1}}{\partial \xi} - \frac{1}{2}\zeta_z\frac{\partial}{\partial \zeta}\zeta_z\frac{\partial \phi_u^{n+1}}{\partial \zeta} = \frac{M_\infty^2}{2(\Delta t)^2}\left(7\phi_u^n - 5\phi_u^{n-1} + \phi_u^{n-2}\right) + \frac{2M_\infty^2}{\Delta t}\xi_x\frac{\partial \psi}{\partial \xi} - \frac{1}{2}\zeta_z\frac{\partial}{\partial \zeta}\zeta_z\frac{\partial \phi_u^n}{\partial \zeta} \qquad (31)$$

in conjunction with the updated $\langle \phi_u^n \rangle$ values along the shock wave,

$$\langle \phi_u^{n+1} \rangle = \langle \psi \rangle \qquad (32)$$

4.2 Spatial discretisation

In the finite difference schemes, the first streamwise and vertical derivatives are differenced using standard second-order accurate upwind and central rules, respectively. While a second-order accurate Engquist-Osher type-dependent difference rule (Gear *et al.*[1] and Engquist and Osher[20]) is used for the second streamwise derivatives. As the flow changes from subsonic to supersonic, Engquist-Osher type-dependent operators smoothly change from a central difference rule (to account for the domain of dependence of elliptic region) to an upwind difference rule (to account for the absence of downstream influence in hyperbolic region). This ensures a smooth transition from subsonic to supersonic flow. Hence, entropy violating decompression shock waves will not develop. As the flow changes from supersonic to subsonic, the Engquist-Osher type-dependent operators change to an appropriate shock point operator (Murman[21]), and for the computation of ϕ_u the shock jump correction is implemented at this stage. The correction procedure disregards the actual variation in φu, and thus, is only able to account for small-amplitude shock wave motions.

Table 1: Case studies.

Motion Mode	Case	Aerofoil	M_∞	k	α_m	$\Delta\alpha$	δ_m	$\Delta\delta$	Figs.
Flap oscillation	1	NACA 0003	0.93	0.125	0	0	0	1	2,3
	2	NACA 0003	0.93	0.25	0	0	0	1	2,3
Pitching oscillation	3	NACA 0012	0.84	0.25	0	0.25	0	0	4,5
	4	NACA 0012	0.84	0.25	0	0.5	0	0	4,5
	5	NACA 0012	0.8	0.25	1.25	0.25	0	0	6,7

5.0 ASSESSMENT OF MODIFIED THEORY

The first author has confirmed the validity of the time-linearised calculations by demonstrating that the time-linearised theory is capable of generating results which are similar to that predicted by the nonlinear scheme of Gear *et al.*[1] (solving the full nonlinear TSD equation) for transonic flows over an aerofoil in small-amplitude motions, see Ly and Gear[2] for more details. In this section we apply

the MTL-TSD theory and code (version 2 of *TranFlow2D*) to compute the time-linearised results for the cases tabulated in Table 1, and to show that Euler-like solutions can be obtained by comparing present results with those predicted by the JAXA's Euler code (details on the Euler solver can be found in Kheirandish *et al.*[22] and Nakamichi and Kheirandish[23]). All unsteady results become periodic within four cycles of oscillation, with the last cycle providing the estimate of the unsteady pressure distributions. In addition, linear results obtained from solving the unsteady compressible subsonic small disturbance equation are presented for reference, so that the pressure peaks generated by the shock waves (shown in the transonic results which follow) can easily be distinguished. All angles are positive for trailing edge down, and moments are positive for nose up, taken about the aerofoil quarter-chord point.

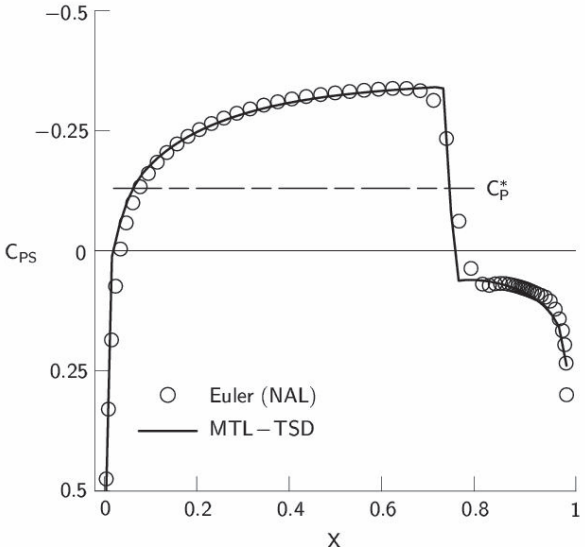

Figure 2. Comparison of steady pressure distributions for the NACA 0003 aerofoil with a 9.6% chord flap at $M_\infty = 0.93$ and $\delta_m = 0$ deg.

5.1 NACA 0003 aerofoil results

The first two cases consider flows over an NACA 0003 aerofoil with a harmonically oscillating 9.6% chord flap (flap hinge located at 90.4% chord). The results are compared in Figures 2 and 3. The steady pressure distribution corresponds reasonably well with the Euler result as shown in Figure 2, except for the very small regions adjacent to the shock wave located at 74.7% chord, where the MTL-TSD theory gives a much sharper shock profile. The steady shock wave strength is also well predicted, with the jump in C_{ps} approximating the steady shock wave and $C_{ps}/C^*_p > 1$ indicating locally supersonic point. To assist in the comparison of the unsteady results, an approximating trace of the pressure responses in the form of a truncated Fourier series with only one harmonic is fitted to the result by a least squares procedure. The fitted parameters are then written in complex-valued form, so that the real (in-phase) and imaginary (out-phase) parts of ΔC_p per unit of flap deflection, where $\Delta C_p = (\Delta C^+_p - \Delta C^-_p)/\Delta\delta$, can be extracted and plotted as shown in Figure 3 for reduced frequencies of

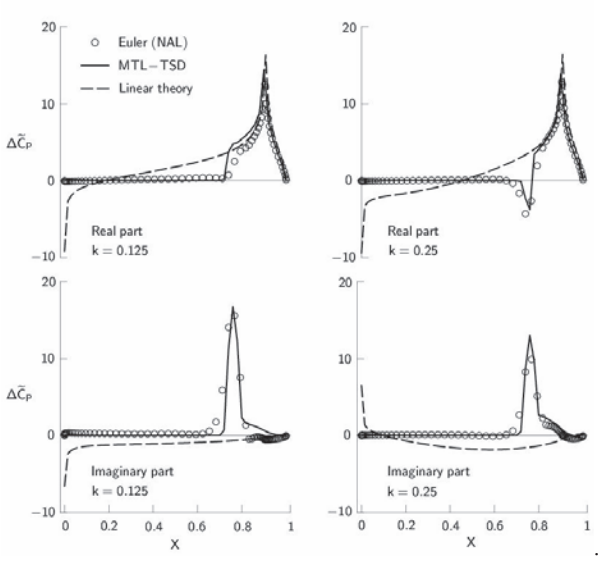

Figure 3. Comparison between the Euler, MTL-TSD and linear results for the NACA0003 aerofoil with a harmonically oscillating 9.6% chord flap at $M_\infty = 0.93$, $k = 0.125$ and 0.25, $\delta_m = 0$ deg and $\Delta\delta = 1$ deg.

125 and 0.25. The positive peak of the real pressure part is caused by the changes in aerofoil slopes across the flap hinge. While the peak of the imaginary part is due to the existence of steady shock wave, leading to the observation that the embedded shock waves in the steady flowfield require corresponding shock waves in the unsteady perturbation flowfield, which in effect result in harmonic changes in shock wave strength. Also noting that the comparison of the imaginary part behind the shock wave for case 2 ($k = 0.25$) is much better than that of case 1 ($k = 0.125$).

The amplitude of shock excursion is proportional to $1/k$, and so, the flow region influenced by the shock wave motion for high-frequency flows is small, which suits the application of the time-linearised methods. Hence, resulting in the improvement of the imaginary part of the solution. If the time-linearised theory is formulated in the frequency domain, one can in fact show that the amplitude of shock excursion is proportional $1/k$ via the following relation,

$$\Lambda_u = -\Re\left\{\frac{i(\gamma+1)}{2k}\overline{\xi_x}\frac{\partial\phi_o}{\partial\xi}e^{ikt}\right\} \tag{33}$$

where ϕ_u and ϕ_0 are related by

$$\phi_u = \Re\left\{\phi_0 e^{ikt}\right\} \tag{34}$$

Even though the MTL-TSD theory slightly over predicts the pressure perturbation peaks, the comparison is good in general, since both methods give the same trend of pressure perturbation distributions along the aerofoil surfaces. Furthermore, all pressure peaks are correctly captured, particularly the negative peak appearing in Figure 3 for $k =$

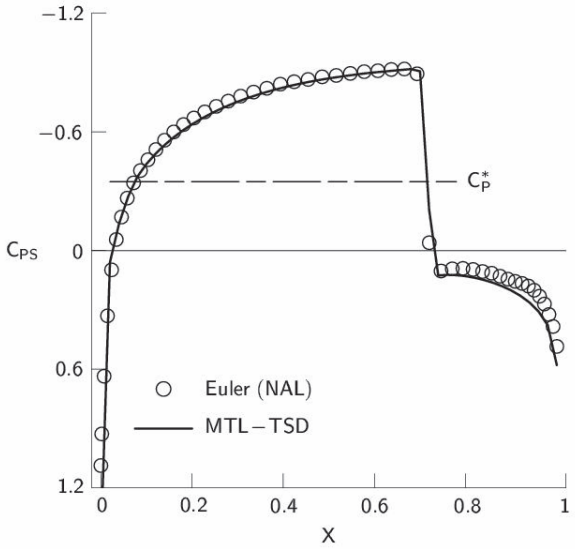

__ _____ ù_X+_ ü"__#%$_þ___ÿ___K__'Gÿ__þ__(__$___ÿÿ___ _&___ÿ___*__(_ _____ÿ" _____ ,__W-/._ü".Y0_0(S_T_þ_____'___ 3(þ__

:_;Z**Figure 4.** Comparison of steady pressure distributions for the NACA 0012 aerofoil at $M_\infty = 0.84$ and $\alpha_m = 0$ deg.

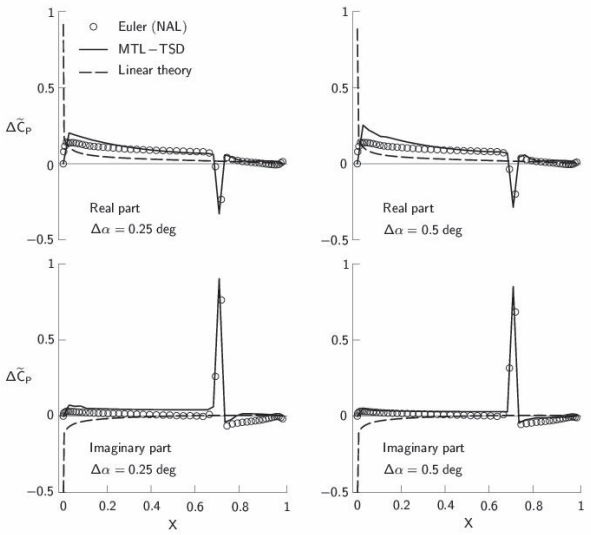

Figure 5. Comparison between the Euler, MTL-TSD and linear results for the NACA0012 aerofoil undergoing a sinusoidal pitching oscillation about quarter-chord point at $M_\infty = 0.84$, $k = 0.25$, $\alpha_m = 0$ deg and $\Delta\alpha = 0.25$ and 0.5 deg.

0.25. The authors suspect that the small discrepancies in the comparison are due to the amount of incorporated (numerical) entropy being not exactly the same as the true value, and due to the fact that the unsteady flowfield is treated as a small pertubation about the steady flowfield instead of the true mean flowfield. However, the discrepancies in the shock region being small indicate that taking the steady flowfield and steady shock position to represent the mean flowfield and mean shock position, respectively, is reasonable. The mean shock position determined by the Euler code is about 75.6% chord, which is very close to the steady shock position predicted by the present MTL-TSD theory of 74.7% chord, a difference in distance of less than 1% chord. Note that it is essential to have a well defined steady (mean) flowfield, because a good agreement on the steady pressure distribution is a prerequisite to obtain a good agreement on the unsteady pressure distribution for the time-linearised computations. In future work we may consider taking the mean flowfield

from a complete nonlinear unsteady solution of Equation (1) for cases where the steady and mean shock waves are not close to each other. The linear theory, as expected, is only able to capture the pressure peaks due to the flap hinge.

5.2 NACA 0012 aerofoil results

The next three cases are for flows over an NACA 0012 aerofoil undergoing a sinusoidal pitching oscillation about quarter-chord point, and the results are compared in Figures 4 to 7. The steady part of cases 3 and 4 is also studied by Whitlow *et al.*[4] and Fuglsang and Williams[24], and the steady part of case 5 is an AGARD (Advisory Group for Aerospace Research and Development) test case for assessment of inviscid flow methods. The comparison of the steady pressure distributions in Figures 4 and 6 is exceptional good, specifically in the accurate prediction of both the shock wave positions and strengths.

The perturbation pressure for the NACA 0012 aerofoil cases is extracted based on the following formula,

$$\Delta\tilde{C}_p = \frac{ik}{\pi\,\Delta\alpha}\oint C_p e^{ikt}\,dt \qquad (35)$$

The MTL-TSD theory is able to capture the trend of the pressure distributions determined by the Euler theory (i.e. giving the same signs of the real and imaginary parts), but the unsteady results are usually slightly over predicted, see Figures 5 and 7.

Since the NACA 0012 aerofoil has no flap or moveable lifting surface where the aerofoil slopes change rapidly, the sharp pressure peaks shown in these plots are due to the shock wave only, and again, are well captured by the present theory. The steady shock positions are located very close to the mean locations, thus increasing the accuracy of the present results. The Euler method employs a body conformed dynamic grid system (Kheirandish *et al.*[22] and Nakamichi and Kheirandish[23]), in which a new grid configuration is generated at each time level corresponding to the changes in the aerofoil position. While the present theory uses a stationary grid system with the flow tangency boundary condition imposed on a flat mean surface (approximation to the actual aerofoil) in terms of aerofoil slopes. Because of the

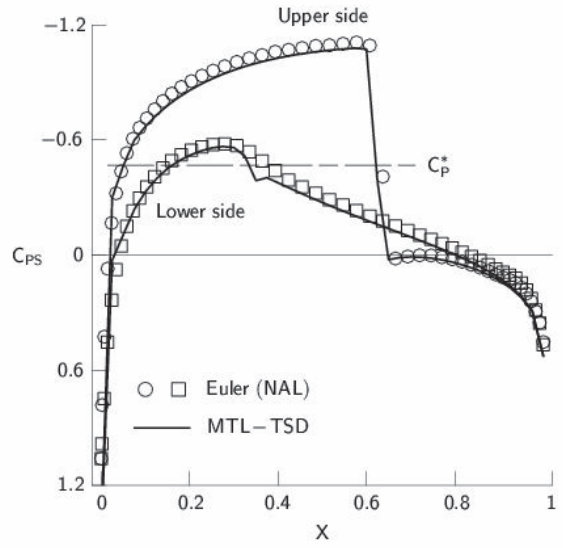

Figure 6. Comparison of steady pressure distributions for the NACA 0012 aerofoil at $M_\infty = 0.8$ and $\alpha_m = 1.25$ deg.

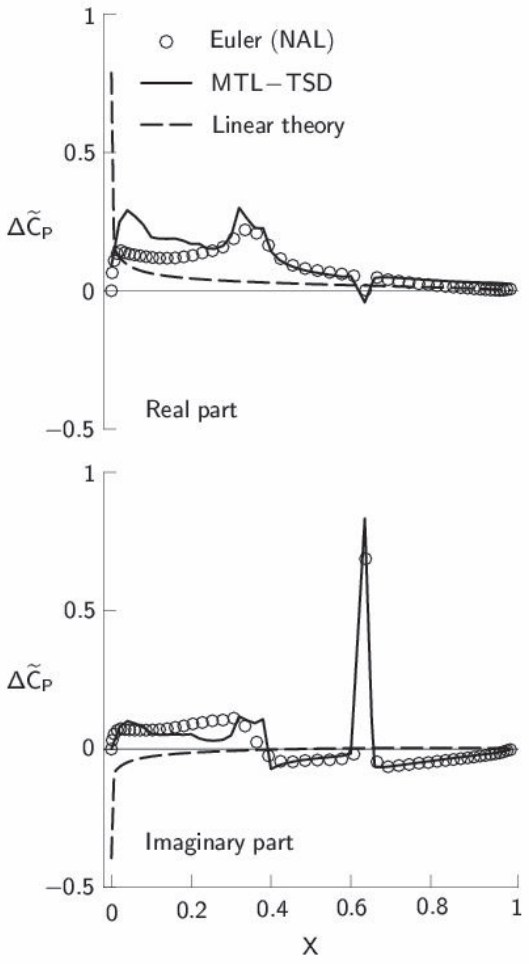

Figure 7. Comparison between Euler, MTL-TSD and linear results for NACA0012 aerofoil in a sinusoidal pitching oscillation about quarter-chord point at $M_\infty = 0.8$, $k = 0.25$, $\alpha_m = 1.25$ deg and $\Delta\alpha = 0.25$ deg.

different grid systems, the authors expected some discrepancies to occur around the aerofoil nose. The discrepancy occurs only for the real pressure part, and becomes large for increasingly large maximum angle of attack. For example, in Figure 5 the discrepancy for case 4 is larger than that of case 3, since the angle of attack can reach upto 0.5 deg in case 4 compared to 0.25 deg in case 3. Similarly, Figure 7 shows much larger discrepancy for case 5 where the maximum angle of attack is 1.5 deg. This observation is consistent with the expectation that the distribution of the real (in-phase part) depends on the aerofoil profile and motion, since if comparing to cases 1 and 2 where only the flap that moves and 90.4% of the aerofoil is stationary, no such discrepancies occur around the aerofoil nose. The small peaks that appear in Figure 7 around 30 to 40% chord are generated by the vortex development in this region. Again, the MTL-TSD method captured such flow phenomenon remarkably well.

6.0 CONCLUDING REMARKS

An effective treatment of unsteady transonic flows, with moving shock waves, as a small perturbation about the steady (mean) flowfield was described. The solution method, in conjunction with the shock jump correction procedure and the inclusion of shockgenerated entropy and vorticity effects, has successfully produced accurate time-linearised time-domain solutions for transonic flows with embedded strong shock waves. The modifications made to the inviscid TSD theory leads to the development of a second version of *TranFlow2D* code. Solutions can be obtained in an acceptable turn-around time on current high performance personal computers, hence making it an ideal tool for performing two-dimensional transonic aeroelastic analysis and for students to experience numerical aerodynamic computations. Based on the present study, we obtained the following conclusions:

1. The satisfactory correlation of the results demonstrated that the presented theory is capable of predicting unsteady transonic flow with embedded strong shock waves.
2. The presented time-linearised formulation illustrated the importance of proper modeling of the shock wave motion in order to obtain accurate time-linearised transonic solutions.
3. The theory has been demonstrated to be successful, in a sense that it could be used to provide input for aeroelastic computations for which only infinitesimal magnitude motions need be considered.
4. In future work we may consider taking the mean flowfield from a complete nonlinear unsteady solution of the general-frequency TSD equation for cases where the steady and mean shock waves are not close to each other.
5. There is a future potential for a three-dimensional version as a fast method to be used for flutter predictions.

REFERENCES

[1] Gear, J. A., Ly, E. and Phillips, N. J. T. Time marching finite difference solution of the modified transonic small disturbance equation, Proceedings of the 8th Biennial Computational Techniques and Applications Conference (CTAC97), Australian and New Zealand

Industrial and Applied Mathematics (ANZIAM), Adelaide, Australia, 29 Sep.–1 Oct. 1997, pp. 209–216.

[2] Ly, E. and Gear, J. A. Time-linearized transonic computations including shock wave motion effects, Journal of Aircraft, Nov./Dec. 2002, Vol. 39, No. 6, pp. 964–972.

[3] Hafez, M. and Lovell, D. Entropy and vorticity corrections for transonic flows, AIAA Paper 83-1926, July 1983.

[4] Whitlow, W., Jr., Hafez, M. M. and Osher, S. J. An entropy correction method for unsteady full potential flows with strong shocks, Journal of Fluids and Structures, 1987, Vol. 1, pp. 401–414.

[5] Batina, J. T. Unsteady transonic small-disturbance theory including entropy and vorticity effects, Journal of Aircraft, 1989, Vol. 26, No. 6, pp. 531–538.

[6] Dang, T. Q. and Chen, L. T. An Euler correction method for two- and three dimensional transonic flows, AIAA Paper 87-0522, 1987.

[7] Traci, R. M., Albano, E. D. and Farr, J. L., Jr. Small disturbance transonic flows about oscillating airfoils and planar wings, AFFDL TR-75-100, Air Force Flight Dynamics Lab., Wright-Patterson AFB, OH, USA, Aug. 1975.

[8] Traci, R. M., Albano, E. D. and Farr, J. L., Jr. Perturbation method for transonic flows about oscillating airfoils, AIAA Journal, 1976, Vol. 14, No. 9, pp. 1258–1265.

[9] Schippers, H. and Hounjet, M. H. L. Two complementary approaches to transonic potential flow about oscillating airfoils, Journal of Aircraft, 1988, Vol. 25, No. 5, pp. 395–398.

[10] Hounjet, M. H. L. NLR inviscid transonic unsteady loads prediction methods in aeroelasticity, Transonic Unsteady Aerodynamics and Aeroelasticity, Paper CP-507, AGARD, March 1992, pp. 12.1–12.16. [11] Greco, P. C., Lan, C. E. and Lim, T. W. Frequency domain unsteady transonic aerodynamics for flutter and limit cycle oscillation prediction, AIAA Paper 97-0835, Jan. 1997.

[12] Fung, K. Y., Yu, N. J. and Seebass, R. Small unsteady perturbations in transonic flows, AIAA Journal, 1978, Vol. 16, No. 8, pp. 815–822.

[13] Ly, E., Gear, J. A. and Phillips, N. J. T. Simulated shock motion using a timelinearised transonic code, Proceedings of the 3rd Biennial Engineering Mathematics and Applications Conference (EMAC98), The Institution of Engineers of Australia and Australian and New Zealand Industrial and Applied Mathematics (ANZIAM), Adelaide, Australia, 13–16 July 1998, pp. 331–334.

[14] Ly, E. Improved approximate factorisation algorithm for the steady subsonic and transonic flow over an aircraft wing, Proceedings of the 21st Congress of the International Council of the Aeronautical Sciences (ICAS 1998), AIAA and ICAS, Melbourne, Australia, 13–18 Sep. 1998, Paper A98-31699.

[15] Batina, J. T. Unsteady transonic algorithm improvements for realistic aircraft applications, Journal of Aircraft, 1989, Vol. 26, No. 2, pp. 131–139.

[16] Tijdeman, H. Investigations of the transonic flow around oscillating airfoils, NLR TR 77090 U, National Aerospace Lab. NLR, Amsterdam, The Netherlands, Oct. 1977

[17] Kwak, D. Nonreflecting far-field boundary conditions for unsteady transonic flow computation, AIAA Journal, 1981, Vol. 19, No. 11, pp. 1401–1407.

[18] Ly, E., Gear, J. A. and Phillips, N. J. T. Improved approximate factorisation algorithm, Proceedings of the 8th Biennial Computational Techniques and Applications Conference (CTAC97), Australian and New Zealand Industrial and Applied Mathematics (ANZIAM), Adelaide, Australia, 29 Sep.–1 Oct. 1997, pp. 393–400.

[19] Catherall, D. Optimum approximate-factorization schemes for two-dimensional steady potential flows, AIAA Journal, 1982, Vol. 20, No. 8, pp. 1057–1063.

[20] Engquist, B. and Osher, S. Stable and entropy satisfying approximations for transonic flow calculations, Mathematics of Computation, 1980, Vol. 34, No. 149, pp. 45–75.

[21] Murman, E. M. Analysis of embedded shock waves calculated by relaxation methods, AIAA Journal, 1974, Vol. 12, No. 5, pp. 626–633.

[22] Kheirandish, H. R., Goro, B. and Nakamichi, J. Numerical investigation of flutter, International Journal of Computational Fluid Dynamics, 1999, Vol. 12, pp. 279–290.

[23] Nakamichi, J. and Kheirandish, H. R. Nonlinear flutter simulation of NAL non-powered SST experimental airplane and related wind tunnel tests, CEAS/AIAA/AIAE International Forum on Aeroelasticity and Structural Dynamics, Madrid, Spain, April 2001.

[24] Fuglsang, D. F. and Williams, M. H. Non-isentropic unsteady transonic small disturbance theory, AIAA Paper 85-0600, April 1985.

THE ULTRA-GREEN AIRCRAFT - SOME ASPECTS FROM THE AEROELASTIC POINT OF VIEW

Martin Spieck
DLR - German Aerospace Center
Institute of Aeroelasticity
Bunsenstrasse 10, D-37073 Göttingen, Germany
Phone: (+49)-551-709-2382 Fax: (+49)-551-709-2862
E-Mail: martin.spieck@DLR.de

1 Summary

This article describes selected aspects of multidisciplinary aircraft design in general, and aeroelasticity in particular, on the example of a new class of civil transport aeroplanes: the "ultra-green" aircraft. It is to be expected that this new class will demand for novel design solutions, probably up to a degree which can be described as an entirely new configuration.

The article reflects the personal opinion of the author and is intended to serve as a stimulus for an open and fruitful discussion at the UCLA/Univ. of Tokyo/Kyushu Univ./JAXA workshop "Lectures and Workshop International - Recent Advances in Multidisciplinary Technology and Modeling", to be held from May 23rd to May 25th at Tokyo, Japan.

2 Introduction

The early days of air travel were exciting times - not only for the passenger, but also for the aircraft designer and engineer. Fundamentally new ideas, concepts and technologies were evolving every year, many manufacturers and their sometimes very individual products were competing on the developing market, and the general progress could be seen by everybody at the first glance. Figure 1 is intended to capture that rapid development in a sequence of transport aircraft. It is covering a period of 25 years, ranging from the times of propeller-driven biplanes to the first commercial jet airliner, the de Havilland Comet. And less than five years later, the famous Dash 80 took off for its maiden flight - the prototype of the Boeing 707 which proved to be the "blueprint" of the modern jetliner.

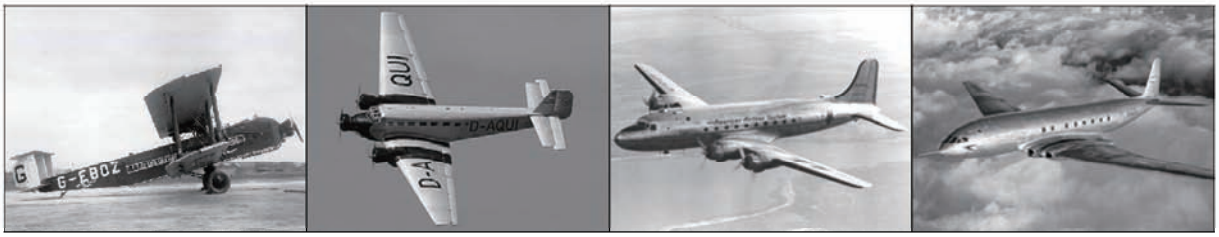

Figure 1 *Sequence of transport aircraft over a period of 25 years (maiden flight): Armstrong Whitworth A.W. 154 Argosy (1926), Junkers Ju-53/3m (1932), Douglas DC-4/C-54 (1942), de Havilland DH 106 Comet (1949)*

More than twice that time has passed since then. Figure 2 shows a comparison of the Boeing 707, and an artist's view of the Boeing 787 which is currently under development and supposed to have its first flight in less than a year. From the overall picture, not much fundamental difference can be detected between the design of 1954 and that of 2007; the technological

progress is hidden in the detail, and the path since the 1950s has been an evolutionary rather than a revolutionary one.

Figure 2 *The "classical" jet airliner configuration: Boeing 707 (1954) and Boeing 787 (~2007)*[1]

One of the reasons is that the basic requirements have not changed: the business case is still to transport the passenger safely, quickly and with a certain amount of comfort over a distance of several thousand miles - and to be able to make money on it. But with the impressive growth in air travel over the last five decades and the prospect of comparable future development, a new class of design requirements arise. At a time when flights between European capitals or major US cities are offered for less than 50 $, the primary public interest is no longer to further enhance mobility, but to minimise the impact of that mobility on the citizen's everyday life - in particular, to reduce aircraft noise in the vicinity of airports, and to tackle the global issue of climate change. The environmentally friendly, hence "ultra-green" aircraft is not the only, but one of the most important factors in meeting that public demand.

3 The Ultra-Green Aircraft

3.1 The Background

With growing political pressure, increasingly stringent regulations on emissions and noise, and supported by a continuously rising fuel price, environmental friendliness is becoming a hard, **market-driven requirement** in aircraft design.

This is amplified by a growing, and not always rational, public awareness of environmental issues: future growth of air travel depends on the public image. A first impression of this impact could be seen in early 2007 in Germany, when the United Nation's report *Climate Change 2007*, [1], led to an emotional public debate, culminating in public incitements of German politicians to avoid travelling by air.

In 2000, European Community Commissioner Philippe Busquin assembled a group of high-ranking experts, the "Group of Personalities", in order to develop a vision for aviation in the year 2020, entitled *European Aeronautics: A Vision for 2020,* [2]. This report aims to find a balanced perspective between societal and political demands, technological feasibility and economical reasonability. Its findings have been transformed into a roadmap for European research in ACARE's *Strategic Research Agendas SRA 1* and *SRA 2*, [3].

1. Artist's view (© Boeing, picture is licensed under Creative Commons Attribution ShareAlike 2.0 Germany License)

Vision 2020 put forward quantified goals against which future aeronautical products will be measured. The environmental goals for air transport are:

- to reduce fuel consumption and CO_2 emissions by 50%,
- to reduce perceived external noise by 50%,
- to reduce NO_x by 80%, and
- to make substantial progress in reducing the environmental impact of the manufacture, maintenance and disposal of aircraft and related products.

These goals are by no way mandatory for aeronautical products, but they may serve as a reasonable benchmark of what the market will demand from the next generation of civil transport aircraft. Extrapolating the achievements in emissions and noise reduction of the last 30 years reveals that evolutionary improvements along the current trend line will not result in the 2020 targets being met. To achieve the step change in performance required to meet the environmental challenge demands for the incorporation of breakthrough technologies. It is probable that this breakthrough will lead to aircraft configurations which are different to that we grew accustomed to since the B 707 made its first transatlantic crossing, like the concept depicted in Figure 3.

Figure 3 *Concept of an ultra-green transport aircraft, presented by D. Schmitt, VP R&T and Future Projects, Airbus (France) at ICAS 2004 Congress, [4]*

3.2 "Ultra-Green" and Aeroelasticity

A major driver towards the ultra-green aircraft design is weight reduction. Reducing structural weight directly translates to increased flexibility of the airframe - a "wake-up call" for aeroelasticians:

- *New aircraft configurations are "terra incognita".*
  There is little empirical knowledge to rely on, analysis tools may not suit the particular needs of that design, modelling techniques will have to be adapted or improved, decision makers and authorities may be reluctant to go ahead, etc. This "climate of uncertainty" also raises the bar for aeroelastic analysis and certification.
- *Increased structural flexibility of the airframe, although in certain ways a disadvantage, may also be exploited.*
  Concepts like aeroelastic tailoring or actively controlled aerodynamic measures may reduce fatigue, gust or manoeuvre loads. The flexibility may also be used to adapt to off-design conditions and thus increase the actual cruise performance.
- *Low-drag wings will be a challenge for the aeroelastic design.*
  The future low-drag wing is expected to have: high-aspect-ratio, little or even negative

sweep, laminar flow and complex flap/slat systems. Local flow separation and shock waves will make high demands on CFD analysis and wind tunnel experiments. Large high-bypass-ratio engines, if attached to the wing, will add additional complexity. For laminar flows, little is known so far of the effects of oscillations of the transition point on aeroelastic stability.

- *A higher level of integration usually results in an increased probability of aeroelastic interactions.*
  Even for new, unacquainted configurations there is one experience the designer or engineer can rely on - pushing the limits in terms of performance and efficiency often leads to unforeseen, and sometimes critical aeroelastic interactions, such as wing-store-LCO, wing-tail-buffet or engine oscillations.
- *The benefits of new technologies have to materialise for the flying aircraft.*
  Local improvements by new technologies may result in adverse effects for the actual aircraft, e.g. because of unfavourable structural deflections or increased trim drag. Designers and engineers must be able to evaluate the eventual gain of a new technology for the overall aircraft.

Designing an ultra-green aircraft design raises high demands on researchers, designers and engineers. This also holds for the discipline of aeroelasticity.

3.3 Activities at the DLR Institute of Aeroelasticity

The *DLR Institute of Aeroelasticity* prepares for this challenge by focusing its strategic research on two key aspects: to further advance its capabilities for detailed investigation of local and global aeroelastic mechanisms, and to embed its methods and tools in an integrated aircraft design environment.

The DLR project *High Performance Flexible Aircraft* (HighPerFLEX, 2004-2006) has paved the way towards these goals. The successor *Integrated Green Aircraft* (iGREEN, 2007-2010) continues the research of HighPerFLEX, concentrating on questions which are of particular interest for aircraft concepts which are designed to achieve a technology leap in respect of environmental sustainability, but will also be beneficial if the trend of the last three decades of evolutionary "small steps" prevails.

The work of HighPerFLEX and iGREEN, as well as that of other projects, has lead to some observations which are connected with aeroelasticity (the only established aeronautical discipline which, by definition, addresses multidisciplinary design), or with the somewhat wider frame of multidisciplinary design and optimisation. These observations will follow in the next section. The reader should keep in mind that these aspects are a personal view and intended to initiate an open discussion at a workshop on *Multidisciplinary Technology and Modeling*, and do not necessarily represent the opinion of all researchers, scientists or engineers at the Institute of Aeroelasticity, or DLR in general.

4 Some Aspects of Multidisciplinary Design on the Example of the Ultra-Green Aircraft

▶ In times of supercomputing and high-fidelity CAx, low- and medium-fidelity methods are important as ever.

Computer power is getting very cheap these days. A combination of off-the-shelf PCs, like Beowulf-Clusters, are matching the performance of the most advanced supercomputers of the 1980ies, but are affordable for the budget of rather small units like institutes and departments.

It is a sweet temptation to use sheer computer power to run parameter variations and optimisations of large high-fidelity models, in the hope to receive the optimal, high-fidelity solution.

But unfortunately, in the real world it is often not that easy:

- Although high-fidelity jobs can nowadays be executed comparatively fast, they still take their time. This limits the number of variations which can be examined. It often pays off to investigate a large design space with analyses of moderate complexity, than to limit the design space to a first, hopefully good guess and then explore it in high-fidelity.
- Performing a medium-fidelity analysis which captures all relevant physical effects, but is still relatively cheap to compute, is a job for an experienced engineer. But inexperienced users are not necessarily achieving better results when applying high-fidelity methods.
- If a good, feasible and robust design has been found by not-so-high fidelity methods, the results can still be crosschecked, "verified" and adjusted by high-fidelity analysis.
- Generating complex models which represent reality down to the tiny detail is more an art than a routine job. Automatically adapting complex models to design changes, e.g. as required in optimisation loops, may lead to very detailed results - but if these results still reflect reality is questionable.
- Last but not least, low- and medium fidelity methods prove to still deliver relevant results, even for complex problems.

An illustrative example which may underline this plea for medium-fidelity analysis derives from the HighPerFLEX/CTARP project WIONA (wing with oscillating nacelle), a joint DLR/ONERA experiment. The objective of this experiment was to investigate an nacelle-pylon-wing interference effect which can cause violent nacelle/engine oscillations, [6]. This potential aeroelastic instability was caused by unsteady shock wave/boundary layer interactions, Figure 4.

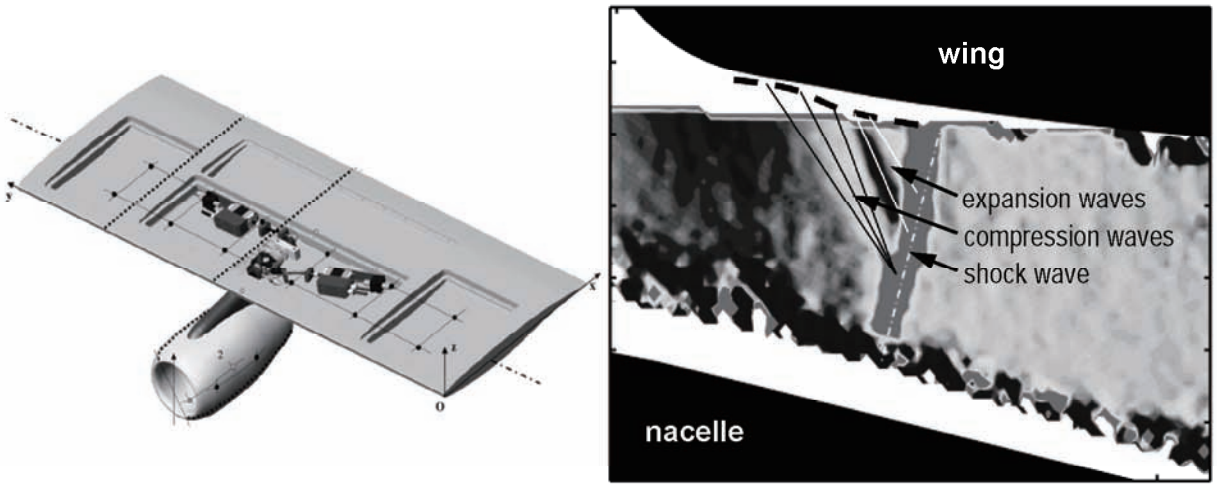

Figure 4 *Research project WIONA: sketch of the model with excitation system (left) and PIV-evaluated, streamwise development of mechanical energy for the maximum downstream shock location*

Engine-wing interference scenarios, including the WIONA experiments, were also simulated, using the low-/medium-fidelity method TDLM (transonic doublet lattice method) and steady and unsteady RANS computations with the DLR-code TAU and the ONERA-code elsA, [7-9]. The results revealed that even for complex problems like this, the unpretentious but fast TDLM gave a fair representation of the real-world behaviour, Figure 5. The take-away of these

tests: for verifying a clearly defined setting, the RANS solvers performed superbly and cannot be substituted, but for most design purposes, a cost/benefit-comparison would have clearly favoured a conceptual/preliminary, multidisciplinary lay-out using methods like TDLM, and few RANS verification jobs to receive supporting points or investigate equivocal results.

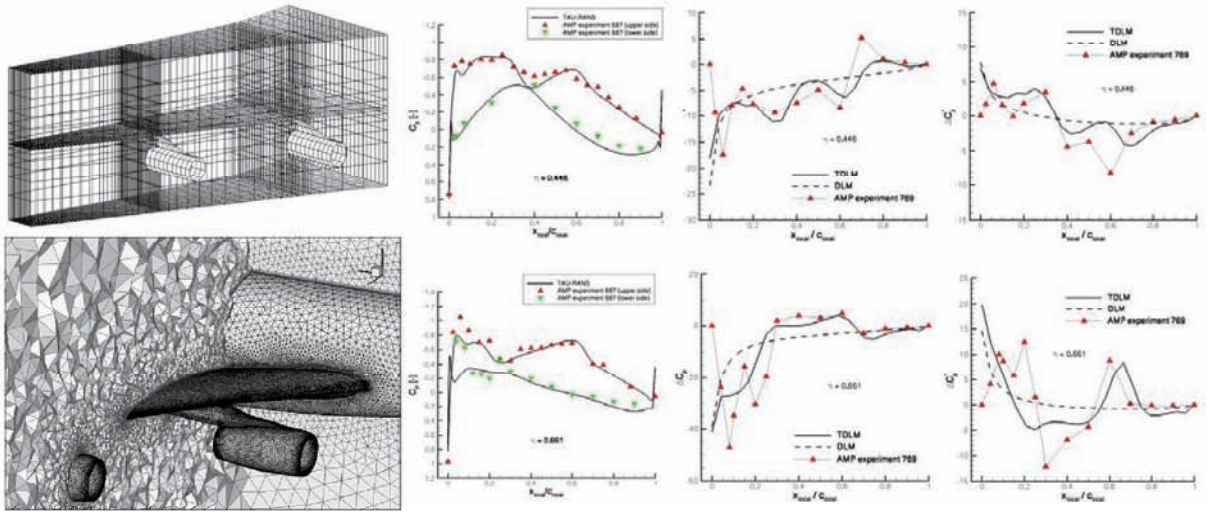

Figure 5 *Unsteady C_p distribution (real and imaginary components) for AMP WBPN model comparing TDLM and steady RANS results with experimental data (pure pitching motion, ω*=0.369, Ma=0.820, α=1.80°, Re=3.57*10^6)*

▶ Surrogate modelling by RSM, Kriging or splines is not the answer to everything

Especially on conceptual and preliminary design level and for multidisciplinary and/or multi-level optimisation, surrogate modelling techniques are used to take the place of expensive disciplinary analyses. These surrogate models are basically approximation methods to interpolate between supporting points. Methods like response surface methods (RSM), Kriging, n^{th}-order splines and, to some extent, neural networks are simple to use and (with some restrictions in respect to Kriging) robust in optimisation. Supporting points are often defined using design of experiment (DOE) methods, allowing to cover a wide parameter field with a minimum of points, and to run all necessary computations automatically.

The number of supporting points, each of which requires its own high-fidelity analysis, may grow with $O(c^n)$ in respect to the number of (independent) design variables, respectively the number of those which are picked as explanatory variables, depending on the DOE method used. This may prove to be quite costly for time-consuming jobs like CFD. Additionally, the problem of having to adapt the high-fidelity model to cover the design space does also exist here. The most important point, however, is that during complex optimisations, when a design variable which is not an explanatory variable is modified, the surrogate model has to be re-generated for the DOE parameter set.

An alternative is the use of physically reduced models. The idea of this class of models is to extract the important physical properties of a disciplinary model, e.g. using linearisation or Taylor series, or, sometimes, "engineering intuition" to condense on the important characteristics of the high-fidelity model, respectively reality. Well-known, established physically reduced models can be found in structural mechanics, such as the beam models of *Euler-Bernoulli* and *Timoshenko* for long, slender ("one-dimensional") elements, or the *Ritz approach* to use eigen- and/or static modes to represent a more complex flexible structure.

With setting up a number of well-defined boundary conditions, like the Kirchhoff assumptions of the Euler-Bernoulli beam, the strengths and limitations of the model reduction can be assessed more reliably, and the region of trust is usually larger than that of surrogate models. Alterations of global design variables may also necessitate a re-computation to modify the reduced model, but those are usually cheap compared to the effort necessary to generate an entirely new surrogate model for a large set of explanatory variables.

An example of adapted model reduction is the multibody simulation of a landing aircraft, which was used in an integrated design exercise to harmonise the work share between airframer and landing gear manufacturer. The simulation brings together the disciplines of mechanical dynamics, structural mechanics, aerodynamics and control. Controlled elements are included by co-simulation or code-export, structural flexibility is represented by a set of linearised base functions, and the aerodynamic effects of structural deformation are coupled directly in the equation of motion, [10]. The result is a fast-performing analysis of a complex scenario with a very reasonable level of fidelity.

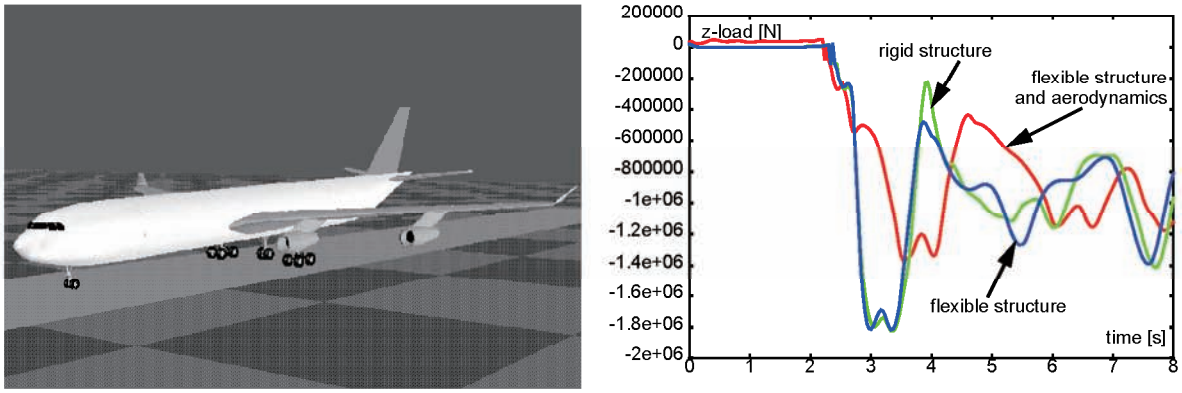

Figure 6 *Multibody simulation of the touch-down of a large transport aircraft (left), vertical load on the main landing gear leg attachment (right) comparing: certification requirement (rigid airframe), industry standard (flexible airframe) and including aerodynamic effects of airframe deformation (flexible and aerodynamics)*

▶ The optimal solution to a local problem is not the solution to the optimal aircraft

Today's aircraft are highly integrated systems, and it is safe to assume that an ultra-green commercial transport aircraft will have an even higher degree of internal interrelations. The consequences are well explained by a quote from Curtis Johnson of Sierra Engineering, Inc., a provider of liquid propulsion systems, (2006):

"Lately our program for doing optimization of this upper stage rocket engine (the USET program) has been showing much success. We now can routinely run overnight optimizations that show a much higher degree of fidelity than anything we have seen before. The system optimizations are pretty interesting too. For example the results are showing that overall engine weight can be minimized by de-tuning some components (and making them heavier) so that other components can be made smaller and lighter. This was something that was not previously done in this field where everything is made to push performance."

The application of multidisciplinary optimisation (MDO) in industry has, for the most part, started in the detail design phase and is now moving upstream into the preliminary design stages. MDO has also been introduced at the conceptual design level, where low complexity models are handled by a manageable number of software tools. Applications there are now

moving in the opposite direction further downstream, but it will still take its time until both lines of attack merge in preliminary design. The ultimate goal, however, is to achieve a highly integrated but flexible, physics-based multidisciplinary optimisation. Figure 7 is a depiction of Boeing's systematic progress toward full aircraft MDO, [11].

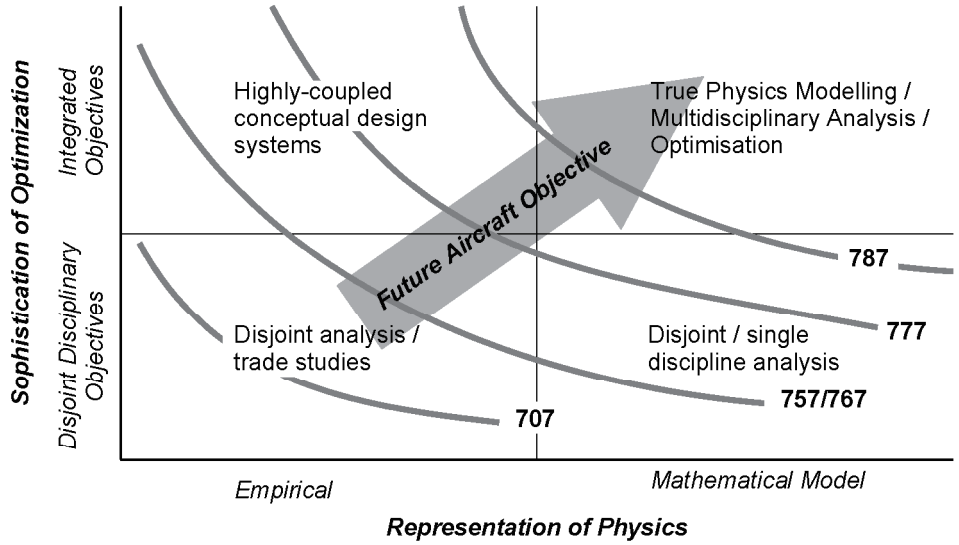

Figure 7 *Development of MDO in aircraft design across the successive jet airliner families of Boeing*

DLR is devoting considerable effort to enhance its R&D activities on system, i.e. the overall aircraft, and to even look beyond the single aeroplane and to investigate the air transport system in a holistic approach. iGREEN is the institute's strategic approach to closely connect aeroelasticity with the systems level:

- Being part of the integrated design platform will boost the efficiency, especially for generating or modifying models, and to feed back the results into "the system".
- Highly flexible novel configurations require the aeroelastician to be part of the entire design cycle, from conceptual design until roll-out and certification.

▶ Multidisciplinary design is communication - not only between software tools, but between people

R. Belie, [12], distinguishes between four layers which have to be connected in multidisciplinary problems: the disciplinary layer, the data layer, the human layer and the organisational layer. When challenged by a multidisciplinary problem, aircraft designers, engineers, managers and especially IT specialists are often enthusiastic about tackling the disciplinary and data layer. The human layer is about people-to-people communication, mostly team members. The negative effects of too little, wrong and also too much communication as well as the manifold pitfalls of misunderstanding are known. Overcoming these shortcomings is possible, albeit in no way easy - an entire consulting branch is living quite well from it. Most critical, and also most political, is the organisational layer. People may recognise the need for multidisciplinary work, but in the end of the day the salary of an employee and the budget of a department depends on how the very own work was done - in most cases, providing help to other entities to do a better job and to build a better product, e.g. by preparing and exchanging data, is not being rewarded.

A survey, [13], taken in 2006 among American aerospace companies on the current strength and weaknesses of multidisciplinary design revealed that although hardware, simulation software and MDO software limitations exist, a majority of managers and engineers saw organisational barriers as the major obstacle to multidisciplinary design, respectively MDO, Figure 8.

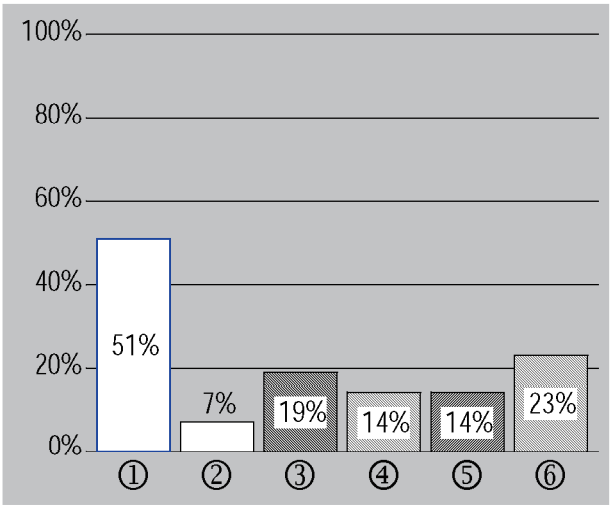

Figure 8 *Barriers for the employment of MDO (multiple answers possible)*

Also illustrative is the success of the Aerospace Systems Design Laboratory (ASDL) of the Georgia Institute of Technology, [14], which brings together designers, engineers and decision makers - not to exchange results generated at their respective working places and return with the intention to work in a multidisciplinary way, but to offer them the possibility to work interactively towards a common goal while at ASDL and then return to further detail the achieved results.

5 Conclusions

Lessons-learned of the last aircraft development programs, in Europe, in the USA and elsewhere, have shown that integration is a critical issue: it offers most potential for improving the product's performance and competitiveness, but getting it wrong can be very costly, and sometimes even dangerous. It is very important to have deep insight into the various disciplinary technologies, but excellent aerodynamics, the ultimate lightweight structure and the best engine alone do not necessarily add up to the best aircraft - harmonising the disciplinary excellence is crucial, too.

This plea for not forgetting the big picture may be concluded by the words of Edgar Allan Poe's narrative character C. Auguste Dupin, [15]:

"He erred continually by the very intensity of his investigations. He impaired his vision by holding the object too close. He might see, perhaps, one or two points with unusual clearness, but in so doing he, necessarily, lost sight of the matter as a whole. Thus there is such a thing as being too profound. Truth is not always in a well."

6 Acknowledgements

The author wishes to express his gratitude to all his collegues at the DLR Institute of Aeroelasticity, whose hard work and resulting achievements have made this paper possible. Special thanks go to Dr. R. Voß and the team of HighPerFLEX.

7 References

[1] *Climate Change 2007*, 4th Assessment Report (AR4) of the United Nations Intergovernmental Panel on Climate Change (IPCC), 2007;
http://ipcc-wg1.ucar.edu/wg1/wg1_ar4.html

[2] *European Aeronautics: A Vision for 2020*, 2001;
http://www.acare4europe.com/docs/Vision%202020.pdf

[3] ACARE: *Strategic Research Agenda 1*, Advisory Council for Aeronautics Research in Europe , 2002, and
ACARE: *Strategic Research Agenda 2*, Advisory Council for Aeronautics Research in Europe, 2004;
http://www.acare4europe.com/html/background.shtml

[4] D. Schmitt: *Bigger, Faster, Greener, Cheaper? Developing the AIRBUS Response to the Vision 2020 Demands*;
in: *Proceedings of the 24th ICAS Congress*, International Council of the Aeronautical Sciences; Yokohama, Japan; 2004.

[5] A.D. Gardner, J. Nitzsche, J. Neumann, K. Richter, H. Rosemann, R. Voss: *Adaptive Load Redistribution Using Mini-TEDs*;
in: *Proceedings of the 25th ICAS Congress*, International Council of the Aeronautical Sciences; Hamburg, Germany; 2006.

[6] G. Dietz, H. Mai, A. Schröder, C. Klein, N. Moreaux, P. Leconte: *Unsteady Wing-Pylon-Nacelle Interference in Transonic Flow*;
in: *Proceedings of the 48th AIAA/ASME/ASCE/AHS/ASC Structures, Structural Dynamics and Materials Conference*; AIAA American Institute of Aeronautics and Astronautics; Waikiki, Hi, USA; 2007.

[7] A. Soda, R. Voss: *Analysis of Transonic Aerodynamic Interference in the Wing-Nacelle Region for a Generic Transport Aircraft*;
in: *Proceedings of the International Forum on Aeroelasticity and Structural Dynamics (IFASD) 2005*; Munich/München, Germany; 2005.

[8] A. Soda, T. Tefy, R. Voß: *Numerical Simulation of Steady and Unsteady Aerodynamics of the WIONA (Wing with Oscillatine Nacelle) Configuration*;
in: *New Results in Numerical and Experimental Fluid Mechanics*, Vol. V, pp. 330-337; edited by H.-J. Rath, C. Holze, H.-J. Heinemann, R. Henke, H. Hönlinger; Springer, Berlin,Germany; 2006.

[9] J. Nitzsche, A. Schröder: *Unsteady Transonic Wing- Pylon- Nacelle Interference - Investigation and CFD Validation by the WIONA Test*;
ONERA-DLR Aeropace Symposium ODAS 2007; Göttingen, Germany; 2007.

[10] M. Spieck, W. R. Krüger, J. Arnold: *Multibody Simulation of the Free- Flying Elastic Aircraft*;
in: *Proceedings of 46th AIAA/ASME/ASCE/AHS/ASC Structures, Structural Dynamics*

and Materials Conference / 1st AIAA Multidisciplinary Design Optimization Specialist Conference; AIAA American Institute of Aeronautics and Astronautics; Austin, TX, USA; 2005.

[11] K. Fowler: *Application of Multidisciplinary Optimization Methods on the Boeing 787 Dreamliner*;
in: *Proceedings of 2006 European-U.S. MDO Colloquium*; Göttingen, Germany; 2006

[12] R. Belie: *Nontechnical Barriers to Multidisciplinary Optimization in the Aerospace Industry*;
in: *Proceedings of the 9th AIAA/ISSMO Symposium on Multidisciplinary Analysis and Optimization*; AIAA American Institute of Aeronautics and Astronautics; Atlanta, GA, USA; 2002.

[13] Brett Malone: *Network Based MDO Integration*;
in: *Proceedings of 2006 European-U.S. MDO Colloquium*; Göttingen, Germany; 2006

[14] D. Mavris, P. Biltgen, N. R. Weston: Advanced Design of Complex Systems Using the Collaborative Visualization Environment (CoVE);
in: Proceedings of the 43rd AIAA Aerospace Sciences Meeting and Exhibit; AIAA-2005-0126; AIAA American Institute of Aeronautics and Astronautics; Reno, NV, USA; 2005.

[15] Edgar Allan Poe: *The Murders In The Rue Morgue*

Optimum Aeroelastic Design of Flapping Wing for Micro Air Vehicles

Koji Isogai, Yuichi Kamisawa, Yohei Harino, and Hiroyuki Sato
Nippon Bunri University
1727 Oaza Ichigi, Oita, Japan

Abstract

A method is presented for the optimum aeroelastic design of a flapping wing employing lifting-surface theory as an aerodynamic tool and the complex method as the optimization algorithm. The method is applied to the optimum design of a flapping wing of a Kite Hawk (Milvus migrans) UAV and the optimum thickness distribution of the main-spar is determined. As the result of the optimization, a high propulsive efficiency of 75% is attained considering only dihedral flapping of the main spar. By evaluating the viscous effect for this optimum design using a three-dimensional Navier–Stokes code, the effectiveness of the design is confirmed.

I. Introduction

Bird-type aerial vehicles with flapping wings have attracted considerable interest for their possible use in wide ranging monitoring and surveillance activities. Although several such vehicles have been developed to date, most have employed membrane type wings. However, membrane wings are not efficient since the feathering (twisting) motion, which is essential for efficient flapping flight, does not occur in an ideal manner (a 90 deg advance phase angle of feathering motion ahead of flapping motion is usually the most efficient). However, Delaurier and Harris [1, 2] have developed an ornithopter that has double solid surface airfoil sections and uses aeroelastic deformation to generate a twisting motion by dihedral flapping. To obtain favorable aeroelastic deformation, they developed a design program called ComboWing that determines the optimum aeroelastic design of a flapping wing. They employed strip theory as an aerodynamic tool and conducted the optimization manually, without using an automated optimization algorithm.

The purpose of the present study is to develop an automated optimum aeroelastic design method using a more accurate aerodynamic tool, namely, unsteady lifting-surface theory. The new method is then applied to the design of the flapping wing of a Kite Hawk (Milvus migrans) UAV (Unmanned Air Vehicle). The optimum design thus obtained is examined by numerical simulation using a

three-dimensional Navier–Stokes code.

II. Equations of Motion for Elastic Flapping Wing and Solution Procedure Using Doublet Lattice Method

In this section, the basic equations of motion for an elastic flapping wing are derived using Lagrange's equations of motion. The solution procedure using the Doublet Lattice Method (DLM) [3] as the aerodynamic tool is also described. In Fig. 1, the coordinates and the definition of the wing displacement are shown. In the figure, T is time and F(X,Y,T) is the displacement of the wing mean surface at an arbitrary point (X,Y) on the wing. F can be expressed by the following equation:

$$F(X,Y,T) = F_r(X,Y,T) + \sum_{i=1}^{N} \phi_i(X,Y) q_i(T) \qquad (1)$$

where $F_r(X,Y,T)$ is the displacement of the rigid wing due to forced oscillation, $\phi_i(X,Y)$ is the i-th natural vibration mode of the wing and $q_i(T)$ is the i-th generalized coordinate of the elastic deformation. For this wing displacement, the kinetic energy of the wing can be expressed as

$$K = \iint_S \tfrac{1}{2} m(X,Y)(dZ/dT)^2 \, dXdY \qquad (2)$$

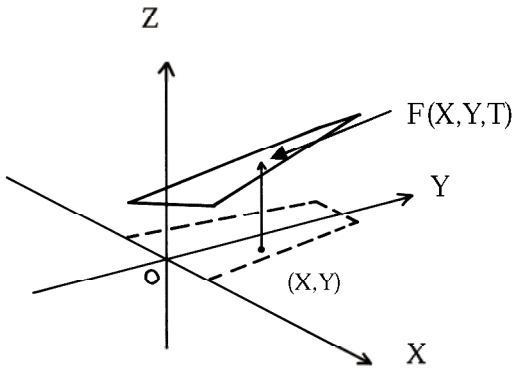

Fig. 1 Definitions of coordinates.

where m(X,Y) is the wing mass per unit area and where $\iint_S$ represents the surface integral on the full span wing area. The strain energy of the wing can be expressed as

$$U = \tfrac{1}{2} \omega_i^2 M_i q_i^2(T) \qquad (3)$$

where ω_i is the i-th natural circular frequency of the wing, and where M_i is the generalized mass given by

$$M_i = \iint_S m(X,Y)\phi_i^{\,2}(X,Y)dXdY \qquad (4)$$

The virtual work done by the external force (aerodynamic force) due to the virtual displacement δq_i of the i-th generalized coordinate can be given by

$$\delta W = \iint_S \Delta P(X,Y,T)\phi_i(X,Y)dXdY\delta q_i \qquad (5)$$

where ΔP is the pressure difference between the upper and lower surfaces of the wing. From Eq. (5) and by the definition of the generalized force Q_i, that is $\delta W=Q_i\delta q_i$, Q_i can be given by

$$Q_i = \iint_S \Delta P(X,Y,T)\phi_i(X,Y)dXdY \qquad (6)$$

Substituting Eqs. (2), (3) and (6) into Lagrange's equations of motion, we finally obtain the general expressions for the equation of motion of an elastic flapping wing as

$$M_i(d^2q_i/dT^2) + \omega_i^{\,2}M_iq_i =$$

$$-\iint_S m(X,Y)\phi_i(X,Y)(d^2F_r(X,Y,T)/dT^2)dXdY$$

$$+\iint_S \Delta P(X,Y,T)\phi_i(X,Y)dXdY, \quad i=1,\ldots,N \qquad (7)$$

In deriving Eq. (7), we use the orthogonal condition of the natural vibration modes. In Eq. (7), the displacement $F_r(X,Y,T)$ of the rigid wing or the forced oscillation of the un-deformed wing can be expressed as

$$F_r(X,Y,T) = (H_r + \phi_0 Y)\cos(\omega T) - (\theta_r + b_\theta Y)(X-A)\cos(\omega T + \phi) \qquad (8)$$

where H_r and θ_r are the amplitudes of the heaving and pitching oscillations at the root station, respectively, ϕ_0 is the flapping oscillation amplitude, b_θ is the rate of twist of the feathering oscillation amplitude, A is the X coordinate of the feathering axis and ϕ is the advance phase angle of the feathering oscillation ahead of the flapping oscillation. (See also Fig. 2 for the definitions of flapping wing motion.)

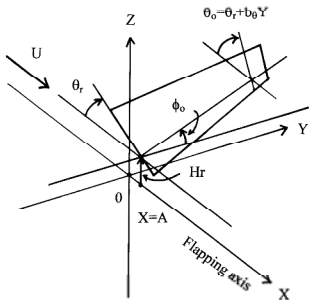

Fig. 2 Definitions of wing motion.

The load distribution $\Delta P(X,Y,T)$ is expressed as

$$\Delta P(X,Y,T) = \tfrac{1}{2}\rho U^2\{\Delta C_P^{(F)}(X,Y,T) + \sum_{j=1}^{N}\overline{\Delta C_{Pj}}(X,Y)q_j(T)\} \qquad (9)$$

where $\Delta C_P^{(F)}$ is the pressure difference coefficient due to the rigid wing displacement and $\overline{\Delta C_{Pj}}$ is the pressure difference coefficient due to the j-th natural vibration mode. By assuming sinusoidal wing motion and introducing a complex expression, $\Delta C_P^{(F)}$ and q_j can be expressed as

$$\Delta C_P^{(F)}(X,Y,T) = \overline{\Delta C_P^{(F)}}(X,Y)e^{i\omega T} = \overline{\Delta C_P^{(F)}}e^{ikt}$$

$$q_i = \overline{q_i}e^{i\omega T} = \overline{q_i}e^{ikt} \qquad (10)$$

where $\overline{\Delta C_P^{(F)}}$ and $\overline{q_i}$ are complex quantities.

$F_r(X,Y,T)$ of Eq. (8) can be expressed as

$$F_r(X,Y,T) = (H_r + \phi_0 Y)e^{i\omega T} - (\theta_r + b_\theta Y)(X-A)e^{i(\omega T+\phi)} \qquad (11)$$

By substituting Eqs. (9), (10) and (11) into Eq. (7), and by non-dimensionalizing Eq. (7) using the root semichord b_0, we obtain the matrix form of Eq. (7) as

$$\left\{\left[(\omega_i/\omega)^2 - 1\right] - \left[A_{ij}\right]\right\}\left\{\overline{q_j}\right\} = \left\{\overline{F_i}\right\} \qquad (12)$$

where

$$A_{ij} = \frac{1}{k^2}\left(\frac{\rho b_0^4}{M_i}\right)\left\{\int_0^s\int_{\xi_l}^{\xi_t} \overline{\Delta C_{pj}}(x, y)\phi_i(x, y)dxdy\right\} \qquad (13)$$

$$\overline{F_i} = \frac{2b_0^3}{M_i}\int_0^s\int_{\xi_l}^{\xi_t} m(x, y)(h_r + \phi_0 y - (\theta_r + b_\theta z)(x - a)e^{i\phi})\phi_i(x, y)dxdy$$

$$+\frac{1}{k^2}\left(\frac{\rho b_0^4}{M_i}\right)\int_0^s\int_{\xi_l}^{\xi_t} \overline{\Delta C_p^{(F)}}(x, y)\phi_i(x, y)dxdy \qquad (14)$$

$\overline{\Delta C_{pj}}$ can be computed by solving the integral equations of the lifting-surface theory [3], namely,

$$(ik\phi_j + \frac{\partial\phi_j}{\partial x})/b_0 = \frac{1}{8\pi}\iint_S \overline{\Delta C_{pj}}(\xi,\eta)K_{WT}(x, y;\xi,\eta)d\xi d\eta \qquad (15)$$

where K_{WT} is the kernel function. Similarly, $\overline{\Delta C_p^{(F)}}$ in Eq. (14) can be found by solving the integral equation of the lifting surface theory [3], namely,

$$ik(h_r + \phi_0 y - (\theta_r + b_\theta y)(x - a)e^{i\phi}) - (\theta_r + b_\theta y)e^{i\phi} = \frac{1}{8\pi}\iint_S \overline{\Delta C_p^{(F)}}(\xi,\eta)K_{WT}(x, y;\xi,\eta)d\xi d\eta \qquad (16)$$

In Eqs. (13)–(16), x, y, ξ and η are dimensionless coordinates obtained by dividing the physical coordinates by b_0, a is the x coordinate of the feathering axis, h_r is the dimensionless heaving amplitude at the root station, ξ_l and ξ_t are the x coordinates of the leading and trailing edges, respectively, and s is defined by l/b_0 with l the semi-span length. We employ the DLM to solve Eqs. (15) and (16).

By solving Eq. (12) for a given forced motion and the natural vibration characteristics of the wing, we can compute the load distributions $\Delta P(X, Y, T)$ using Eq. (9) in complex form as

$$\overline{\Delta P}(x, y)e^{ikt} = \tfrac{1}{2}\rho U^2\overline{\Delta C_p}(x, y)e^{ikt} = \tfrac{1}{2}\rho U^2(\overline{C_p^{(F)}}(x, y) + \sum_{j=1}^{N}\overline{\Delta C_{pj}}(x, y)\overline{q_j})e^{ikt} \qquad (17)$$

Once $\Delta P(x, y, t)$ is given, the time averaged thrust and necessary power can be computed as follows. The time averaged thrust $\overline{T}$ is composed of two components, the leading edge suction $\overline{T_L}$ and the thrust induced by tilting the normal force vector due to the feathering motion $\overline{T_D}$:

$$\overline{T} = \overline{T_L} + \overline{T_D} \tag{18}$$

$$\overline{T} = \tfrac{1}{2}\rho U^2 S\overline{C_T} = \tfrac{1}{2}\rho U^2 S(\overline{C_{TL}} + \overline{C_{TD}}) \tag{19}$$

where $\overline{C_{TL}}$ is the thrust coefficient due to leading edge suction and $\overline{C_{TD}}$ is the thrust coefficient due to the tilt of the normal force vector. $\overline{C_{TL}}$ can be computed by a procedure similar to that proposed by Lan [4] for the quasi-vortex lattice method.

First, we compute the leading-edge singularity parameter [4] $\overline{C_S}$ using $\overline{\Delta C_p}$ in Eq. (17):

$$\overline{C_S}(y) = \tfrac{1}{2}\overline{\Delta C_p}(x_{l,lp}, y)\sqrt{\frac{(x_{l,lp} - x_l)}{2}} \tag{20}$$

where $x_{l,lp}$ is the x coordinate of the midpoint of the lifting line of the leading edge panel [3] and x_l is the x coordinate of the leading edge. It should be noted that $x_{l,lp}$ and x_l are functions of y. Using $\overline{C_S}$ thus determined, we finally compute $\overline{C_{TL}}$ as

$$\overline{C_{TL}} = \frac{2b_0^2}{S}\int_0^s \left\{\pi\overline{C_s^2}/(2\cos\Lambda_e)\right\}C(y)dy \tag{21}$$

where C(y) is the dimensionless local chord length and Λ_e is the sweep angle of the quarter chord line of the leading edge panel. In Eq. (21), $\overline{C_S^2}$ can be given by

$$\overline{C_S^2}(y) = (C_{SR}^2(y) + C_{SI}^2(y))/2 \tag{22}$$

where C_{SR} and C_{SI} are the real and imaginary parts of $\overline{C_S}$ given by Eq. (20). It should be noted that the number of chord-wise and span-wise panels should be more than 30 in order to obtain a converged solution of $\overline{C_{TL}}$.

$\overline{C_{TD}}$ can be given by

$$\overline{C_{TD}} = \overline{T_D}/(\tfrac{1}{2}\rho U^2 S)$$
$$= \tfrac{1}{T^*}\int_0^{T^*}\left\{\iint_S \mathrm{Re}(\overline{\Delta P}(X,Y)e^{i\omega T})\,\mathrm{Re}(\frac{\partial F}{\partial X})dXdY\right\}dT/(\tfrac{1}{2}\rho U^2 S) \tag{23}$$

where Re indicates the real part of a complex quantity and T* is the period of the forced oscillation. We can easily derive the working form of $\overline{C_{TD}}$ by substituting Eq. (17) and the complex form of Eq. (1) into Eq. (23). The time mean necessary power coefficient $\overline{C_{PW}}$ can be given by

$$\overline{C_{PW}} = \overline{W}/(\tfrac{1}{2}\rho U^3 S)$$
$$= -\tfrac{1}{T^*}\int_0^{T^*}\left\{\iint_S \mathrm{Re}(\overline{\Delta p}(X,Y)e^{i\omega T})\,\mathrm{Re}(\frac{\partial F}{\partial T})dXdY\right\}dT/(\tfrac{1}{2}\rho U^3 S) \tag{24}$$

where $\overline{W}$ is the time mean rate of work. We can easily derive the working form of $\overline{C_{PW}}$ by substituting Eq. (17) and the complex form of Eq. (1) into Eq. (24). Then the propulsive efficiency η_p is defined by

$$\eta_p = \frac{\overline{TU}}{\overline{W}} = \frac{\overline{C_T}}{\overline{C_{PW}}} \tag{25}$$

III. Optimum Aeroelastic Design Using the Complex Method

By combining the general method for computing the aeroelastic effects of an elastic flapping wing, described in the previous section, and an optimization algorithm, we can conduct an optimum structural design of a flapping wing. For the optimization algorithm, we employed the complex method, originally proposed by Box [6]. The complex method is a direct search method that can handle multiple constraints without recourse to gradients. In the present study, we applied the optimization procedure to the design of a bird-like UAV that flies slowly like a Kite Hawk (Milvus migrans). As is well known, Kite Hawk is an expert of an efficient flight, namely, it finds the thermal convection and can perform continuous flight only by occasional flapping. If we could develop an UAV which imitates such flight of Kite Hawk, it might provide a highly efficient (long duration) UAV. In Fig. 3, the planform and structural arrangement of the semispan wing of the Kite Hawk

UAV are shown. The full span of the wing is 1.68 m and the root chord length is 0.28 m. The full span aspect ratio and wing area are 6 and 0.471 m^2, respectively. The total mass of the UAV is assumed to be about 300 g. The wing can sustain a total weight of 2.94 N at a cruising speed of 4.13 m/s at $C_L = 0.598$. The structural component consists of only a straight main-spar that can bend and twist and which is located near the leading edge, as shown in the Fig. 3. The ribs are assumed to be firmly attached to the main spar and are chord-wise rigid. It is assumed that the flapping wing motion is caused only by the dihedral flapping motion of the main spar. Therefore, the feathering motion is induced only by the aeroelastic response.

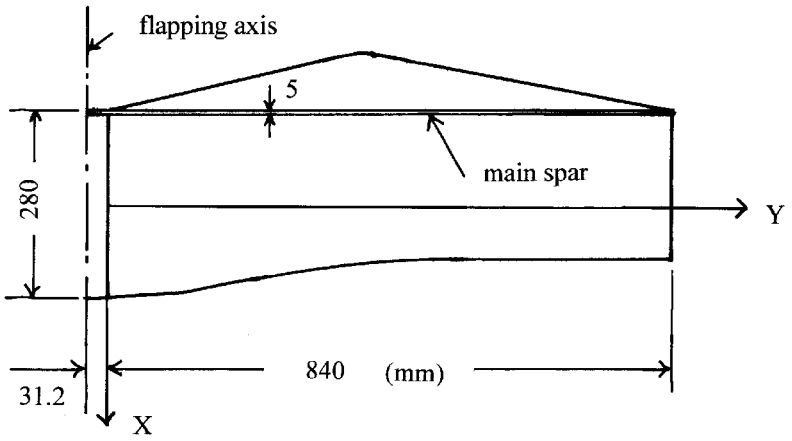

Fig. 3 Planform of Kite Hawk (Milvus migrans) UAV.

The purpose of the optimization study is to determine the thickness distribution of the main spar that generates the ideal bending and twisting motions to attain maximum propulsive efficiency. The section of the main spar is assumed to be rectangular and its width is assumed to be a constant 5 mm in the span-wise direction. The thickness distribution is assumed to be a parabolic function of y. We select thicknesses t_1, t_2 and t_3 at the root, mid-semispan and tip stations, respectively, as design variables to determine the structural characteristics. In addition to these design variables, we select k, ϕ_0 and a as design variables that determine the flapping wing motion. Therefore, there are six design variables in total. The objective function is the propulsive efficiency η_p. The following constraints are imposed, $\overline{C_T} \geq C_D$ and $t_1 \geq t_2 \geq t_3$, where C_D is the total drag coefficient of the UAV. Since the flapping wing is composed of a single-spar, we employ simple beam theory [7] to compute the natural vibration modes. The distributions of the mass m, static unbalance S_y and the moment of inertia I around the main spar are taken to be the concentrated quantities at the center of

the segment obtained by dividing the main spar into 13 equally spaced portions. It should be noted that the inetial data of the main spar itself changes at each iteration step of the optimization process. The value of the concentrated mass, imbalance and inertia at each segment are assumed to be equal and given as $m_i = 0.005$ kg, $Sy_i = 7.0\times10^{-5}$ kgm and $I_i = 5.0\text{x}10^{-5}$ kgm^2, for i = 1−13. The main spar is assumed to be a quasi-isotropic laminate construction of CFRP with elastic properties E_L = 181 Gpa, E_T = 10.3 GPa, G_{LT} = 7.17 GPa and $\nu = 0.28$.

In the present problem we set C_D to be 0.15. This value is considerably higher than the value of 0.055 estimated by the DLM code (assuming a minimum drag coefficient of 0.04 and an induced drag coefficient of 0.015 at $C_L = 0.598$). However, we assumed the DLM code would underestimate C_D as it does not account for viscous effects. This choice of C_D=0.15 will be justified in the next section by the numerical simulation using a Navier−Stokes code.

A converged solution was obtained after 50 iterations. The results were as follows:

$\eta_p = 0.754$, $\overline{C_T} = 0.166$ ($\overline{C_{TL}} = 0.089$, $\overline{C_{TD}} = 0.077$),

$\overline{C_{PW}} = 0.220$,

$k = 0.213$, $\phi_0 = 48.9$ deg., $a = -0.986$,

$t_1 = 5.76$ mm, $t_2 = 2.08$ mm, $t_3 = 0.92$ mm

The propulsive efficiency of 75% seems quite high. (Note that 75% of η_p is obtained for mean angle of attack 0 deg. Therefore, the induced drag due to the averaged lift is not taken into account in evaluating η_p.) Since the optimum value of the reduced frequency is 0.213, we can easily determine the cruising velocity to be U_C = 4.13 m/s by assuming a forced flapping frequency of 1 Hz. We can then easily estimate $C_L = 0.598$ to sustain a weight of 2.94 N at U_C = 4.13 m/s. The time mean necessary power $\overline{W}$ is 4.47 W and the power–mass ratio for this UAV is 14.9 W/kg, which seems quite efficient. The natural frequencies of the wing are f_1 = 1.65 Hz (1st bending predominant), f_2 = 5.93 Hz (1st torsion predominant), f_3 = 13.7 Hz (2nd torsion predominant). The six total natural vibration modes are employed in computing the aeroelastic responses. In Figs. 4, the wing deformations during one cycle of oscillation are shown. (Note that the wing displacement shown in Fig. 4 is not exaggerated.) As can be seen, the wing is very flexible and bends in the span-wise direction and twists around the main spar. From animations of the wing deformation sequence we can confirm that a span-wise traveling wave is generated.

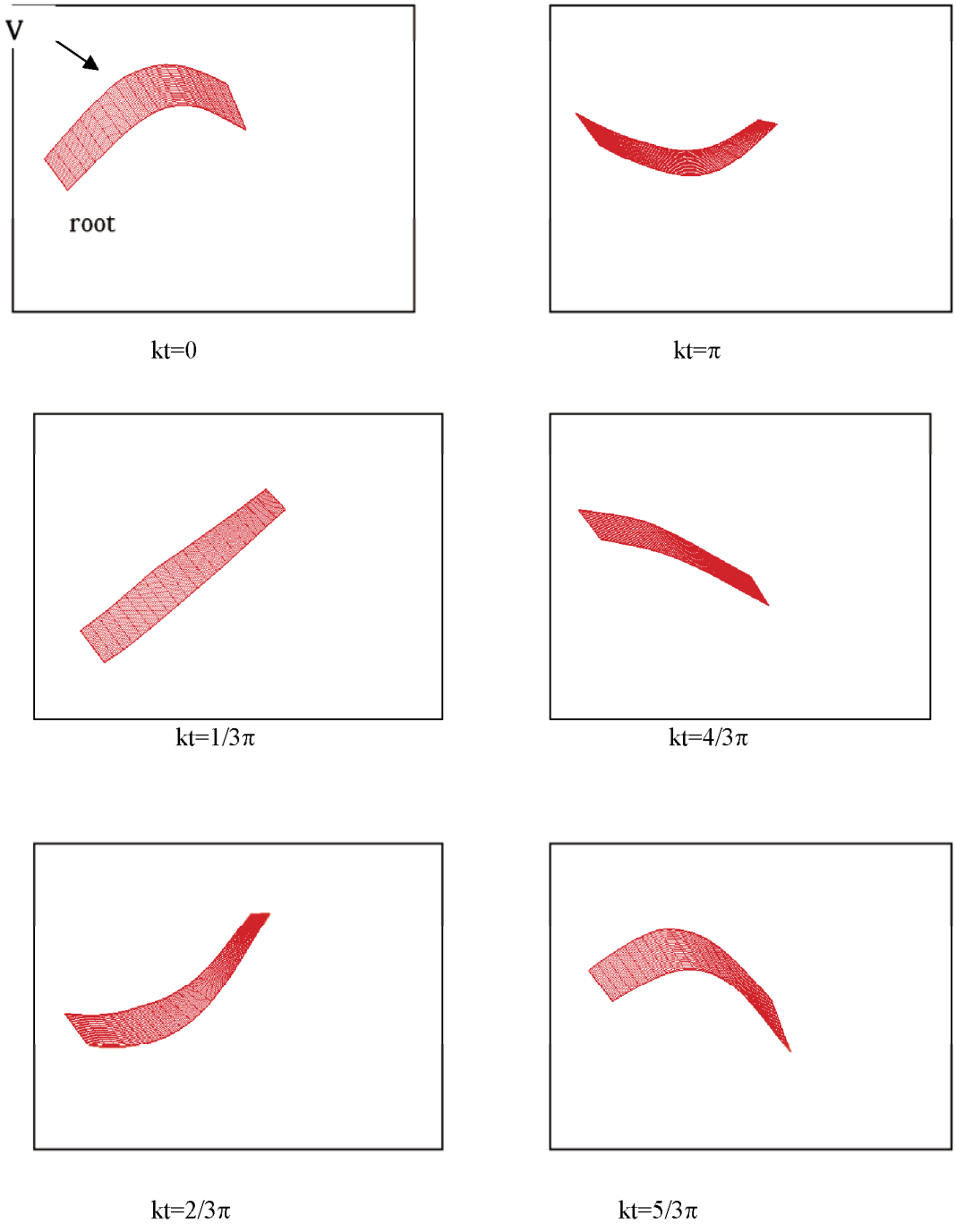

Fig. 4 Wing deformation during one cycle of oscillation.

IV. Numerical Simulation of Kite Hawk UAV Using Navier–Stokes Code

In order to evaluate the viscous effect on the optimum design of the Kite Hawk UAV, which is obtained using DLM as the aerodynamic tool, a numerical simulation was conducted using the three-dimensional Navier–Stokes (NS) code developed by Isogai [9]. Eq. (7) was incorporated into the NS code and the aeroelastic response of the wing was computed by solving Eq. (7) at each time step using the wing boundary condition (computed from the wing deformation obtained at one time step before). The natural vibration modes obtained for the optimum aeroelastic design described in the previous section were used for the aeroelastic response computation using the NS code. A C-H type structural grid system was used with 240 grid points in the chord–wise direction, 23 span-wise and 51 in the direction normal to the wing surfaces. The wing sections employed in the present NS simulation were generated by modifying the NACA0012 airfoil section by changing the thickness ratio, introducing camber and setting the maximum camber location. The amount of camber for local airfoil sections was changed parabolically from the root to the tip stations so that the camber at the root was maximum and that at the tip was zero. The thickness ratio of the present section was 6% and the maximum camber was 6% of the chord located 30% from the leading edge. The mean angle of attack was set as 8 deg, The Reynolds number based on the root chord was 7.63×10^4 and the Baldwin and Lomax algebraic turbulence model [10] was employed.

The results obtained are as follows:

$$\overline{C_T} = 0.046, \quad \overline{C_L} = 0.552, \quad \overline{C_{PW}} = 0.242$$

These coefficients give the following physical values at $U_C = 4.13$ m/s:

$$\overline{T} = 0.227\mathrm{N}, \quad \overline{L} = 2.71\mathrm{N}, \quad \overline{W} = 4.91\mathrm{W}$$

Based on these results, the wing can sustain a drag of 0.227 N and a weight of 2.71 N with a time mean power of 4.91 W and a power–mass ratio of 17.7 W/kg. These results show that the optimum aeroelastic design using DLM is still good even when viscous effects are taking into account. In Fig. 5, the wing deformations and flow patterns (iso-vorticity ω_y) during one cycle of oscillation are shown. In order to see the flow patterns in detail, the iso-vorticity distributions around the airfoil sections at 91% and 30% semispan stations are also shown in Figs. 6 and 7, respectively. As seen in Fig. 6, no flow separation is observed at 91% semispan station, which attains efficient thrust generation. However, as shown in Fig. 7, large scale flow separation can be seen at 30% semispan station, which seems to generate the drag. The flow separation observed in the inboard portion of the wing might be the main cause of the reduction of $\overline{C_T}$ compared with that predicted by DLM. In Figs. 8-10, the time histories of lift, thrust and rate of work during one cycle of oscillation are shown, respectively.

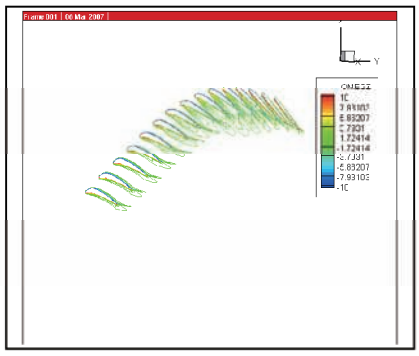

kt=0

kt=π

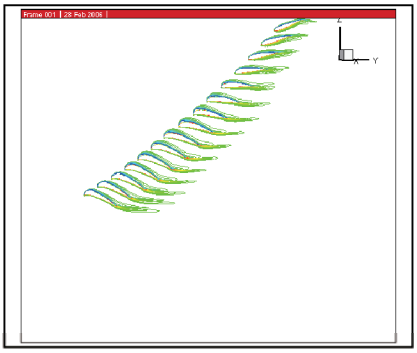

kt=1/3π

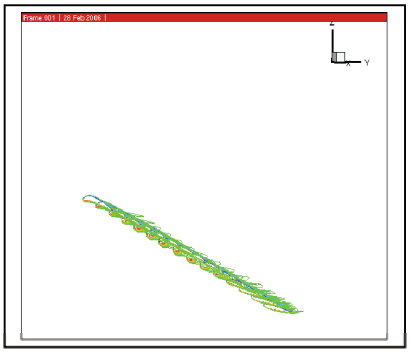

kt=4/3π

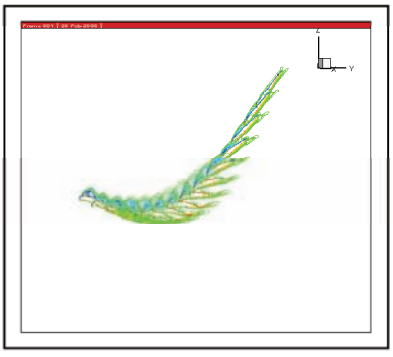

kt=2/3π

kt=5/3π

Fig. 5 Wing deformation and flow patterns (ω_y) during one cycle of oscillation.

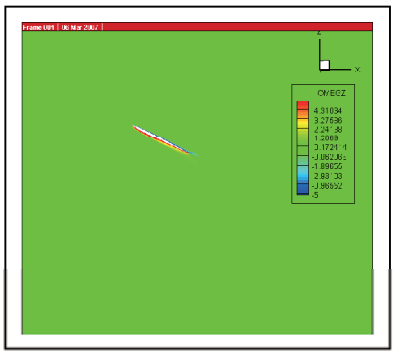

kt=0

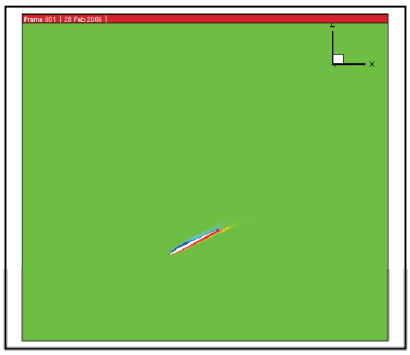

kt=π

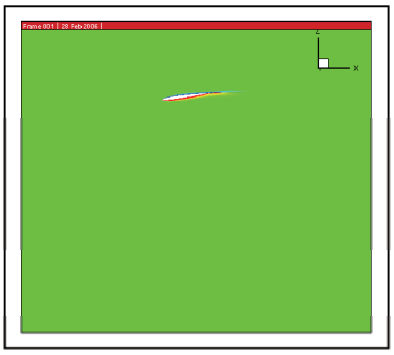

kt=1/3π

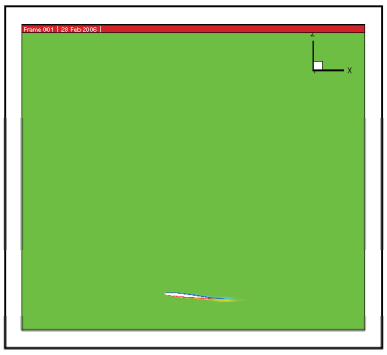

kt=4/3π

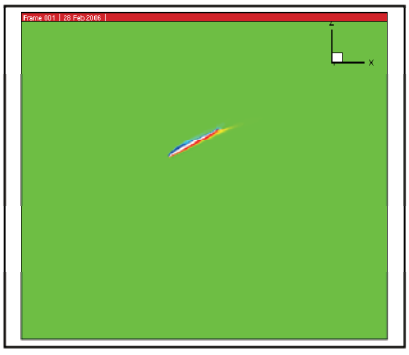

kt=2/3π

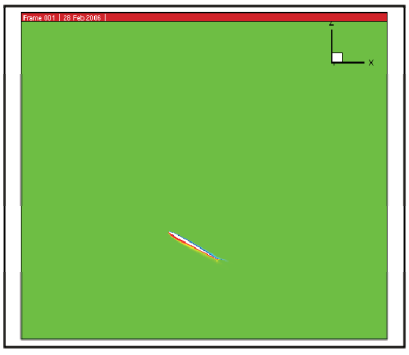

kt=5/3π

Fig. 6 Flow pattern (ω_y) at 91% semispan station.

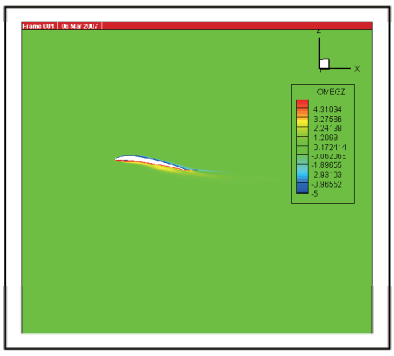

kt=0

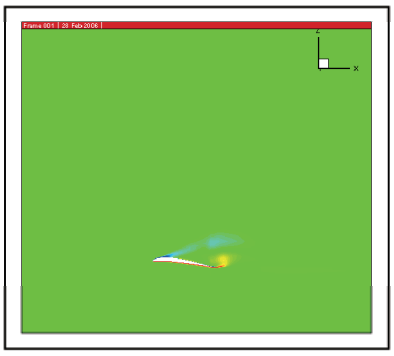

kt=π

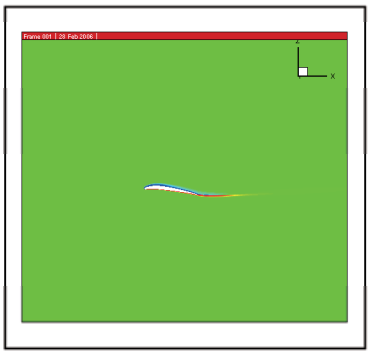

kt=1/3π

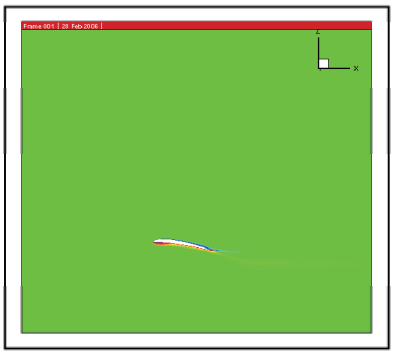

kt=4/3π

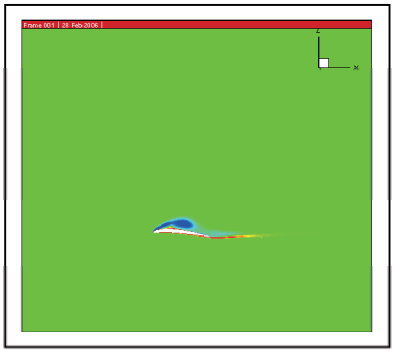

kt=2/3π

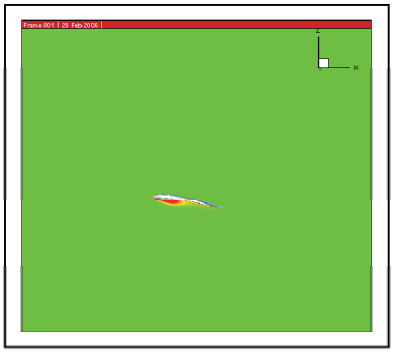

kt=5/3π

Fig. 7 Flow pattern (ω_y) at 30% semispan station.

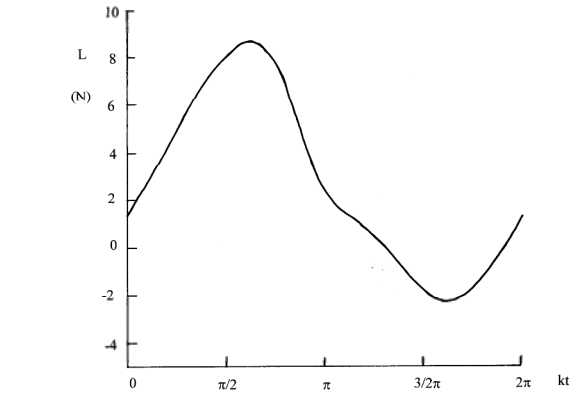

Fig. 8 Variation of lift during one cycle of oscillation.
$(\overline{L} = 2.71N)$

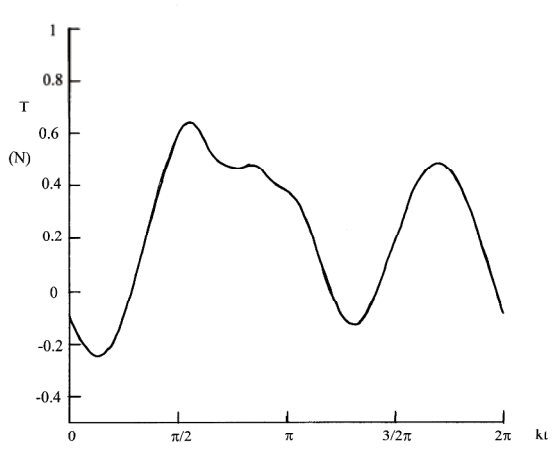

Fig. 9 Variation of thrust during one cycle of oscillation.
$(\overline{T} = 0.227N)$

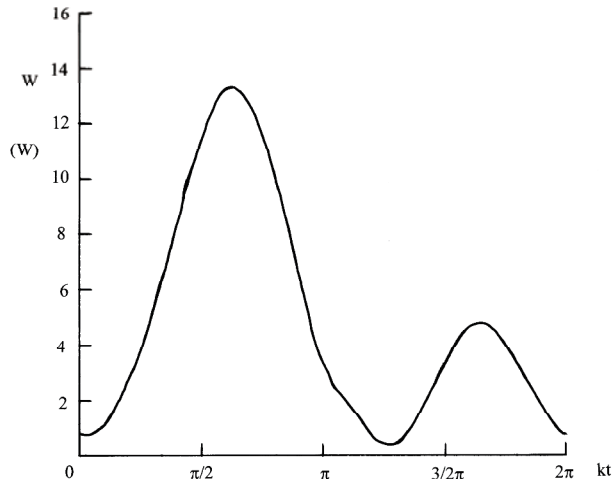

Fig. 10 Variation of rate of work during one cycle of oscillation. ($\overline{W} = 4.91W$)

V. Conclusion

A general method for the optimum aeroelastic design of a flapping wing employing lifting-surface theory as an aerodynamic tool and the complex method as the optimization algorithm is presented. The present optimum design method is applied to the Kite Hawk UAV and the optimum thickness distribution of the main-spar is determined. As a result of optimization, a high propulsive efficiency of 75% is attained considering only dihedral flapping of the main-spar. In order to evaluate the viscous effect on this optimum design using DLM, the numerical simulation using the Navier-Stokes code is conducted. It is found that the flow separation is suppressed around the out-board potion of the wing, that enables the efficient thrust generation, while the large scale flow separation is observed around the in-board potion, that degrades the propulsive efficiency. Although some degradation of the propulsive efficiency due to viscous effect is expected, it is believed that the present optimum design method using DLM might provide a useful aeroelastic design tool for a flapping wing of UAV.

References

[1] DeLaurier, J. D., and Harris, J. M., "A Study of Mechanical Flapping-Wing Flight," Aeronautical Journal, Oct. 1993, pp. 277-266.

[2] DeLaurier, J. D., "The Development of an Efficient Ornithopter Wing," Aeronautical Journal, May 1993, pp. 153-162.

[3] Albano, E., and Rodden, W. P., "Doublet-Lattice Method for Calculating Lift Distributions on Oscillating Surfaces in Subsonic Flows," AIAA Journal, Vol. 7, Feb. 1969, pp. 279-285.

[4] Lan, C. E., "The Unsteady Quasi-Vortex-Lattice Method with Applications to Animal Propulsion," Journal of Fluid Mechanics, Vol. 93, Part 4, 1979, pp. 747-765.

[5] Chopra, M. G., and Kambe, T., "Hydromechanics of Lunate-Tail Swimming Propulsion. Part 2," Journal of Fluid Mechanics, Vol. 79, part 1, 1977, pp. 49-69.

[6] Box, M. J., "A New Method of Constrained Optimization and a Comparison with Other Methods," Computer Journal, Vol. 8, 1965, pp. 42-52.

[7] Bisplinghoff, R. L., Ashley, H., and Halfman, R. L., Aeroelasticity, Addison Wesley, 1955.

[8] Beveridge, G.. S. G., and Schecheter, R. S., Optimization, Theory and Practice, Chemical Engineering Series, McGraw Hill, New York, 1970, pp. 453-456.

[9] Isogai, K., "Numerical Simulation of Unsteady Viscous Flow Around a Flapping Wing," Computational Fluid Dynamics 2002, Proceedings of the Second International Conference on Computational Fluid Dynamics, ICCFD, Sydney, Australia, July 2002, pp. 701-706.

[10] Baldwin, B. S., and Lomax, H., "Thin Layer Approximation and Algebraic Model for Separated Turbulent Flows," AIAA Paper 78-257, Jan. 1978.

Advanced Computational Aeroelasticity and Multidisciplinary Application for Composite Curved Wing*1

By Dong-Hyun Kim[1)] and Yu-Sung Kim[1)]

[1)]*School of Mechanical and Aerospace Engineering,*
GyeongSang National University (GSNU), Jinju City, 660-701, Republic of Korea

This article preferentially describes advanced computational aeroelasticity and its multidisciplinary applications based on the coupled CFD and CSD method. A modal-based coupled nonlinear aeroelastic analysis system incorporated with unsteady Euler aerodynamics has been developed based on the high-speed parallel processing technique. It is clearly expected to give accurate and practical engineering data in the design fields of generic flight vehicles. Also, efficient and robust computational system for the flutter optimization has been developed using the coupled computational method with the micro genetic algorithm. Vibration and flutter characteristics of composite curved wing are also investigated in this study. Virtual flutter tests for the spanwise curved composite missile fin are effectively conducted using the present advanced computational method with high speed parallel processing technique. As computational demonstrations, the effects of ply orientation and stacking sequence on the flutter speed have been investigated and compared with the case of isotropic curved shell model with the same structural weight.

Key Words: Aeroelasticity, Flutter, CFD, CSD, Euler, Unstructured Grid, Numerical Simulation, Genetic Algorithm, Curved Wing

1. Introduction

Nowadays, the accurate prediction of flutter boundary becomes a really important technology to reduce the structural weight and to estimate its actual flight performance in the design process. The main purposes of this article are to introduce a delicate and general computational analysis system. This article preferentially describes advanced computational aeroelasticity and related numerical backgrounds based on the coupled CFD and CSD method based on the high-speed parallel processing technique. In the development of new weapon systems such as bomb, projectile, guided or unguided missile, primary emphasis should be placed on the simplicity and reliability. A weapon will have far greater reliability if it can be sealed in a container of minimum volume and geometry. The solution for this problem can be efficient solved by using a wrap around fin or simply called spanwise curved wing concept. The curved wing offers a solution for many geometric constraints and at the same time can be sized to provide aerodynamic stabilizing characteristics equal to flat wing stabilizers. Because of its unique aerodynamic characteristics and geometry shape, it is also interesting for aerospace research engineers to investigate the flutter characteristics of the curved wing model.

The composite materials since its invention have been used widely in engineering especially for aircraft structures because of its advantage compared to the conventional engineering materials. Composite materials have many characteristics that are different from the conventional engineering materials such as high specific strength and directional stiffness. Use of all the characteristics advantage allows the tailoring of composite materials to meet a particular structural requirement. It is well-known that the optimum design of wing can be achieved by aeroelastic tailoring of composite wing structures[1-7)]. However, it is hard to find previous research works for the flutter analysis of composite curved wing shapes.

Nowadays, the accurate prediction of flutter boundary becomes a really important one to reduce the structural weight and to estimate its actual flight performance in the design process. This paper has focus on the compressible flutter analyses for the laminated composite curved wing. It also describes the development of a delicate and general computational analysis system and to exactly consider the effect of curved wing configuration. In this study, a modal-based numerical flutter analysis system in the time domain has been developed including the physical matched point concept. The parallel unstructured Euler solver was adopted and newly modified to be coupled with the dynamic aeroelastic solver. Finally, efficient and robust computational system for the flutter optimization has been developed using the coupled computational method with the micro genetic algorithms. Structural free vibration analyses have been performed using finite element method. Detailed nonlinear time responses are computed by the simultaneous coupled time-integration method in the compressible flow regions. Various computational results are presented and investigated in detail.

2. Unsteady Aerodynamic Modeling

The compressible Euler equations can be written in an integral form over a control volume V moving with a velocity $\vec{V}_g$.

$$\frac{\partial}{\partial t}\int_V Q dV + \oint_S F(Q)\cdot\vec{n} dS = 0 \tag{1}$$

where

$$Q = \begin{pmatrix} \rho \\ \rho u \\ \rho v \\ \rho w \\ e_0 \end{pmatrix}, \quad F(Q,\vec{n}) = \begin{pmatrix} \rho\bar{u} \\ \rho u\bar{u} + pn_x \\ \rho v\bar{u} + pn_y \\ pw\bar{u} + pn_z \\ e_0\bar{u} + pV_n \end{pmatrix}$$

Also,

$$\bar{u} = \vec{n}\cdot\left(\vec{V} - \vec{V}_g\right)$$
$$V_n = \vec{n}\cdot\vec{V}$$

where $\vec{V}_g$ and $\vec{n}$ are the grid velocity and the outward unit normal vector. Pressure and total enthalpy can be expressed from ideal gas relations:

*1 This is a reduced version of the presented paper at the conference.

$$p = (\gamma - 1)[e_0 - \frac{1}{2}\rho(u^2 + v^2 + w^2)] \quad (2)$$

$$h = \frac{\gamma}{(\gamma - 1)}\frac{p}{\rho} + \frac{1}{2}\rho(u^2 + v^2 + w^2) \quad (3)$$

where γ is the specific ratio.

The inviscid flux across each cell face is computed by using the Roe's flux-difference splitting formula. For high-order spatial accuracy, estimation of the state variables at each cell face is achieved by interpolating the solution with a Taylor series expansion in the neighborhood of each cell center. The cell-averaged solution gradient required at the cell center for the above expansion is computed by using the Gauss' theorem by evaluating the surface integral for the closed surface of the tetrahedrons. This process can be simplified using some geometrical invariant features of the tetrahedral. The expansion also requires the nodal value of the solution, which can be computed from the surrounding cell center data using a second-order accurate pseudo-Laplacian averaging procedure as suggested by Holmes and Connell[8].

For steady-state computations, the governing equations are linearized and advanced in time using the first-order Euler backward time integration.

$$\left[\frac{V}{\Delta\tau}I + \frac{\partial R}{\partial Q}\right]^n \Delta Q^n = -R^n \quad (4)$$

where $\Delta Q^n = Q^{n+1} - Q^n$. Also, $\Delta\tau$, R, n, and V mean the nondimensional time step, the residual, the time integration counter, and the cell volume, respectively. The nondimensional time is normalized as the reference chord length and freestream sonic speed.

For unsteady computations, Eq. (4) can be recast to include temporal numerical subiterations as a dual-time stepping. With the subiteration counter denoted by m, the solution vector Q at advancing time level n+1 is now defined as

$$\left[(\frac{V}{\Delta\tau^*} + \frac{3V}{2\Delta\tau})I + \frac{\partial R}{\partial Q}\right]^m \Delta Q^m = -R^*(Q^m) \quad (5)$$

where $\Delta Q^m = Q^{m+1} - Q^m$. Also, τ* denotes the pseudo time for the dual-time stepping and $R^*(Q^m)$ is the unsteady residual newly defined as follow:

$$R^*(Q^n) = R(Q^n) + \frac{3Q^mV^{n+1} - 4Q^nV^n + Q^{n-1}V^{n-1}}{2\Delta\tau} \quad (6)$$

The solution vector ΔQ denotes the change in state variables between numerical subiterations during a certain time step. When the subiterations drive the residual towards zero, not only second order time accuracy is achieved, but the linearization errors are also driven to zero. Typically, three to five subiterations with a certain convergence criteria per each time step are effectively used to reduce the magnitude of numerical residuals. Direct solution of the system of simultaneous equations resulting from equation for overall cells requires the inversion of a large sparse matrix, which is computationally very expensive. Thus, Gauss-Seidel relaxation method is used to iteratively solve the system of flow equations.

Furthermore, to avoid numerical errors induced by the deforming or moving mesh, the cell volumes are integrated forward in time adopting the geometric conservation law (GCL). The geometric conservation law used in this study is of the same integral form as the mass conservation law and defined by

$$\frac{\partial}{\partial\tau}\int_\Omega dV - \oint_{\partial\Omega} V_g \cdot \vec{n} d\Omega = 0 \quad (7)$$

Discretization of above equation yields

$$V_i^{n+1} = V_i^n + \Delta\tau\sum V_g \cdot \vec{n} \quad (8)$$

The local cell volumes at time level (n+1) in Eq. (6) are computed to satisfy the GCL by applying above equation at every global time step.

Parallel Implementation of the Solver

Parallelization of the Gauss-Seidel implicit scheme is fairly straightforward and has been well described in a literature[9]. The present flow solver is parallelized by partitioning the global computational domain into local subdomains. The intermediate decomposition or partitioning is performed using the MeTiS library[10]. The local domain mesh data is allocated on each processor and the calculation is performed on the local computational domain by updating the solution information among subdomain boundaries. The inter-boundaries commonly included in each subdomain are considered as artificial boundaries for data communication. To do this, ghost cells attached to these inter-boundaries for the present cell-centered scheme were also introduced. Initially, face-center values of the flow variables are interchanged through the inter-boundary faces. These values are used to calculate the flux Jacobian on the inter-boundary. Data communication among processors is achieved using the standard message passing interface (MPI) library installed on LINUX operating system. Next, the cell-center values are exchanged across the boundary during the Gauss-Seidel iteration (GSI). Boundary node values and the weighting factors for Laplacian averaging are also communicated to achieve the high-order reconstruction. In the present study, cell data are exchanged in each GSI, and face and node data are transferred for the next global iteration. Since 25~30 numerical iterations are typically required in each time step to get the local converged solution, much communication time is spent during the GSI process. Therefore, three or five times of actual communications are generally performed to reduce the communicational overhead due to the GSI.

Modified Spring Analogy for Robust Moving Grid

For the analyses on the complex moving body problems, the modified type of spring analogy technique[11] is adopted to compute the deformation of the mesh during the time integration of the fluid. In the spring analogy, the mesh is considered as fictitious springs. Boundary nodes are moved by aeroelastic computations and interior nodes are moved by the spring analogy with several iterations. In the present research, segment spring method is basically used. Here, the equilibrium lengths of the springs are equal to the initial lengths of the segments. It may be noted here that since the present moving grid technique combined with parallel processing is applied locally on each processor, the disagreement of nodes at the communication boundaries may be occurred due to the independent local iterations for the spring analogy. To avoid this kind of nonsynchronization problem, coordinates of nodes at the communication boundaries have to be also transferred into each other as the numerical constraints.

3. Aeroelastic Modeling

The governing aeroelastic equations of motion of a flexible wing are obtained by using the Rayleigh-Ritz method. In this method, the resulting aeroelastic displacement at any time can be expressed as a function of a finite set of selected modes. The

general motion of the wing assumed to be described by the separation of time and space variables as follows

$$\begin{aligned}\{u(t)\} &= [\Phi_x(x,y,z)]\{q(t)\}\\ \{v(t)\} &= [\Phi_y(x,y,z)]\{q(t)\}\\ \{w(t)\} &= [\Phi_z(x,y,z)]\{q(t)\}\end{aligned} \tag{9}$$

where {u}, {v} and {w} are the structural deflections and $[\Phi_X]$, $[\Phi_Y]$ and $[\Phi_Z]$ are the matrices of x-, y- and z-direction displacements of the natural vibration modes. Usually, the column size of modal matrix [Φ] is depends on the selection of considering natural mode in the flutter analysis.

The aeroelastic equations of motion for an elastic wing may be formulated in terms of generalized displacement response vector $\{q(t)\}$ which is a solution of the following equation:

$$[M_g]\{\ddot{q}(t)\}+[C_g]\{\dot{q}(t)\}+[K_g]\{q(t)\}=\{Q(t,q,\dot{q})\} \tag{10}$$

where t is the physical time, $[M_g]$ is the generalized mass matrix, $[C_g]$ is the generalized damping matrix, $[K_g]$ is the generalized stiffness matrix, and $\{Q\}$ is the vector of generalized aerodynamic forces computed by integrating the pressure distributions on the wing surface as

$$Q(t)_i = \frac{1}{2}\rho U^2 c_r{}^2 \iint_S -Cp(x,y,z,t)\left(n_x\psi_{xi}+n_y\psi_{yi}+n_z\psi_{zi}\right)\frac{dS}{c_r{}^2} \tag{11}$$

where ρ is the free stream air density, U is the free stream velocity, c_r is the reference chord length, S is the wing area, Cp is the unsteady pressure coefficient on the arbitrary wing surface, n_x, n_y and n_z means the surface normal vectors for x, y and z direction, respectively and ψ_i are the *i-th* natural mode shape vectors interpolated on the aerodynamic surface mesh. The generalized aerodynamic forces of Eq. (11) are integrated numerically for the wing, pylon and store configurations. In this study, to consider the characteristics of nonlinear aeroelastic responses in detail, the coupled time-marching method (CTM) has been applied.

In general, the computation time needed in solving the structural equation is much less than those required in the decomposed fluid domains. Thus, to the parallel coupling with the unsteady fluid domains, one single computer node is usually prepared for solving the structural equations. At each global time step, all the local generalized forces computed from each computer node are to be transferred into the node for structure solver. Then, the generalized displacements can be obtained and the classified data for physical moving boundary are to be transferred into the each corresponding computer nodes for spring analogy and unsteady fluid solution. In addition, this includes the staggered coupling algorithm with internal iterations to increase the temporal coupling accuracy. Data communications among computer nodes are also conducted using the standard message passing interface (MPI) library installed on a LINUX operating system.

In this study, the time marching process of the structure-fluid coupling was performed by similarly adopting the second-order staggered algorithm. It is well known that this algorithm is constructed as a leap-frog scheme where the fluid subsystem is always computed at half time-stations, while the structure subsystem is always computed at full time-stations. The road map of the numerical coupling process applied in this study is shown in Fig.1. Here, the transferred structural displacement and velocity are to be normalized to keep the numerical consistency with the normalized fluid domain.

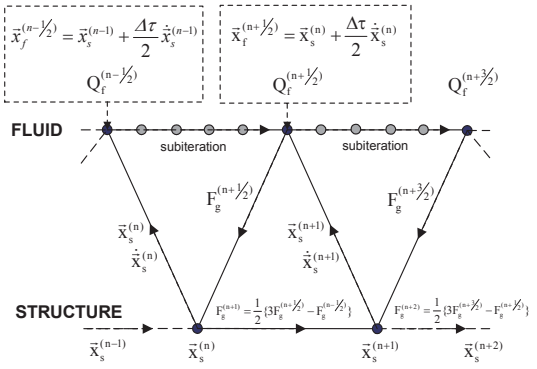

Fig. 1. Computation process of the second-order time-accurate staggered procedure.

Introducing the state vector {x} in order to efficiently perform the numerical integration, Eq. (12) can be recast into the first order form as

$$\{\dot{x}(t)\} = [A]\{x(t)\} + [B]\{u(t)\} \tag{12}$$

where

$$[A]=\begin{bmatrix}[0] & [I]\\ -[M_g]^{-1}[K_g] & -[M_g]^{-1}[C_g]\end{bmatrix}$$

$$[B]=\begin{bmatrix}[0]\\ [M_g]^{-1}\end{bmatrix} \tag{13}$$

$$\{x(t)\}=\begin{Bmatrix}\{q(t)\}\\ \{\dot{q}(t)\}\end{Bmatrix}, \quad \{u(t)\}=\begin{Bmatrix}\{0\}\\ \{Q(t)\}\end{Bmatrix}$$

Generally, to calculate the time response of Eq. (13) due to the initial conditions, external forces or control inputs are needed to analyze the behavior of the system. For nonlinear structural systems, a typical numerical technique like Runge-Kutta method can be commonly used but for linear structural systems we can use other approaches. One of the most robust and fast techniques for the linear system analysis can be derived from the assumption of setting the external force or control input constant, called zero order hold, during a certain small interval of time marching process. Thus, we can use the accurate analytical form of the solution obtained through the Laplace transform and inverse transform processes as

$$\{x(t)\} = e^{[A]t}\{x(0)\} + \int_0^t e^{[A](t-\tau)}[B]\{u(\tau)\}d\tau \tag{14}$$

The solution of Eq. (14) can be obtained numerically by replacing the continuous system by a discrete time system. Considering a computational time interval so that $n\Delta t < t \le (n+1)\Delta t$, and through the useful matrix manipulation for the integration of transition matrix, Eq. (14) can be derived as the following closed form:

$$\{x\}^{n+1} = e^{[A]\Delta t}\{x\}^n + [A]^{-1}\left(e^{[A]\Delta t} - I\right)[B]\{u\}^n \tag{15}$$

Then Eq. (15) can be effectively integrated in time to predict the modal displacement and velocity as presented in Ref.11.

The computed natural vibration mode shapes are interpolated into the aerodynamic grid points using the surface spline methods. A surface spline method can map the structural model into the

aerodynamic model. Unlike structured grid system, the unstructured aerodynamic grids automatically generated from a grid solver can hardly give ideally symmetric distributions on the object surface. In this study, thin-plate spline (TPS) technique is adopted. The global natural vibration mode shapes interpolated on the surface mesh of aerodynamic grid can be effectively displayed by the post-combination process using a general purpose plotting program. Recent useful information for several numerical spline techniques with numerical experiments can be found in Ref.12.

4. Multi-Disciplinary Aeroelastic Optimization

Typical frequency-domain flutter analyses technique based on p-k flutter method can be used to efficiently determine the flutter speed of the given wing configuration. The eigenvalue problem for classical flutter equation based on the p-k method can be written as follows:

$$\left([M_g]p^2+[C_g]p+[K_g]-\frac{1}{2}\rho U^2[A(M,k_b)]\right)\{\overline{q}\}=0 \qquad (16)$$

where p is the eigenvalue defined by $\rho=\omega(\gamma\pm i)$, ω is circular frequency, γ is transient decay rate coefficient, and $[A]$ is the generalized aerodynamic influence coefficient (GAIC) matrix of complex form as a function of Mach number M and reduced frequency k_b. The GAIC matrix can be calculated using linear subsonic doublet-lattice method, supersonic doublet-point method and transient pulse method (TPM) based on unsteady CFD aerodynamics. The numerical validation of the present flutter analysis method can be found in Refs.13-15.

Genetic algorithm is an optimization technique based on concepts of natural evolution and revolves around genetic reproduction processes and survival of the fittest strategies with some randomization or mutation. During the evolution, individuals with higher fitness will have a higher probability to survive and gradually dominate the population as the individuals with lower fitness die off. The micro genetic algorithm (mGA) is employed in this study as an alternative way to reduced the computational time compared to the classical genetic algorithm. In the micro genetic algorithm, jump and creep mutation processes are not required because the new generation process of population restarts whenever the diversity is lost. During the evolution, individuals with higher fitness tend to have higher probability to survive and gradually dominate the population as the individuals with lower fitness die off. The optimization model used in the generic algorithm can be represented by

Maximize $F(x)$:

$$\text{subject to} \quad \begin{aligned} & x \in \{A|(\theta_1,\theta_2,...,\theta_i)\}, \\ & \theta_i \in [0,\pm 30,\pm 45,\pm 60,90] \end{aligned} \qquad (17)$$

where F(x) is the objective function and is the flutter dynamic pressure defined by $q=1/2\ \rho V_f^2$ and V_f is the flutter speed. The ply orientation angles are used as the design variables (x) in the algorithm to give the maximum flutter dynamic pressure.

Figure 2 shows the present multidisciplinary computation procedure based on the coupling technique among genetic algorithm, finite element and aeroelastic analysis system.

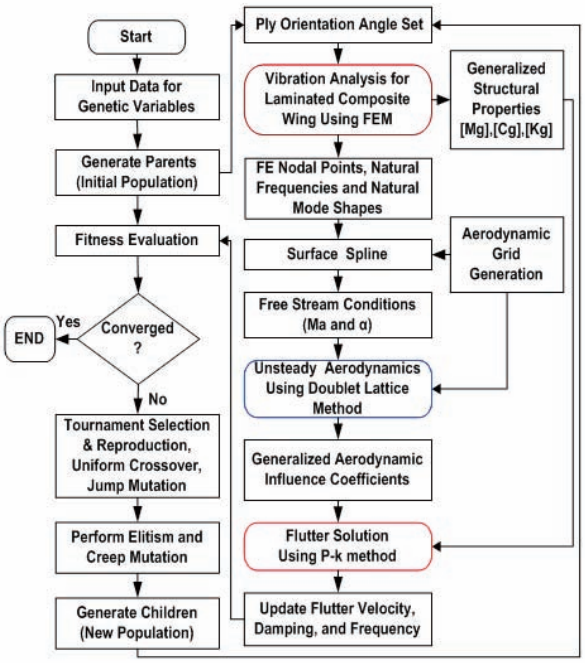

Fig. 2. Computational road map for the flutter optimization of laminated composite wings.

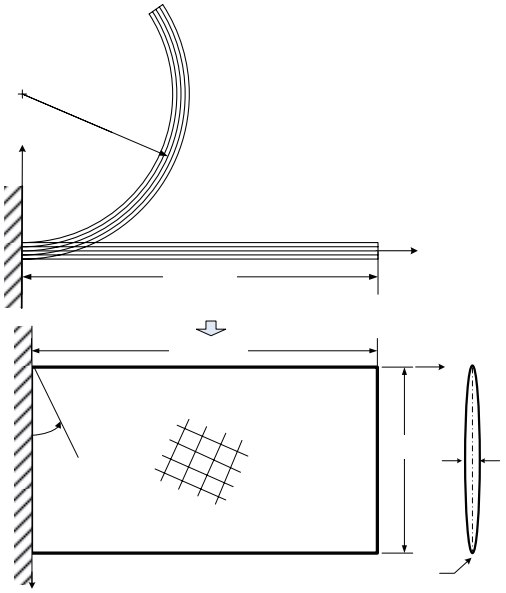

Fig. 3. Configuration of flat and curved composite wing.

5. Results and Discussion

In order to achieve strong potential for the practical application to realistic wing structures, the numerical algorithm and computational analysis system is practically designed. Developed aeroelastic computation system can be integrated with inhouse code or commercial finite element programs for linear and nonlinear composite structures. In this study, structural dynamic analyses of laminated composite curved wing models have been conducted using the MSC/NASTRAN (Ver.2005) which is a well-known and fully verified commercial finite element program. The curved wing structure is modeled using quadrilateral (CQUAD4) plate element with PCOMP entry to impose the composite material properties. The geometric configuration of the present curved wing

model is presented in Fig.3.

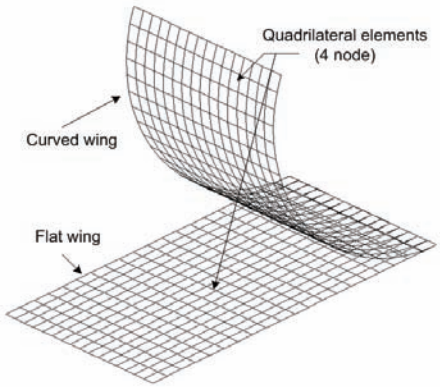

Fig. 4. Finite element models of flat and curved wing structures.

Figure 4 shows the corresponding finite element models for composite wings. The root chord of the wing is fixed in order to impose structural boundary conditions. The composite material properties used here are E_1=138 GPa, E_2=9.7 GPa, G_{12}=5.5 GPa, ν_{12}=0.28, ρ=1,543 kg/m^3 and ply thickness is 0.125 mm. The total number of plies is assumed as 32 and among them 24 inner plies can be changed according to the computational iteration coupled with the genetic algorithm. The lamination sequence is practically assumed as a symmetric lamination of $[0/90/45/-45/...\theta_{12}...]_s$. The variable angles of sets are practically selected based on the combination of 0°, 30°, 45°, 60°, and 90° ply orientations which is measured clockwise from the x-axis line. Symmetric flow boundary condition on the x-z plane is assumed for the unsteady aerodynamic analysis. The flight condition is assumed as sea-level with the free stream Mach number of 0.7.

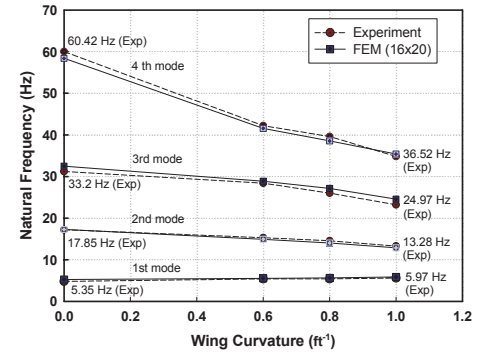

(a) Isotropic spanwise curved wing

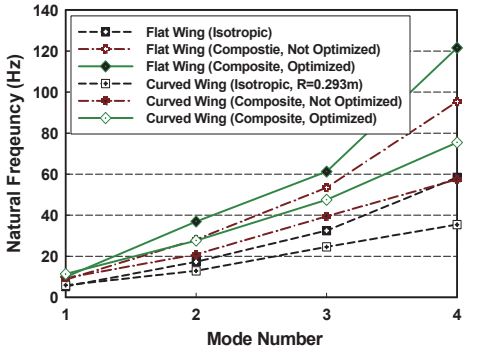

(b) Composite flat and curved wings

Fig. 5. Comparison of natural frequencies.

In the application of genetic algorithms, the variable ply angles considered is expressed in binary number such as: [0]=000, [30]=001, [-30]=010, [45]=011, [-45]=100, [60]=101, [-60]=110, and [90]=111. Numerical computations have been conducted using a server computer: Intel Pentium-D Processor 3.0 GHz, 2 GB DDR2 RAM and 240 GB HDD. The total run-time of the converged solution for each case using the standard genetic algorithm is about 33 hours for 20,000 iterations but the total run-time using the micro genetic algorithm is just about 1.67 hours for 1,000 iterations. One of the parameter sets used for micro GA is that the population size is 5, number of children is 1, crossover probability is assumed as 0.5, and elitism concept is used.

Figure 5 represents the comparison of natural frequencies for the isotropic and composite wing models. For the isotropic curved wing model presented in Fig.5(a), calculated natural frequencies show very good agreement with the experimental data[16]. For composite wing models, comparison of natural frequencies is given in Fig.5(b). Here, it is found that the natural frequency of curved wing model is generally lower than that of the flat wing model. Furthermore, natural frequencies for optimized composite wing models to achieve a maximum flutter dynamic pressure are higher than those of not optimized composite wing models.

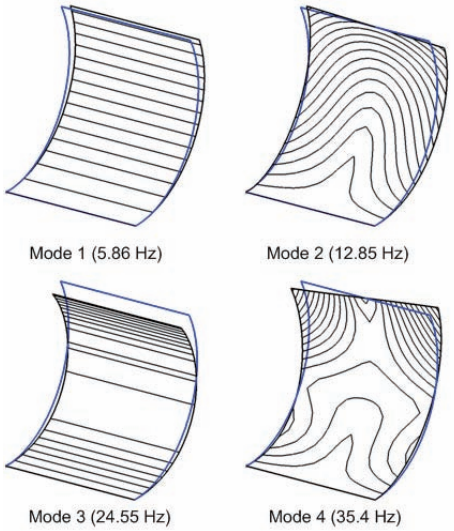

(a) Isotropic

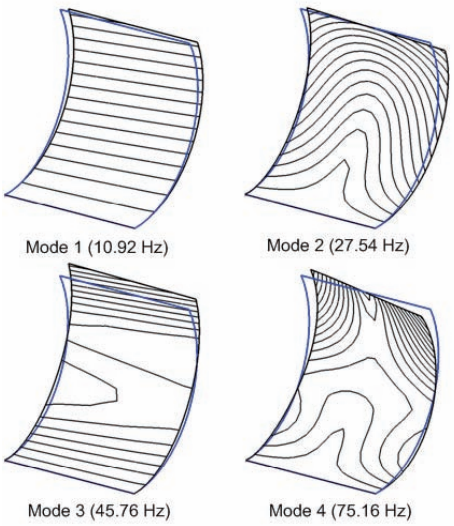

(b) Composite (Optimized)

Fig. 6. Comparison of natural mode shapes.

Figure 6 shows the comparison of natural vibration modes between isotropic and composite curved wings. For the isotropic

curved wing model, mode 1 is a typical first bending mode, mode 2 is a first torsion mode, mode 3 is a second bending model, and mode 4 is a second torsion model. The natural mode shapes of the optimized composite curved wing model are similar with those of isotropic model. However, it can be noted that the mode shapes of composite curved wing model has some combination of bending-torsion mode.

Table 1 Comparison of optimized flutter solution

Model Case	Stacking Sequence	Flutter Dynamic Pressure (kPa)	Flutter Freq. (Hz)
Isotropic Curved wing	N/A (A1 6061-T6)	2.58	9.72
Not Optimized	[0/90/45/-45/…**θ**…]s **θ** = 0/0/0/0/0/0/0/0/0/0/0	7.15	15.92
Optimized Using Standard GA	[0/90/45/-45/…**θ**…]s **θ** =45/45/45/-45/-45/-30/45/60/-60/-60/-30/30	16.47	20.43
Optimized Using Micro GA	[0/90/45/-45/…**θ**…]s **θ** =45/45/60/-45/-60/45/-45/45/-30/90/30/45	16.48	20.62

Computational results for optimum flutter design are summarized in Table 1. It is shown that the optimized flutter dynamic pressures are extremely higher than the case of the isotropic model under the condition of the same structural weight and aerodynamic shape. Flutter dynamic pressure of the isotropic material case is just 2.58 kPa. The flutter dynamic pressure of the initial composite wing models (flat and curved configuration) are higher than the case of the isotropic material model under the same weight and shape condition. This result basically indicates the benefits of composite material properties and characteristics compared to the isotropic materials. Moreover, the flutter dynamic pressure of optimized composite wing is 6.4 times greater than that of the isotropic wing model. Optimized results practically show that nearly same maximum flutter dynamic pressure by standard genetic algorithm can be also obtained using the efficient micro genetic algorithm.

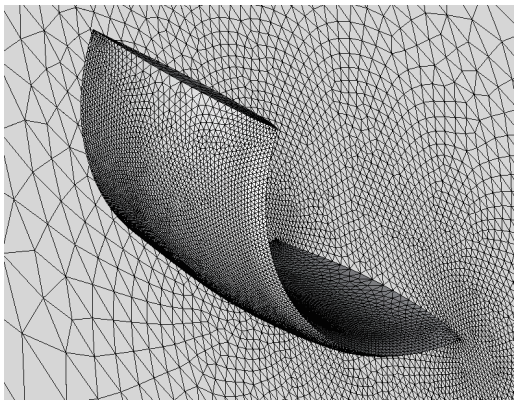

Fig. 7. Computational grids used for unsteady aerodynamic computations for flutter analyses.

Computational grid used for unsteady aerodynamic calculations using three-dimensional Euler code with deforming grid algorithm is presented in Fig.7. The grid is carefully stretched and distributed in order to decrease the total number of volume and increase the numerical accuracy. Here, whole computational grid domain is composed of about 200,000 tetrahedrons.

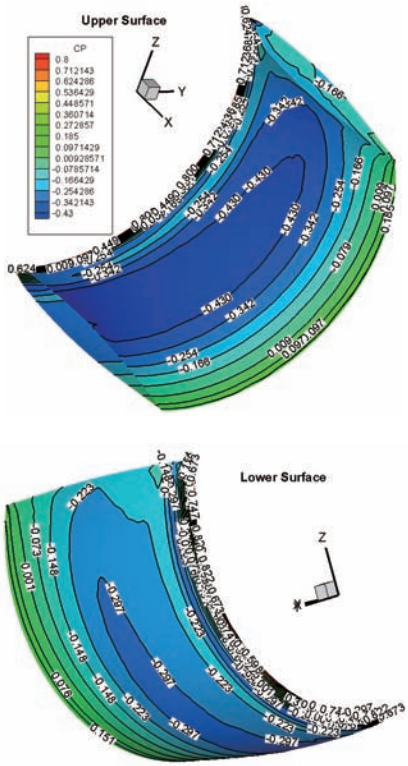

Fig. 8 Comparison of surface pressure distribution at the Mach number of 0.7.

Figure 8 represents the comparison of pressure distribution on the upper and lower wing surfaces. It is noted that although the present curved wing has a symmetric airfoil section such as NACA 65A010, the pressure distributions on the upper and the lower wing surfaces are different because of its spanwise curvature effect. For the isotropic wing model, experimental flutter test data[16] is available. The verification of the present computational flutter analysis for the curved wing model is presented in Table 2. The calculated flutter dynamic pressure and frequency using the developed computational program show good agreements with the experimental data.

Table 2 Comparison of flutter dynamic pressure and flutter frequency

Model	Experiment		Present (CFD/CSD)	
	q_F (kPa)	f_F (Hz)	q_F (kPa)	f_F (Hz)
Curved wing (Isotropic)	2.38	9.4	2.16	9.1

On the other hand, to account for physical aspect of structural responses for both the isotropic and composite curved wing models, verified advanced computational method based on the time-domain approach is also applied. Figure 9 shows the comparison of dynamic aeroelastic responses for the isotropic curved wing and the optimized composite wing models. For the response case of the composite curve wing model, one of the optimized laminations presented in Table 1 is considered: $[0/90/45/-45/45/45/60/-45/-60/45/-45/45/-30/90/30/45]_s$. Here, one can see that the maximum static aeroelastic defection of the isotropic curved wing is about -0.035 m for the dynamic pressure of 2.2 kPa while the maximum deflection of the composite curved wing is just about -0.022 m even for three times higher dynamic pressure level. Moreover, the dynamic response of the isotropic curved wing is clearly unstable for the low dynamic pressure level of 2.2 kPa. However, the optimized composite wing model which

has the same structural weight compared to that of the isotropic curved wing still shows the stable dynamic responses even for the high dynamic pressure level of 6.13 kPa. This result clearly indicates that the flutter dynamic pressure of a curved missile fin can be significantly increased using laminated composite materials.

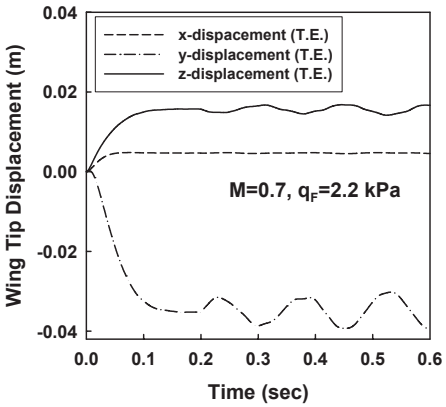

(a) Isotropic curved wing

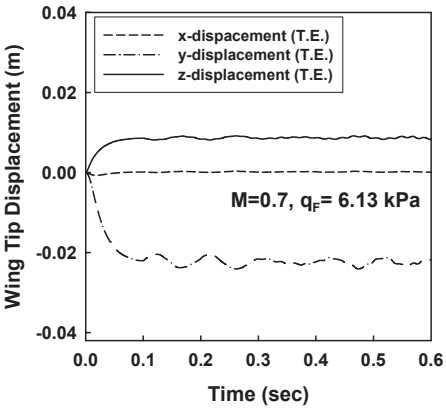

(b) Optimized composite wing

Fig. 9 Comparison of dynamic aeroelastic responses at the wing tip.

6. Concluding Remarks

Advanced computational methods for multi-disciplinary aeroelastic analysis are introduced in this article. The developed analysis system was based on the advanced numerical techniques such as CFD, CSD, FEM and parallel processing. Also, the design studies of aeroelastic tailoring were conducted on the laminated composite curved wing configuration. Using the developed analysis system, dynamic aeroelastic behaviors of a composite curved wing configuration were simulated in compressible flow. As computational demonstrations, the effects of ply orientation and stacking sequence on the flutter stability have been investigated and compared with the case of isotropic curved shell model with the same structural weight. The present results indicate that aeroelastic stability of a curved missile fin can be significantly increased using optimized composite lamination under the same design weight condition.

Acknowledgements

This work was partially supported by the 2nd Stage BK21 program and the Agency for Defense Development under the contact of UD060023AD. The authors would like to acknowledge the supports.

References

1) Weisshaar, T.A. : Aeroelastic Tailoring of Forward Swept Composite Wings, *Journal of Aircraft*, **18** (1981), pp.669-676.
2) Lottai, I. : Flutter and Divergence Aeroelastic Characteristics for Composite Forward Swept Cantilevered Wing, *Journal of Aircraft*, **22**, No. 11, (1985), pp.1001-1007.
3) Georghiades, G.A., Guo, S., and Banerjee J.R. : Flutter Characteristics of Laminated Wings, *Journal of Aircraft*, **33** (1996), pp.1204-1206.
4) Eastep, F.E., Tischler, V.A., Venkayya, V.V., and Khot, N.S. : Aeroelastic Tailoring of Composite Structures, *Journal of Aircraft,* Vol. **36** (1999), pp. 1041-1047.
5) Kim, D.H., and Lee, I. : Nonlinear Flutter Characteristics of a Composite Missile Wing in Transonic and Low-Supersonic Flows, *Journal of Aircraft*, **39** (2002), pp.889-892.
6) Guo, S., Banerjee, J.R., and Cheung, C.W. : The Effect of Laminate Lay-Up on the Flutter Speed of Composite Wings, *Journal of Aerospace Eng*, **217** (2003), pp. 115-122.
7) Kim, D.H., and Lee, I. : Static Aeroelastic Optimization of a Composite Wing Using Genetic Algorithm, 7th International Conference on Composites Engineering, ICCE/7, July 2-8 (2000), Denver Colorado, USA.
8) Holmes, D. G., and Connell, S. D. : Solution of the 2D Navier-Stokes Equations on Unstructured Adaptive Grids, AIAA Paper 89-1932 (1989).
9) Bruner, C., "Parallelizations of the Euler Equations on Unstructured Grids," *Ph.D. Thesis, Department of Aerospace Engineering, Virginia Polytechnic Institute and State University* (1996).
10) Karypis, G., and Kumar, V., "Analysis of Multilevel Graph Partitioning," *TR 95-037*, *Department of Computer Science, University of Minnesota*, 1995.
11) Kim, D. H., Park, Y. M., Lee I. and Kwon O. J. : Nonlinear Aeroelastic Computation of a Wing/Pylon/Finned-Store Using Parallel Computing, *IAA Journal*, **43** (2005), pp.53-62.
12) Smith, M. J., Cesnik C. E. S., Hodges, D. H., and Moran, K. J. : An Evaluation of Computational Algorithms to Interface between CFD and CSD Methodologies, AIAA Paper 96-1400-CP, (1996), pp.745-754.
13) Kim, D. H. and Lee, I., "Transonic Flutter Analysis for 3D Wing using Transonic Small Disturbance Equation," *Journal of The Korean Society for Aeronautical and Space Science*, **26** (1998), pp.73-82.
14) Kim, D. H. and Lee, I. : CFD-Based Matched-point Linear and Nonlinear Flutter Analysis of Sweptback Wings in Transonic and Supersonic Flows, Computational Fluid Dynamics Journal, **11** (2002), pp.35-49.
15) Kwon, H. J., Kim D. H., and Lee, I., "Frequency and Time Domain Flutter Computations of a Wing with Oscillating Flaperon Including Shock Interference Effects," *Journal of Aerospace Science and Technology*, **8**, (2004), pp. 519~532.
16) Rivera, J. A. Jr. : Experimental and Analytical Investigation of the Effect of Spanwise Curvature on Wing Flutter at Mach Number of 0.7, Langley Research Center, NASA TM 4096 (1989).

An example of a multidisciplinary process applied to an Airbus design: Optimisation of the A380 weight and ride comfort by an active flight control system

Marc Humbert

Loads & Aeroelastics, Airbus
e-mail: marc.humbert@airbus.com

Abstract. Multidisciplinary Design Optimisation is frequently looked at as the use of new computational tools, coupling together models of various disciplines in a single numerical environment, integrating a mathematical optimisation algorithm with tuned design characteristics so as to optimise the objective criteria.
Although this "tool" aspect is an important one, the deployment of Multidisciplinary Design also represents challenges in terms of organisation, competence, and engineering processes. The objective of this paper is to illustrate such aspects of MDO, focusing on one particular example: the optimisation of the interactions between the electronic flight control system and the structural loads and dynamic behaviour of the A380 aircraft. These processes will be presented along with the well-known V&V cycle of the system development where each part of this "V" has different objectives and induces differences in engineering activities and the relationships between disciplines. It will be shown that this MDO process not only relies on integrated multidisciplinary models and mathematical optimisation dependent on the phase and part of the FCS design, but also on engineers from the different disciplines sharing their knowledge, models, and exchanging technical information.

1 INTRODUCTION

Multidisciplinary Design Optimisation is frequently looked at as the use of new computational tools. Two main specifications are attached to these methods and these are compared to a more traditional engineering approach.
- MDO methods represent interactions between different disciplines, coupling together various models in a single numerical environment. For example, a traditional set of disciplines considered in an MDO framework is aerodynamics, loads, structure, and weight prediction.
- Aircraft design requirements and design variables are defined and modelled by the tools within this framework. A mathematical optimisation algorithm is incorporated in the tool to tune the design characteristics and optimise the objective criteria.

Although this "tool" aspect is an important one, the deployment of Multidisciplinary Design also represents challenges in terms of organisation, competence, and engineering processes. This second aspect of MDO is recognised in several papers, which highlight the potential impact of its application on the mindsets, responsibilities, and organisations of engineering teams [1],[2].
This paper will illustrate such aspects of MDO, focusing on one particular example: the optimisation of the interaction between the electronic flight control system and the structural loads and dynamic behaviour of the A380.
These interactions (effect of the flight control system on manoeuvre and gust loads, aeroelastic stability, passenger ride

comfort) are well known and must be studied at least in a "checking mode" to guarantee the aircraft safety. However, since the first introduction of flight control system technology on a civil aircraft -the A320- Airbus wanted to go beyond checking. Their Enginners took advantage of this interaction for product optimisation by introducing an active control of gust loads that allowed wing structural weight savings to be made. This first introduction of active load control was then pushed further on all subsequent Airbus products: manoeuvre loads alleviation function and active structural mode response control for increased passenger comfort on the Long Range A330 and A340 (first introduction on civil aircraft) [3], optimum control techniques to perform integrated flexible aircraft control design on A340-600 [4]. The A380 inherited this extensive Airbus experience with Fly-by-Wire technology on civil transport aircraft, and pushed the flight control system optimisation for structural load alleviation much further, delivering a level of load reductions and ride quality never accomplished before. This was achieved together with meeting the challenges of aeroservoelastic stability and manoeuvrability.

This achievement was both the result of the competence and motivation of engineers contributing to this program as well as the clear and efficient processes allowing structure, loads, and system specialists to capture the key inter-disciplinary relationships and transform them into shared activities of modelling, design, and validation. This paper will describe these processes by reference to the well-known V&V cycle of the system development where each part of this "V" has different objectives and induces differences in engineering activities and the relationships between disciplines.

2 THE SYSTEM "V&V" (VALIDATION AND VERIFICATION) PLAN

The development of the system is commonly summarised in a sketch representing the activities "at aircraft level" compared to more "component specific" activities as a function of the development schedule:

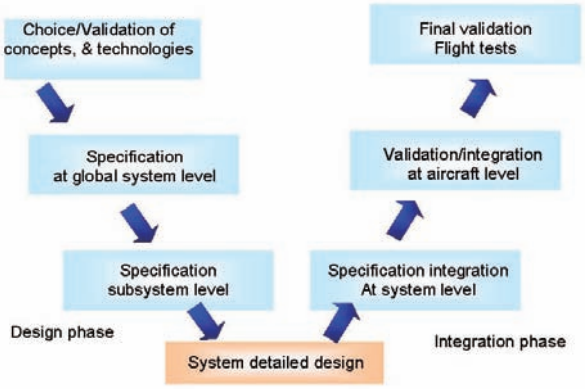

This part is then followed by the actual detailed design and manufacturing of the system itself, which is normally considered at a very system-specific level. For most of the components of the flight control system, they are not developed and manufactured by Airbus directly. They are developed and manufactured by a system supplier who works on their own site.

The next phase is the right hand side of the "V". This describes the validation activities. Such validation activities call for both simulation analyses and test analyses. Validation is performed firstly at subcomponent levels of the flight control system, which is typically the role of the "elementary test rig" (e.g. servocontrol, sensors, or computer specific tests).. This FCS validation is performed on the whole system using a simulated environment (typically the role of the "flight control test rig, or the so called "iron bird"), before the final validation, which is achieved by the flight tests.

These three phases are sometimes not clearly separated, but this classification is used in the following paragraphs to show the different kind of activities that took place among system designers and loads and aeroelastic specialists to support a multidisciplinary flight control system

design for the structural optimisation of the A380.

3 MULTIDISCIPLINARY SYSTEM-LOADS AND AEROELASTIC PROCESS DURING SYSTEM INITIAL DESIGN PHASE

As far as the system load and aeroelastic interactions are concerned, the first key outcome of this phase is the definition of the objectives that must be met by the flight control system and the selection of the concepts and technologies that will enable the realisation of these objectives. For this purpose, an important pre-requisite is a good load and aeroelastic culture among system designers, and vice versa, allowing the development of a shared understanding between the different specialists of all potential EFCS effects. Such competence was already available at the beginning of the A380 program thanks to experience of past aircraft programs and research and technology projects. As an illustration, many specialists of control law design were fully familiar with the famous "flutter plots" that are frequently considered outside the aeroelastic community as an awful superposition of many curves. Similarly, some load and aeroelastic engineers had good backgrounds in both modern automatic control techniques (like H2/H°° that were used to define some control laws used on the A380) and detailed features of Airbus's FCS philosophy. This cross culture has always been favoured, in order to allow system specialists to anticipate potential aeroelastic or load increases linked to particular design features by themselves and to allow loads specialists to propose an innovative flight control system strategy and tuning resulting in load reductions. This knowledge sharingmust not muddle clearly defined responsibilities: system specialists keep the full responsibility of system specification design and validation, and load or aeroelastic specialists keep all responsibilities linked to load levels supplied for structure sizing or flutter statements.

The initial FCS structure interaction analyses done in the early stages of the FCS delivered many important design decisions on the A380 and influenced nearly all system requirements written in this phase. Some examples of these requirements are given below:

The servocontrol specification took the bandwidth and duty cycles into account to allow the introduction of structural mode control later on; the servocontrol damping mode characteristics were specified from aeroelastic analyses in failure conditions; the necessary introduction of a 5000psi hydraulic circuit was immediately recognised so as to have a reduced servocontrol stiffness - specific analyses were launched early on to manage control surface aeroelastic instability risks; the FCS sensors locations were defined based on aeroelastic control and stability objectives and structural mode shape characteristics. An unusual asymmetric FCS architecture replaced a failure case where both outer elevators were oscillating by a case where one inner elevator and one outer elevator oscillates - this is much less severe for the tailplane dynamic excitation (see the figure below which is an extract of an FCS architecture showing the inner and outer left and right elevator power supplies shared between green and yellow hydraulic circuits and 1 and 2 electrical circuits).

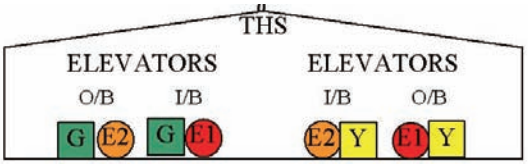

The early analyses of the load case hierarchy and structural weight drivers resulted in the agreement between loads and control specialists on the top level objectives/requirements for active load control and identify the control strategies to be developed during the detailed design phase of the control laws. For example, the benefit of active control of wing fatigue in

turbulence was recognised. This makes the A380 the first ever civil aircraft to use active control for alleviating fatigue loads.
In summary, this initial system design stage permitted the definition of objectives, concepts and technologies, and also led to the identification of potential risks. A successful initial phase is a key milestone towards the optimisation of the flight control system for loads and aeroelastics. However, its process relies more on engineers sharing their understanding of their respective disciplines, developing a common vision and goal, and exchanging their "mono disciplinary" models and tools, rather than on new-coupled multidisciplinary models and simulation tools or mathematical optimisation algorithms.

4 MULTIDISCIPLINARY SYSTEM-LOADS AND AEROELASTIC PROCESS DURING SYSTEM DETAILED DESIGN PHASE

As mentioned earlier, this stage corresponds to detailed design and manufacturing activities that are performed in the system supplier company for many components of the EFCS.
The control laws are an exception firstly because its detailed design is performed internally by control specialists and secondly because the multidisciplinary optimisation cannot be managed only by specifications.A classic process to handle the control law design interaction with loads and aeroelastics was: once an updated tuning performed by the systems group. Its definition was provided to the loads or aeroelastic team to analyse its effects on the structure. In case issues were encountered, the adaptations to resolve them were defined in conjunction with system engineers an example of which would be adding a filtering if an aeroservoelastic instability occurred.
Airbus moved away from this "trial and error" control synthesis since the stretched versions of the long range A340 (A340-500 and A340-600), as it was considered that this methodology would take a long lead time to converge and would not guarantee the best control performance for these large flexible aircraft These aircraft are characterised by a small separation between rigid-body and structural dynamic frequency domains.
The design process used in Airbus is based on multidisciplinary control optimisation algorithms where all objectives from various disciplines are introduced as design criteria from the beginning. Key enablers of such processes are: engineers having sufficient competence in various disciplines (automatic control, handling qualities and loads and aeroelastics); the formulation of structure objectives as a mathematical criterion in the control laws design environment (eg comfort, aeroelastic stability and loads) and; introduction of loads and aeroelastic models into the control law design models. It is worth noting that for the development of the A340-600 where such a highly integrated control design process was used, the loads and aeroelastic specialists provided the control designers with aeroelastic models at a set of agreed flight and mass conditions, and these models where run in a specific control law synthesis environment. On the A380, the process integration was pushed further, and control law designers had the direct access of tools that generate the aeroelastic models. They also used some of the tools aircraft behaviour analyses routines.
This optimisation process proved to be very efficient for the aeroelastic stability aspects and was beneficial in terms of the aircraft response in gust and turbulence (for both loads and passenger comfort). However, the optimisation of the flight control system for manoeuvre loads could not follow the same mathematical approach for two reasons. Firstly, manoeuvre load analyses require non linear models that are more difficult to manipulate during optimisation runs. Secondly and more importantly, manoeuvre alleviation very

often raises questions about the level of manoeuvrability necessary for the aircraft. In some cases decisions cannot be made without pilot-in-the-loop analyses, for example, simulator tests and flight tests. However, a high level of alleviation of the manoeuvre loads has been reached on the A380 wing, fuselage, vertical tailplane, and horizontal tailplane, but this alleviation system was designed thanks to engineers' physical understanding of loads and handling quality drivers, rather than an automatic mathematical optimisation. Among the various strategies used in the pitch and lateral normal laws for this optimisation, one can mention gain scheduling, non linear filtering of control pre-command, and optimum usage of the kinematics. As an illustration, the figures below show loads during a lateral one engine out simulation with two standard control laws, the improved one (the red curves) providing a significant VTP loads reduction thanks to non-linear filtering.

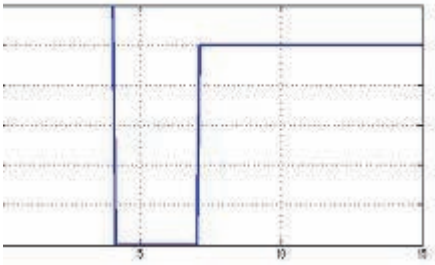

Pedal input

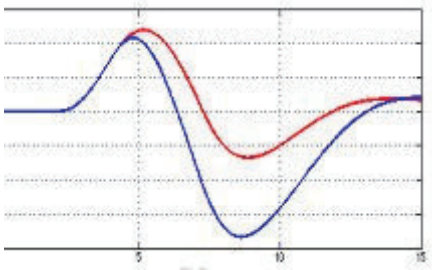

sideslip

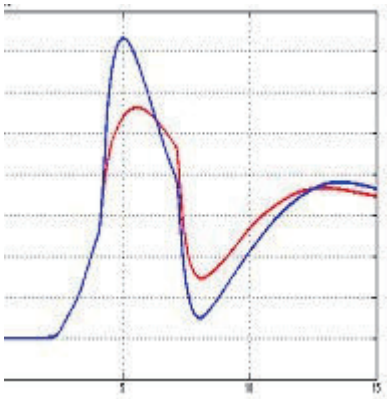

VTP bending

In addition to optimum normal law design, specific manoeuvre load alleviation functions were introduced, with appropriate compensations and activation/deactivation logics to ensure unchanged handling quality characteristics. Finally, some envelope EFCS protection functions (load factor, stall, and high speed protections) were used to reduce limit loads. It is worth noting that the specific Airbus philosophies on flight domain protections (which the pilot cannot override) dramatically reduce the probability of excursion of the limit loads in extreme manoeuvre situations.

And this high level of manoeuvre alleviation on the A380 has been reached together with outstanding handling qualities, acknowledged by all pilots who have flown the A380.

In addition to loads optimisation, the effect of the flight control system on passenger comfort in gust and manoeuvres was a key control design criterion. The A380 flight control system improves passenger comfort through several strategies.*!* Among others we can mention the normal law active damping of rigid body modes, structural mode control as part of Airbus's state-of-the-art since the A340-300, and precommand optimum design through 'dynamic precommand', or optimum phase management between control surfaces as described in [5].

5 MULTIDISCIPLINARY SYSTEM-LOADS AND AEROELASTIC PROCESS DURING SYSTEM VALIDATION PHASE

The final flight control systems validation before certification was done by an extensive flight test campaign, where all of the functions of the system were evaluated in nominal and failure conditions. However, as represented in the V&V process, numerous simulations and tests on ground preceded the flight tests.

The multidisciplinary work between loads and aeroelastic specialists that took place during the specification phase and the detailed design phase was of course pursued during the validation phase. The responsibility of system tests remained within the hands of the flight control system specialists. The driving idea of other actors involvement was to take benefit of simulations or tests planned for the "usual" FCS validation, and to expand them when necessary to capture expected effects (benefits or risks) of the structure – FCS interactions.

For example, servocontrol performance and stability tests were used to validate the behaviour of the structural mode control; some computer partial tests were dedicated to identify and guarantee computer delays for aeroservoelastic stability; many simulations performed on a desktop simulator for handling quality validation at the limits of the flight envelope (eg for protection function validation, or handling quality certification manoeuvres) were used for the manoeuvre load analyses.

An important innovation that enhanced the multidisciplinary EFCS validation on A380 was the wide usage of the system integration simulator for loads and aeroelastics, made possible thanks to the introduction of real time loads and aeroelastic models [6]. This test bench is named "iron bird", or "a/c0". Electric and hydraulic circuits, servocontrols, flight computers, and cockpits are all part of this test bench. All of these systems can be "flown" on the ground in real time, responding to pilot orders as if they were at 35000ft. The pictures below show some views on the A380 iron bird.

An automatic monitoring of loads and structural dynamic response was introduced to provid warning messages to specialists leading the simulation test whenever high loads or structural dynamic oscillations occurred. A 30seconds record of key parameters was also registered. This information is transmitted to loads and aeroelastic specialists for analyses (without stopping the simulation) as is done with a flight data recorder for technical investigation after an accident.

Thanks to this, the large numbers of tests performed for system integration are now useful for the structure – FCS interaction validation. This largely improves the vali

dation of the flight control system's impact on load and aeroelastic behaviour and provides unique possibilities to validate this interaction with real hardware before the first flight.
For example, the usual flutter validation is performed in the frequency domain with linear models of the flight control system. This procedure is adequate for the safety demonstration and the system certification. However, the flexible aircraft iron bird allows an aeroservoelastic validation with the real flight computers, offering the exact system behaviour in terms of time delays and transitory phases during switches between control law modes or failure cases. These are hardly represented at all with the usual frequency domain system models.
Similarly, introduction of the loads model into the iron bird allowed performing load simulations with pilot-in-the-loop. This offers a loads check for more complex and realistic manoeuvres than the "stylised" ones defined for loads certification. In addition, the loads domain conducted a systematic clearance prior to flight-testing at the limit of the flight envelope, as these limits can be reached during some handling quality tests.
This enhanced loads validation was considered as a must because engineers always question if the alleviation seen on the particular gust or manoeuvre shapes used for producing loads for structure sizing and certification is still maintained during other scenarios. This additional effort can be considered as "the price to pay" when introducing a high level of loads alleviation through the flight control system. Integrated multidisciplinary validation processes and tools as described above are key conditions to achieve this extended validation efficiently.

6 CONCLUSIONS

This paper presents the processes developed within Airbus to improve the optimisation of the A380 loads, aeroelastics and comfort characteristics, while achieving outstanding handling qualities. This is achieved thanks to multidisciplinary optimisation of the whole electronic flight control system. It was highlighted that the process depends on the development phase to some extent, and is partially based on integrated multidisciplinary models of the aircraft and mathematical optimisation as MDO is usually understood. However, common to all phases of the process was the fact that engineers from different disciplines shared their experiences, models, and technical knowledge..
It clearly demonstrated that the loads and aeroelastic engineering community has a big role to play in aircraft design that goes much beyond their "basic" responsibilities of delivering load results for structural sizing or flutter statements. Load and aeroelastic engineers are key players in today's aircraft optimisation. As "multidisciplinary thinking" is a natural culture within this domain, there is no doubt that their contribution into the methods and the deployment of advanced MDO techniques in future aeronautics will be of the highest importance.

REFERENCES

[1] "Network-Based MDO Integration", B Malone, 2006 European-U.S. MDO-Colloquium

[2] "integrated system-of-system synthesis ISSS", J Sobieski, 2006 AIAA/ISSMO Multidisciplinary Analysis and Optimization Conference

[3] „Comfort in turbulence for a large civil transport aircraft" K. Seyffarth, M. Lacabanne, K. König, H. Cassan: IFASD congress, 1993, Strasbourg

[4]"Passenger comfort improvement by integrated control law design", F. Kubica, B. Madelaine, ICAS congress, 1999

[5] „A380 roll kinematics design“, S Delannoy, (to be presented in IFAC congress 2007, Toulouse)

[6] „real time structural dynamics and loads simulation for flight control system testing on a large civil aircraft“., M Humbert, H Ribet, IFASD congress, Munich, 2005

Workshop at the University of Tokyo, Japan
23-25. May 2007

COMPONENT CONCEPTS FOR MORPHING STRUCTURES

Wolfgang Luber*
EADS
Military Air Systems OPES
P.O. Box 80 11 60
81663 Munich, Germany

ABSTRACT

As part of the "Advanced Aircraft Structures Program", feasibility studies of different structural concepts of active and morphing structures have been performed. These studies have revealed significant problems related to system complexity and functionality under environmental conditions and severe problems combined with the development of adequate materials.

In the first part, comparison of active smart structure - piezoelectric control systems and aerodynamic active systems for vibration alleviation and elastic mode damping of a military aircraft structure is presented. The vibration alleviation systems which are operative at flight in turbulence or during maneuvers at high incidence reduce severe buffeting levels on the vertical tail structure.

The active systems for elastic mode damping (ASD) are designed as digital systems to provide vibration alleviation and have an interface to the Flight Control System (FCS) or are directly part of the FCS.
The sensor concept of all different systems is the same as the sensor concept used for the FCS with the corresponding benefits of redundancy and safety.
The design of systems and the comparisons of system properties are based on open and closed loop response calculations, performed with the dynamic model of the total aircraft including coupling of flight mechanics, structural dynamics, FCS dynamics and hydraulic actuator or piezo-actuator dynamics.
Aerodynamic systems, like active foreplane and flap concepts, rudder and auxiliary rudder concepts, and piezoelectric systems, like piezo interface at the interconnection fin to rear fuselage and integrated piezo concepts are compared. Besides the essential effects on flexible aircraft mode stability and vibration alleviation factors system complexity and safety aspects are described.

Recently, aerodynamic investigations of adaptive deformable aircraft structures on a scale model of an actual aircraft have been performed with aerodynamic CFD simulations and wind tunnel tests on a complete aircraft model with different shapes of the wing trailing edge. The aerodynamic investigations have shown a considerable drag reduction.

Novel concepts are now under investigation, which might lead to a promising way ahead. One of these concepts uses transversal actuators, which are distributed in the aircraft skin. Detailed analyses of this approach have shown the potential and viability of this approach. Especially it could be shown that the expected weight increase of the adaptive wing structure including actuators is lower than the achieved overall weight decrease of the airplane due to the reduced drag.

NOMENCLATURE

C	unsteady aerodynamic matrix
F	reference area
K	stiffness matrix
M	mass matrix
V	airspeed
b_r	reference length
$\bar{c}, s$	reference length
k	reduced frequency
m_r	reference mass

*Chief engineer Structural Dynamics and Aeroelasticity ,
Email: Wolfgang.Luber@eads.com

q	generalized coordinate
β	sideslip
δ	generalized coordinate
ρ_r	air density
$\rho/2 V^2$	dynamic pressure
ω_r	reference frequency
ω_x	roll rate
ω_z	yaw rate
φ	roll angle
ψ	yaw angle
ξ	differential flap
ζ	rudder
ε	piezo actuator
r	control variables

INTRODUCTION, first part

The development of vibration alleviation control systems for a modern military aircraft as shown in Fig. 1 is strongly influenced by flight mechanic, flight control and aeroservoelastic effects. The flexible aircraft behavior has significant effects on the active vibration alleviation control system. The sensor signals i.e. transducer signals on wing, fuselage and fin and the signals of the Aircraft Motion Sensor Unit (AMSU) - the gyro platform - contain besides the necessary information of rigid aircraft rates and accelerations the flexible aircraft rates and accelerations in the frequencies of the aircraft elastic modes. The 'flexible' accelerations measured by the accelerometers are passed through the active vibration flight control system control paths; they are multiplied by appropriate gains filters and inserted in the control surface actuator (rudder or auxiliary rudder) or integrated piezo, interface actuator inputs. The flexible aircraft is excited by the high frequency actuation inputs and might therefore experience aeroservoelastic instabilities i.e. flutter or limit cycle oscillations, and/or decrease dynamic load and fatigue loads. The adaptive vibration alleviation system design therefore has to minimize all structural coupling effects to avoid aero elastic instabilities through the available means like optimum sensor positioning, notch filtering.

The first part of the paper describes the major aspects, problem areas to be considered in the adaptive system for vibration alleviation (ASD) design with respect to hydraulic and piezoelectric actuator design and total aircraft aeroservoelastic effects, it outlines an integrated design of ASD with FCS. Many of the design and clearance aspects described here have been addressed in previous publications, Ref.'s 1 to 6 for the aircraft with flight control system.

DESIGN OF ACTIVE FLIGHT CONTROL SYSTEM FOR VIBRATION ALLEVIATION

Design philosophy

The design shall include the derivation of adaptive vibration alleviation (ASD) gains, phase advance filters and notch filters to minimize vibrations and dynamic loads on fin, wing and fuselage structure. In addition the structural coupling effects on total aircraft vibration modes shall be minimized in the ASD optimization process. The ASD shall be de-

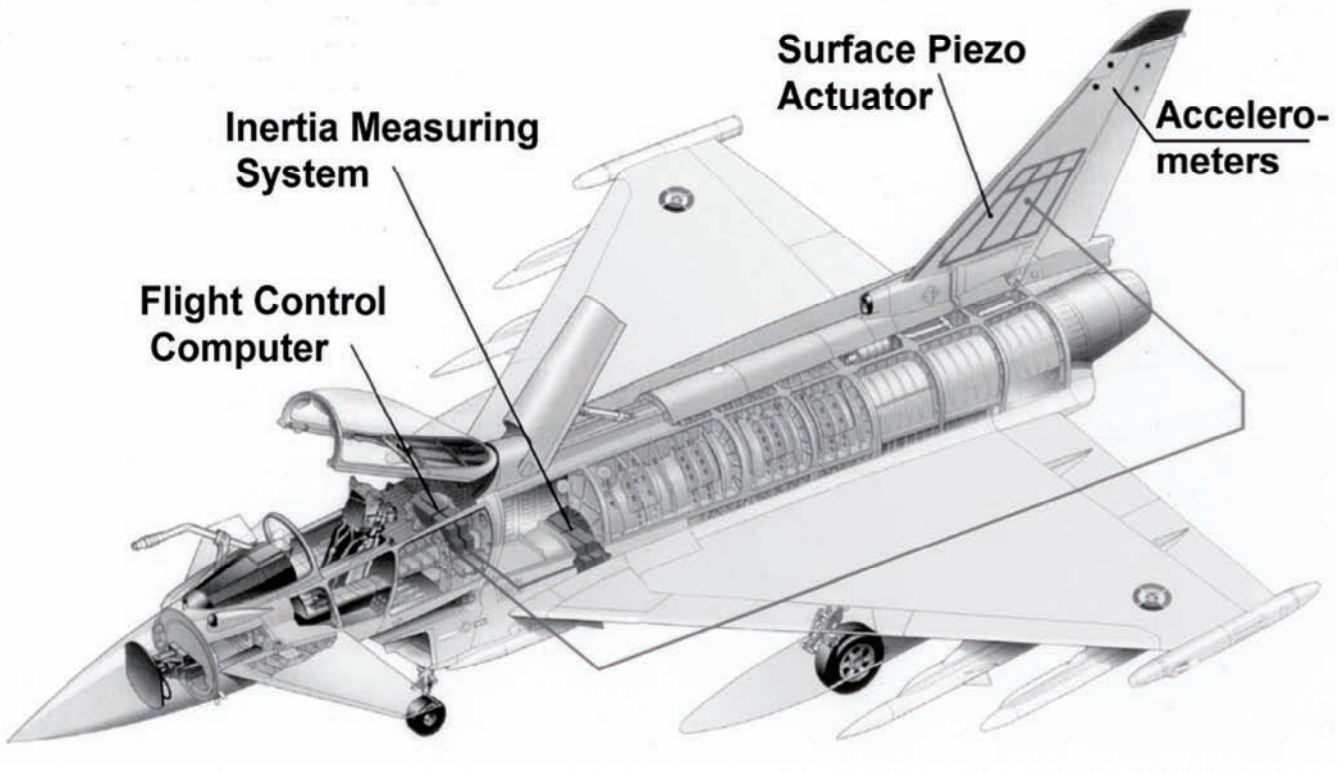

Figure 1: Aircraft with integrated surface piezos

signed to cover the full rigid, flexible aircraft frequency range with respect to aircraft rigid mode and structural mode induced dynamic loads and coupling stability requirements on ground and in flight. The structural coupling influences shall be minimized by ASD and FCS notch filters and notch filters in the wing, fin accelerometer signal feedback signals. The ASD shall be designed to be as robust as possible with respect to all possible aircraft configurations and configuration changes. That includes that all structural changes with configuration should be covered by a constant set of filters to avoid system complexity due to configuration switches for different sets of filters.
In addition scheduling of ASD gains and filters with flight conditions should be introduced to cover the flight envelope. In order to avoid problems in the ASD design due to non-linear unsteady elastic mode and control surface aerodynamics and non-linear piezo-actuator dynamics the elastic mode stability requirements should mainly be based on gain stabilization of the flexible modes. Phase stabilization shall be applied if it can be demonstrated by test.
The ASD design is based upon an analytical model of the total aircraft structure including a linear ASD and FCS model. The analytical model must however be verified through ground test results both from ground resonance and structural coupling testing on aircraft or aircraft components, for example on a component with integrated piezos or with piezo interface. If an ASD demonstrator is envisaged, verification of model technique has to be performed by in flight flutter and structural coupling testing. The model should be updated by the test results for different configurations.

DESIGN REQUIREMENTS

Stability Requirements

The design requirements are primarily stability requirements for all adaptive vibration modes from ASD and flight control rigid/flexible aircraft modes. The stability is achieved by the introduction of notch filters. The Military Specification MIL-F-9490 D for FCS requirements shall be met.

Vibration Alleviation and Dynamic Loads Requirements

The aircraft vibrations on all locations shall meet the requirements of the aircraft without ASD.
The dynamic loads with ASD shall meet the allowable load for the aircraft without ASD for the purpose of increasing the existing incidence range.
The dynamic loads with ASD shall reduce the dynamic loads for the aircraft with ASD for the purpose of increasing the aircraft life cycle.

Flutter Requirements

The FCS design for ASD has to fulfill the flutter requirements of the aircraft without ASD and FCS. The aircraft with ASD and FCS shall meet the 15 % flutter speed margin as well as the minimum elastic mode damping requirements as described in Military Specification MIL-A-8870C.

DESIGN TOOLS

The ASD design for the flexible aircraft is possible with the assumption that the aircraft characteristics are predictable to the necessary accuracy to optimize notch filters which meet the requirements. The characteristics of the controlled flexible aircraft shall be described in the form of open loop frequency transfer functions of the ASD control path feedback loops to a sufficient high frequency, see for example the block diagram in Fig. 2.

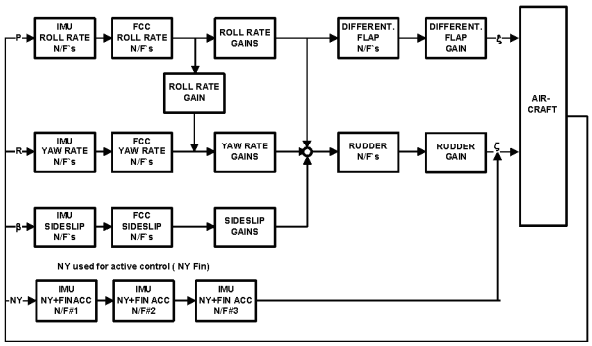

Figure 2: Flow chart for ASD with rudder

For the lateral control the roll rate -, yaw rate-, lateral acceleration - and flow sensor signal β open loop signal has to be described. The open loop signal consists of the transfer function of the aircraft due to control surface input sensed at the inertia measuring unit (rates and accelerations) and at the flow sensors, and the transfer function of the ASD and FCS from the sensor to the opening point and from the opening point to the actuators.
The individual transfer function can be derived from two different methods the first using the analytical dynamic model calculation, the second using on ground measured sensor to actuator input transfer functions from the structural coupling test superimposed with calculated magnitudes of unsteady aerodynamic transfer functions. The applicability of the analytical dynamic model calculation depends on the accuracy of the modeling and its verification. Both methods depend on the accuracy of the unsteady aerodynamic transfer functions which are in both methods derived from theoretical predictions of unsteady aerodynamics for elastic modes and control surface deflection.

Analytical Model of the Flexible Aircraft with Flight Control System

The analytical model of the flexible aircraft with ASD and FCS consists of the linear dynamic description of the flight mechanic equations of motion, the description of the flexible aircraft through modal description using generalized coordinates, generalized masses, stiffness and model structural damping and generalized aerodynamic forces of the

flexible modes and generalized control surface inertia and unsteady aerodynamic terms or generalized piezo actuator forces, the ASD and FCS is described through linear differential equations. In addition hardware and software, i.e. all sensors, actuators, computer characteristics are described by differential equations. The flexible aircraft with FCS can be demonstrated in a matrix form.

The equations of motion for the forced dynamic response of an aeroelastic system can be written in matrix differential equation form for the aerodynamic or piezoelectric ASD systems:

$$m_r b_r^2 \begin{bmatrix} M_{qq} & M_{q\delta} \\ M_{\delta q} & M_{\delta\delta} \end{bmatrix} \begin{Bmatrix} \ddot{q} \\ \ddot{\delta} \end{Bmatrix} +$$

$$+\frac{s_R}{kV}\left\{ \omega_r^2 m_r b_r^2 \begin{bmatrix} gK_{qq} & 0 \\ 0 & K''_{\delta\delta} \end{bmatrix} + \frac{\rho}{2} V^2 F s_R \frac{b_r}{S_R} \begin{bmatrix} C''_{qq} & C''_{q\delta} \\ C''_{\delta q} & C''_{\delta\delta} \end{bmatrix} \right\} \begin{Bmatrix} \dot{q} \\ \dot{\delta} \end{Bmatrix} +$$

$$+\left\{ \omega^2 m_r b_r^2 \begin{bmatrix} K_{qq} & 0 \\ 0 & K'_{\delta\delta} \end{bmatrix} + \frac{\rho}{2} V^2 F s_R \frac{b_r}{s_R} \begin{bmatrix} C'_{qq} & C'_{q\delta} \\ C'_{\delta q} & C'_{\delta\delta} \end{bmatrix} \right\} \begin{Bmatrix} q \\ \delta \end{Bmatrix} = \{Q(t)\}$$

The generalized mass and stiffness matrices are calculated using a finite element model (FEM) of the total aircraft. For dynamic response calculation the FEM is reduced to representative generalized dynamic DOF`s. The true airspeed V and semi span s_R of the reference plane are used to form the reduced frequency k = (ωs_R)/V. F is the area of reference plane and g is the structural damping of the elastic modes. The generalized forces Q(t) are equal to zero for the conventional flutter problem. The generalized coordinate q describes the amplitude of the elastic airplane modes including elastic control surface modes for a system with actuators whereas δ_0 denotes the rotation of the rigid control deflection according to the complex actuator stiffness represented by the impedance function of equation (2).

$$K_{\delta_0\delta_0} = K'_{\delta_0\delta_0} + iK''_{\delta_0\delta_0}$$

For the ASD and FCS controlled aircraft the induced control deflection $\Delta\delta$ has to be introduced as an additional degree of freedom for each control surface or piezo actuator.

The generalized forces generated by the induced control deflections $\Delta\delta$ can be described as the right-hand term of equation (1) for aerodynamic control surfaces and for piezo actuators by

$$\{Q(t)\} = -m_b b_r^2 \begin{Bmatrix} M_{q\Delta\delta} \\ M_{\delta_0\Delta\delta} \end{Bmatrix} \Delta\ddot{\delta} - \frac{\rho}{2} V^2 F s_R \frac{b_r^2}{s_R^2} \frac{s_R}{k \cdot V} \begin{Bmatrix} C''_{q\Delta\delta} \\ C''_{\delta_0\Delta\delta} \end{Bmatrix} \Delta\dot{\delta} -$$

$$-\frac{\rho}{2} V^2 F s_R \frac{b_r^2}{s_R^2} \begin{Bmatrix} C'_{q\Delta\delta} \\ C'_{\delta_0\Delta\delta} \end{Bmatrix} \Delta\delta$$

Assuming normalized rigid control surface modes or piezo actuator mode δ_0 and $\Delta\delta$, the deflection of each control surface or piezo actuator can be superimposed by

$$\delta = \delta_0 + \Delta\delta$$

δ is used here as abbreviation for rudder, and differential inboard and outboard flap or piezo actuator deflection.
The state-space-description of (1) is as follows:

$$\{\dot{x}\} = [A]\{x\} + [B]\{x\}$$

The matrix in equation (1) describing the flexible aircraft with ASD and FCS is enlarged by linearized rigid flight mechanic equations. For example the state vector for lateral control includes then rigid aircraft state variables

$$X = \lceil \beta,\ \omega_x,\ \omega_z,\ \varphi,\ \psi,\ \xi,\ \zeta,\ \varepsilon,\ r,\ q,\ d\xi/dt,\ d\zeta/dt,\ d\varepsilon/dt,\ dr/dt,\ dq/dt \rfloor$$

The flight mechanic equations may in a first approximation contain elastified aerodynamic derivatives as function of incidence, Mach number and they are for low frequency assumed to be decoupled from the flexible aircraft equations. In another approximation the flight mechanic equations are fully rigid and theoretical inertia and unsteady aerodynamic coefficients are introduced.
The flight mechanic equations for lateral control are described below:

Rigid aircraft equations,

Side Force equation

$$\left[-mV + \frac{\rho}{2} V^2 F s / V c_{y\dot{\beta}} \right] \dot{\beta} + \frac{\rho}{2} V^2 F c_{\beta} \beta +$$

$$+\left[-mV \sin\alpha_0 - \frac{\rho}{2} V^2 F s / V c_{yp} \right] \omega_x +$$

$$+\left[mV \cos\alpha_0 - \frac{\rho}{2} U^2 F s / V c_{yr} \right] \omega_z - mg \cos\alpha_0 \varphi = \tilde{Y}(t)$$

Roll Moment equation

$$\frac{\rho}{2} V^2 F s^2 / V c_{l\dot{\beta}} \dot{\beta} + \frac{\rho}{2} V^2 F s c_{l\beta} \beta - \frac{\rho}{2} V^2 F s^2 / V c_{lp} \omega_x -$$

$$-\frac{\rho}{2} V^2 F s^2 / V c_{lr} \omega_z - I_x \dot{\omega}_x - I_{xz} \dot{\omega}_z = \tilde{L}(t)$$

Yaw moment equation

$$\frac{\rho}{2} V^2 F s^2 / V c_{n\dot{\beta}} \dot{\beta} + \frac{\rho}{2} V^2 F c_{l\beta} \beta - \frac{\rho}{2} V^2 F s^2 / V c_{np} \omega_x -$$

$$-\frac{\rho}{2} V^2 F s^2 / V c_{nr} \omega_z - I_{xz} \dot{\omega}_x + I_z \dot{\omega}_z = \tilde{N}(t)$$

MODELING

Structural Modeling

Consideration of the full travel of the flexible mode frequencies with flight condition, fuel contents and actuator failure cases is necessary. The minimum experienced structural damping shall be applied. In order to be accurate, the analytical model has to be updated from ground resonance test results mainly with respect to mode frequencies.

In addition the aircraft identification test results from structural coupling test shall be adopted. Flexible mode frequency shifts with actuator demand amplitude shall be adapted to the modeling to represent minimum and maximum possible mode frequency.
In case of integrated piezo actuators the affected structural component FEM shall include finite element representation of the piezo actuators and corresponding interaction effects piezo to component structure. The properties of the integrated piezo structure shall be derived from coupon tests for the update of the FEM.

Unsteady Aerodynamic Modeling
The unsteady forces used in the dynamic model calculation shall be represented in a conservative manner.
The magnitude (modulus) of the unsteady forces of the flexible modes and of the control surface defection shall be predicted to represent a realistic high value for all Mach numbers and incidences. Since flow separation at higher incidences is leading to alleviation in the motion induced pressure distributions of the flexible modes and of the control surface deflections the introduction of unsteady aerodynamic forces from pure linear theory is regarded to be conservative. Special attention has to be put to transonic effects on the unsteady aerodynamic forces. The assumption of linear unsteady subsonic and supersonic aerodynamics derived by linear theory or numerical Euler code calculations Ref 10 in the linear range is believed to be conservative throughout the full flight envelope.
It shall be stated that the unsteady forces must be calculated for a number of reduced frequencies to cover the full frequency range.

The Phase of the unsteady Aerodynamic forces
For the phase stabilization of low frequency flexible modes like the first wing/fin bending the unsteady aerodynamic phase shall be represented in a conservative manner. A reasonable approach for the phase of the first elastic mode is again the application of linear theory. The argumentation is that at high incidence and combined high FCS gains the aerodynamic damping is increased compared to low incidence from experience found for different wing configurations. In terms of phase stability margin Ref. 3 explains the difference in a Nichols diagram, where linear theory shows the more critical condition.

FCS Model
In order to design in a robust manner the calculation of open loop transfer functions shall consider the worst ASD and FCS gain conditions. The worst trimmed end to end gain conditions have to be included into the model calculations.

Ground Test Results
Ground vibration test results and structural coupling tests are needed to verify or update the calculated results from dynamic model predictions. In general the total aircraft structural dynamic model consisting of sub components can be refined by updating the sub component stiffness and damping using the results from component ground resonance tests and aircraft ground resonance and structural coupling tests. The update of the analytical model is described in Ref. 6.

Flight Test Results
Flight test results from structural coupling/flutter tests are needed to verify or update the predicted results of open loop frequency response functions by the update of unsteady aerodynamic forces used in the dynamic model. This can be achieved through the comparison of predicted and flight test measured closed loop converted into open loop frequency transfer functions.
The comparison there is not only restricted to loop signals, also predicted accelerations at significant aircraft locations are compared, i.e. outer wing, front, rear fuselage, upper fin.
The flight test results are derived through frequency sweep excitation of the control surfaces or of the integrated piezo actuators or piezo-interface, which should be possible through a special software in the FCC's.

EXAMPLES AND RESULTS

Analytical investigations have been performed for the different ASD concepts using the analytical model of a total modern fighter aircraft including a description of ASD and FCS. Open loop frequency response calculations have been calculated first for the different systems with normalized ADS gains and filters as design input for the ASD gain and filter optimization. A first preliminary ASD control law optimization was performed for the aerodynamic systems (rudder and auxiliary rudder concept) and ASD closed loop calculations have been carried out after definition of ASD gains and filters in order to demonstrate the effects of ASD in comparison to the aircraft without ASD. For the integrated piezo system and the piezo interface only the excitation of the aircraft via piezo actuators was investigated until now, an ASD optimization for these systems will be available soon. Since all investigation of the different systems is based on the same analytical model, the results achieved can directly be compared. The inputs for generalized integrated piezos and the generalized piezo interface forces which are used here for the excitation of the total aircraft have been generated by EADS, for the piezo interface. The generalized piezo forces are derived from analytical model calculation of the fin component which includes a FEM representation of the integrated piezo actuators.
Fig. 1 shows for example the aircraft with integrated piezo actuators. The flight control computer will include the ASD control laws besides the FCS control laws. The sensors system for ASD is based on IMU signal together with accelerometer signals on the fin

Results of Rudder Concept

The block diagram for the rudder concept is demonstrated in Fig. 2. Besides the feedback loops necessary for FCS the diagram shows the lateral acceleration feedback to the rudder from fuselage and fin for the ASD.

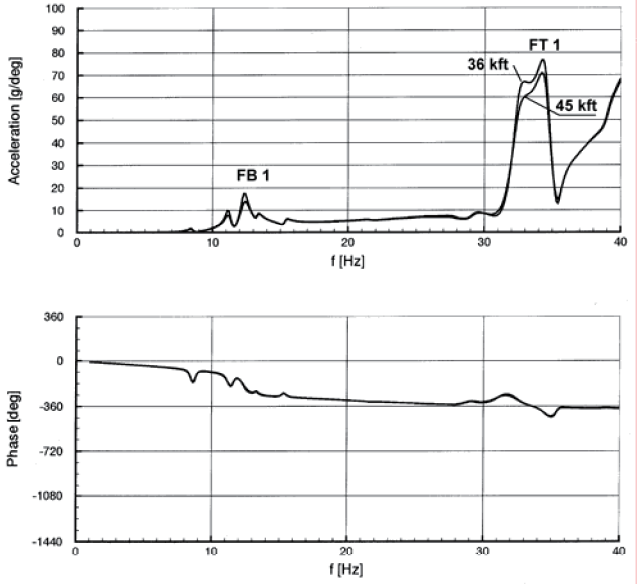

Figure 3: Open loop frequency response: Fin lateral acceleration due to rudder input; Mach = 0.8; 1g; h = 45000ft

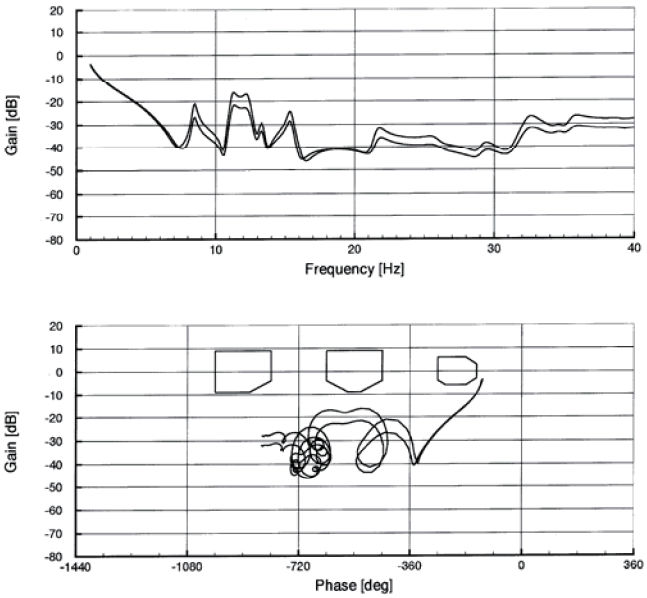

Figure 4: Open loop frequency response due to rudder input with notch filters - lateral path included; Mach = 0.8; 1g; h = 36000ft / 45000ft

Fig. 3 depicts the fin lateral acceleration open loop frequency response function due to rudder excitation for two flight conditions. The figure shows peak in the frequencies of the aircraft elastic modes:
Antisymmetric wing bending at 8 Hz, antisymmetric fuselage bending at 11 Hz, fin bending mode at 12.4 Hz and fin torsion mode at 34 Hz.

Fig. 4 and 5 demonstrates the ASD design by for Bode and Nichols plot of the open loop frequency response at the rudder breakpoint. Fig. 4 depicts the response for normalized ASD gain and Fig. 5 shows the open loop response for an ASD gain and indicates that the stability requirements are met for all elastic modes (no encroachments into the requirements for gain and phase margins). Improvements of ASD are possible by increasing the gain and still meeting the phase requirements. This step has to be performed in a safe manner, i.e. by introducing phase tolerances for actuator non-linearity.

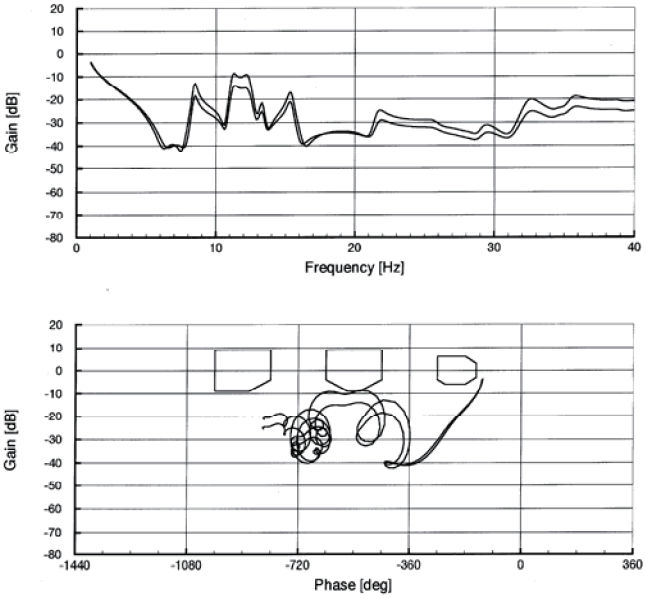

Figure 5: Open loop frequency response function due to rudder input with notch filters - lateral path included with additional gain; Mach = 0.8; 1g; h = 36000ft / 45000ft

The alleviation effect of the ASD rudder concept is demonstrated in Fig. 6, showing the comparison of fin acceleration with and without closed loop ASD. The alleviation shown can be achieved by full use of phase stabilization of the modes and using actuator maximum amplitudes still in the linear range.

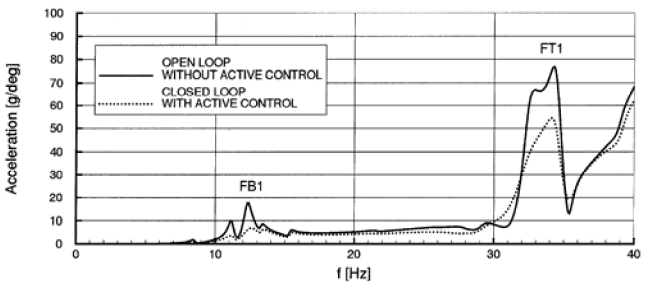

Figure 6: Open loop versus closed loop frequency response: Fin lateral acceleration due to rudder input, damping effect of active control; Mach = 0.8; 1g; h = 45000ft

Results of Auxiliary Rudder Concept

The block-diagram for the auxiliary rudder concept is demonstrated in Fig.7. Besides the feedback loops necessary for FCS the diagram shows the lateral acceleration feedback to the auxiliary rudder from fuselage and fin for the ASD.

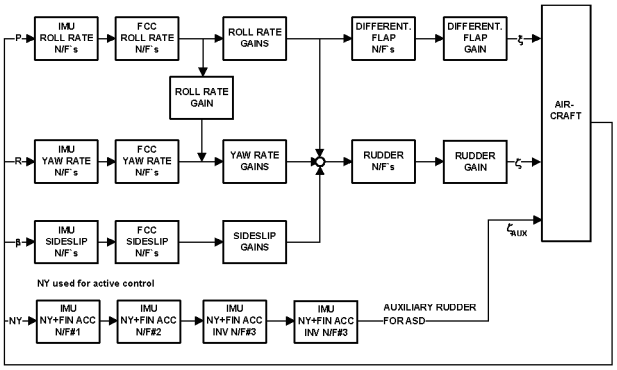

Figure 7: Control loop for ASD with auxiliary rudder

The FCS drives the full span rudder whereas the ASD drives only the auxiliary rudder (upper part of rudder).
Fig. 8 shows the comparison of the fin lateral acceleration frequency response function, FCS in closed loop, ASD in closed and open loop due to auxiliary rudder excitation. These figure shows peak in the frequencies of the aircraft elastic modes: Antisymmetric wing bending at 8 Hz, antisymmetric fuselage bending at 11 Hz, fin bending mode at 12.4 Hz and fin torsion mode at 34 Hz.

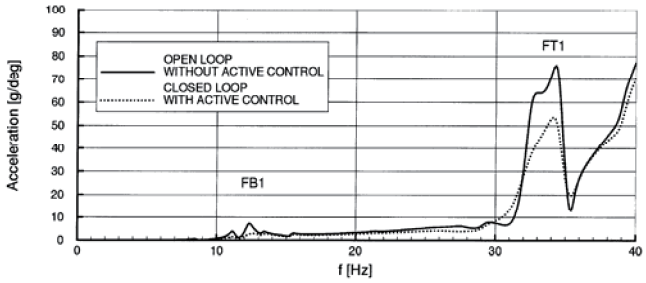

Figure 8: Open loop versus closed loop frequency response: Fin lateral acceleration due to auxiliary rudder input, damping effect of active control; Mach = 0.8; 1g; h = 45000ft

The alleviation effect of the ASD auxiliary rudder concept is demonstrated in Fig. 8, explaining the comparison of fin acceleration with and without closed loop ASD. The alleviation can be achieved by full use of phase stabilization of the modes and using actuator maximum amplitudes still in the linear range.

Results of the Integrated Surface Piezoelectric Actuator Concept

The block-diagram for the integrated surface piezo concept is demonstrated in Fig. 9. Besides the feedback loops necessary for FCS the diagram shows the lateral acceleration feedback to the piezo-actuators from fuselage and fin for the ASD.

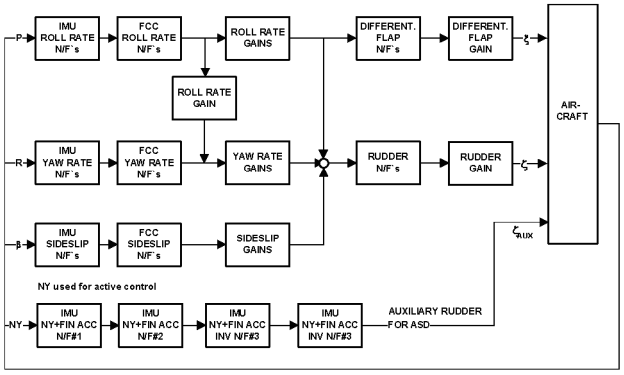

Figure 9: Flow chart of control loop with integrated piezos

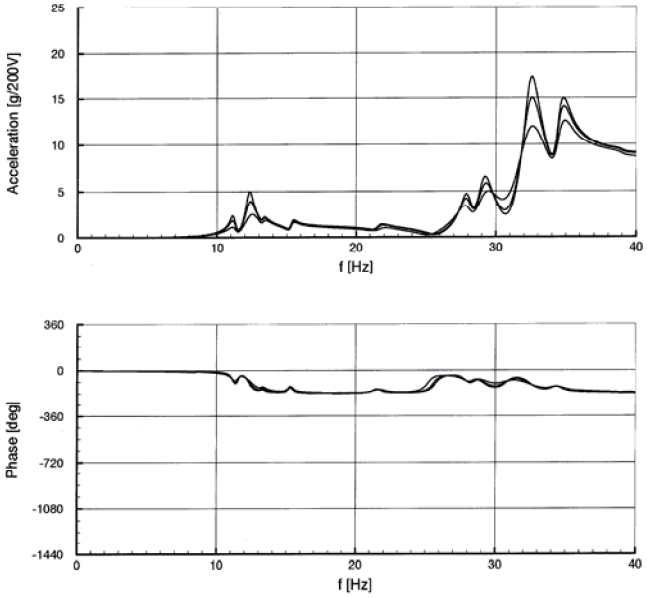

Figure 10: Open loop frequency response: Fin lateral acceleration due to integrated piezo input; Mach = 0.8; 1g; h = 21000ft / 36000ft / 45000ft; piezo input ± 200V, 600W

Fig. 10 shows the fin lateral acceleration open loop frequency response function due to piezo excitation for three flight conditions. The figure shows peak in the frequencies of the aircraft elastic modes: Antisymmetric wing bending at 8 Hz, antisymmetric fuselage bending at 11 Hz, fin bending mode at 12.4 Hz and fin torsion mode at 34 Hz.
No ASD control design has been performed yet for this system; therefore an interpretation of the result can be performed by comparison to other system open loop responses.
Fig. 10 can be compared to previous fin responses due to rudder (Fig. 3) and auxiliary rudder input (Fig. 8) in order to assess the efficiency of the piezo concept.

Results of the Interface Piezoelectric Concept

The block-diagram for the piezo interface concept is demonstrated in Fig. 9. Besides the feedback loops

necessary for FCS the diagram shows the lateral acceleration feedback to the piezo actuators from fuselage and fin for the ASD.
Fig. 11 shows the fin lateral acceleration open loop frequency response function due to piezo excitation for three flight conditions. The figure shows peak in the frequencies of the aircraft elastic modes: Antisymmetric wing bending at 8 Hz, antisymmetric fuselage bending at 11 Hz, fin bending mode at 12.4 Hz and fin torsion mode at 34 Hz.

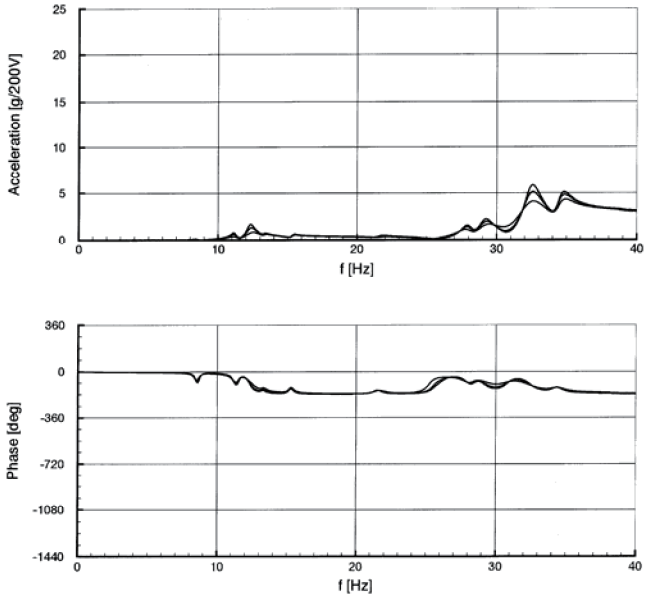

Figure 11: Open loop frequency response: Fin lateral acceleration due to piezo interface input; Mach = 0.8; 1g; h = 21000ft / 36000ft / 45000ft; piezo input ± 200V, 600W

No ASD control design has been performed yet for this system; therefore an interpretation of the result can be performed by comparison to other system open loop responses.
Fig. 11 can be compared to previous fin responses due to rudder (Fig. 3) and auxiliary rudder input (Fig. 8) in order to assess the efficiency of the piezo concept.

Comparison of the different systems

A comparison of the possible excitation of fin response due to excitation for the different systems is shown in Table 1. The comparison shows that the aerodynamic ASD systems as well as the integrated piezo system show similar excitation levels in the frequency range considered. The interface piezo concept shows less excitation. The comparison is performed on the basis of maximum actuator amplitude and max. Volt input at the same level of applied energy.

VALIDATION OF THE TOTAL AIRCRAFT MODEL

The analytical model for the present investigation is validated by on ground test and flight test results.

The validation was based on comparisons of predicted and measured on ground GRT and structural coupling test results on ground and in flight. Further validation is needed for the auxiliary rudder concept; this will be performed on a total aircraft wind tunnel model. Further validation is also needed for the modeling of integrated piezo concept and of the interface piezo concept. This validation will be performed in a first step on an already existing test box which simulates the aircraft fin structure.

Comparison of max. excitation of fin tip acceleration for fin bending mode (12.3 Hz)

CONCEPT	FIN TIP acceleration	POWER [kW]
Rudder	7.2 g / 2 deg (2 deg. Actuator limit)	2 kW
Auxiliary Rudder	9.0 g / 3 deg.	2 kW
Surface Piezo	10 g / 200 V (200V → max)	2 kW max Power
Interface Piezo	3.2 g / 200 V (200V → max)	2 kW max Power

Comparison of max. excitation of fin tip acceleration for fin torsion mode (34 Hz)

CONCEPT	FIN TIP acceleration	POWER [kW]
Rudder	20 g / 0.25 deg. (2 deg. Actuator limit)	2 kW
Auxiliary Rudder	20 g / 0.25 deg.	2 kW
Surface Piezo	34 g / 200 V (200V → max)	2 kW max Power
Interface Piezo	35.8 g / 200 V (200V → max)	2 kW max Power

Table 1: Comparison of the different concepts, Mach = 0.8; h = 45000ft, 1g;

CONCLUSION, vibration alleviation system

The present total flexible aircraft investigations performed for the different adaptive vibration alleviation system, the ruder and auxiliary rudder concept, the integrated surface piezo and the piezo-interface concept came to the following results:

- The analytically investigated different adaptive vibration alleviation systems rudder, auxiliary rudder and integrated piezo concept show similar high vibration alleviation at the aircraft fin related to equivalent power of the systems.

- The piezo interface system shows less alleviation at the moment.
- The results presented for integrated surface piezo and piezo interface concept as well as the auxiliary rudder concept have to be verified through already prepared test box tests and wind tunnel test in case of auxiliary rudder.
- Investigations shall be performed to detail the achievable alleviation of the systems in relation to maximum buffet induced vibrations for different subsonic flight conditions.

INTRODUCTION, second part

In the past decade EADS Military Air System division has investigated also different concepts for actively / adaptive deformable aircraft wing structures as part of its investigation on future structural concepts [8, 13]. Through the control of the local wing twist and camber the optimum local deformation can be achieved also with consideration of controlled aeroelastic deformations.

Besides the investigation of structural concepts, aerodynamic research programs had been initiated in order to demonstrate and validate the benefits with respect to maneuver performance, drag reduction, enhancement of aircraft maneuver control and aircraft stabilization

As part of the "Advanced Aircraft Structures Program", feasibility studies of different structural concepts of active wings have been performed. These studies have revealed significant problems related to system complexity and functionality under environmental conditions and severe problems combined with the development of adequate materials. However, promising approaches have been identified

AERODYNAMIC INVESTIGATIONS

Recently performed aerodynamic investigations of adaptive deformable aircraft structures featuring optimum aerodynamic shape control of outer wing and leading and trailing edge on a scale model of an actual aircraft have been performed with aerodynamic CFD simulations and wind tunnel tests on a complete aircraft with different shapes of the wing trailing edge, see Fig. 12.

Aeroelastic simulations, i.e. coupled structural dynamic response and computational fluid dynamics (CFD) at trimmed flight conditions, have been carried out using the dynamic model of a total aircraft trimmed both with conventional trailing edge flap deflections and with adaptive trailing edge. The calculations have been performed at high dynamic pressure assuming that the adaptive trailing edge has similar torsional stiffness compared to the conventional flap. From the simulation elastified pitch moment derivatives for the inboard and outboard trailing edge deflection have been derived which show a considerable increase in the moment derivatives. This gives an indication of the enhancement the adaptive trailing edge provides on control performance w.r.t. maneuvering and aircraft stabilization.

Figure 12: Wind tunnel test of a fighter aircraft model with simulated adaptive trailing edges.

The wind tunnel measurements have been performed on a complete aircraft model with conventional trailing edge flaps and an adaptive trailing edge in the low speed wind tunnel of the Technical University of Munich (TUM) 11-12]. The adaptive trailing edge was simulated by several rigid trailing edges for different deflections. The model support allowed measurement of total aircraft model lift, drag, pitch and roll moment. From the measurement results, considerable improvements could be demonstrated of the adaptive trailing edge as follows:

- Considerable drag reduction
- Improvement of pitch control at different lift conditions.
- Improvement of roll control at different lift conditions.

STRUCTURAL CONCEPTS

Primarily as part of the "Advanced Aircraft Structures Program" [10], different structural concepts of active wings have been investigated at EADS during the last decade.

Shape memory alloy (SMA) trailing edge

Very early, a first demonstrator (see Fig.13) of an active airfoil trailing edge has been built and tested [8]. In this approach, a network of shape memory alloy (SMA) wires stabilizes a glass fiber reinforced plastic (GFRP) structure. By sequentially contracting

counter-acting SMA wire actuators, upward and downward deflections of the trailing edge can be achieved. At a length of 200 mm, a deflection of ±25 mm was demonstrated. Beside this, the structure was able to carry all the necessary aerodynamic loads.

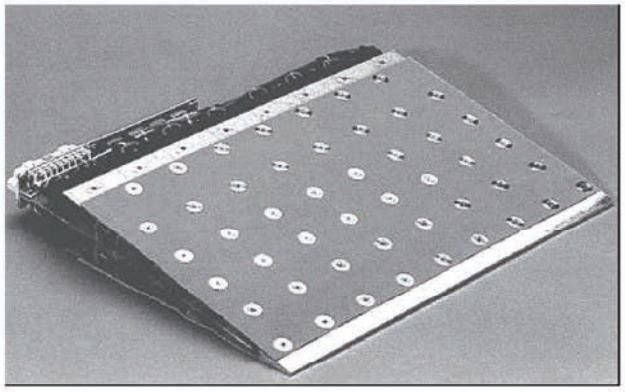

Figure 13: Trailing edge demonstrator with GFRP structure and SMA wire actuators.

Unfortunately, there are some drawbacks of the SMA wire approach, which, at the end, lead to the cancellation of the program:

- The energy efficiency of the SMA actuating system is poor.
- The SMA wire actuators are comparably slow; movement cycles are far below 1 Hz. Therefore, SMA wire actuators are not suitable for the movement of control surfaces.
- Due to the different tensile modulus in the martensitic and austenitic state, a spring back occurs if the heating circuit is switched off.

External actuator concept

The active wing program starting in 2000, investigated new concepts for active wings. The SMA active wing had demonstrated both that smart actuators where not yet ready for the task, and that a major focus has to lie on the structural concept. Therefore, the principal idea of the active wing program was to find an efficient structural design, which can be coupled to more or less conventional actuators.

The final designs had two external actuators installed in extensions of already existing pylons, Fig 14. This approach resulted in optimum actuator efficiency while minimizing additional drag. To account for the different elongation between top and bottom skin, the upper and lower skins have been joined together using flexible stringers. At the trailing edge, both skins were sliding relative to each other. This approach resulted in an extremely complex structural design, which lead to weight and cost drawbacks.

Intensive tests have been performed on flexible stringers, see Fig.15. Dynamic testing has demonstrated sufficient fatigue life, but the available translational range limits the application to the forward part of the flexible trailing edge.

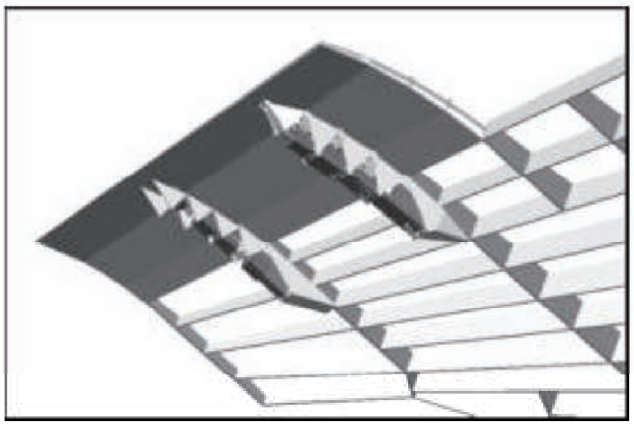

Figure 14: Design of an active wing with a flexible structure and external actuators. The external actuators are installed in extensions of already existing pylons.

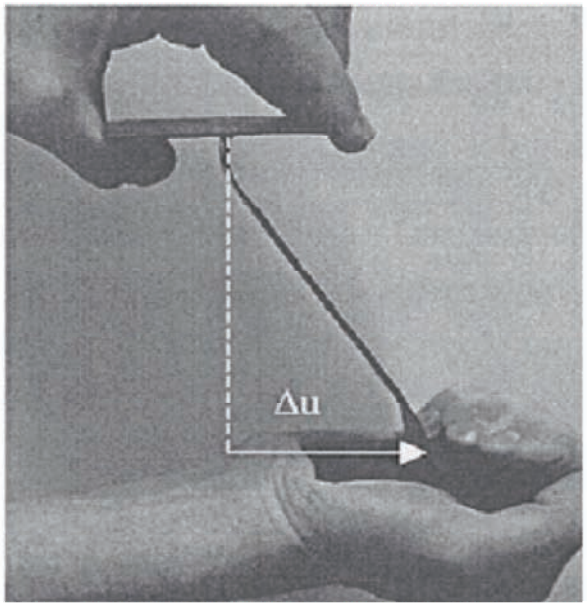

Figure 15: Structural test sample of a flexible stringer

Integrated actuator designs

At present novel concepts are under investigation that might lead to a promising way ahead. One of this concept uses torsional hydraulic actuators within the wing, another one uses transversal hydraulic actuators (patent pending), which are distributed in the aircraft skin, see Fig. 16 & 17.

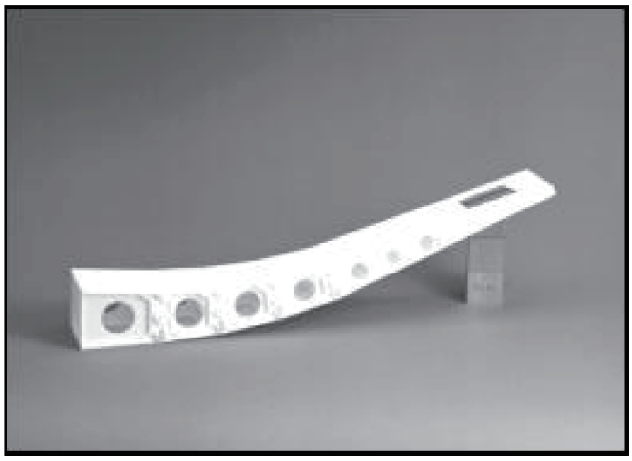

Figure 16: Mockup of the tube actuator structure with integrated actuators.

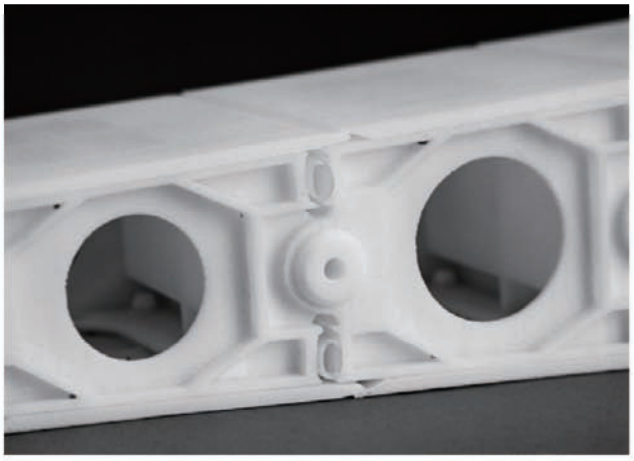

Figure 17: Detail view of a tube actuator node element mockup.

Detailed analyses of this approach have shown the potential and viability of this approach. Especially it could be shown that the expected weight increase of the adaptive wing structure including actuators is lower than the achieved overall weight decrease of the airplane due to the reduced drag. In Fig. 18, a comparison is shown for a generic fighter aircraft design, where the perceptual weight changes of the different components of the active wing are compared to a conventional wing. Despite requiring more weight for structure, actuators, hydraulics and electronics, the higher efficiency of the adaptive wing causes an overall weight decrease compared to the conventional wing.

Another interesting aspect is the reduction of power requirements. Both the torsional actuator and the tube actuator concepts are using multiple actuator lines. The moment the actuators have to counter decreases in the direction to the trailing edge, but it should be noted that the first actuator line has to counter roughly the same moment as the conventional one.

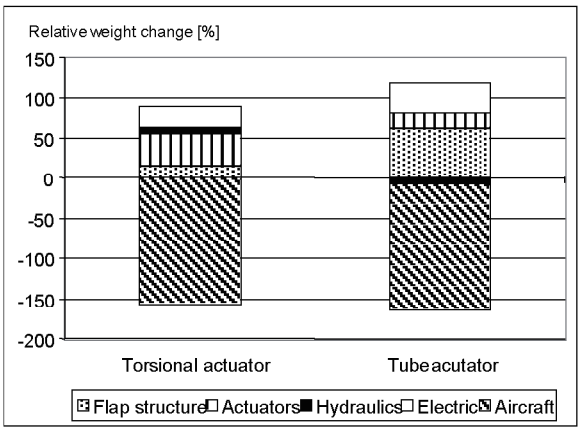

Figure 18: Weight comparison of two concepts of active wings, relative to a conventional one

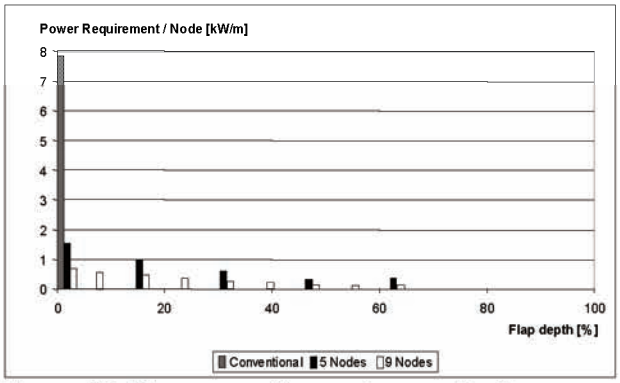

Figure 19: Power requirement per actuator for conventional (1 node), torsional actuator (5 nodes) & tube actuator (9 nodes) flap.

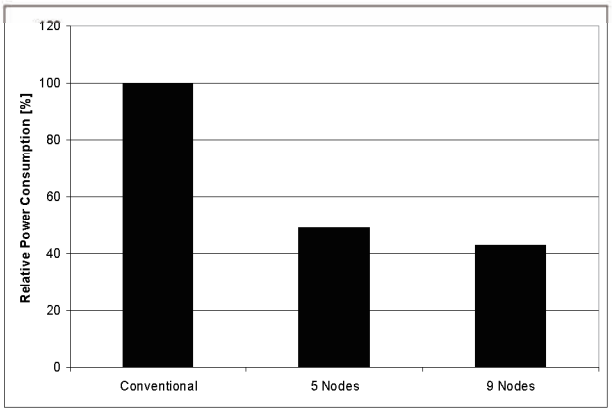

Figure 20: Total power requirement for conventional (1 node), torsional actuator (5 nodes) & tube actuator (9 nodes) flap

The difference lies in the required angular velocity at each actuator to achieve the necessary deflection within the specified time. Fig. 19 shows a comparison of the conventional, torsional actuator (with 5 nodes) and tube actuator (with 9 nodes) wing. Regarding mechanical power only, the total power requirement drops with increasing number of nodes, as shown in Fig. 20.

CONCLUSION, morphing concepts

The wind tunnel results demonstrate and validate the benefits of the adaptive trailing edge with respect to maneuver performance, drag reduction, enhancement of aircraft maneuver control and aircraft stabilization at low speed. At high dynamic pressure the improvements might reduce due to aeroelastic effects. However, as demonstrated by aeroelastic simulations there are still significant benefits available.

Structural concepts like the tube actuator concept and the torsional actuator concept have been developed that actually are capable of sustaining the structural loads and still perform the desired shape deformation. The weight of the trailing edge itself is considerably higher than that of a conventional trailing edge. However, this is more that compensated for by the improved efficiency of the wing, resulting in an overall weight reduction on aircraft level.

An interesting aspect is the reduced mechanical power requirement of the adaptive wing. As the movement of the wing is spread over a couple of actuators each performing a fraction of the movement, the total power consumption is actually lower compared to the conventional trailing edge.

The investigations have shown the potential of the concept of an adaptive wing; however a lot of development work is still necessary until an implementation of this concept can be considered.

REFERENCES

[1] A. Lotze, O. Sensburg and M. Kühn
Flutter Investigations on a Combat Aircraft with a Command and Stability Augmentation System
AIAA Paper No. 75-1025, AIAA 1975 Aircraft Systems and Technology Meeting, Los Angeles

[2] O. Sensburg, J. Becker, H. Hönlinger
Active Control of Flutter and vibrations of an Aircraft.
Proceedings of the International IUTAM, Symposium on Structural Control, university of Waterloo, Ontario, Canada, June 1979

[3] W. Luber; J. Becker
High Incidence Unsteady Aerodynamic for Aeroservoelasticity Predictions
85th AGARD Structures and Material Panel Specialist Meeting, Aalborg, Denmark, October 1997

[4] H. Hönlinger, H. Zimmermann, O. Sensburg, J. Becker
Structural Aspects of Active Control Technology
AGARD Conference Proceedings on Active Control Technology, FMP Symposium Turin, Italy, May 1994
AGARD SMP Meeting on Advanced Aeroservoelastic Testing, Rotterdam, NL, May 1995.

[5] J. Becker, W. Luber
Unsteady Aerodynamic Forces at High Incidence and their Application in Structural- and Flight Control Design. International Forum on Aeroelasticity and Structural Dynamics; Manchester, UK; June 1995

(6) J. Becker, .V. Vaccaro
Aeroservoelastic Design, Test verification and Clearance of an Advanced Flight Control System. AGARD SMP Specialist Meeting on Advanced Aeroservoelastic Testing, Rotterdam, May 1995

[7] Ch. Breitsamter
Turbulente Strömungsstrukturen an Flugzeug konfigurationen mit Vorderkantenwirbeln Dissertation TUM 1997

[8] K. Dittrich,
Prospects of Smart Structures for Future Aircraft"; NATO Advanced Study Institute „Mechanics of Composite Materials and Structures"; Tróia, Portugal, July 12-24, 1998.

[9] J. Becker et al.,
The Advanced Aircraft Structures Program - An Overview", Proceedings of the SPIE smart structures conference, Newport Beach, USA, 1999.

[10] K. Dittrich,
Formveränderung von Flügel Strukturen mittels integrierter Shape Memory Alloy Aktuatoren Proceedings of the DGLR conference, Erlangen, Germany, 1994

[11] Ch. Breitsamter,
Aerodynamik hochmanövrierfähiger Flugzeuge mit formvariablen Hinterkantenklappen,
DGLR annual conference, Germany, 2003

[12] Ch. Breitsamter,
Aerodynamic Efficency of high maneuverable aircraft applying adaptive wing trailing edge section, 24th International Congress of the Aeronautical Sciences, 2004.

[13] K. Dittrich, J. Becker, W. Luber
Structural Concepts for Morphing Wing
Third European Conference on Structural Control, 2004 Vienna, Austria

Flutter LCO in Isentropic Flow: Analytical Theory

A. V. Balakrishnan *

Abstract: Using full continuum models, we establish purely theoretically that in two-dimensional isentropic flow, the flutter speed for a slender high-aspect ratio wing is a Hopf bifurcation point of the aeroelastic structure dynamics which can be expressed as a non-linear convolution evolution equation. The flutter speed is determined by the linearized model and the LCO is periodic with period $\left(\frac{2\pi}{\omega}\right)$where ω is the angular flutter frequency in the linear model, and can be expressed as a harmonic series.

Introduction

Using full continuum models, we establish purely theoretically that in two-dimensional isentropic flow, the flutter speed for a slender high-aspect ratio wing is a Hopf bifurcation point of the aeroelastic structure dynamics which can be expressed as a non-linear convolution evolution equation. The flutter speed is determined by the linearized model and the LCO is periodic with period $\left(\frac{2\pi}{\omega}\right)$where ω is the angular flutter frequency in the linear model, and can be expressed as a harmonic series.

We have taken some pains to describe the model in enough detail since continuum models are rare. Because of the page limitation we have had to omit all details of proofs of results.

The structure model, which goes back to Goland [1], is described in section 2. Of course, the main simplification is to neglect camber, but it is not expected that this significantly alters the qualitative nature of the results and certainly not the flutter speed, which is based on the linearized model. In section 2 we also describe the isentropic flow model and the boundary conditions in more detail than has been done in the standard texts on aeroelasticity [2, 3].

Some attention is paid to the linearized model in section 3, in particular to the role of the Possio equation, which is practically ignored in [3]. The importance of the linear model is that the solution to the non-linear problem can be boot-strapped on the linear, as we show in section 4. It is shown that the aeroelastic structure equation can be described as a non-linear convolution-evolution equation, for fixed M, with U as the speed parameter for which the Hopf bifurcation theory applies. The flutter LCO is not sinusoidal but periodic, with period $\left(\frac{2\pi}{\omega}\right)$ where ω is the angular flutter frequency determined from the linear model, and is expressed as a harmonic series.

*Flight Systems Research Center, UCLA. Research supported in part under NSF grant no. ECS-0400730.

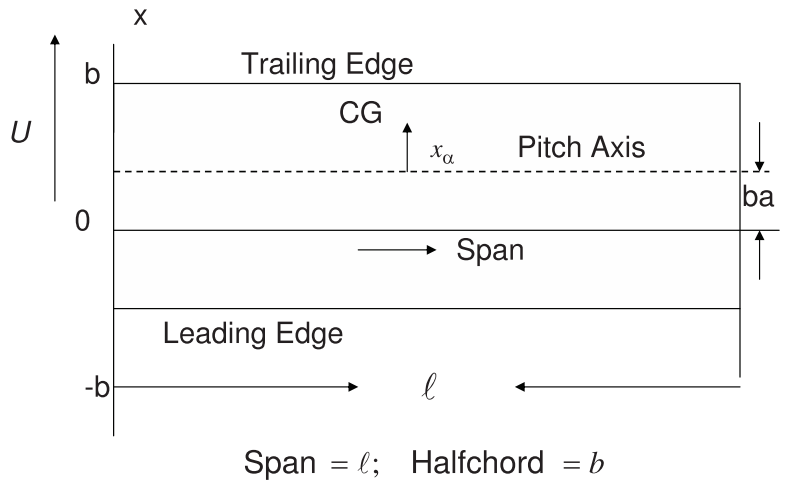

Figure 1: Wing Structure Beam Model

1 The Structure Model

The earliest model of a wing structure stated in terms of a partial differential equation would appear to be that of Goland [1, 2], which utilizes a uniform slender (i.e. zero thickness disregarding camber) rectangular 'beam' model with two degrees of freedom—plunging (beam bending) and pitching (beam torsion)—a cantilever beam attached to the fuselage and free at the other end. With $h(t, y)$ denoting the displacement normal to the structure plane and $\theta(t, y)$ denoting the pitch angle about an axis parallel to the y-axis (see figure 1),

$$-b < x < b;\ 0 < y < \ell < \infty,\ t > 0$$

the structure dynamics can be described as:

$$\left.\begin{array}{l} m\ddot{h} + S\ddot{\theta} + EIh'''' = L(t,y) \\ I_\theta\ddot{\theta} + S\ddot{h} - GJ\theta'' = M(t,y) \end{array}\right\}, \quad 0 < y < \ell \tag{1.1}$$

where prime denotes derivative with respect to the y-variable, with appropriate boundary conditions (cantilever or free-free). The forcing functions on the right-hand side, the lift $L(t, \cdot)$ and the moment $M(t, \cdot)$, are determined by the aerodynamics model described in the next section, and will depend on the structure dynamic variables $h(\cdot)$ and $\theta(\cdot)$.

We can also add a control term as in [4] but the emphasis in this paper is on the aerodynamics, by far the more complicated part.

2 The Aerodynamic Model

The basic references here are [5, 6, 7]. The airflow is described in terms of Eulerian dynamics where q is the 3×1 flow vector

$$q(t, x, y, z) \quad t > 0 \quad x, y, z \in R^3$$

supplemented by the positive-valued thermodynamical variables:

$$\begin{array}{ll} \text{Pressure } p, & p(t,x,y,z) \geq 0 \\ \text{Density } \rho, & \rho(t,x,y,z) \geq 0 \\ \text{Temperature } T, & T(t,x,y,z) \geq 0 \end{array}$$

We may also include the entropy $S(t,x,y,z)$. Any two of the variables will determine the other two. A basic assumption is the Perfect Gas Law,

$$p = \rho R T$$
$$R = c_p - c_v, \quad \gamma = \frac{c_p}{c_v} > 1$$

where $c_p,\ c_v$ denote specific heat at constant pressure and volume, respectively. Far field values ($|z| + |y| + |x| \to \infty$) will be denoted $q_\infty,\ p_\infty,\ \rho_\infty,\ T_\infty$ and assumed finite.

2.1 The Field Equations

All relations we need to describe the dynamics are to be deduced from two laws:
1. Law of Conservation of Mass:

$$\frac{\partial \rho}{\partial t} + \nabla \cdot (\rho q) = 0 \tag{2.1}$$

2. Law of Conservation of Momentum:

$$\rho \frac{Dq}{Dt} + \nabla p = \lambda \Delta q + (\lambda + \mu/3)\nabla(\nabla \cdot q) \tag{2.2}$$

where μ, λ are constants (may depend on T) describing the fluid (air). μ is the shear viscosity and λ is the bulk viscosity. To this we must add an "energy equation" [5, p. 33] which we shall need to discuss more below. We note that μ is very small for perfect gases. In air, $\mu = 1.85 \times 10^{-5}$kg/m/s, $\lambda = 0.6\mu$. The question of smallness of μ, λ has to be ultimately referred to the Reynolds number [see 5, 6].

2.2 Aeroelastic Boundary Conditions

In viscous flow, the boundary condition on the wing boundary is characterized by

$$q(t,x,y,0) = q_\infty(t,x,y,0) + k\frac{Dz}{Dt}, \quad |x| < b,\ 0 < y < \ell \tag{2.3}$$

where z is the wing displacement: in the direction normal to the wing,

$$z(t) = h(t,y) - (x-a)\theta(t,y), \quad 0 < y < \ell,\ |x| < b. \tag{2.4}$$

All we are interested to obtain from the flow is the pressure differential over the wing

$$\delta p(t,x,y) = p(t,x,y,0+) - p(t,x,y,0-)$$

from which we calculate what we need in (1.1), the lift and monent:

$$L(t,y) = \int_{-b}^{b} \delta p(t,x,y)dx, \quad 0 < y < \ell \tag{2.5}$$

$$M(t,y) = \int_{-b}^{b} (x-a)\delta p(t,x,y)dx, \quad 0 < y < \ell. \tag{2.6}$$

It is convenient to consider $\frac{Dz(t)}{Dt)}$ as the "input" and $\delta p(t,\cdot)$ as the "output"—relating the Lagrangian dynamics of wing structure to the Eulerian flow dynamics. q_∞ is the air speed, the far-field ($|x|,|y|,|z| \to \infty$) flow,

$$q_\infty = U(i\cos\alpha + j\cos\beta + k\cos\gamma)$$

in the usual way. α is the "angle of attack".

2.3 Isentropic Flow

Our first simplification is to consider the non-viscous case

$$\mu = 0 = \lambda \tag{2.7}$$

where the flutter phemonema are not lost. However, we need to invoke a thermodynamic assumption, that the entropy $S(t,x,y,z)$ is constant, and thus the flow is "isentropic". This is a remarkably simplifying assumption that makes the flow irrotational. For this however we need to invoke the Gibbs relation,

$$T\nabla S + \frac{\nabla p}{\rho} = \nabla(c_p T) \tag{2.8}$$

By the Perfect Gas Law,

$$\nabla(c_p T) = \frac{c_p}{R}\nabla(p/\rho)$$

and hence

$$\frac{\nabla p}{\rho} = \frac{c_p}{R}\left[\frac{\nabla p}{\rho} - \frac{p}{\rho^2}\nabla\rho\right],$$

relating the pressure to density. With

$$\gamma = \frac{c_p}{c_v} > 1,$$

this yields

$$\nabla \log\left(\frac{p}{\rho^\gamma}\right) = 0$$

or

$$p = A\rho^\gamma, \tag{2.9}$$

where A is a constant. Now by definition

$$\frac{dp}{d\rho} = a_\infty^2$$

where a_∞ is the speed of sound, and we have that

$$\gamma\frac{p_\infty}{\rho_\infty} = a_\infty^2$$

where p_∞, ρ_∞ are the undisturbed or far-field values of pressure and density assumed constant.

Getting back now to the inviscid version of the momentum conservation law, we have

$$\frac{\partial q}{\partial t} + (q \cdot \nabla)q + \frac{\nabla p}{\rho} = 0. \tag{2.10}$$

Hence with

$$\Omega = \nabla \times q$$

we have

$$\frac{\partial \Omega}{\partial t} + \nabla \times (q \cdot \nabla)q = 0.$$

Using the identity

$$(q \cdot \nabla)q = \frac{1}{2}\nabla ||q||^2 - q \times \Omega$$

we obtain

$$\frac{\partial \Omega}{\partial t} + \nabla \times (q \times \Omega) = 0, \quad t \geq 0.$$

For given q, we may consider this as a linear equation

$$\dot{\Omega} = L(t)\Omega$$

where

$$\Omega(0) = 0.$$

Hence it follows that

$$\Omega(t) = 0$$

or

$$\nabla \times q = 0.$$

Hence

$$q = \nabla \phi \tag{2.11}$$

where ϕ is the velocity potential, and we have "potential flow". The point to be noted here is that we do not invoke Crocco's Theorem as in [8]. This idea is borrowed from [6, p. 71]. Note that we can have isentropic flow which is rotational depending on the initial flow (see [5, p. 24], for more).

Hence

$$\frac{\partial q}{\partial t} + \frac{1}{2}\nabla ||q||^2 + \frac{\Delta p}{\rho} = 0$$

or

$$\nabla \left[\frac{\partial \phi}{\partial t} + \frac{1}{2}|\nabla \phi|^2 + \frac{p}{\rho} \right] = 0.$$

Hence

$$\frac{\partial \phi}{\partial t} + \frac{1}{2}|\nabla \phi|^2 + \frac{p}{\rho} = \text{Far Field Values} = \frac{1}{2}U^2 + \frac{p_\infty}{\rho_\infty}$$

$$U = ||q_\infty||$$

and

$$\frac{p}{\rho} = A\rho^{\gamma-1} = \frac{a_\infty^2}{\gamma - 1}\left(\frac{\rho}{\rho_\infty}\right)^{\gamma-1}$$

or

$$\rho^{\gamma-1} = \rho_\infty^{\gamma-1}\frac{(\gamma-1)}{a_\infty^2}\left[\frac{1}{2}U^2 + \frac{a_\infty^2}{\gamma-1} - \frac{\partial\phi}{\partial t} - \frac{1}{2}|\nabla\phi|^2\right].$$

We can now invoke the law of Conservation of Mass and obtain

$$\begin{aligned}\frac{\partial}{\partial t}\rho^{\gamma-1} &= (\gamma-1)\rho^{\gamma-2}\frac{\partial\rho}{\partial t}\\ &= (\gamma-1)\rho^{\gamma-2}[\nabla\cdot\rho\nabla\phi].\end{aligned}$$

After a little analysis this leads to the Euler Full Potential Equation for the velocity potential ϕ

$$\frac{\partial^2\phi}{\partial t^2} + \frac{\partial}{\partial t}|\nabla\phi|^2 = a_\infty^2\left(1 + \frac{\gamma-1}{a_\infty^2}\Big(\frac{U^2}{2} - \frac{\partial\phi}{\partial t} - \frac{|\nabla\phi|^2}{2}\Big)\right)\nabla^2\phi - \nabla\phi\cdot\nabla\frac{|\nabla\phi|^2}{2}. \quad (2.12)$$

The main thing to note in this equation in contrast to the Navier-Stokes is that there are no (spatial) second derivatives of the flow velocity $\nabla\phi$. Because of this the boundary condition (2.3) is now simplified to "no slip" on the boundary flow, or

$$k\cdot\nabla\phi = \nabla\phi_\infty\cdot k + \frac{Dz}{Dt} \text{ on } z=0,\ |x|<b,\ 0<y<\ell.$$

Unfortunately this is not enough for uniqueness of solution. For that, we have to add

$$\delta p = 0,\ z=0,\ |x|>b,\ y>\ell,\ y<0$$

and the Kutta condition

$$\delta p = 0, \quad z=0,\ x\to b-.$$

We still need to show how to calculate δp from the flow equation. Let ψ denote the acceleration potential

$$\psi = \frac{\partial\phi}{\partial t} + \frac{1}{2}|\nabla\phi|^2.$$

Then

$$p = \frac{\rho_\infty a_\infty^2}{\gamma}\left(1 + \frac{\gamma-1}{a_\infty^2}\Big(\frac{1}{2}U^2 - \psi\Big)\right)^{\frac{\gamma}{\gamma-1}},$$

which is usually simplified to

$$p = \frac{\rho_\infty a_\infty^2}{\gamma}\left(1 + \frac{\gamma}{a_\infty^2}\Big(\frac{1}{2}U^2 - \psi\Big)\right)$$

so that at $z=0$

$$\delta p = -\rho_\infty\delta\psi.$$

Again we may think of $\frac{Dz}{Dt}$ as the input and δp as the output. We shall show how this connection is provided by the Possio Integral Equation [9]. We only consider the subsonic case:

$$\frac{U}{a_\infty} < 1.$$

3 Linear Aeroelasticity

We specialize from now on to 2D, or Typical Section (Airfoil) Theory, where we drop the dependence on the y-coordinate but only in the aerodynamic flow equation. In particular,

$$\phi_\infty = U(x\cos\alpha + z\sin\alpha)$$

where α is the angle of attack.

Our focus is on the question of stability about the 'equilibrium'—steady or time-invariant—state. We can readily verify that

$$\phi = \phi_\infty$$

$$\theta = 0; \quad h = 0$$

is a time-invariant solution of the aeroelastic equations, where U, α are totally arbitrary. There are other time-invariant solutions but only for a discrete sequence of values of U (see [10]), which we shall not consider here.

3.1 Linearization

It is natural to begin with the aeroelastic system linearized about the equilibrium state because stability is completely determined by the linearized system. For this purpose we exploit the unique feature of the problem in the boundary conditions

$$\frac{\partial\phi}{\partial z} = \frac{\partial\phi_\infty}{\partial z} + \frac{Dz(t)}{Dt}$$

where

$$\frac{Dz(t)}{Dt} = -\dot{h}(t,y) - (x-a)\dot{\theta}(t,y) + \theta(t,y)\frac{\partial\phi}{\partial x}, \quad z = 0,\ |x| < b$$

$$= w_a(t,x),\ \text{the downwash for fixed } y$$

and, as far as the flow is concerned, the structure state variables are just scalar parameters for fixed y. Hence for each $t > 0$ we may start by assuming that the solution is analytic in them, in some neighborhood of the zero structure state. Thus let $\phi(\lambda, t, x, z)$ denote the solution corresponding to $\lambda\theta(t,y)$, $\lambda h(t,y)$, for scalar λ, with

$$\phi(0,t,x,z) = \phi_\infty(x,z)$$

and

$$\frac{\partial\phi(\lambda,t,x,0)}{\partial z} = U\sin\alpha - \lambda\Big(\dot{h}(t,y) + (x-a)\dot{\theta}(t,y)\Big) - \lambda\theta(t,y)\frac{\partial\phi}{\partial x}(\lambda,t,x,0), \quad |x| < b,$$

and $\phi(\lambda,t,x,z)$ satisfies the Full Potential Equation in 2D. We assume the power series expansion

$$\phi(\lambda,t,x,z) = \sum_1^\infty \frac{\lambda^k}{k!}\phi_k(t,x,z) + \phi_\infty(x,z), \quad -\infty < x < \infty,\ z \neq 0 \tag{3.1}$$

where

$$\phi_k(t,x,z) = \left.\frac{\partial^k \phi(\lambda,t,x,z)}{\partial \lambda^k}\right|_{\lambda=0} \tag{3.2}$$

for each $t>0,\ -\infty<x,z<\infty$ excepting $z=0,\ |x|>b$, for $|\lambda|<R,\ 0<R$.

Note that the no-slip boundary condition can be stated

$$\frac{\varphi(\lambda,t,x,0)}{\partial z} = -\lambda[\dot{h}(t,y)+(x-a)\dot{\theta}(t,y)] - \lambda U\theta(t,y)\cos\alpha - \lambda\theta(t,y)\frac{\partial\varphi}{\partial x},$$

$$z=0,\ |x|<b \tag{3.3}$$

and the 2D potential field equations can be expressed:

$$\begin{aligned}
&\frac{\partial^2\phi(\lambda,\cdot)}{\partial t^2} + \frac{\partial}{\partial t}\left[\left(\frac{\partial\phi}{\partial x}\right)^2 + \left(\frac{\partial\phi}{\partial z}\right)^2\right] + (\gamma-1)\frac{\partial\phi}{\partial t}\left(\frac{\partial^2\phi}{\partial x^2}+\frac{\partial^2\phi}{\partial z^2}\right)\\
&= a_\infty^2\left[1+\frac{\gamma-1}{2a_\infty^2}\left(U^2-\left(\frac{\partial\phi}{\partial x}\right)^2-\left(\frac{\partial\phi}{\partial z}\right)^2\right)\right]\left(\frac{\partial^2\phi}{\partial x^2}+\frac{\partial^2\phi}{\partial z^2}\right)\\
&-\frac{1}{2}\frac{\partial\phi}{\partial x}\frac{\partial}{\partial x}\left[\left(\frac{\partial\phi}{\partial x}\right)^2+\left(\frac{\partial\phi}{\partial z}\right)^2\right] - \frac{1}{2}\frac{\partial\phi}{\partial z}\frac{\partial}{\partial z}\left[\left(\frac{\partial\phi}{\partial x}\right)^2+\left(\frac{\partial\phi}{\partial z}\right)^2\right]
\end{aligned} \tag{3.4}$$

To obtain the $\phi_k(t,\cdot,\cdot)$, we differentiate (3.4) with respect to λ and set $\lambda=0$.

3.2 The Linear Problem

For $k=1$ we obtain the linearized field equation

$$\begin{aligned}
&\frac{\partial^2\varphi_1}{\partial t^2} + 2U\cos\alpha\frac{\partial^2\varphi_1}{\partial t\partial x} + 2U\sin\alpha\frac{\partial^2\varphi_1}{\partial t\partial z}\\
&= a_\infty^2\left[(1-M^2\cos^2\alpha)\frac{\partial^2\varphi_1}{\partial x^2} + (1-M^2\sin^2\alpha)\frac{\partial^2\varphi_1}{\partial z^2}\right.\\
&\left.-2M^2\sin\alpha\cos\alpha\frac{\partial^2\varphi_1}{\partial x\partial z}\right]
\end{aligned} \tag{3.6}$$

omitting the airfoil $|x|<b,\ z=0$.

From (3.4), we obtain that the no-slip boundary condition becomes

$$\frac{\partial\varphi_1(t,x,0)}{\partial z} = -\Big(\dot{h}(t,y)+(x-a)\dot{\theta}(t,y)\Big) - \theta(t,y)U\cos\alpha \tag{3.6}$$

with $\psi(\lambda,t,x,z)$ defined by

$$\psi(\lambda,t,x,z) = \frac{\partial\varphi(\lambda,t,x,z)}{\partial t} + \frac{1}{2}|\nabla\phi(\lambda,t,x,z)|^2$$

$$\delta p(\lambda,t,x) = -\rho_\infty\delta\psi(\lambda,t,x), \quad |x|<b.$$

Defining

$$\delta p_1(t,x) = \frac{\partial}{\partial\lambda}\delta p(\lambda,t,x)\bigg|_{\lambda=0} \tag{3.7}$$

we have

$$\delta p_1(t,x) = -\rho_\infty \delta\psi_1(t,x)$$

where

$$\begin{aligned}\psi_1(t,x,z) &= \frac{\partial}{\partial\lambda}\psi_1(0,t,x,z)\\ &= \frac{\partial\varphi_1}{\partial t} + \frac{\partial\varphi_1}{\partial x}U\cos\alpha + \frac{\partial\varphi_1}{\partial z}U\sin\alpha\end{aligned}$$

and

$$\begin{aligned}\delta\psi_1(t,x) &= 0, \quad x \to b-\\ &= 0, \quad |x| > b.\end{aligned}$$

Hence the linear problem is given by (3.5) with boundary conditions, with the structural equation (1.1) with

$$\delta p_1(t,x) = -\rho_\infty \delta\psi_1(t,x)$$

$$L(t,y) = \int_{-b}^{b} \delta p_1(t,x)dx \tag{3.8}$$

$$M(t,y) = \int_{-b}^{b} (x-a)\delta p_1(t,x)dx \tag{3.9}$$

Let

$$\begin{aligned}A_1(t,x) &= -\frac{\delta\psi_1}{U}(t,x), \quad |x| < b\\ &= \frac{\delta p_1(t,x)}{U\rho_\infty}\end{aligned}$$

which is the Kussner pressure doublet function [2]. Then the Possio equation relates the 'input' $w_a(t,\cdot)$ to the 'output' $\delta p_1(t,\cdot)$, linking the Lagrangian dynamics to the Eulerian. Extant treatises on aeroelasticity [e.g. 3] end at approximately this point.

3.3 The Possio Equation: Zero Angle of Attack

To reduce complexity we shall only consider the case $\alpha = 0$, referring to [8, 11] for non-zero angle of attack. We shall also need to state it for more general 'down-wash' functions than (3.6), subject to the condition

$$w_a(t,\cdot) \in L_p[-b,b], \quad 1 \le p < 2$$

and $w_a(t,\cdot)$ is absolutely continuous in $t \ge 0$. The Possio equation is usually stated in terms of the Laplace transform (actually the Fourier transform; see [12] for the time domain version). The Possio equation is

$$\hat{w}_a(\lambda,x) = \int_{-b}^{b} \hat{P}(\lambda,x-\xi)\hat{A}(\lambda,\xi)d\xi, \quad |x| < b,\ \mathrm{Re}\,\lambda > 0 \tag{3.10}$$

where the kernel is given in terms of its spatial Fourier transform:

$$\begin{aligned}\hat{P}(\lambda, i\omega) &= \int_{-\infty}^{\infty} e^{-i\omega x}\hat{P}(\lambda, x)dx, \quad -\infty < \omega < \infty \\ &= \frac{1}{2}\frac{1}{\kappa + i\omega}\sqrt{\kappa^2 M^2 + 2\kappa M^2 i\omega + (1-M^2)\omega^2}, \quad \kappa = \frac{\lambda b}{U} \qquad (3.11) \\ &= \int_0^{\infty} e^{-\lambda t}P(t, i\omega)dt, \quad \mathrm{Re}\lambda > 0\end{aligned}$$

where

$$A(t,x) \to 0 \text{ as } x \to b-$$

$$A(t,\cdot) \in L_p[-b,b], \quad 1 \le p < 2,$$

absolutely continuous in $[0,\infty]$ with $\dot{A}(t,\cdot) \in L_p[-b,b]$ also.

$$\hat{A}(\lambda,\cdot) = \int_0^{\infty} e^{-\lambda t}A(t,\cdot)dt$$

$$\hat{w}_{a,1}(\lambda, x) = \int_{-b}^{b} \hat{P}(\lambda, x-\xi)\hat{A}_1(\lambda,\xi)d\xi, \quad \mathrm{Re}\,\lambda > 0,\ |x| < b$$

where

$$w_{a,1}(t,x) = -\dot{h}(t,y) - (x-a)\dot{\theta}(t,y) - \theta(t,y)U\cos\alpha.$$

Because of the similar property required of the structure state variables we have that

$$\int_0^{\infty} e^{-\sigma t}\Big(||A_1(t,\cdot)||_p + ||\dot{A}_1(t,\cdot)||_p\Big)dt < \infty \qquad (3.12)$$

Moreover, with

$$\hat{\varphi}_1(\lambda, x, z) = \int_0^{\infty} e^{-\lambda t}\varphi_1(t, x, z)dt, \quad \mathrm{Re}\ \lambda > 0$$

with the $L_p - L_q$ transform

$$\hat{\hat{\varphi}}_1(\lambda, i\omega, z) = \int_{-\infty}^{\infty} \hat{\varphi}_1(\lambda, x, z)e^{-i\omega x}dx, \quad -\infty < \omega < \infty$$

we have

$$\hat{\hat{\varphi}}_1(\lambda, i\omega, z) = \frac{-1}{2}\cdot\frac{1}{\kappa + i\omega}\hat{\hat{A}}_1(\lambda, i\omega)e^{-\sqrt{M^2\kappa^2 + 2M^2\kappa i\omega + (1-M^2\omega^2}|z|}, \quad -\infty < \omega < \infty. \qquad (3.13)$$

To obtain the time-domain version, let

$$\begin{aligned}\gamma_1(t,x) &= \int_0^t A_1(t-\sigma, x-U\sigma)dt, \quad -b < x < b + Ut \qquad (3.14) \\ &= 0 \text{ otherwise.}\end{aligned}$$

Then (see [13]), for $z \neq 0$,

$$\varphi_1(t,x,z) = \int_0^t \int_{-\infty}^{\infty} \frac{\partial}{\partial z} G(t-\sigma, x-\xi, z)\dot{\gamma}_1(\sigma,\xi)d\xi\ d\sigma, \tag{3.15}$$

where

$$G(t,x,z) = \frac{1}{2\pi\sqrt{1-M^2}} \int_1^{\frac{1}{r}(t+\frac{Ux}{c_1{}^2})} \frac{d\sigma}{\sqrt{\sigma^2-1}}$$

$$r^2 = \frac{1}{(1-M^2)}\left(\frac{x^2}{c_1^2} + \frac{z^2}{c_2^2}\right)$$

$$c_1^2 = a_\infty^2(1-M^2), \quad c_2^2 = a_\infty^2$$

which is the potential flow solution to the linear case.

Stability of the linearized aeroelastic system is then determined by:

$$m\ddot{h} + S\ddot{\theta} + EIh'''' = \int_{-b}^{b} U\rho_\infty A(t,\xi)d\xi, \quad t>0,\ 0<y<\ell$$

$$I_\theta\ddot{\theta} + S\ddot{h} + GJ\theta'' = \int_{-b}^{b} U\rho_\infty (x-a)A(t,x)dx, \quad t>0,\ 0<y<\ell$$

See [14] for a solution and the detailed study of flutter instability speeds as a function of M.

For the non-linear problem, we need the time-domain solution of (3.10). This is best expressed in operator form

$$A(t,\cdot) = P\mathcal{T}w_a(\cdot,\cdot)$$

where $\mathcal{T}$ is the Tricomi operator

$$\mathcal{T}f = g \quad g(x) = \frac{1}{\pi}\sqrt{\frac{b-x}{b+x}} \int_{-b}^{b} \sqrt{\frac{b+\xi}{b-\xi}} \frac{f(\xi)}{\xi - x} d\xi, \quad |x| < b$$

and P is a Volterra operator of the form

$$PA = g; \quad g(t,\cdot) = \int_0^t P(t-\sigma)A(\sigma,\cdot)d\sigma.$$

The kernel is known explicitly only for $M=0$ and contains delta function derivatives [9], but only δ-functions for $M \neq 0$ (see [14].

4 Flutter as an LCO

Here we begin with the key result [18], the solution of the non-linear Possio equation. For each $y,\ 0<y<z$:

$$\delta p = \rho_\infty U\Big(I - P\mathcal{T}L(\theta)\Big)^{-1} P\mathcal{T}w_{a,1}(\cdot,\cdot) \tag{4.1}$$

where $w_{a,1}$ is the linearized downwash and $L(\theta)$ is the operator defined by

$$L(\theta)A = g$$

$$g(t,\cdot) = \theta(t,y)\Big(- A(t,\cdot) + \dot{\gamma}_1(t,\cdot)\Big) \tag{4.2}$$

We can now state the non-linear aeroelastic system equations. Let $\ell_1,\ \ell_2$ denote the functionals corresponding to lift and moment.

$$\ell_1(A) = \int_{-b}^{b} A(x)dt$$

$$\ell_2(A) = \int_{-b}^{b} (x - ab)A(x)dx.$$

Then we have

$$m\ddot{h}(t,y) + S\ddot{\theta}(t,y) - EIh''''(t,y) = \ell_1(\delta p) \tag{4.3}$$

$$I_\theta\ddot{\theta}(t,y) + S\ddot{h}(t,y) + GJ\theta''(t,y) = \ell_2(\delta p) \tag{4.4}$$

where $\delta(p)$ is given by (4.2). This can be expressed as a non-linear convolution-evolution equation in a Hilbert space for each M with the speed U as a parameter to which Hopf-bifurcation theory applies. We naturally omit the details. The flutter speed is determined by the linearized model as in [14]. Let ω denote the corresponding angular frequency in the linear model, with structure response

$$x_1(t,y) = \sin\omega t \begin{vmatrix} h(0,y) \\ \theta(0,y) \end{vmatrix} \quad 0 < y < \ell$$

being the solution to (4.3), (4.4) with

$$\delta p = \delta p_1$$

$$= \rho_\infty U P\mathcal{T} w_{a,1}(\cdot).$$

More generally we define

$$\delta p_k = \rho_\infty U\Big(P\mathcal{T}L(\theta_1(\cdot)\Big)^k P\mathcal{T}w_{a,1}(\cdot)$$

and $x_k(\cdot,\cdot)$ the solution to (4.3), (4.4), with

$$\delta p = \delta p_k.$$

Then the LCO can be expressed

$$\sum_1^\infty x_k(t,y)$$

which is no longer sinusoidal, but is a harmonic series with period $\left(\frac{2\pi}{\omega}\right)$. We omit details.

As for the corresponding flow solution, it is shown in [15] that it can be decomposed into the sum of two parts, one part which has no shocks and is solely responsible for the lift, and the second part which may contain shocks but produces no lift and cannot be linearized.

References

[1] Goland, M. "The Flutter of a Uniform Cantilever Wing." *Journal of Applied Mechanics,* 1945. V. 12, no. 4, pp. 197–208.

[2] Bisplinghoff, R. L., Ashley, H. and Halfman, R. L. *Aeroelasticity.* New York: Addison-Wesley Publishing Co., 1955.

[3] Dowell, E. ed. *A Modern Course in Aeroelasticity.* Dordrecht: Kluwer Academic Publishers, 2004.

[4] Balakrishnan, A. V. "Subsonic Flutter Suppression Using Self-straining Actuators." *Journal of the Franklin Institute,* 2001. V. 338, no. 2/3, pp. 149–170.

[5] Chorin, A. J. and Marsden, J. E. *A Mathematical Introduction to Fluid Mechanics,* 3rd ed. Texts in Mathematics, vol. 4. New York: Springer, 1993.

[6] Thompson, P. A.. *Compressible Fluid-Dynamics.* New York: McGraw-Hill, 1972.

[7] Meyer, R. E. *Introduction to Mathematical Fluid Dynamics.* New York: Dover Publications, 1982.

[8] Balakrishnan, A. V. "On the Transonic Small Disturbance Potential Equation." *AIAA Journal* 2004. V. 42, no. 6, pp. 1081–1088.

[9] Balakrishnan, A. V. "Possio Integral of Aeroelastic Theory." *Journal of Aerospace Engineering* 2003. V. 16, no. 4, pp. 139–154.

[10] Balakrishnan, A. V. "Nonlinear Aeroelasticity: The Steady State Theory." Unpublished paper; submitted to *AIAA Journal*, March 2007.

[11] Balakrishnan, A. V. "The Possio Integral Equation of Aeroelasticity: A Modern View." In: *System Modeling and Optimization.* Proceedings of the 22nd IFIP TC7 Conference, July 18-22, in Turin, Italy. Ed. F. Ceragioli, A. Dontchev, H. Futura, K. Marti, L. Pandolfi. New York: Springer, 2006. Pp. 15-22.

[12] Balakrishnan, A. V. "An Integral Equation in Aeroelasticity." To be published in: Proceedings of the Conference on Evolution Equations (EVEQ) in memory of G. Lumer. Ed. F. Neubrander. Basel: Birkhäuser, 2007.

[13] Balakrishnan, A. V. "Nonlinear Aeroelastic Theory: Continuum Models." In: *Control Methods in PDE-Dynamical Systems*, eds. F. Ancona, I. Lasiecka, W. Littman, R. Triggiani. Series: Contemporary Mathematics 426. Providence, Rhode Island: American Mathematical Society, 2007. Pp. 79–101.

[14] Balakrishnan, A. V. and Iliff, K. W. "A Continuum Aeroelastic Model for Inviscid Subsonic Wing Flutter." *Journal of Aerospace Engineering,* forthcoming June 2007.

[15] Balakrishnan, A. V. "A Mathematical Theory of Flutter Instability Phenomena in Aeroelasticity." Paper to be delivered at the IX International Chetayev Conference, "Analytical Mechanics, Stability and Control of Motion," Irkutsk, Russia, June 12–16, 2007.

Novel Architecture for Preventing Interference between Automation and Pilot Maneuvers

Eri Itoh
Electronic Navigation Research Institute (ENRI), Japan
e-mail: eri@enri.go.jp
and
Shinji Suzuki
The University of Tokyo

Abstract

In a pilot/automation interface, it is said that pilots tend to get confused about the unforeseeable behavior of automated airplanes when responding to an abnormal situation; such confusions trigger disasters. For preventing interference between automation and pilot maneuver, this research has proposed a new architecture termed "Human As a Control Module architecture (HACM architecture)". The proposed architecture treats a pilot as one module of controlling aircraft. This paper introduces the HACM architecture and explains the concept and mechanism. The effectiveness of the architecture is confirmed via numerical simulation which mimics the situation of an aircraft accident in the past.

1 Introduction

While automation can reduce the frequency of pilot errors, it is still a potential cause of new types of errors induced by the confusion in pilot/automation interfaces [1–3]. According to reference [2, 3], pilots tend to get confused about the unforeseeable behavior of automated airplanes when responding to an abnormal situation; such confusions trigger disasters. An improvement of the pilot/automation interface is required to avoid conflicting actions taken by pilots and automated systems.

In automation design, there are two main types of approaches for achieving pilot-friendly automation: 1) creation of better environments for pilots to prevent mistakes and 2) adaptive management and modification of inappropriate actions by pilots and/or automatic systems. The first approach includes improvement in the cognitive and decision-making tasks, for example, flight deck and display design, design of flight management systems, etc. Although some of these designs are being used in practice, this approach is not the only solution for pilot-friendly automation. During the design process, the first approach is required to hypothesize how a design coordinates between a pilot and automation. However, it is difficult to define automation designs that support pilots because

we might not foresee or understand autoflight systems and pilot behaviors under all circumstances including abnormal situations during flight. Because these conflicts are mainly attributed to the dynamics change of the pilots and automated flight systems during a flight, a context-sensitive support based on the adaptive approaches is required. With the background in mind, this research has proposed a new architecture termed Human As a Control Module (HACM) architecture to advance coordination between automation and pilot maneuver [4]-[7].

In this paper, the concept and the mechanism of the HACM architecture is explained and the effectiveness is shown via numerical simulation. Firstly, we explain the modular structures of which concept are highly influenced to proposing the HACM architecture. One of the aircraft accidents caused by the interference between automation system and pilot is picked up as to specify the conflicts between automation and pilot. Secondly, the HACM architecture is introduced to show the concept and mechanism. Thirdly, the effectiveness of the proposing architecture is confirmed via numerical simulation which mimics the aircraft accident in the past. Lastly, we conclude the paper.

2 Confliction Between Automated Aircraft and Pilot

Modular Structure in the Human Brain

The modular structure has been proposed to mimic neural circuit of human brain and applied for learning system/controller. As a learning system using modular structure, "Mixture of expert" is well known [8]. As shown in Fig. 1, the multiple module of the expert networks are connected in parallel using the independent gating networks, and the gating networks calculate the weight on the learning parts and the outputs corresponding to the each expert networks. Fig. 2 shows one of the module structures termed "Multiple Paired Forward-Inverse Model (MPFIM)" proposed by Wolpert and Kawato [9]. Multiple pairs of the forward model (Predicted controlled dynamics) and the inverse model (controller) of the controlled dynamics are connected in parallel as shown in Fig. 2. Based on the predicted error values between the forward model and the real controlled dynamics, these modules are adaptively switched, and the selected module contributes to control the dynamics and pursue learning of the forward model.

In this way, these modular structures contribute to control the dynamics by adaptively switching modules (controllers). From this point of view, recent flight control system equipped in aircraft consists of the modular structure. Each module has a controller of which characteristic is different from the others, for example, different values and combinations of feedback gains and target values, flight mode, etc. The appropriate modules are selected depending on the altitude, speed, and the other conditions. It can be said that recent highly

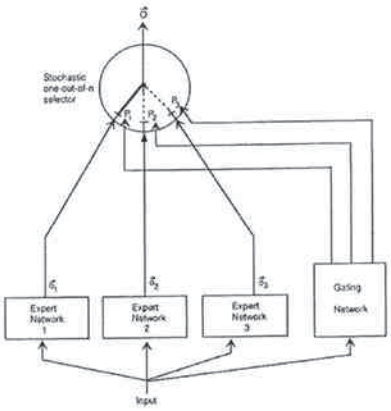

Fig.1 Mixture of expert [8]

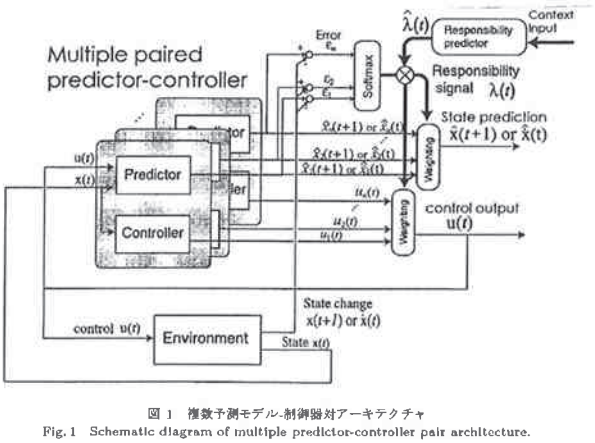

図 1 複数予測モデル-制御器対アーキテクチャ
Fig. 1 Schematic diagram of multiple predictor-controller pair architecture.

Fig.2 Multiple Paired Forward-Inverse Models (MPFIM) [9]

automated aircraft is flying with the artificial intelligence which has modular architecture and the brain of the aircraft consists of various types of flight controllers (autopilot) and pilot operation/control, combination of the artificial intelligence and human brains.

Artificial Intelligence and Human Brain on the Aircraft

The recent aircraft is flying with automatic flight controllers, a kind of artificial intelligence, and pilot, human brain, and it is still a potential cause of new types of accidents/incidents induced by the confusion in pilot/automation interfaces [1–3]. In 2002, a B747-400 flying at around 40,000 ft with autopilot in the Japanese airspace met with atmospheric turbulence [10]. The airspeed dramatically increased and the autopilot changed the flight mode from the altitude control to the speed control and started to control airspeed by changing the pitch angle. The pitch angle was increased by the autopilot to reduce the airspeed, however the airspeed was increased to around V_{mo} (the maximum limitation of the airspeed). Then, the pilot shift to manual control and the pitch angle oscillation was caused by the pilot's elevator control. Because of the vertical oscillation, 4 people were seriously injured and 29 people were slightly injured, and a part of the airborne was damaged. The pilots in the cockpits commented that they had no time to check the information displayed on the monitor and cannot remember whether or not they disconnected the autopilot. In this way, especially in the emergency situation, pilots tend to get confused about the unforeseeable behavior of automated airplanes; such confusions trigger disasters.

How should we resolve the conflicts between the artificial intelligence and the human brain on the aircraft? As one of the solutions, we propose a new architecture termed "Human As a Control Module architecture (HACM architecture) [4]-[7]" and explain the concept and the mechanism in the next section. The HACM architecture is inspired by the modular structure mentioned in the previous section.

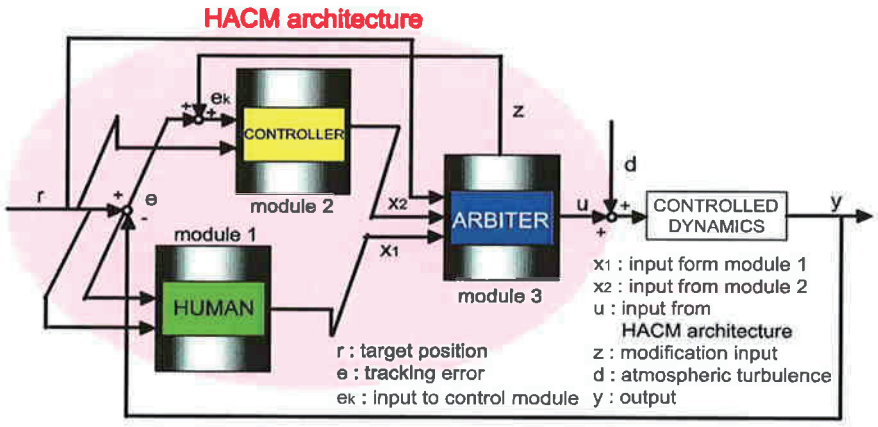

Fig.3 Human As a Control Module architecture

3 Human As a Control Module architecture

3.1 Concept of the HACM architecture

The HACM architecture treats a pilot as a single module for controlling aircraft. Fig.3 shows a block diagram that includes the fundamental structure of the HACM architecture and a controlled dynamics, which in this case is the dynamics of the aircraft. As shown in Fig. 3, the HACM architecture consists of modular structure including a human (pilot) and the basic structure of the HACM architecture comprises three types of modules—the human module, controller module, and arbiter module. The characteristics and roles of each module are described below:

Human module: This module corresponds to pilot. It is difficult to represent pilots using numerical models because pilots flexibly change their dynamics depending on the situation within the bounds of their physiological abilities. It is advantageous for a pilot to assess situations well and track their performance. On the other hand, their physiological ability is limited. In addition, they sometimes make mistakes during cognition and decision making. Humans also tend to take conflicting actions intentionally.

Controller module: This module corresponds to an automatic controller that is appropriately designed with controlled dynamics. The automatic controllers can achieve good performance within the design conditions. The disadvantage is that a trade-off exists between the tracking performance and the robustness toward the disturbance input and modeling error. In addition, the controllers are subject to deteriorating control ability beyond the design conditions. Various design approaches can be applied to this module. This paper precedes discussions on a simple feedback controller because the purpose of this paper is to introduce HACM architecture and confirm its effectiveness.

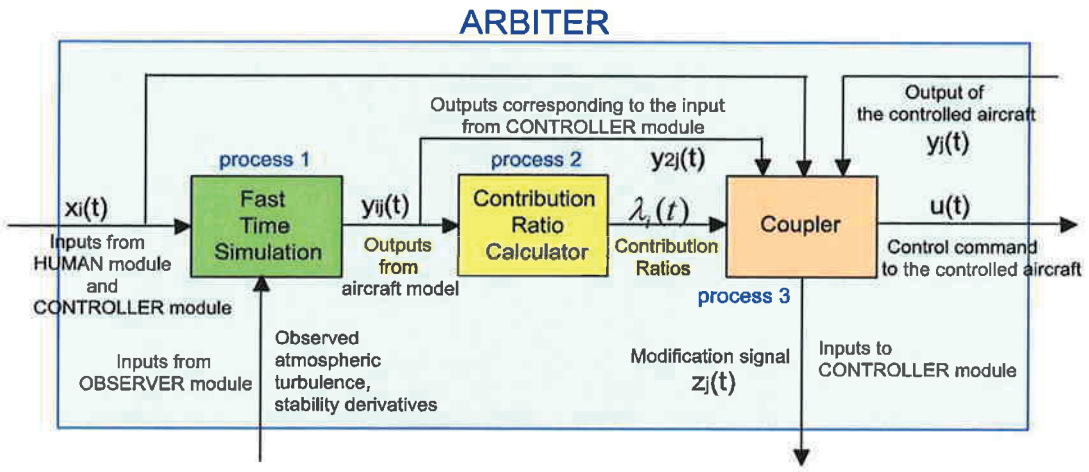

Fig. 4 Arbiter Mechanism

Arbiter module: This module manages inputs $x_i(t)$ $(i=1,2)$ from both the human and controller modules that simultaneously provide control commands to the aircraft. These commands are gated in the arbiter module by the contribution ratios, which are calculated using the softmax function. The contribution ratio represents the extent to which each module presently accounts for the behavior of the controlled dynamics. The role of the arbiter module is to eliminate inappropriate control commands from the other two modules to the controlled dynamics and generate appropriate control inputs that suit the present conditions. Through the arbiter module, the HACM architecture enables us to realize a control system that compensates for the limitations of the human module and controller module and utilizes their advantages in the aircraft control. As a result, the module realizes a backup system that comprises the pilot and the automated controller that have different characteristics as mentioned above. When either the human or controller modules provide irrelevant inputs, the arbiter module ignores the input and provides another suitable one.

3.2 Arbiter Mechanism

Fig. 4 shows the mechanism of the arbiter module that arbitrates the control commands inputted by the pilot (human module) and the autopilot (controller module). As shown in Fig. 4, the control commands, the elevator commands in this paper, from the human module $x_1(t)$ and controller module $x_2(t)$ are inputted to the arbiter module. The general mechanism in the arbiter module comprises the following three processes—a real time simulation, a contribution ratio calculator, and a coupler.

Real time simulation: First, the arbiter module simulates the outputs of the aircraft corresponding to the control commands of both the human and the controller modules online. The arbiter module possesses the dynamic model of the controlled aircraft within its

framework. By using the dynamic model, the outputs $y_{ij}(t)$ $(i=1,2 \quad j=1,2,\ldots l)$ for inputs $x_i(t)$ to the aircraft are numerically simulated. l corresponds to the number of outputs from the aircraft model that are used to calculate the contribution ratios in the next process. The values of $y_{1j}(t)$ correspond to the outputs when the control command $x_1(t)$ is inputted to the aircraft model. The values of $y_{2j}(t)$ correspond to the outputs when the control command $x_2(t)$ is inputted to the aircraft model.

Contribution ratio calculator: Second, contribution ratios $\lambda_i(t)$ $(i=1,2)$ are calculated by using the outputs of the aircraft model predicted in the previous process. $\lambda_1(t)$ is a contribution ratio for the human module, and $\lambda_2(t)$ is for the controller module. The contribution ratio represents the extent to which each inputs presently accounts for the behavior of the aircraft dynamics.

In order to calculate the contribution ratio, first, the performance of the pilot and the autopilot are individually quantified. We measure the performances of each control commands based on the following index $E_{ij}(t)$ $(i=1,2 \quad j=1,2,\ldots l)$, which is given by

$$E_{ij}(t)=\frac{\sum_{s=n-m}^{n}\left(\varepsilon_{ij}(t_s)\right)^2 e^{(s-n+m)/m}}{\sum_{s=n-m}^{n} e^{(s-n+m)/m}} \qquad (1)$$

where $\varepsilon_{ij}(t)$ is the error between $y_{ij}(t)$ and target values, which are the desired outputs of the aircrafts at present time t and n is the number of time steps at present time t. In this case, t is equal to t_n. m is the number of time steps of the past tracking errors considered in the index.

In order to calculate $\varepsilon_{ij}(t)$ in Eq. (1), flight envelope protection is applied. In this paper, the flight envelope protection implies that the arbiter module adaptively adjusts the control authority when the human module (pilot) does not control the aircraft to satisfy the defined flight envelope; this envelope defines that the range aircraft safely continues its flight. In this paper, the HACM architecture is applied for longitudinal control of the aircraft, so the flight envelope is defined as follows:

$$\begin{aligned} \theta_{\min} &\le \theta_1(t) \le \theta_{\max} \\ \dot{\omega}_{\min} &\le \dot{\omega}_1(t) \le \dot{\omega}_{\max} \\ \ddot{\omega}_{\min} &\le \ddot{\omega}_1(t) \le \ddot{\omega}_{\max} \end{aligned} \qquad (2)$$

where $\theta_1(t)$, $\dot{\omega}_1(t)$, and $\ddot{\omega}_1(t)$ are the outputs of the aircraft model corresponding to the input from the human module calculated in the arbitrating system. As shown in (2), the upper and lower limits are introduced for the pitch angle, vertical acceleration, and rate of vertical acceleration. This paper yields $\theta_{\min} = -11(\deg)$, $\theta_{\max} = 11(\deg)$, $\dot{\omega}_{\min} = -1.0(G)$, $\dot{\omega}_{\max} = 2.5(G)$, $\ddot{\omega}_{\min} = -0.3(G/\sec)$, and $\ddot{\omega}_{\max} = 0.3(G/\sec)$. The upper and lower value of $\dot{\omega}$ is the designated value at which B747-400 flies safely. The limitation of $\ddot{\omega}$ is the rate limitation of the vertical acceleration in the speed control mode of the autopilot in the distressed aircraft. $\varepsilon_{ij}(t)$ is defined as follows:

$$\text{If} \qquad y_{ij}(t) < y_{j\min},$$

$$\text{then} \qquad \varepsilon_{ij}(t) = \frac{y_{ij}(t) - y_{j\min}}{y_{j\min}}. \qquad (3)$$

$$\text{If} \qquad y_{j\max} < y_{ij}(t),$$

$$\text{then} \qquad \varepsilon_{ij}(t) = \frac{y_{j\max} - y_{ij}(t)}{y_{j\max}}. \qquad (4)$$

where

$$\begin{aligned} & y_i(t) \quad (i = 1,2) \\ &= \left[y_{ij}(t)\right]^T (j = 1,2,3) \\ &= \left[y_{i1}(t), \quad y_{i2}(t), \quad y_{i3}(t)\right]^T \\ &= \left[\theta_i(t), \quad \dot{\omega}_i(t), \quad \ddot{\omega}_i(t)\right]^T. \end{aligned} \qquad (5)$$

$y_1(t)$, the output vector of the aircraft model, corresponds to the input from human module and $y_2(t)$, the output of aircraft model, corresponds to the input from the controller module.

By using the index as shown in (1), the performances of each command are numerically evaluated. The index (1) measures the performances of each input from the human module and the controller module by using the value of errors predicted in the past.

The contribution ratios of each module $\lambda_i(t)$ are calculated by using (1) and the softmax function. The contribution ratios are given as follows:

$$\lambda_i(t) = \frac{\sum_{j=1}^{l} e^{-(E_{ij}(t)/\sigma)}}{\sum_{i=1}^{2}\sum_{j=1}^{l} e^{-(E_{ij}(t)/\sigma)}} \qquad (6)$$

where σ is a scaling constant. In this simulation, we set $\sigma = 10.0$. The softmax function normalizes the tracking errors across the modules so that the contribution ratios lie between 0 and 1 and the sum of the contribution over the modules is 1.

Coupler: Third, the control commands from the human module and the controller module are adjusted and added in this process. The input from the arbiter module $u(t)$ to the aircraft is given as follows:

$$u(t) = \sum_{i=1}^{2} \lambda_i(t) x_i(t) \qquad (7)$$

The input from the human module or the controller module with a smaller error index than that of the other greatly contributes to input $u(t)$. Conversely, the other input has a low contribution to $u(t)$.

Another function of this process is to generate a modification signal $z_j(t)$ $(j = 1,2\cdots l)$ that is inputted to the autopilot as a feedback signal. In order to avoid high gain feedback, modification signal $z_j(t)$ is defined as follows.

$$z_j(t) = y_{ij}(t) + \lambda_i(t)(y_j(t) - y_{ij}(t)) \qquad (8)$$

$y_j(t)$ is the output of the real aircraft. (8) yields $y_{ij}(t)$ where $\lambda_i(t) = 0$ in order to prevent the autopilot from sensing the other's control input as disturbance. Where $\lambda_i(t) \neq 0$, the modification signal (8) will make the autopilot to stabilize the aircraft movement caused by the interference of the inputs the human module or the controller module gives.

4 The effectiveness of the HACM architecture

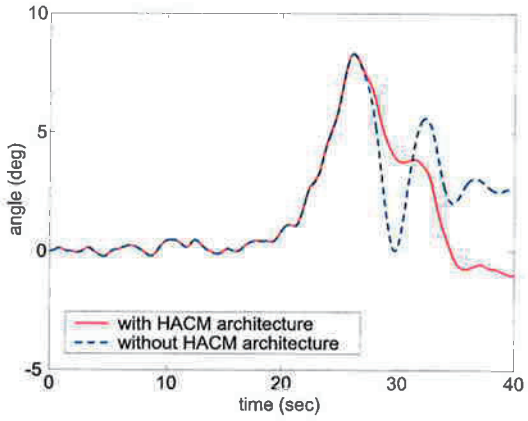

Fig. 5 Pitch angle

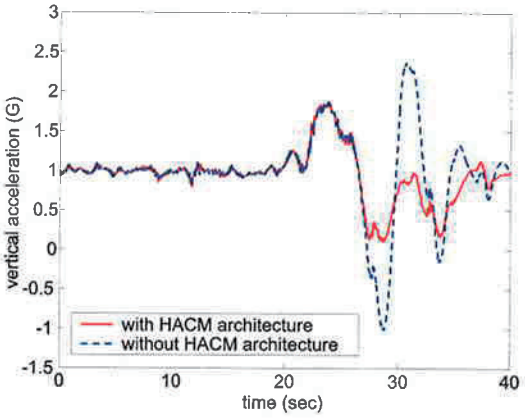

Fig.6 Vertical acceleration

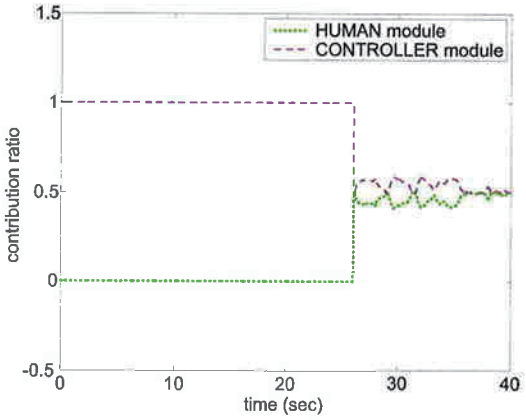

Fig. 7 Contribution ratio

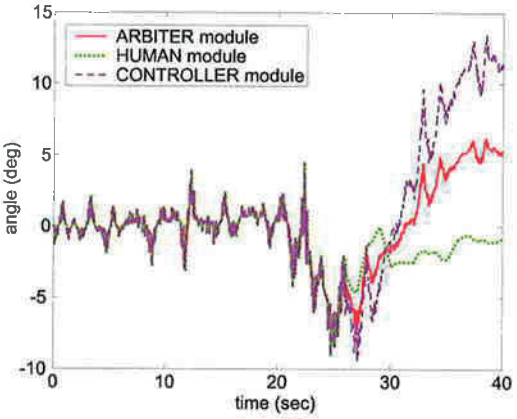

Fig. 8 Elevator angle

In order to confirm the effectiveness of the HACM architecture, we conduct numerical simulation which mimics the aircraft accident mentioned in section 2.2. Since the dynamics of the B747-400 is not officially published, this simulation uses the nonlinear dynamics of the B747-100 flying at 40,000 feet with 871 ft/sec [11]. The details of autopilot design are not disclosed, so we design an autopilot that captures the characteristics of an equipped autopilot in a distressed aircraft based on the accident analysis report. Figs. 5-8 show the effectiveness of the HACM architecture that is applied to the situation of the aircraft accident.

Fig. 5 shows that the HACM architecture works to reduce the amplitude of the pitch angle oscillation comparing with the oscillation in the accident situation. Thus, the HACM architecture contributes toward reducing the change in the vertical acceleration (Fig. 6). As shown in Fig. 6, the results of the aircraft accident show that the maximum value of the change in the vertical acceleration is around 3.4 G. On the other hand, the maximum value of the change in the vertical acceleration is reduced to around 1.1 G in the case that the

HACM architecture is applied for the same condition. This means that the HACM architecture achieves 74 % of the PIO reduction.

Fig. 7 shows the contribution ratios $\lambda_1(t)$ and $\lambda_2(t)$ are respectively given to the human module and the controller module, and Fig. 8 shows the elevator angle which the arbiter module input to the aircraft and the simulated elevator angle when the human module and the controller module are acting alone. In the arbiter module, the value of the elevator inputs from the human module and the controller module are adjusted by the contribution ratios and the arbiter module generates the elevator input given to the aircraft as shown in Figs. 7 and 8.

5 Conclusion

This paper introduced a novel architecture, the Human As a Control Module architecture (HACM architecture), which includes the human in the modular structure. Conventionally, the modular architecture contributes to mimic a human brain and is applied for the learning system/controller. On the other hand, the HACM architecture discusses the modular structure which combines the human and the artificial intelligence system.

There are two potential benefits in employing the HACM architecture. First, the use of HACM architecture allows us to realize a control system comprising the pilots and the automated flight control systems. The arbiter module adaptively adjusts the control authority between the pilot and an automated flight controller and generates an appropriate an input command to the controlled aircraft. Second, the HACM architecture has a simple framework and its algorithm comprises three types of modules—human, controller, and arbiter. Therefore, it is possible to utilize the architecture online. In addition, it is convenient to add modules with various functions to the architecture in order to develop a better automation system.

In this paper, we introduce the concept and the mechanism of the HACM architecture and applied it for the situation of the aircraft accident caused by the confliction between the automated aircraft and the pilot. It is confirmed that the proposing architecture achieves 74 % of the PIO reduction.

References

[1] Hawkins F K. *Human Factors in Flight,* Gower Technical Press Ltd., 1987.

[2] Federal Aviation Administration Human Factors Team. The Interfaces between Flightcrews and Modern Flight Deck Systems, 1996.

[3] Miyagi M. *Serious Accidents and Human Factors,* American Institute of Astronautics and Astronautics, Inc., 2005.

[4] Itoh E. and Suzuki S. A New Architecture to Coordinate Automation with Pilot Maneuver, Transactions of the Aeronautical and Astronautical Society of the ROC, Vol.37, No.3, pp. 203-214, 2005.

[5] Itoh E. and Suzuki S. Resolving Conflicts between Pilot and Automation. Proc. 4th Eurocontrol Innovative Research Workshop & Exhibition, Paris, pp. 191-200, 2005.

[6] Itoh, E. and Suzuki, S., "A New Approach to Automation that Takes Account of Adaptive Nature of Pilot Maneuver", World Automation Conference (WAC 2006), Budapest, Jul. 2006.

[7] Itoh, E., "A New Architecture to Harmonize Automation and Pilot Maneuver", 25th Congress of International Council of Aeronautical Sciences (ICAS 2006), Hamburg, Sep. 2006.

[8] Jacobs, R.A., Jordan, M.I., Nowlan S.J., and Hinton, G.E., "Adaptive Mixture of local experts", Neural Computation, Vol.3, pp.79-87, 1991.

[9] Wolpert, D.M. and Kawato, M., "Multiple Paired Forward and Inverse Models for Motor Control", Neural Networks, Vol.11, pp.1317-1329, 1998.

[10] Aircraft and Railway Accidents Investigation Commission. Aircraft Accident Analysis Report AA2006-1, 2006.

[11] Roskam J. *Airplane Design,* Part VI, Design Analysis & Research, 2000.

Decentralized Flight Trajectory Planning of Multiple Aircraft

Nobuhiro Yokoyama*
National Defense Academy, Yokosuka , Kanagawa, Japan

Abstract: Conventional decentralized algorithms for optimal trajectory planning tend to require prohibitive computational time as the number of aircraft increases. To overcome this drawback, this paper proposes a novel decentralized trajectory planning algorithm adopting a constraints decoupling approach for parallel optimization. The constraints decoupling approach is formulated as the path constraints of the real-time trajectory optimization problem based on nonlinear programming. Due to the parallelization and no-redundancy, the computational time for one cycle in the proposed algorithm is not so sensitive to the number of aircraft as the conventional algorithms. Several results of numerical simulations are presented to demonstrate the effectiveness of the proposed algorithm.

I. Introduction

Autonomous flight trajectory planning will play an important role in free flight operations [1] in which each aircraft is capable of dynamically updating its flight plan and assuming responsibility for maintaining conflict-free trajectory (i.e. maintaining sufficient vertical or horizontal distance from own aircraft's trajectory to the other aircraft's trajectory). Thus far, many algorithms have been proposed for trajectory planning with conflict prevention and resolution [2-12]. These algorithms can roughly be characterized as follows: 1) Protocol-based or optimization-based: Although the optimization-based algorithms [6-12] tend to require substantial computational time, they offer desirable trajectory which minimizes specified criterion (e.g., arrival time delay, fuel consumption, etc.). The advantage of the protocol-based algorithms [3-5] is their simplicity. 2) Applicable to only a pair of aircraft or multiple aircraft [2]: From a practical viewpoint, applicability to multiple aircraft is more desirable. 3) Centralized or decentralized: Centralized algorithms [9-12] are well-suited to conventional ground-based air traffic controls, while decentralized algorithms [3-8] may be more suited to free flight operations because of their distributed nature.

This paper covers the optimization-based decentralized algorithms for trajectory planning of multiple aircraft, because they are most advantageous in view of safety and efficiency. This class of algorithms can further be distinguished between sequential algorithms [8] and simultaneous algorithms [6,7]. In the sequential algorithms, during the computation and update of an aircraft's trajectory, the computations and updates of the other aircraft's trajectories are stopped. Thus, the computations and updates of the trajectories are executed in one by one manner, and the computational time for one cycle (i.e., time to update all the relevant aircraft's trajectories) grows prohibitively as the number of aircraft increases. On the other hand, the simultaneous algorithms optimize each aircraft's trajectory at the same time in a decentralized fashion. The simultaneous algorithms use the computers distributed in each aircraft more efficiently than the sequential algorithms in the sense that there are no sleeping times for the computers in the simultaneous algorithms. Nevertheless, the conventional simultaneous algorithms usually require prohibitive computational time in multiple aircraft cases. For example, the approach by Bicchi et al. [7] requires the optimization of not only the own aircraft's trajectory but also the other aircraft's trajectories.

* Research Associate, Department of Aerospace Engineering, 1-10-20 Hashirimizu, Yokosuka.

Therefore, the computational time for this approach grows combinatorially as the number of aircraft increases. A game-theoretic approach by Tomlin, et al. [8] does not include this type of redundancy. However, the algorithmic complexity of this approach also grows combinatorially as the number of aircraft increases, and hence it may become computationally prohibitive for more than three aircraft.

In order to overcome this drawback, this paper proposes a simultaneous decentralized algorithm using constraints decoupling approach for parallel optimization. The constraints decoupling approach is formulated as the path constraints of the real-time trajectory optimization problem based on nonlinear programming. Due to the parallelization and no-redundancy, the computational time for one cycle in the proposed algorithm is not so sensitive to the number of aircraft as the conventional decentralized algorithms. The effectiveness of the proposed algorithm is evaluated through several numerical simulations.

II. Trajectory planning algorithm

A. Description of aircraft's motion and trajectory

The state equations are based on the kinematics of an aircraft. For simplicity, only the horizontal motion is covered in this study. Let us define M as the number of aircraft and $j\ (=1,\cdots,M)$ as the aircraft index. The state equations of an aircraft j are described as follows,

$$\dot{X}_j(t) = V_j(t)\cos\psi_j(t) \tag{1}$$

$$\dot{Y}_j(t) = V_j(t)\sin\psi_j(t) \tag{2}$$

$$\dot{\psi}_j(t) = \omega_j(t) \tag{3}$$

$$\dot{V}_j(t) = a_j(t) \tag{4}$$

where t : the time, X_j, Y_j : the position of the aircraft, V_j : the horizontal velocity, ψ_j : the heading angle, ω_j : the heading angular rate caused by the aircraft's bank, a_j : the horizontal acceleration. In this simple kinematic model, the state variables $\boldsymbol{x}_j(t)$ and the control variables $\boldsymbol{u}_j(t)$ are described as

$$\boldsymbol{x}_j(t) = [X_j(t), Y_j(t), \psi_j(t), V_j(t)]^T, \quad \boldsymbol{u}_j(t) = [\omega_j(t), a_j(t)]^T \tag{5}$$

In addition, the motion of the aircraft is constrained by the following inequalities,

$$(V_j)_{\min} \le V_j(t) \le (V_j)_{\max} \tag{6}$$

$$-(\omega_j)_{\max} \le \omega_j(t) \le (\omega_j)_{\max} \tag{7}$$

$$-(a_j)_{\max} \le a_j(t) \le (a_j)_{\max} \tag{8}$$

where $(V_j)_{\min}, (V_j)_{\max}, (\omega_j)_{\max}, (a_j)_{\max}$ are the constants.

Let us define the reference time as t_0 and the horizon interval as T_h. Discretizing the time domain $[t_0, t_0 + T_h]$ into N uniform intervals, let us express the nodal time as $t_0, t_1, \cdots, t_N\ (= t_0 + T_h)$, i.e.,

$$t_i = t_0 + i(\Delta T)\ \ (i = 0,\cdots,N),\ \ \Delta T = \frac{T_h}{N} \tag{9}$$

The trajectory at time $t \in [t_0, t_0 + T_h]$ is described by the nodal values of the state variables $\boldsymbol{x}_j(t_i)$ as well as the control variables $\boldsymbol{u}_j(t_i)$. In addition, the control variables are assumed to be piecewise constant at each interval

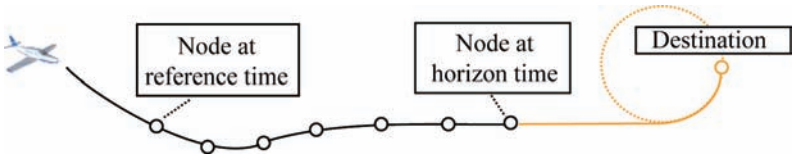

Fig. 1 Trajectory Description

$[t_i, t_{i+1}]$. As shown in Fig. 1, the trajectory beyond the horizon time ($t = t_0 + T_h$) is described by the straight line and the circular arc that connect the node at the horizon time with the destination point.

B. Configurations of algorithm

A unit cycle of the algorithm completes in the time interval ΔT. This unit cycle is split into three phases - the conflict reduction (CR) phase, the trajectory optimization (TO) phase, and the trajectory broadcast (TB) phase. It is assumed that the clocks of all the aircraft are synchronous. At the beginning of the cycle, the currently planned trajectory is modified in the CR phase to reduce the degree of conflicts with the other aircraft's trajectories. Then the trajectory modified in the CR phase is updated in the TO phase to minimize a given objective function. After the TO phase, the updated trajectory is broadcasted as the aircraft's latest trajectory. It should be noted that the role of the CR phase is to offer appropriate initial solution to the optimization algorithm in the TO phase. The details of the CR phase and the TO phase are described in subsection C and D, respectively.

Let us define t_B as the time when the current cycle starts. The reference time t_0 is set to be $t_0 = t_B + 2\Delta T$. It is assumed that the aircraft is always controlled to track the trajectory at $t \in [t_B, t_B + \Delta T]$, which is fixed in the current cycle of the algorithm.

C. Conflict reduction (CR) phase

In the CR phase, a kind of force field method [3, 4] is adopted to reduce the degree of conflicts of the aircraft's trajectories. The algorithm in the CR phase is described below.

Step 1: Conflict Search For $j = 1, \cdots, M$, search the time $(t_C)_j$ when the first conflict of the aircraft j with any other aircraft occurs based on the currently planned trajectories. Then, for $j = 1, \cdots, M$, obtain the starting time of the trajectory modification $(t_S)_j$ by the following equation.

$$(t_S)_j = \max[t_0, (t_C)_j - 2\Delta T] \tag{10}$$

Step 2: Time Initialization Set the inner simulation time τ and the index i to t_0 and zero, respectively.

Step 3: Control Calculation For $j = 1, \cdots, M$, if $\tau \geq (t_S)_j$, modify the control variables $\boldsymbol{u}_j^P(t_i)$ of the current trajectory based on the following procedure. (The superscript P denotes the component of currently planned trajectory.)

Using the force field method, generate the control command vector composed of a repulsive element for steering the aircraft away from the other aircraft and an attracting element for steering the aircraft to its destination [3]. Figure 2 shows the schematic view of the force field method. The repulsive element is obtained by using the necessary separation vector at the closest point of approach (CPA), which is determined by the linear extrapolation of the position in the direction of the aircraft's destination. Let us define t_{ijk}^A as the time of the CPA with regard to aircraft j and k determined by the linear extrapolation of the positions at time $\tau = t_i$. In

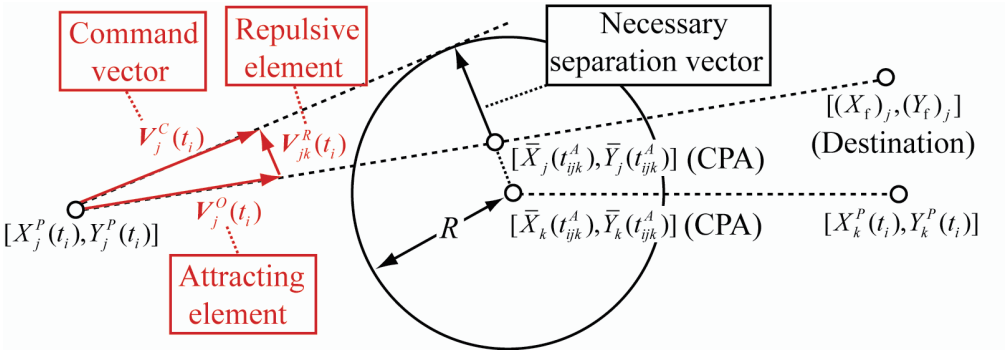

Fig. 2 Force field method

addition, let us define the extrapolated positions as $[\bar{X}_j(\tau), \bar{Y}_j(\tau)]$ and $[\bar{X}_k(\tau), \bar{Y}_k(\tau)]$. The control command vector $\boldsymbol{V}_j^C(t_i)$ for aircraft j is obtained by the following equations.

$$\boldsymbol{V}_j^C(t_i) = \boldsymbol{V}_j^O(t_i) + \sum_{k(\neq j)=1}^{M} \boldsymbol{V}_{jk}^R(t_i) \tag{11}$$

$$\boldsymbol{V}_j^O(t_i) = \max\left[(V_{\min})_j, \min\left[\frac{\sqrt{[(X_f)_j - X_j^P(t_i)]^2 + [(Y_f)_j - Y_j^P(t_i)]^2}}{\max[1, (t_f)_j - t_i]}, (V_{\max})_j\right]\right] \boldsymbol{e}_j^O(t_i) \tag{12}$$

$$\boldsymbol{e}_j^O(t_i) = \frac{[(X_f)_j - X_j^P(t_i), (Y_f)_j - Y_j^P(t_i)]}{\sqrt{[(X_f)_j - X_j^P(t_i)]^2 + [(Y_f)_j - Y_j^P(t_i)]^2}} \tag{13}$$

$$\boldsymbol{V}_{jk}^R(t_i) = \frac{\max[0, R - \sqrt{[\bar{X}_j(t_{ijk}^A) - \bar{X}_k(t_{ijk}^A)]^2 + [\bar{Y}_j(t_{ijk}^A) - \bar{Y}_k(t_{ijk}^A)]^2}]}{t_{ijk}^A - t_i} \boldsymbol{e}_{jk}^R(t_i) \tag{14}$$

$$\boldsymbol{e}_{jk}^R(t_i) = \frac{[\bar{X}_j(t_{ijk}^A) - \bar{X}_k(t_{ijk}^A), \bar{Y}_j(t_{ijk}^A) - \bar{Y}_k(t_{ijk}^A)]}{\sqrt{[\bar{X}_j(t_{ijk}^A) - \bar{X}_k(t_{ijk}^A)]^2 + [\bar{Y}_j(t_{ijk}^A) - \bar{Y}_k(t_{ijk}^A)]^2}} \tag{15}$$

where $\boldsymbol{V}_j^O(t_i)$: the attracting element for steering the aircraft j to its destination, $\boldsymbol{e}_j^O(t_i)$: the unit vector of the attracting element, $\boldsymbol{V}_{jk}^R(t_i)$: the repulsive element for steering the aircraft j away from the other aircraft $k(\neq j)$, $\boldsymbol{e}_{jk}^R(t_i)$: the unit vector of the repulsive element, $[(X_f)_j, (Y_f)_j]$: the destination point of the aircraft j, $(t_f)_j$: the specified time to arrive at the destination, $[X_j^P(t_i), Y_j^P(t_i)]$: the currently planned position of the aircraft j at time $\tau = t_i$. If the distance of the aircraft j and k is zero at the CPA, a line passing through $[X_j^P(t_i), Y_j^P(t_i)]$ and being tangent to a circle centering on the CPA with radius R is calculated. Then $\boldsymbol{e}_{jk}^R(t_i)$ is determined as the unit vector normal to this line instead of Eq. (15).

Subsequently, convert the control command vector $\boldsymbol{V}_j^C(t_i)$ to the control variables $\omega_j^P(t_i), a_j^P(t_i)$ by the following equations,

$$\omega_j^P(t_i) = \max\left[-(\omega_j)_{\max}, \min\left[\frac{\psi_j^C(t_{i+1}) - \psi_j^P(t_i)}{\Delta T}, (\omega_j)_{\max}\right]\right] \tag{16}$$

$$\psi_j^C(t_{i+1}) = \tan^{-1}\left[\boldsymbol{V}_j^C(t_i)_y / \boldsymbol{V}_j^C(t_i)_x\right] \tag{17}$$

$$a_j^P(t_i) = \max\left[(a_j)_{\min}, \min\left[a_j^C(t_i), (a_j)_{\max}\right]\right] \tag{18}$$

$$a_j^C(t_i) = \frac{\max\left[(V_j)_{\min}, \min\left[\|\boldsymbol{V}_j^C(t_i)\|, (V_j)_{\max}\right]\right] - V_j^P(t_i)}{\Delta T} \tag{19}$$

Step 4: Integration of the State Equations For $j = 1, \cdots, M$, integrate the state equations (1)-(4) from $\tau = t_i$ to $\tau = t_{i+1}$, and update the state variables of the current trajectory $\boldsymbol{x}_j^P(t_{i+1})$ to the results obtained by the integration. Set τ to t_{i+1}, and increase i by one. If $\tau < t_N$, go back to Step 3. Otherwise, terminate the CR phase and go to the TO phase.

It should be noted that the trajectories modifications of all the aircraft are executed in each aircraft, i.e., the same computations are executed simultaneously in all the aircraft in the CR phase. Thus, the trajectories modified in the CR phase are consistent and their conflicts are substantially reduced. Although the computational time for this approach grows as the number of aircraft increases, it is still negligible compared to that of the TO phase.

D. Trajectory optimization (TO) phase

In the TO phase, the trajectory modified in the CR phase is updated to the optimal trajectory, which minimizes the squared error between the specified time $(t_f)_j$ and the time to arrive at the destination. The separation constraints on the trajectories of aircraft j and k are usually described as the following coupled form.

$$\sqrt{[X_j(t_i) - X_k(t_i)]^2 + [Y_j(t_i) - Y_k(t_i)]} - R \geq 0 \ (i = 1, \cdots, N) \tag{20}$$

In order to parallelize the computation in the TO phase, this inequality condition is decoupled as follows. As shown in Fig. 3, a feasible region for update of each node of each aircraft's trajectory is introduced based on the trajectories modified in the CR phase. The feasible region for update of the node $[X_j(t_i), Y_j(t_i)]$ of aircraft j relative to the aircraft k is expressed as follows,

$$a_{jk}(t_i)[X_j(t_i) - p_{jk}(t_i)] + b_{jk}(t_i)[Y_j(t_i) - q_{jk}(t_i)] - \frac{R}{2} \geq 0 \ (i = 1, \cdots, N) \tag{21}$$

$$a_{jk}(t_i) = \frac{X_j^P(t_i) - p_{jk}(t_i)}{d_{jk}(t_i)}, b_{jk}(t_i) = \frac{Y_j^P(t_i) - q_{jk}(t_i)}{d_{jk}(t_i)} \tag{22}$$

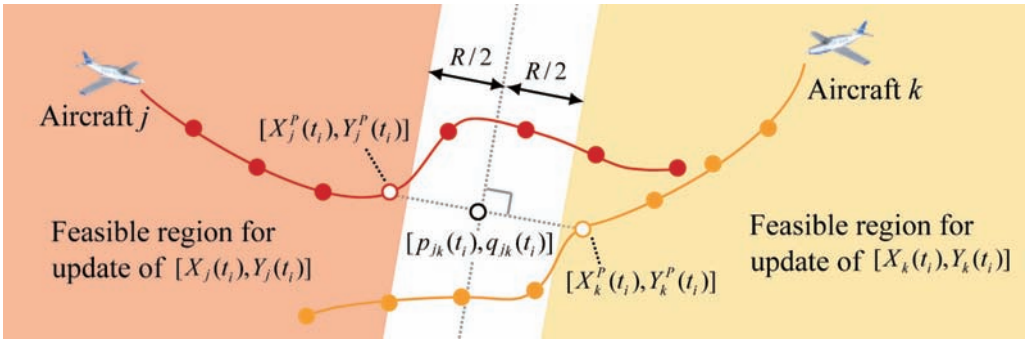

Fig. 3 Feasible region for update of node

$$d_{jk}(t_i) = \sqrt{[X_j^P(t_i) - p_{jk}(t_i)]^2 + [Y_j^P(t_i) - q_{jk}(t_i)]} \tag{23}$$

where the point $[p_{jk}(t_i), q_{jk}(t_i)]$ denotes the midpoint of $[X_j^P(t_i), Y_j^P(t_i)]$ and $[X_k^P(t_i), Y_k^P(t_i)]$. It should be noted that the sufficient separation between $[X_j(t_i), Y_j(t_i)]$ and $[X_k(t_i), Y_k(t_i)]$ is assured as long as the update of each node is constrained within the assigned feasible region. Thus, the parallel computation is enabled by the inequality constraint (21). Considering all the other aircraft's nodes at time t_i, the eventual feasible region for update of $[X_j(t_i), Y_j(t_i)]$ is described as the product set of Eq. (21) with $k = 1, 2, \cdots M$ $(k \neq j)$.

Let us define the state variables and the control variables to be optimized as

$$(\boldsymbol{x}_j)_i = [(X_j)_i, (Y_j)_i, (\psi_j)_i, (V_j)_i]^T, \quad (\boldsymbol{u}_j)_i = [(\omega_j)_i, (a_j)_i]^T \tag{24}$$

where the subscript i denotes the value at time t_i. The trajectory optimization problem is defined as follows.

- The objective function to be minimized:

$$\phi_j = [t_N + (T_e)_j - (t_f)_j]^2 + \rho_j \delta_j \tag{25}$$

  where $(T_e)_j$: the time interval between the horizon time t_N and the planned time to arrive at the destination, ρ_j : the positive penalty parameter, δ_j : the constraint relaxation variable which is explained later. The calculation of $(T_e)_j$ is based on the line and circular arc trajectory beyond the horizon.
- The initial condition:

$$(\boldsymbol{x}_j)_0 = \boldsymbol{x}_j^P(t_0) \tag{26}$$

- The terminal condition:

$$\sin\left[\frac{\psi_j(t_N + T_e) - (\psi_f)_j}{2}\right] = 0 \tag{27}$$

  where $(\psi_f)_j$ denotes the specified heading angle at the destination, and $\psi_j(t_N + T_e)$ is calculated by the line and circular arc trajectory beyond the horizon. Although Eq. (27) is equivalent to $\psi_j(t_N + T_e) - (\psi_f)_j = 2n\pi$ (n is an arbitrary integer), it is adopted due to its suitability to the numerical optimization.
- The integration condition of the state equations:

$$(\boldsymbol{x}_j)_{i+1} - \int_{t_i}^{t_{i+1}} [\boldsymbol{f}(\boldsymbol{x}_j(\tau), \boldsymbol{u}_j(\tau)) \,|\, \boldsymbol{x}_j(t_i) = (\boldsymbol{x}_j)_i, \boldsymbol{u}_j(\tau) = (\boldsymbol{u}_j)_i] d\tau = \boldsymbol{0}, \ (i = 0, \cdots, N-1) \tag{28}$$

  where $\boldsymbol{f}$ denotes the right hand side of Eqs. (1)-(4). Since the control variable $\boldsymbol{u}_j(\tau)$ is piecewise constant vector $(\boldsymbol{u}_j)_i$ in the interval $[t_i, t_{i+1}]$, the second term of the above equation can be analytically integrated.
- The path constraints: Instead of the separation constraint (21), the following constraints are enforced.

$$a_{jk}(t_i)[(X_j)_i - p_{jk}(t_i)] + b_{jk}(t_i)[(Y_j)_i - q_{jk}(t_i)] - \left[\frac{R}{2} + \left(d_{jk}(t_i) - \frac{R}{2}\right)\delta_j\right] \geq 0, [i = 1, \cdots, N, k = 1, \cdots, M(k \neq j)] \tag{29}$$

$$0 \leq \delta_j \leq 1 \tag{30}$$

  Even if it is impossible to obtain conflict-free solutions due to the geometric relationships among the currently planned trajectories, the introduction of the relaxation variable δ_j makes it substantially easier to obtain conflict-reduced solutions. On the other hand, strong relaxation of Eq. (29) by large δ_j is penalized as the deterioration of the objective function (25).

The optimization problem described above is simultaneously solved in each aircraft j $(= 1, \cdots, M)$. The variables to be optimized for the aircraft j are $(\boldsymbol{x}_j)_0, (\boldsymbol{x}_j)_1 \cdots, (\boldsymbol{x}_j)_N, (\boldsymbol{u}_j)_0, (\boldsymbol{u}_j)_1, \cdots, (\boldsymbol{u}_j)_{N-1}$ and δ_j. The trajectory modified

in the CR phase is used as the initial solution of the optimization algorithm, and the initial solution of δ_j is set to be zero. In the optimization problem described above, the Jacobian of the constraints and the Hessian of the Lagragian have special sparse structure. Thus, the sparse sequential quadratic programming (SQP) [13] is adopted as the optimization algorithm. It is well known that the sparse SQP can compute the optimal solution substantially faster than the conventional dense matrix approach. In this way, the real-time optimization is enabled in the proposed algorithm.

III. Examples of simulation

Some example scenarios were considered to evaluate the effectiveness of the proposed algorithm. In all the scenarios, the separation minimum was specified as R = 9260 [m]. The performance of each aircraft was assumed to be the same, and the constants were specified as follows.

$$(V_j)_{\min} = 51.44\,[\text{m/s}],\ (V_j)_{\max} = 72.02\,[\text{m/s}],\ (\omega_j)_{\max} = 0.02401\,[\text{rad/s}],\ (a_j)_{\max} = 1.0\,[\text{m/s}^2] \tag{31}$$

A numerical simulation environment, which was composed of multiple PCs (personal computers) connected by LAN (local area network), was developed for evaluating the proposed algorithm. In this environment, the PCs corresponded to the aircraft, and the LAN corresponded to the airborne data link system. The period of the unit cycle and the number of nodes were specified as ΔT = 10.0 [sec] and 61, respectively.

Five aircraft, whose initial and terminal states are listed in Table 1, were assumed. In each aircraft, the time to arrive at the destination was specified as $(t_{\mathrm{f}})_j = 1000\,[\text{sec}]$, and the initial horizontal velocity was specified as $61.73\,[\text{m/s}]$. The aircraft's trajectories before applying the proposed algorithm were supposed to be straight. On the basis of these specifications, the following five conflict scenarios were considered: 1) aircraft A and B, 2) aircraft A and C, 3) aircraft A and E, and 4) aircraft A, C, and E, 5) aircraft A, B, C, and D. In each scenario, the initial straight trajectories converged to a point at the same time, i.e., the initial trajectories were assumed to be severely conflicted.

Figure 4 shows the final trajectories tracked by the aircraft in these scenarios. In this figure, the CPAs in the final trajectories are plotted as the circles. It can be observed that the final trajectories computed by the proposed algorithm are conflict-free and have reasonableness as the near-optimal solution, because the distance of every pairs of CPAs is equal to or slightly larger than the separation minimum R (=9260 [m]). As an example of planned trajectories obtained by the proposed algorithm, Fig. 5 shows the trajectories planned at the cycle of $t_0 = 200\,[\text{sec}]$. The CPAs detected in the planned trajectories are also plotted as the circles in this figure. It was observed that the distance of every pairs of CPA is equal to or slightly larger than the separation minimum R. Thus, the reasonableness of the planned trajectories can also be confirmed.

With respect to the computational speed, the proposed algorithm showed sufficient performance, because the time to compute a feasible solution was substantially smaller than the cycle period ΔT (= 10 [sec]) in each scenario (in the worst case, it took 0.38 [sec]). Table 2 shows the average of the computational time per iteration of the sparse

Table 1 Initial and terminal states of the aircraft

Aircraft	A	B	C	D	E
Initial position [m]	(0, 36000)	(0, -36000)	(36000, 0)	(–36000, 0)	(25456, 25456)
Initial heading angle [rad]	$-\pi/2$	$\pi/2$	π	0	$-3\pi/4$
Terminal position [m]	(0, –36000)	(0, 36000)	(–36000, 0)	(36000, 0)	(-25456, -25456)
Terminal heading angle [rad]	$-\pi/2$	$\pi/2$	π	0	$-3\pi/4$

Table 2 Comparison of the computational time

Scenario	(1)	(2)	(3)	(4)	(5)
Number of aircraft	2	2	2	3	4
Average computational time per iteration of sparse SQP [sec]	0.20	0.20	0.16	0.l4	0.37

SQP in the TO phase. In the conventional simultaneous algorithms, this criterion is sensitive to the number of aircraft, and it generally grows combinatorially. Although the number of scenarios is not sufficient, it can be seen that the proposed algorithm is not so sensitive to the number of aircraft as the conventional algorithms.

IV. Conclusions

A decentralized algorithm for optimal trajectory planning of multiple aircraft was presented in this paper. The novelty of the proposed algorithm lies in its decoupling of the separation constraints for parallel optimization. Through the application to some numerical simulations, it was observed that the proposed algorithm could compute reasonable conflict-free trajectories with sufficient computational speed. Our future work will include extensive evaluations and convergence assurance of the algorithm, as well as the algorithm enhancement for the three-dimensional problem.

References

[1] RTCA, “Final Report of RTCA Task Force 3: Free Flight Implementation,” RTCA Inc., Washington, D.C., 1995.
[2] Kuchar, J. K. and Yang, L. C., “A Review of Conflict Detection and Resolution Modeling Methods,” IEEE Transactions on Intelligent Transportation Systems, Vol. 1, No. 4, 2000, pp.179–189.
[3] Eby, M. S., “A Self-organizational Approach for Resolving Air Traffic Conflicts,” Lincoln Laboratory Journal, Vol. 7, No. 2, 1994, pp.239–254.
[4] Hoekstra, J. M., van Grent, R. N. H. W., and Ruigrok, R. C. J., “Designing for Safety: the ‘Free Flight’ Air Traffic Management Concept,” Reliability Engineering and System Safety, Vol. 75, 2002, pp.215–232.
[5] Frazzoli, E., Pallottino, L, Scordio, V., and Bicchi, A., “Decentralized Cooperative Conflict Resolution for Multiple Nonholonomic Vehicles,” AIAA Paper 2005–6048, 2005.
[6] Tomlin, C., Pappas, G., and Sastry, S., “Conflict Resolution for Air Traffic Management: A Study in Multi-Agent Hybrid Systems,” IEEE Transactions on Automatic Control, Vol. 43, No. 4, 1998, pp.509–521.
[7] Bicchi, A. and Pallottino, L., “On Optimal Cooperative Conflict Resolution for Air Traffic Management Systems,” IEEE Transactions on Intelligent Transportation Systems, Vol. 1, No. 4, 2000, pp.221-232.
[8] Schouwenaars, T., How, J., and Feron, E., “Decentralized Cooperative Trajectory Planning of Multiple Aircraft with Hard Safety Guarantees,” AIAA Paper 2004–5141, 2004.
[9] Menon, P. K., Sweriduk, G. D., and Sridhar, B., “Optimal Strategies for Free-Flight Air Traffic Conflict Resolution,” Journal of Guidance, Control, and Dynamics, Vol. 22, No. 2, 1999, pp.202–211.
[10] Frazzoli, E., Mao, Z. H., Oh, J. H., and Feron, E., “Resolution of Conflicts Involving Many Aircraft via Semidefinite Programming,” Journal of Guidance, Control, and Dynamics, Vol. 24, No. 1, 2001, pp.79–86.
[11] Hu, J., Prandini, M., and Sastry, S., “Optimal Coordinated Maneuvers for Three-dimensional Aircraft Conflict Resolution,” Journal of Guidance, Control, and Dynamics, Vol. 25, No. 5, 2002, pp.888–900.
[12] Raghunathan, A. U., Gopal, V., Subramanian, D., Biegler, L. T., and Samad, T., “Dynamic Optimization Strategies for Three-dimensional Conflict Resolution of Multiple Aircraft,” Journal of Guidance, Control, and Dynamics, Vol. 27, No. 4, 2004, pp.586–594.
[13] Betts, J. T., “Practical Methods for Optimal Control Using Nonlinear Programming,” SIAM, Philadelphia, 2001.

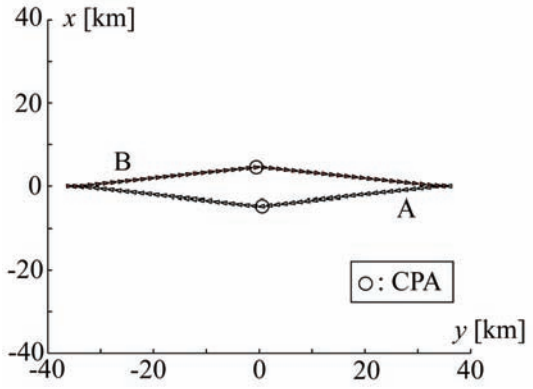

(1) Two aircraft scenario (head-on case)

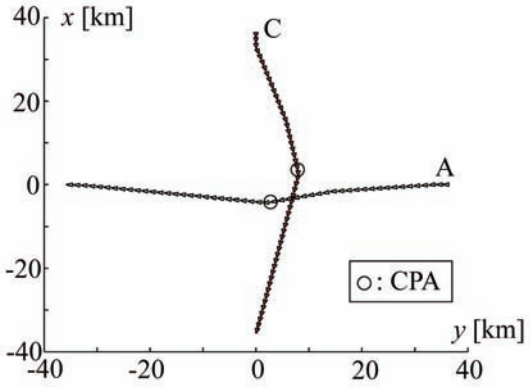

(2) Two aircraft scenario (90 [deg] crossing case)

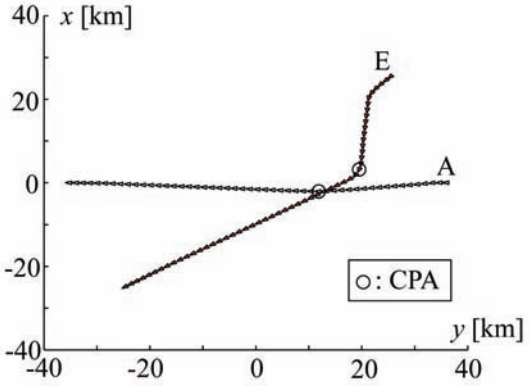

(3) Two aircraft scenario (45 [deg] crossing case)

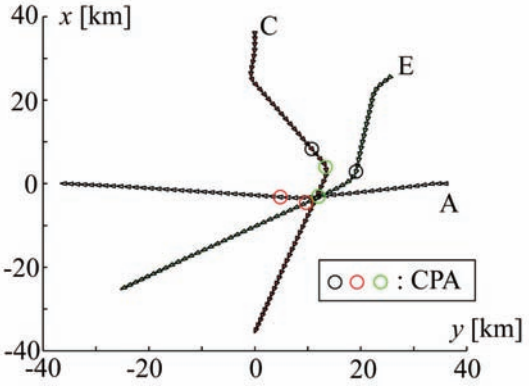

(4) Three aircraft scenario

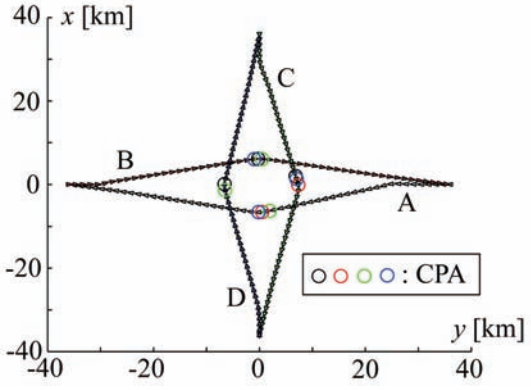

(5) Four aircraft scenario

Fig. 4 Final trajectories tracked by the aircraft

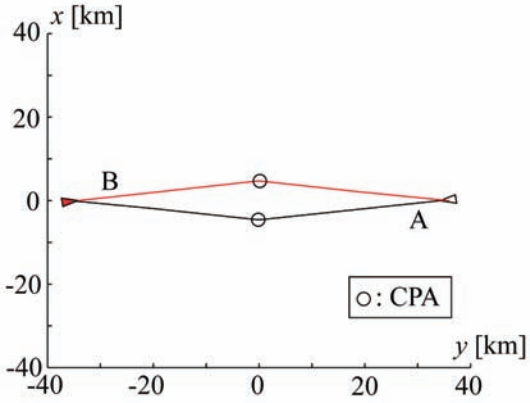

(1) Two aircraft scenario (head-on case)

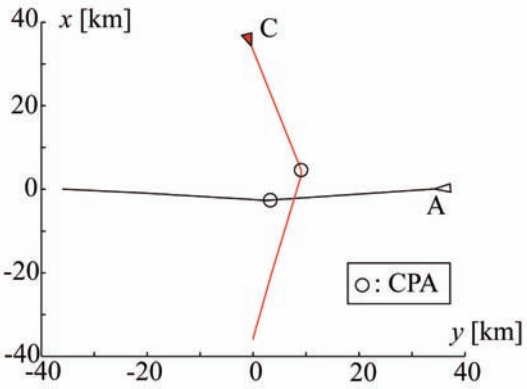

(2) Two aircraft scenario (90 [deg] crossing case)

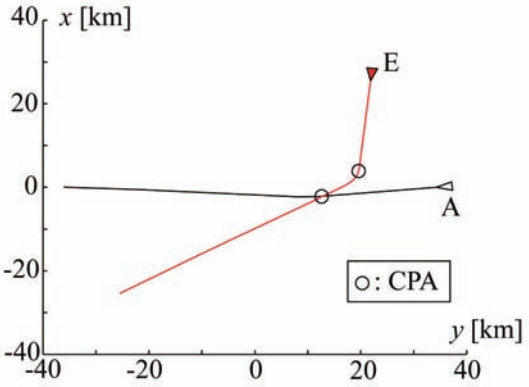

(3) Two aircraft scenario (45 [deg] crossing case)

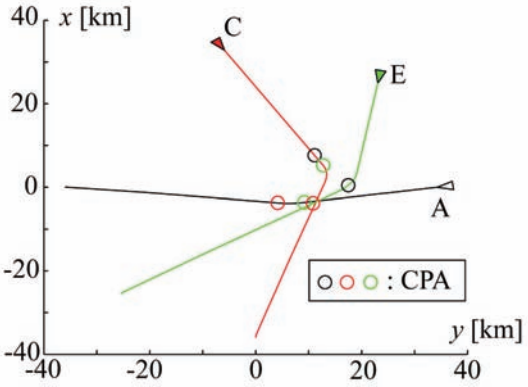

(4) Three aircraft scenario

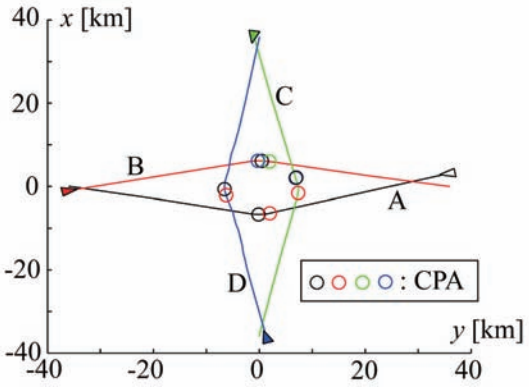

(5) Four aircraft scenario

Fig. 5 Trajectories planned at the cycle of $t_0 = 200$ [sec]

Sliding Mode Control for Space Debris Elimination

Hirohisa KOJIMA
Tokyo Metropolitan University, Hino, Tokyo, 191-0065, Japan

I. Introduction

Simple and reliable controllers are generally desired for spacecraft control, because it is very difficult to repair spacecraft on orbit. Classical control methods, such as PI, or PID, are simple and still quite often used for spacecraft control. Those linear control methods are, however, not adequate for conducting formation flight, which is a key technology to conduct feature space mission such as space telescope by multi-satellite, mitigation of space debris from orbit by flying around, approaching, and grasping the debris by means of a space robot. Because the motion required to the satellite conducting formation flying is nonlinear due to coupling between the attitude and position of the satellite relative to the other satellites. In addition, the malfunctioning target satellite is not always cooperative with the chaser, that is, motion of the target satellite may not be controlled by the chaser satellite, and is hard to predict because its inertia properties, which dominate the rotational motion, are not precisely known by the chaser in advance. These coupling and uncertainties or device fault situation may make the control problems more difficult. Thus it is desired to develop more suitable control methods for relative position/attitude control problem in space debris mitigation operation and extension of spacecraft lifespan. Sliding mode control can be such one of the promising control methods to meet this requirement, because it has desired properties such as simplicity of design, control of independent motion, invariance to process dynamics characteristics, and robustness to external perturbations. Those desired characteristics lead to wide variety of operational modes such as regulation, trajectory control, model following, and observation. Thanks to those good properties of sliding mode control, a great deal of applications of sliding mode control to spacecrafts has been studied up to date. The following are examples: formation flying, attitude control, space-robot manipulator control, and two-torque control.

However, by comparing the candidate debris elimination process or extension of spacecraft lifespan with the properties of the usual sliding model control method, it is found that the controllers do not still have sufficient properties for the requirements. The following are deficiencies of the usual sliding mode controllers in case of using them for debris mitigation, or extension of a spacecraft lifespan.

(1) Although it is assumed in the operation that cameras are used for inspecting the target, a function to prevent the violation of the chaser's line of sight (LOS) constraint is not explicitly formulated in the controller.
(2) Although the rotational motion behavior of the target depends on its moment inertia, and its uncertainties make the attitude-tracking problem more difficult, an adaptive law to estimate the moment inertia is not combined to the controller.
(3) Although it is difficult to repair the satellite on-board devices on orbit, a case of PWPF modulator fault is not considered for the two-control torque problem.

The research objective of this paper is to overcome these deficiencies of existing research by modifying the sliding-mode controllers. The following two topics are focused: fly-around motion, and an under-actuated control that may extend the lifespan of a satellite with malfunctioning RCS.

II. Fly-around Motion Control Based on Exact Linearization with Adaptive Law

Research Background

Several schemes have been proposed for attitude control problems[1-15]. For debris eliminating, fly-around motion must first be achieved because this motion is suitable for determining condition of a malfunctioning satellite. In order to achieve this motion, the development of an advanced control scheme for large-position and large-angle maneuvers is needed. Furthermore, if an on-board sensor on the chaser satellite, such as a camera, is the only means used to measure the relative position and attitude, tracking control based on the LOS angles is required. The LOS angles are nonlinear systems due to the dependence on the relative position and attitude between the target satellite and the chaser satellite. Therefore, the position and attitude of the chaser satellite relative to the target satellite are difficult to control by traditional linear schemes such as the linear quadratic regulator (LQR) method and are not able to be controlled independently if the tracking control is based on the LOS angles. The sliding-mode control technique is a nonlinear control method that has been applied in the position and attitude-tracking problem in [11]. The exact (or complete) linearization method [12] is another powerful method for controlling nonlinear systems. This method linearizes a nonlinear system by utilizing a nonlinear transformation of state variables and nonlinear feedback terms. Dwyer el al.[13] have proposed an exact nonlinear controller in which a reaction wheel is applied to the attitude control problem. Kida et al.[14] have studied a position and attitude regulation problem using an exact linearization method. However, their method was based on the Euler angle representation, and the singular problem of orientation representation was not avoided in the formulation. In [15], a method based on exact

linearization was proposed for the position and attitude control problem in which the listing parameter was used to represent the relative attitude. This parameter is not as common as quaternions because this parameter is not suitable for representing the relationship between the angular velocity and the derivative of the parameter. For this reason, some terms in the formulation are neglected for the exact linearization in [15]. Moreover, the inertia of the target satellite was assumed to be known in [15]. This assumption is not satisfied in reality, because determining exactly the inertia of a malfunctioning target satellite in advance is almost impossible.

In this chapter, an exact-linearization formulation is introduced, utilizing quaternions to represent the relative attitude of satellites. In the formation, control inputs are calculated from the relative position and attitude, line of sight(LOS) parameters, and the angular velocity of the chaser satellite, which can be measured on the chaser satellite. In other words, the control scheme does not require measurement of the absolute position of the chaser satellite in the inertia frame. LOS is defined based on the position of the target on a camera screen on the chaser satellite. This parameter can be controlled independently from the relative attitude, because the LOS angles depend on not only relative attitude, but also on relative position, and are decoupled from the relative attitude motion by controlling the relative position of the chaser satellite via the proposed nonlinear control scheme. The proposed control method is thus suitable for achieving fly-around motion, as well as multiple spacecraft formation flight, using an on-board sensor on the chaser satellite. Furthermore, an adaptive law is added to the present nonlinear controllers to estimate the inertia ratios of the target satellite. This law is effective for the case in which the target is a non-cooperative satellite. The effectiveness of the proposed exact-linearization method is demonstrated by numerical simulations.

Model Description

In this chapter, the satellite maneuvering near the target satellite is referred to as the chaser satellite. Figure 1 shows the system model treated in this study. When gravitational and orbital influences such as the Coriolis force are neglected, the equations of motion and attitude kinematics for the chaser satellite and the target satellite can be represented as follows:

$$m_c v_c + m_c \omega_c \times v_c = f_c \tag{1-1a}$$

$$I_c \omega_c + \omega_c \times I_c \omega_c = t_c \tag{1-1b}$$

$$\dot{q}_c = \frac{1}{2}\Omega(\omega_c) q_c \tag{1-1c}$$

$$m_t v_t + m_t \omega_t \times v_t = 0 \tag{1-2a}$$

$$I_t \omega_t + \omega_t \times I_t \omega_t = 0 \tag{1-2b}$$

$$\dot{q}_t = \frac{1}{2}\Omega(\omega_t) q_t \tag{1-2c}$$

where the subscripts c and t denote the chaser and target satellite, respectively, f_c and t_c are the control forces and torques, respectively, given to the chaser satellite, r, v, ω and q are the position, velocity, angular velocity and quaternions, respectively, of the satellites in their body-fixed frames, m and I are the mass and the inertia tensor, respectively, of the satellites and

$$\Omega(\omega) = \begin{bmatrix} -\omega^{\times} & \omega \\ -\omega^{T} & 0 \end{bmatrix} \tag{1-3}$$

The notation $x^{\times}, x = [x_1\ x_2\ x_3]^T$ denotes the following skew-symmetric matrix:

$$x^{\times} = \begin{bmatrix} 0 & -x_3 & x_2 \\ x_3 & 0 & -x_1 \\ -x_2 & x_1 & 0 \end{bmatrix} \tag{1-4}$$

The elements of the quaternions $q = [\tilde{q}^T q_4]^T = [q_1, q_2, q_3, q_4]^T$ are defined as follows:

$$q_1 = \lambda_1 \sin(\beta/2) \tag{1-5a}$$

$$q_2 = \lambda_2 \sin(\beta/2) \tag{1-5b}$$

$$q_3 = \lambda_3 \sin(\beta/2) \tag{1-5c}$$

$$q_4 = \cos(\beta/2) \tag{1-5d}$$

where $\lambda = [\lambda_1\ \lambda_2\ \lambda_3]^T$ is the direction cosine of the Euler unit vector and β is the rotation angle about the Euler vector. Any set of quaternions satisfies

$$\tilde{q}^T \tilde{q} + q_4^2 = 1 \tag{1-6}$$

In this study, differences in position, velocity, and angular velocity between the chaser and target are defined in the frame of the chaser satellites as follows:

$$r_e = r_c - C_t^c r_t \tag{1-7}$$

$$v_e = v_c - C_t^c v_t \tag{1-8}$$

$$\omega_e = \omega_c - C_t^c \omega_t \tag{1-9}$$

where C_t^c is the direct cosine matrix between the body frame of the chaser satellite and that of the target satellite. This matrix can be represented using the relative quaternions as follows:

$$C_t^c = (q_{e4}^2 - \tilde{q}_e^T \tilde{q}_e) U_{3\times 3} + 2\tilde{q}_e \tilde{q}_e^T - 2q_{e4}\tilde{q}_e^{\times} \tag{1-10}$$

where $U_{3\times 3}$ is the 3×3 unit matrix. The attitude error is defined as follows:

$$q_e = Q_1(q_t) q_c \tag{1-11}$$

where

$$Q_1(q)=\begin{bmatrix} q_4 U_{3\times3}-\tilde{q}^{\times} & -\tilde{q} \\ \tilde{q}^T & q_4 \end{bmatrix} \quad (1\text{-}12)$$

It is not difficult to show that the attitude error satisfies the following equation:

$$\tilde{q}_e^T\tilde{q}_e+q_{e4}^2=1 \quad (1\text{-}13)$$

Since Eq.(1-1c) or Eq.(1-2c) can be used to represent the kinematics of the attitude errors between the chaser satellite and the target satellite, the first derivative of quaternion errors is obtained as follows:

$$\dot{q}_e=\frac{1}{2}\Omega(\omega_e)q_e \quad (1\text{-}14)$$

Equations (1-13) and (1-10) indicate that when $\|\tilde{q}_e\|^2=0$, the direct cosine matrix C_t^c becomes the eigen matrix ($=U_{3\times3}$). From Eq.(1-14), the angular velocity error can be represented using the quaternion errors (q_e) as follows:

$$\omega_e=2\left[q_{e4}U_{3\times3}-\tilde{q}_e^{\times} \quad -\tilde{q}_e\right]\dot{q}_e \quad (1\text{-}15)$$

Thus, the attitude errors and angular velocity errors become zero when $\|\tilde{q}_e\|$ and $\|\tilde{\dot{q}}_e\|$ become zero. The objective of the following section is to obtain a nonlinear transformation and a feedback control which can convert the nonlinear system into an exact-linearized system. First, the definition of line of sight parameters will be explained. Second, the state vector will be defined, and the corresponding derivatives will be derived. Finally, an exact-linearization feedback controller based on the LOS parameters will be derived.

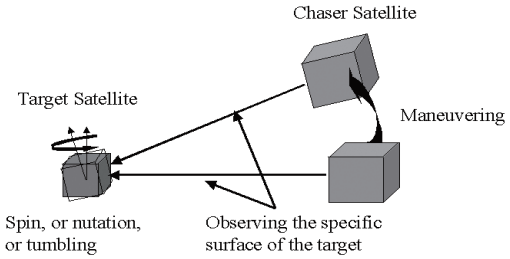

Fig.1 Schematic view of fly-around motion

Line of Sight Parameter

In this section, the definition of line of sight (LOS) parameters as applied in this chapter will be explained. The following assumptions are made: (1) the direction of the camera sight is coincident with the $-x$ direction of the body frame of the chaser satellite, (2) the relative distance of the target in the x direction and the velocity of the target on the camera screen can be sensed by the chaser.

Although the LOS angle is usually referred to as the relative angle between the sight direction of the camera on the chaser satellite and the direction from the chaser to the target, the LOS angle parameter is defined in this paper as follows:

$$L_{ang}=\begin{bmatrix} r_{ex} & d_y & d_z \end{bmatrix}^T=\begin{bmatrix} r_{ex} & s\dfrac{r_{ey}}{r_{ex}} & s\dfrac{r_{ez}}{r_{ex}} \end{bmatrix}^T \quad (1\text{-}16)$$

where s is the focus distance of the camera, and d_y and d_z are the y and z coordinates, respectively, indicating the position of the target on the camera screen, as shown in Fig.2. Note that s can be set as 1 without loss of generality.

The first and second derivatives of the position error can be represented using the position and velocity of the target on the camera screen as follows:

$$\dot{r}_{e_y}=\frac{d(d_y r_{e_x})}{dt}=\dot{d}_y r_{e_x}+d_y\dot{r}_{e_x} \quad (1\text{-}17a)$$

$$\dot{r}_{e_z}=\frac{d(d_z r_{e_x})}{dt}=\dot{d}_z r_{e_x}+d_z\dot{r}_{e_x} \quad (1\text{-}17b)$$

$$\ddot{r}_{e_y}=\ddot{d}_y r_{e_x}+d_y\ddot{r}_{e_x}+2\dot{d}_y\dot{r}_{e_x} \quad (1\text{-}18a)$$

$$\ddot{r}_{e_z}=\ddot{d}_z r_{e_x}+d_z\ddot{r}_{e_x}+2\dot{d}_z\dot{r}_{e_x} \quad (1\text{-}18b)$$

Solving the preceding equations with respect to $\ddot{d}_y$ and $\ddot{d}_z$, one has

$$\ddot{d}_y=-P_y\ddot{r}_{e_x}+P_x\ddot{r}_{e_y}-2P_x\dot{d}_y\dot{r}_{e_x} \quad (1\text{-}19a)$$

$$\ddot{d}_z=-P_z\ddot{r}_{e_x}+P_x\ddot{r}_{e_z}-2P_x\dot{d}_z\dot{r}_{e_x} \quad (1\text{-}19b)$$

where P_x, P_y and P_z are, respectively,

$$P_x=\frac{1}{r_{e_x}},\ P_y=\frac{r_{e_y}}{r_{e_x}^2}=\frac{1}{r_{ex}}d_y,\ P_z=\frac{r_{ez}}{r_{e_x}^2}=\frac{1}{r_{e_x}}d_z \quad (1\text{-}20)$$

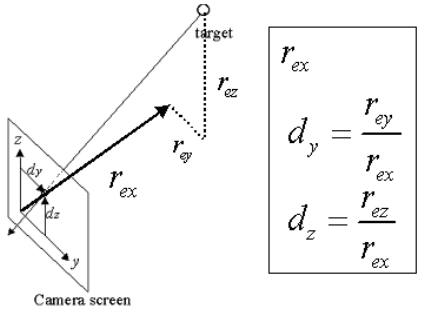

Fig.2 Definition of the line of sight

Relative Attitude

The derivative of quaternion error (Eq.(1-14)) can be rewritten as follows:

$$\dot{q}_e=\frac{1}{2}Q_2(q_e)\{\omega_c\}+\frac{1}{2}Q_3(q_e)\{\omega_t\} \quad (1\text{-}21)$$

where

$$Q_2(q_e)=\begin{bmatrix} q_{e4}U_{3\times3}+\tilde{q}_e^{\times} & \tilde{q}_e \\ -\tilde{q}_e^T & q_{e4} \end{bmatrix} \quad (1\text{-}22a)$$

$$Q_3(q_e)=\begin{bmatrix} -q_{e4}U_{3\times3}+\tilde{q}_e^{\times} & \tilde{q}_e \\ \tilde{q}_e^T & q_{e4} \end{bmatrix} \quad (1\text{-}22b)$$

$$\{\omega\}=[\omega^T\ 0]^T \quad (1\text{-}23)$$

The second derivative of q_e is obtained from Eq.(1-21) as follows:

$$\ddot{q}_e=\frac{1}{2}Q_2(\dot{q}_e)\{\omega_c\}+\frac{1}{2}Q_2(q_e)\{\dot{\omega}_c\}+\frac{1}{2}Q_3(\dot{q}_e)\{\omega_t\}+\frac{1}{2}Q_3(q_e)\{\dot{\omega}_t\} \quad (1\text{-}24)$$

The first three elements of the preceding derivative, $\ddot{\tilde{q}}_e$, can be rewritten as follows:

$$\ddot{\tilde{q}}_e=E_1(\dot{q}_e)\omega_c+E_1(q_e)\dot{\omega}_c-\{E_2(\dot{q}_e)\omega_t+E_2(q_e)\dot{\omega}_t\} \quad (1\text{-}25)$$

where

$$E_1=\frac{1}{2}(q_{e4}U_{3\times3}+\tilde{q}_e^{\times}) \quad (1\text{-}26a)$$

$$E_2=\frac{1}{2}(q_{e4}U_{3\times3}-\tilde{q}_e^{\times}) \quad (1\text{-}26b)$$

From Eqs.(1-1b) and (1-2b), one has

$$\dot{\omega}_c=I_c^{-1}(-\omega_c^{\times}I_c\omega_c+t_c) \quad (1\text{-}27)$$

$$\dot{\omega}_t=I_t^{-1}(-\omega_t^{\times}I_t\omega_t) \quad (1\text{-}28)$$

State Variables

It is assumed that the angular velocity of the chaser satellite can be measured on the chaser satellite using a device such as an inertia reference unit (IRU). Let parameter x consist of the angular velocity of the chaser satellite, relative position and attitude between the chaser and the target satellite, and the relative velocity and angular velocity as measured by the chaser satellite, as follows:

$$x=\begin{bmatrix} \omega_c^T & r_e^T & q_e^T & v_e^T & \omega_e^T \end{bmatrix}^T \quad (1\text{-}29)$$

and the error vector, which is used to represent the difference between the state of the chaser and that of the target satellite, be defined as follows:

$$e=\begin{bmatrix} r_e^T & \tilde{q}_e^T & v_e^T & \omega_e^T \end{bmatrix}^T \quad (1\text{-}30)$$

In addition, it is assumed that the position of the chaser relative to the target satellite in the x-direction of the body frame of the chaser, the LOS parameters, the relative attitude, and the derivatives of these variables can be measured on the chaser satellite. Under this assumption, the state vector $\hat{x}$ is defined as follows:

$$\hat{x}=\begin{bmatrix} \hat{x}_1^T & \hat{x}_2^T & \hat{x}_3^T & \hat{x}_4^T \end{bmatrix}^T=\begin{bmatrix} r_{e_x} & d_y & d_z & \tilde{q}_e^T & \dot{r}_{e_x} & \dot{d}_y & \dot{d}_z & \dot{\tilde{q}}_e^T \end{bmatrix}^T \quad (1\text{-}31)$$

Using Eqs.(1-29) and (1-30), Eq.(1-31) can be rewritten as follows:

$$\hat{x}=T(x)e \quad (1\text{-}32)$$

where

$$T(x)=\begin{bmatrix} R & O_{3\times3} & O_{3\times3} & O_{3\times3} \\ O_{3\times3} & U_{3\times3} & O_{3\times3} & O_{3\times3} \\ -P\omega_c^{\times} & O_{3\times3} & P & O_{3\times3} \\ O_{3\times3} & O_{3\times3} & O_{3\times3} & E_1(q_e) \end{bmatrix} \quad (1\text{-}33)$$

$$R=\begin{bmatrix} 1 & 0 & 0 \\ 0 & 1/r_{e_x} & 0 \\ 0 & 0 & 1/r_{e_x} \end{bmatrix} \quad (1\text{-}34)$$

$$P=\begin{bmatrix} 1 & 0 & 0 \\ -P_y & P_x & 0 \\ -P_z & 0 & P_x \end{bmatrix} \quad (1\text{-}35)$$

Nonlinear Control for Exact-Linearization

Let a nonlinear feedback control that includes forces and torques be as follows:

$$\begin{bmatrix} f_c \\ t_c \end{bmatrix}=\begin{bmatrix} \alpha_1(x) \\ \alpha_2(x) \end{bmatrix}+\begin{bmatrix} \beta_{11}(x) & \beta_{12}(x) \\ \beta_{21}(x) & \beta_{22}(x) \end{bmatrix}\begin{bmatrix} \hat{u}_1 \\ \hat{u}_2 \end{bmatrix} \quad (1\text{-}36)$$

where $\alpha_1(x)$ and $\alpha_2(x)$ are vectors $\in R^3$, $\beta_{11}(x)$, $\beta_{12}(x)$, $\beta_{21}(x)$ and $\beta_{22}(x)$ are matrices $\in R^{3\times3}$, and $\hat{u}_1$ and $\hat{u}_2$ are vectors $\in R^3$. From the preceding equation, one has

$$t_c=\alpha_2(x)+\begin{bmatrix} \beta_{21}(x) & \beta_{22}(x) \end{bmatrix}\begin{bmatrix} \hat{u}_1 \\ \hat{u}_2 \end{bmatrix} \quad (1\text{-}37)$$

First, in order to obtain the nonlinear feedback torques, t_c, substituting Eqs.(1-27) and (1-37) into Eq.(1-1b), and letting the left-side of the equation become $\hat{u}_2$, the nonlinear functions for the exact linearization, $\alpha_2(x)$, $\beta_{21}(x)$ and $\beta_{22}(x)$, are obtained as follows:

$$\alpha_2(x)=\omega_t\times I_c\omega_t+I_cE_1^{-1}(q_e)\{E_2(\dot{q}_e)\omega_t+E_2(q_e)\dot{\omega}_t\}-I_cE_1^{-1}(q_e)E_1(\dot{q}_e)\omega_t \quad (1\text{-}38)$$

$$\beta_{21}(x)=O_{3\times3} \quad (1\text{-}39)$$

$$\beta_{22}(x)=I_cE_1^{-1}(q_e) \quad (1\text{-}40)$$

Next, in order to obtain the nonlinear feedback forces, f_c, one needs to consider the second derivative of r_{e_x}, d_y and d_z. The second derivatives of these variables can be represented by the second derivative of r_e, and r_e can be represented in the terms of r_{e_x}, d_y and d_z. Thus, in this section, the second-derivative of r_e is considered temporally

instead of the second-derivative of r_{e_x}, d_y and d_z, and the nonlinear feedback control force, which converts the position errors between the chaser and target satellites into an exact-linearized system. The first and second derivatives of r_e are represented as follows:

$$\dot{r}_e = v_e - \omega_c \times r_e \tag{1-41}$$

$$\ddot{r}_e = \frac{1}{m_c} f_c - 2\omega_c \times \dot{r}_e - \omega_c \times (\omega_c \times r_e) - \dot{\omega}_c \times r_e \tag{1-42}$$

where Eqs.(1-1a), (1-2a), (1-7) and the relation $\dot{C}_i^T = C_i^T \omega^{\times}$ ($i = c$ or t) are used.

Substituting Eqs.(1-27), (1-37), (1-38), (1-39) and (1-40) into Eq.(1-42), one has

$$\begin{aligned}\ddot{r}_e = {} & \frac{1}{m_c} f_c - 2\omega_c \times \dot{r}_e - \omega_c \times (\omega_c \times r_e) \\ & - E_1^{-1}(q_e)\left\{E_2(\dot{q}_e)\omega_t + E_2(q_e)\dot{\omega}_t\right\} \times r_e \\ & + E_1^{-1}(q_e)E_1(\dot{q}_e)\omega_c \times r_e \; - E_1^{-1}(q_e)\hat{u}_2 \times r_e \end{aligned} \tag{1-43}$$

From Eq.(1-36), the nonlinear feedback control force is represented as:

$$f_c = \alpha_1(x) + \begin{bmatrix}\beta_{11}(x) & \beta_{12}(x)\end{bmatrix}\begin{bmatrix}\hat{u}_1 \\ \hat{u}_2\end{bmatrix} \tag{1-44}$$

Substituting this control force into Eq.(1-43) and comparing both sides of equation in order to convert the relative position system into an exact-linearized system, the nonlinear functions $\alpha_1(x)$, $\beta_{11}(x)$ and $\beta_{12}(x)$ are obtained as follows:

$$\begin{aligned}\alpha_1(x) = {} & 2m_c\omega_c \times \dot{r}_e + m_c\omega_c \times (\omega_c \times r_e) \\ & + m_c E_1^{-1}(q_e)\left\{E_2(\dot{q}_e)\omega_t + E_2(q_e)\dot{\omega}_t\right\} \times r_e \\ & - m_c E_1^{-1}(q_e)E_1(\dot{q}_e)\omega_c \times r_e \end{aligned} \tag{1-45}$$

$$\beta_{11}(x) = m_c U_{3\times 3} \tag{1-46}$$

$$\beta_{12}(x) = -m_c r_e^{\times} E_1^{-1}(q_e) \tag{1-47}$$

Note that the preceding feedback control forces are used to convert the relative position system, rather than the LOS parameters, into an exact-linearized system. Therefore, an additional nonlinear feedback term and a transformation matrix are still necessary in order to exactly linearize the LOS parameter. In order to obtain the required term and matrix, let the position control force be considered by adding a nonlinear term α_1 and matrix D as follows:

$$f_c = \alpha_1(x) + \alpha_1(x) + \begin{bmatrix}\beta_{11}(x)D & \beta_{12}(x)\end{bmatrix}\begin{bmatrix}\hat{u}_1 \\ \hat{u}_2\end{bmatrix} \tag{1-48}$$

Substituting Eqs.(1-45), (1-46), (1-47) and (1-48) into Eq.(1-43), and taking Eqs.(1-19a) and (1-19b) into consideration, the additional nonlinear term α_1 and matrix D can be obtained, respectively, as follows:

$$\alpha_1(x) = \begin{bmatrix}0 \\ 2m_c \dot{r}_{e_x} \dot{d}_y \\ 2m_c \dot{r}_{e_x} \dot{d}_z\end{bmatrix} \tag{1-49}$$

$$D = P^{-1} \tag{1-50}$$

where P is a matrix defined in Eq.(1-35), and is invertiable if r_{e_x} is not zero, that is, if the difference between the chaser and target satellites in the x direction of the chaser body frame is not zero.

Consequently, an exact-linearized system and the nonlinear feedback control inputs for exactly linearizing the system, that consist of the LOS parameters, the relative attitude and their derivatives, can be represented as follows:

$$\dot{\hat{x}} = \hat{A}\hat{x} + \hat{B}\hat{u} \tag{1-51}$$

where

$$\hat{A} = \begin{bmatrix} O_{3\times 3} & O_{3\times 3} & U_{3\times 3} & O_{3\times 3} \\ O_{3\times 3} & O_{3\times 3} & O_{3\times 3} & U_{3\times 3} \\ O_{3\times 3} & O_{3\times 3} & O_{3\times 3} & O_{3\times 3} \\ O_{3\times 3} & O_{3\times 3} & O_{3\times 3} & O_{3\times 3} \end{bmatrix} \tag{1-52}$$

$$\hat{B} = \begin{bmatrix} O_{3\times 3} & O_{3\times 3} \\ O_{3\times 3} & O_{3\times 3} \\ U_{3\times 3} & O_{3\times 3} \\ O_{3\times 3} & U_{3\times 3} \end{bmatrix} \tag{1-53}$$

$$\begin{aligned}\alpha(x) = {} & \begin{bmatrix}\alpha_1(x) \\ O_{3\times 3}\end{bmatrix} + \begin{bmatrix}2m_c\omega_c \times \dot{r}_e + m_c\omega_c \times (\omega_c \times r_e) \\ \omega_c \times I_c\omega_c\end{bmatrix} \\ & + \begin{bmatrix}m_c E_1^{-1}(q_e)E_2(\dot{q}_e)\omega_t \times r_e \\ I_c E_1^{-1}(q_e)E_2(\dot{q}_e)\omega_t\end{bmatrix} + \begin{bmatrix}m_c E_1^{-1}(q_e)E_2(q_e)\dot{\omega}_t \times r_e \\ I_c E_1^{-1}(q_e)E_2(q_e)\dot{\omega}_t\end{bmatrix} \\ & - \begin{bmatrix}m_c E_1^{-1}(q_e)E_1(\dot{q}_e)\omega_c \times r_e \\ I_c E_1^{-1}(q_e)E_1(\dot{q}_e)\omega_c\end{bmatrix} \end{aligned} \tag{1-54}$$

$$\beta(x) = \begin{bmatrix} m_c D & -m_c r_e^{\times} E_1^{-1}(q_e) \\ O_{3\times 3} & I_c E_1^{-1}(q_e) \end{bmatrix} \tag{1-55}$$

From Eq.(1-54), it is found that the nonlinear function $\alpha(x)$ includes the derivative of the angular velocity of the target satellite. This derivative can be estimated using Eq.(1-2b) if the inertia of the target is known and the angular velocity of the target can be sensed. The case in which the inertia of the target is known is almost never satisfied in reality, because the target satellite is assumed to be a malfunctioning, non-cooperative satellite. In order to overcome the problem of the

preceding formulation, an adaptive law to estimate the inertia of the target will be described for a simple case in the next section.

After linearizing the system, any type of control method, such as LQR, can be employed for the exact-linearized system. However, the preceding linearizing formulation requires that matrices E_1 and P are not singular, which occurs when either q_{e4} or r_{e_x} is zero. Applying the LQR method to the preceding exact-linearized system cannot guarantee these requirements. The former singular case can be easily avoided by employing techniques, such as perturbation of the quaternions with small values or skipping control for a short period near the singularity. In the next section, the controller for avoiding both singular cases will be derived from a Lyapunov function that includes a repulsive potential for avoiding both singularities. The attitude part in the controller is basically equivalent to that in [15].

Design of Adaptive Law

In this section, an adaptive law for estimating the inertia ratios of the target satellite is designed under the assumption that the principal axis of the target satellite is coincident with its body axis, and the inertia tensor of the chaser is known exactly. This assumption is at least necessary. This is because the inertia ratios are dominant parameters for the rotational motion of a rigid body, and it is impossible to determine the orientation difference between the body frame and principal axis frame from only the angular velocities. The objective of the law is to improve the performance of the preceding exact-linearization controller. Attitude tracking error, and the velocity and angular velocity of the satellite are used to update the inertia parameters in this study. In order to quantify the parametric mismatch, the parameter estimation error is defined as follows:

$$\tilde{k} = k - \hat{k} \tag{1-56}$$

where k is constant, unknown vector of the inertia parameters and is defined as follows:

$$k = \begin{bmatrix} k_x & k_y & k_z \end{bmatrix}^T = \begin{bmatrix} (I_{t22} - I_{t33})/I_{t11} \\ (I_{t33} - I_{t11})/I_{t22} \\ (I_{t11} - I_{t22})/I_{t33} \end{bmatrix} \tag{1-57}$$

Let η and σ be defined, respectively, as:

$$\eta = a\hat{x}_1 + \hat{x}_3 \tag{1-58}$$

$$\sigma = b\hat{x}_2 + \hat{x}_4 \tag{1-59}$$

where a and b are constant, positive, definite, diagonal matrices or are simply constant scalars, $\hat{x}_2$, $\hat{x}_3$ and $\hat{x}_4$ are defined in Eq.(1-32), and $\hat{x}_1$ is defined as:

$$\hat{x}_1 = \begin{bmatrix} r_{e_x} - r_c & d_y & d_z \end{bmatrix}^T \tag{1-60}$$

A candidate Lyapunov function is selected as:

$$V = \frac{1}{2}\eta^T\eta + \frac{1}{2}\sigma^T\sigma + \frac{1}{2}i\left(1 - r_c/r_{e_x}\right)^2 + \frac{1}{2}j\hat{x}_2^T\hat{x}_2/(1 - \hat{x}_2^T\hat{x}_2) + \frac{1}{2}\tilde{k}^T G^{-1}\tilde{k} \tag{1-61}$$

where G is a constant positive definite diagonal matrix. Taking the time derivative of the preceding equation, one has

$$\dot{V} = \dot{\eta}^T\eta + \dot{\sigma}^T\sigma + ir_c\dot{r}_{e_x}(1 - r_c/r_{e_x})/r_{e_x}^2 + j\hat{x}_2^T\dot{\hat{x}}_2/(1 - \hat{x}_2^T\hat{x}_2) + \dot{\tilde{k}}^T G^{-1}\tilde{k} \tag{1-62}$$

Control inputs $\hat{u}_1$ and $\hat{u}_2$ are designed as follows:

$$\hat{u}_1 = -a\hat{x}_3 - c\eta + \hat{u}_1 \tag{1-63}$$

$$\hat{u}_2 = -b\hat{x}_4 - d\sigma + \hat{u}_2 \tag{1-64}$$

where $\hat{u}_1$ and $\hat{u}_2$ are, respectively,

$$\hat{u}_1 = \begin{bmatrix} -ir_c(1 - r_c/r_{e_x})/r_{e_x}^2 & 0 & 0 \end{bmatrix}^T \tag{1-65}$$

$$\hat{u}_2 = -j\hat{x}_2/(1 - \hat{x}_2^T\hat{x}_2)^2 \tag{1-66}$$

Substituting Eqs.(1-58)-(1-60), and (1-63)-(1-66) into Eq.(1-62), and taking the parameter mismatches (Eq.(1-56)) into account, the time derivative of the candidate Lyapunov function can be rewritten as follows:

$$\dot{V} = -air_c(r_{e_x} - r_c)^2/r_{e_x}^3 - bj\hat{x}_2^T\hat{x}_2/(1 - \hat{x}_2^T\hat{x}_2)^2 - c\eta^T\eta - d\sigma^T\sigma + \tilde{k}^T(Y_2^T\eta + Y_3^T\sigma + G^{-1}\dot{\tilde{k}}) \tag{1-67}$$

where

$$Y_2 = r_e^{\times} NE_2W \tag{1-68}$$

$$Y_3 = -E_2W \tag{1-69}$$

$$W = diag(\omega_{t2}\omega_{t3}, \omega_{t3}\omega_{t1}, \omega_{t1}\omega_{t2}) \tag{1-70}$$

If an adaptive law to estimate the inertia ratios of the target is designed as:

$$\dot{\tilde{k}} = -G(Y_2^T\eta + Y_3^T\sigma) \tag{1-71}$$

the time derivative of the candidate Lyapunov function (Eq.(1-67)) becomes

$$\dot{V} = -air_c(r_{e_x} - r_c)^2/r_{e_x}^3 - bj\hat{x}_2^T\hat{x}_2/(1 - \hat{x}_2^T\hat{x}_2)^2 - c\eta^T\eta - d\sigma^T\sigma \tag{1-72}$$

If the following conditions are satisfied at the initial time

$$r_{e_x}(0) > 0 \text{ and } \hat{x}_2(0)^T\hat{x}_2(0)(= \tilde{q}_2^T(0)\tilde{q}_e(0)) \neq 0 \tag{1-73}$$

From Eqs.(1-61), (1-67) and (1-73), it is easily shown that

$$0 \le V(t) \le V(0) < \infty \tag{1-74}$$

Thus, it is clear that $r_{e_x}(t) \neq 0$ and $\| q_e(t) \|_2 \neq 1$ for all time. Therefore, $N_1(\hat{x}_2)$ is always invertible, and r_{e_x} is always positive. This means that if the target can be seen on the on-board camera installed on the chaser satellite at the initial time, the target never escapes the camera screen as long as the control inputs (Eqs.(1-63)-(1-66)) and the adaptive law (Eq.(1-71)) are employed. In addition, it is obvious from Eq.(1-72) that r_{e_x} converges to r_c and d_y, d_z, $\dot{d}_y$, $\dot{d}_z$, $\dot{r}_{e_x}$, q_e and $\dot{q}_e$ asymptotically become zero as

time increases, that is, the chaser satellite can fly around the target satellite, tracking the attitude motion of the target correctly and maintaining the specified distance r_c from the target.

The estimated inertia ratios of the target satellite, $\hat{k} = [\hat{k}_x \ \hat{k}_y \ \hat{k}_z]^T$ are obtained by integrating the following equation based on the adaptive law (Eq. (1-71)):

$$\hat{k}(t) = \hat{k}(0) - \int_0^t \dot{\hat{k}} dt \qquad (1\text{-}75)$$

where $\hat{k}(0)$ is the estimated inertia ratios for the target satellite at the initial time.

Numerical Simulation

A. Simulation Parameters

Euler rotational motions are classified into four types according to the inertia ratio and angular velocities assuming no internal or external forces or torques on the rigid body: (1) non-symmetric rotational motion, (2) non-periodic rotational motion, (3) symmetric axis rotational motion, and (4) single-axis rotational motion. In this study, only a symmetric axis rotational motion is examined as the target attitude motion.

The validity of the proposed adaptive position and attitude tracking controller based on the exact linearization is verified numerically, compared with the position and attitude tracking controller without the adaptive law, where the chaser satellite is controlled to synchronize its attitude with that of the target satellite and to maintain its relative position to the target at some constant distance so as to avoid collisions with the target. The parameters of the numerical simulations are listed in Table 1.

The following numerical simulations are conducted.

- Case (a) The adaptive law to estimate the inertia ratios of the target satellite is not employed, even though the model parameter for the inertia ratios of the target satellite includes some errors.
- Case (b) The adaptive law to estimate the inertia ratios of the target satellite is employed.

The position of the target is assumed to be on the origin in the inertia frame for all cases. The angular velocities of the target about each axis are chosen as 0.1 rad/s at the initial time.

The performance of the adaptive law is assessed by setting the initial estimated inertia ratios of the target at the same erroneous value for Cases (a) and (b). As mentioned previously, the proposed controller is an adaptive sliding-mode controller including repulsive control inputs to avoid singularities. These repulsive control inputs could have an undesirable influence on the adaptive law used to estimate the parameters. Thus, in the present study, parameters i and j are set small (i.e., 0.001) so as to avoid to the greatest extent possible the effect of the repulsive control inputs on the adaptive law.

B. Simulation Results

The time response of the inertia ratios for the target as estimated by the adaptive law is shown in Fig. 3. The results for Cases (a) and (b) are shown in Figs.4 and 5, respectively. Each figure shows the time responses of LOS errors, quaternion error, control input force and control input torque for the chaser satellite. LOS errors are completely eliminated, but the attitude errors are not completely eliminated for Case (a) even after a long time (i.e. 500 s). This is because the controller for Case (a) does not include the adaptive law, and some errors are contained in the model of the target satellite. On the other hand, although the attitude errors for Case (b) change dramatically at the beginning of a tracking maneuver, the errors are completely eliminated after approximately 100 s, as shown in Fig.5. The correct values of the inertia ratios for the target are $k_x = -0.5$, $k_y = 0.5$, and $k_z = 0$.

The estimated inertia ratios converge to the correct values after approximately 150 s. From a comparison of Fig.4 with Fig.5, and taking the convergence of the estimated inertia ratios for the target satellite into account, the inclusion of the adaptive law improves the tracking performance of the exact-linearization controller effectively.

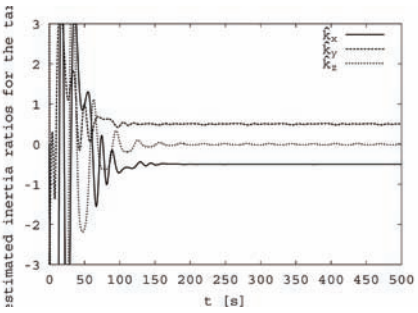

Fig.3 Time response of the estimated inertia ratios of the target satellite.

Table 1. Parameters for numerical simulations.

inertia	**target**	$I_{t11}=10 \quad I_{t22}=10 \quad I_{t33}=15\ \mathrm{kgm}^2$
	chaser	$I_c=\begin{bmatrix}300 & -30 & -50\\ -30 & 400 & -40\\ -50 & -40 & 300\end{bmatrix}\mathrm{kgm}^2 \quad m_c=500\ \mathrm{kg}$
Initial state	**target**	$r_t=\begin{bmatrix}0 & 0 & 0\end{bmatrix}^T\ \mathrm{m} \quad q_t=\begin{bmatrix}0 & 0 & 0 & 1\end{bmatrix}^T$ $v_t=\begin{bmatrix}0 & 0 & 0\end{bmatrix}^T\ \mathrm{m/s} \quad \omega_t=\begin{bmatrix}0.1 & 0.1 & 0.1\end{bmatrix}^T\ \mathrm{rad/s}$
	chaser	$r_c=\begin{bmatrix}10 & 0 & 0\end{bmatrix}^T\ \mathrm{m} \quad \omega_c=\begin{bmatrix}0 & 0 & 0\end{bmatrix}^T\ \mathrm{rad/s}$ $v_c=\begin{bmatrix}0 & 0 & 0\end{bmatrix}^T\ \mathrm{m/s} \quad q_c=\begin{bmatrix}0 & 0 & \sqrt{2}/2 & \sqrt{2}/2\end{bmatrix}^T$
gains		$a=b=c=d=0.1,\ \ i=j=0.001\ \ G=4\times10^3 U_{3\times3}$

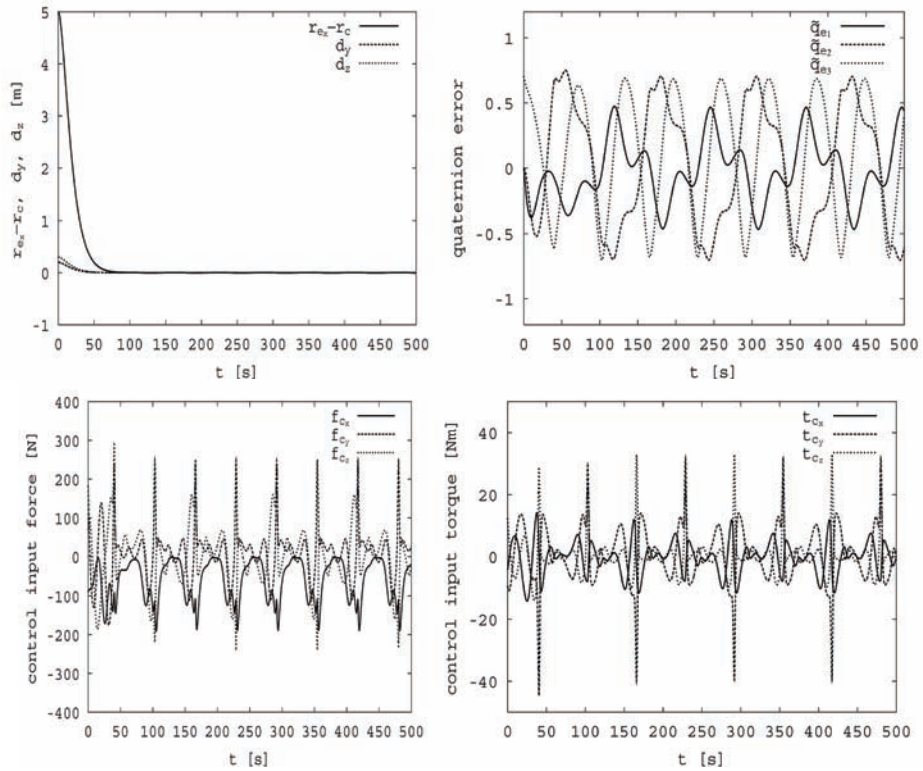

Fig.4 Time response of LOS error, quaternion error, and control input forces and torques for case (a).

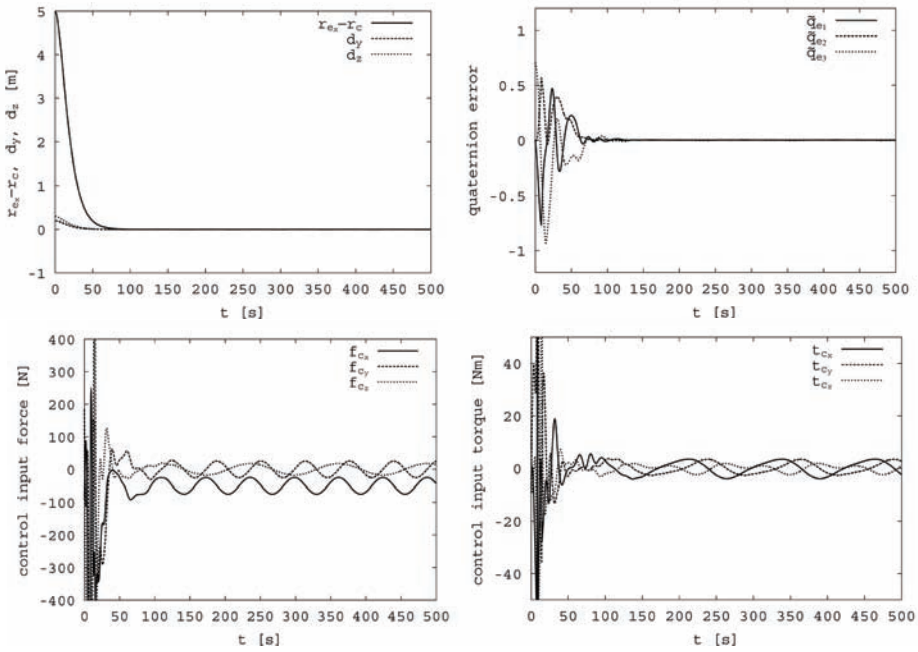

Fig.5 Time response of LOS error, quaternion error, and control input forces and torques for case (b).

III. Stabilization of Angular Velocity of Asymmetrical Rigid Body Using Two Constant Torques

Research Background

The problem of stabilization of angular velocity using less than three control torques has been investigated by several authors[16-26]. The present system can be stabilized by nonlinear control schemes, which may be categorized into three types: time-varying control schemes, discontinuous control schemes, and time-invariant control schemes. In those studies, it is assumed that an arbitrary magnitude of the torques can be fed to a satellite to attenuate its rotational motion using gas jet thrusters employing the Pulse Width Pulse Frequency (PWPF) Modulator. If thrusters provide two control torques without the use of PWPF, then the magnitude of the torque does not linearly respond to the input magnitude, and, indeed, is constant. No previous studies have considered this special case. If a control scheme could be derived for this case, then the resulting control method can facilitate a reduction in the use of PWPF modulation from satellites, or can form a backup system in the event of malfunction of the PWPF modulators, subject to the two-control-torque problem.

In this chapter, provided that the model uncertainties and external disturbances are neglected, a constant control torque method to attenuate the rotational motion of an asymmetric rigid body is proposed. The proposed control method is classed as a discontinuous and open loop control method. Because the magnitude of the control torque is constant, that is, it can only be applied On-Off, and the control timing is pre-determined. In this chapter, the set of angular velocities of an asymmetrical rigid body achievable by employing a single constant control torque is defined as “constant-torque-manifold” or simply referred to as the manifold. In the case when only a single constant control torque is used, this manifold can be analytically obtained by integrating the equations of motion backwards in time from the angular velocities that are accessible to the origin by employing a single constant control torque, where the set of angular velocities that can access the origin by a single constant control torque is hereafter referred to as a transient goal. A trajectory resulting from the proposed control method consists of three steps: If the polhode starting from initial angular velocities has intersection points with the manifolds, then the rotational motion does not need to be either boosted or damped. On the other hand, if the polhode starting from the initial angular velocities has no intersection points with the manifold, the rotational motion must be boosted around the maximum or minimum principal moment of inertia and damped around the middle principal moment of inertia to ensure that the trajectory has at least one point intersecting the manifolds. The first step is thus given by the trajectory of the angular velocities to an intersection point with the manifold, without the control torques, or boosted/damped by the control torques if necessary. The second step is a trajectory sliding on the manifold, by means of a single constant torque, until the transient goal is reached. The final step is a trajectory from the transient goal to the origin. The control timings, durations and the sign of control torques can then be

determined by calculating the intersection points between the manifold and polhode or the boosted/damped trajectory, between the trajectory sliding on the manifold and the transient goal, and between the single spin motion and the origin. A schematic representation of these trajectories is shown in Fig. 6. The idea of the constant-torque-manifold for stabilization of the rotational motion of an asymmetric rigid body is inspired by [27], which describes a method to obtain a trajectory of the angular velocities of an asymmetric rigid body when a single constant torque is employed along either the maximum, minimum, or middle principal moment of inertia axis. Contrary to the robust feedback schemes[24-26], a demerit of the proposed method is that it is not robust to the modeling errors, and external disturbances. On the other hand, a merit of the proposed method is that it can easily estimate the convergence time. This is because the manifolds are obtained analytically and the dynamic control problem is converted into a kinematics problem of the calculation of intersection points between the manifolds and polhode or boosted/damped trajectory, and this converted problem can be solved by the bi-section method. Results of a numerical simulation of the present method applied to a test problem are given later in this chapter to show that the complete attenuation can be achieved by using the proposed manifold, provided that external disturbances and modeling uncertainties are absent, and the intersection point between the manifolds and polhode or boosted/damped trajectories is completely obtained.

Problem Statement and Equations of Motion

Throughout this chapter, it is assumed that the principal axes of a satellite are coincident with its body frame coordinates. Because in this chapter, only the case of an asymmetrical rigid body, principal moments of inertia satisfy $j_1 \neq j_2 \neq j_3$ is treated. Without loss of generality, it is assumed that $j_1 > j_2 > j_3$. Referring to [27], the equation of motion can be rewritten in the form

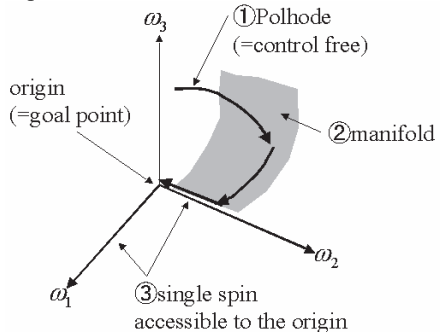

Fig. 6 Schematic view of the trajectory resulting from the constant control torque method.

$$\begin{bmatrix} x_1' \\ x_2' \\ x_3' \end{bmatrix} = \begin{bmatrix} x_2 x_3 \\ -x_3 x_1 \\ x_1 x_2 \end{bmatrix} + \begin{bmatrix} \mu_1 \\ \mu_2 \\ \mu_3 \end{bmatrix} \qquad (2\text{-}1)$$

where ()' denotes the derivative operator $d()/d\tau$ where τ is the scaled time, (x_1, x_2, x_3) is the scaled angular velocity vector and (μ_1, μ_2, μ_3) is the scaled constant torque vector. The detail of the variable changes is described in [27]. In this chapter, the derivation of a control method using less than three constant control torques that can attenuate the rotational motion of an asymmetric rigid body is considered.

Constant Control Torque Method

A. Transient Goals and Constant Torque Patterns

If the angular velocities along the uncontrolled axis and one of the remaining controlled axes are both zero, then the system is both controllable and accessible to the origin. This situation, which is a single spin motion around the one of the controllable axes, can be therefore treated as a transient goal. In this paper, the control torques are assumed to be generated by gas jet thrusters without using PWPF modulators. In this case, the torque takes a plus or minus sign, or can be zero in magnitude (i.e. switched off), and the total number of combinations of the signs of the thrusters is nine. Although all the above sets of signs of the control torques can be used to generate manifolds, the analytical manifolds can be obtained only for the case when a single constant control torque is not along one of the principal axes corresponding to the single spin motion. Therefore in this chapter, only this case will be considered.

Because there exist three possibilities for the uncontrolled axis; the maximum, middle, or minimum principal moment of inertia, and there are two cases for the single spin motion around the controllable axis, there thus exist six cases for generating the manifolds, as listed in Table 2.

B. Manifolds

The manifolds can be obtained by integrating the equations of motion backward in time from transient goals with the employment of a single constant control torque. With reference to [27], and taking the angular velocities of the transient goals into account, the manifold for each case in Table 2 can then be analytically obtained as follows:

(I)
$$x_1^2 = 2\mu_1\theta - A^2 \sin^2\theta \qquad (2\text{-}2a)$$
$$x_2 = -A\sin\theta \qquad (2\text{-}2b)$$
$$x_3 = A\cos\theta \qquad (2\text{-}2c)$$

Table 2. Transient Goals.

maximum	middle	minimum	transient goal*
(I) constant torque	uncontrollable	controllable	$x_1(0)=0, x_2(0)=0, x_3(0)\neq 0$
(II) constant torque	controllable	uncontrollable	$x_1(0)=0, x_2(0)\neq 0, x_3(0)=0$
(III) uncontrollable	constant torque	controllable	$x_1(0)=0, x_2(0)=0, x_3(0)\neq 0$
(IV) controllable	constant torque	uncontrollable	$x_1(0)\neq 0, x_2(0)=0, x_3(0)=0$
(V) controllable	uncontrollable	constant torque	$x_1(0)\neq 0, x_2(0)=0, x_3(0)=0$
(VI) uncontrollable	controllable	constant torque	$x_1(0)=0, x_2(0)\neq 0, x_3(0)=0$

*axis 1: maximum, 2: middle, 3: minimum

(II) $$x_1^2 = 2\mu_1\theta + A^2\sin^2\theta \quad (2\text{-}3a)$$

$$x_2 = A\cos\theta \quad (2\text{-}3b)$$

$$x_3 = A\sin\theta \quad (2\text{-}3c)$$

(III) $$x_1 = A\sinh\theta \quad (2\text{-}4a)$$

$$x_2^2 = 2\mu_2\theta - A^2\sinh^2\theta \quad (2\text{-}4b)$$

$$x_3 = A\cosh\theta \quad (2\text{-}4c)$$

where θ is the parameter determined by integrating the angular velocity along the constant control torque backward in time associated with the initial condition $\theta(0)=0$, and A is the parameter to describe the scaled angular velocity of the transient goal. Note that the manifolds for cases (IV), (V), and (VI) are omitted here, because when x_1 is swapped with x_3, the manifolds for cases (IV), (V), and (VI) are the same as those for cases (III), (I), and (II), respectively. In cases (II) and (VI), θ is not limited and the trajectories on the manifolds are open and non-periodic. In cases (III) and (IV), θ is limited and the trajectories on the manifolds are always closed and periodic. In cases (I) and (V), the trajectories on the manifolds are open or closed, depending on the parameter. Let β be a parameter defined as $\beta := |\mu_i|/A^2$ to simply obtain the separatrix between the closed and open trajectories on the manifolds for cases (I) and (V). Solving the equations $f(\beta,\theta) := 2\beta\theta - \sin^2\theta = 0$ and $f_\theta(\beta,\theta) := 2\beta - 2\sin\theta\cos\theta = 0$ with respect to β and θ yields $\beta^* \cong 0.362306$ and $\theta^* \cong 1.16556$. The scaled angular velocity of the transient goal corresponding to the separatrix, A^*, is given by $A^* = \sqrt{|\mu_i|/\beta^*}$. Note that if $\beta > \beta^*$, then θ for cases (I) and (V) is not limited, that is, the trajectories on the manifold are open and non-periodic. On the other hand, if $\beta < \beta^*$, then θ for cases (I) and (V) is limited, that is, the trajectories on the manifold are closed and periodic. The upper bounded value of parameter θ can be determined by imposing the condition that the angular velocity around the constant control torque equals zero with respect to θ for cases (III) and (IV), and under the condition $\beta < \beta^*$ for cases (I) and (V).

Figures 7(a), 7(b) and 7(c) show the manifolds for cases (I), (III) and (VI), respectively, where the scaled control torques are assumed to be unit for the sake of simplicity.

Note that the periodic parts of the manifolds are shown in Figs. 7(a) and 7(b) as open ones due to the limitation of the programming code based on Mathematica .

C. Calculation of the Points of Intersection with the Manifolds

Let α be the parameter given by $\alpha = H^2/2E$, where H is the magnitude of the angular momentum given by $H = \sqrt{(j_1\omega_1)^2 + (j_2\omega_2)^2 + (j_3\omega_3)^2}$, and E is the rotational energy of the rigid body given by $E = \left(j_1\omega_1^2 + j_2\omega_2^2 + j_3\omega_3^2\right)/2$. The intersection points between the polhode or the boosted or damped trajectory and the manifolds can be obtained numerically by using the bi-section method. There may exist several intersection points; one of these points should be selected according to control criteria, such as settling time or energy optimality. Because the control input is assumed to be constant in this paper, the point with the minimum control duration can be chosen as the energy optimal solution.

C-1. Calculation of the Intersection Point between the Polhode and the Manifolds

By replacing the constant control torque with no control torque, and introducing a new variable ψ, the polhode scaled by the variable changes given in [27] can be expressed in the form of a function of parameter ψ as follows:

For the case $\alpha \geq j_2$,

$$x_{p1} = \mathrm{sgn}(x_{p1}(0))\sqrt{x_{p1}^2(0) + \frac{D^2}{2}\left\{\cos 2\eta - \cos\left(2(\psi+\eta)\right)\right\}} \quad (2\text{-}5a)$$

$$x_{p2} = D\cos\left(\psi+\eta\right) \quad (2\text{-}5b)$$

$$x_{p3} = D\sin\left(\psi+\eta\right) \quad (2\text{-}5c)$$

where

$$D = \sqrt{x_{p2}^2(0) + x_{p3}^2(0)} \quad (2\text{-}6a)$$

$$\eta = \mathrm{a\,tan}\,2\left(x_{p3}(0), x_{p2}(0)\right) \quad (2\text{-}6b)$$

$$\psi(\tau) = \int_0^\tau x_{p1}(\xi)d\xi \quad (2\text{-}6c)$$

For the case $\alpha < j_2$, the expression for the polhode can be obtained by swapping x_{p1} with x_{p3} in Eqs.(2-5) and

(2-6). Note that for the case $\alpha = j_2$, the angular velocities converge to the one around the middle principal moment of inertia, and in this case, by solving $x_{p1} = x_{p3} = 0$ with respect to ψ, the range of parameter ψ is limited between 0 and $\left(\mathrm{sgn}(\eta) + \mathrm{sgn}(x_{p1}(0))\right)\pi/2 - \eta$.

An intersection point between the manifolds and the polhode can be obtained numerically by solving three equations $x_{p1} = x_1$, $x_{p2} = x_2$ and $x_{p3} = x_3$ with respect to A, θ, and ψ. Note that, as mentioned earlier, the range of phase parameter θ is limited for cases (III) and (IV), and under the condition $A > A^*$ for cases (I) and (V), and that the range of ψ is limited for the case of $\alpha = j_2$, This calculation process is repeated until all combinations of the manifolds corresponding to the constant control torque along the controllable axis are completed.

C-2. Calculation of Intersection Point between Boosted or Damped Trajectory and the Manifolds

If the scaled polhode trajectory has no intersection points with the manifolds, then, under the proposed method, the rotational motion has to be boosted or damped until it has at least one intersection point with the manifold. A typical example is the case given by a single spin motion around the uncontrollable axis. If the intersection points exist, then it is obvious that the angular velocity of an asymmetric rigid body can be stabilized to the origin by the presented piecewise steps. A problem left open is whether or not an intersection point exists between the boosted/damped trajectory and the manifolds. This problem is briefly discussed here. Note that hereafter for the purpose of simplicity, the scaled constant torque is assumed to be unit.

The rotational motion of a rigid body with damping around either the middle or minimum principal moment of inertia and boosting around the maximum principal moment of inertia is likely to converge to a flat spin motion around the maximum principal moment of inertia. The polhode near the flat spin motion is a closed loop trajectory around the axis of x_1, the manifold for case (I) is connected with the axis of x_1, and its radius around the axis of x_1 is limited within $|A^*| \cong 1.66135$, as shown in Fig. 7(a). The manifold for case (II) is also connected with the axis of x_1, but its radius around the axis of x_1 is not limited. This implies that the polhode satisfying $\alpha > j_2$ and $\sqrt{x_2^2 + x_3^2} < |A^*|$ always has an intersection point with the manifold for cases (I) and (II), and that the polhode satisfying $\alpha > j_2$ but not $\sqrt{x_2^2 + x_3^2} < |A^*|$ always intersects the manifold for case (II). Therefore, if the axis of the maximum principal moment of inertia is controllable, then to easily have an intersection point with the manifold for case (II), the following control method, which boosts around the maximum principal moment of inertia and damps around the other controllable axis, should be conducted.

$$\mu_1 = \mathrm{sgn}(x_1),\ \mu_3 = -\mathrm{sgn}(x_3) \quad \text{(angular velocity around the axis of } x_3 \text{ is controllable)} \quad (2\text{-}7a)$$

$$\mu_1 = \mathrm{sgn}(x_1),\ \mu_2 = -\mathrm{sgn}(x_2) \quad \text{(angular velocity around the axis of } x_2 \text{ is controllable)} \quad (2\text{-}7b)$$

On the other hand, if the axis around the maximum principal moment of inertia is uncontrollable, then the radius of the manifold around the axis of x_3 is not limited, and the manifold is connected with the axis of x_3, as shown in Fig. 7(c). Beside, the polhode for the case of $\alpha < j_2$ is a closed loop trajectory around the axis of x_3. This implies that polhode for the case of $\alpha < j_2$ always has an intersection point with the manifold for case (VI). Therefore, in this case, to have at least one intersection point with the manifold, the following signs should be selected for the constant control torques.

$$\mu_2 = -\mathrm{sgn}(x_2),\ \mu_3 = \mathrm{sgn}(x_3) \quad (2\text{-}8)$$

Test Problem

An example numerical simulation is conducted to demonstrate the validity of the proposed control method. It is assumed that the uncontrolled axis is around the minimum principal moment of inertia. The parameters for numerical simulation are as follows: the moments of inertia (j_1, j_2, j_3) = (15, 10, 7) [kgm^2], the constant control torque is $T_{1,2} = \pm 20$ [Nm], and the initial angular velocity vector is $(\omega_1(0),\ \omega_2(0),\ \omega_3(0)) = (1.54,\ -1.95\ -0.58)$ [rad/s]. Firstly, to determine if boosting process is needed, it is checked if the polhode intersects the manifolds. Two intersection points between the polhode and the manifold are found, and they are the angular velocity vectors (1.6296, 1.6329, -1.1622) [rad/s], and (1.6296, -1.6329, 1.1622) [rad/s], respectively. This means that no control torque is needed until reaching the manifold. The time response of the angular velocities, the time history of the control torques, the trajectory of the time and energy optimal solution along with the manifold, and the trajectory of the energy optimal but not time optimal solution are shown in Figs. 8(a), 8(b), 8(c), and 8(d), respectively. It can be seen that the angular velocities are successfully controlled to the origin by the proposed method. The time required to reach each intersection point from the initial angular velocities is determined as 1.6848[sec], and 4.1845[sec], respectively. The energy consumption of the second solution is the same as that of the first solution, but the first solution was selected from the viewpoint of the settling time in this paper. When the angular velocity vector reaches the first intersect point, the sign of the control torques is determined to be (-, 0). That is, a trajectory sliding on the manifold is generated by a negative constant control torque along the maximum principal moment of inertia.

The constant control torque is employed until the

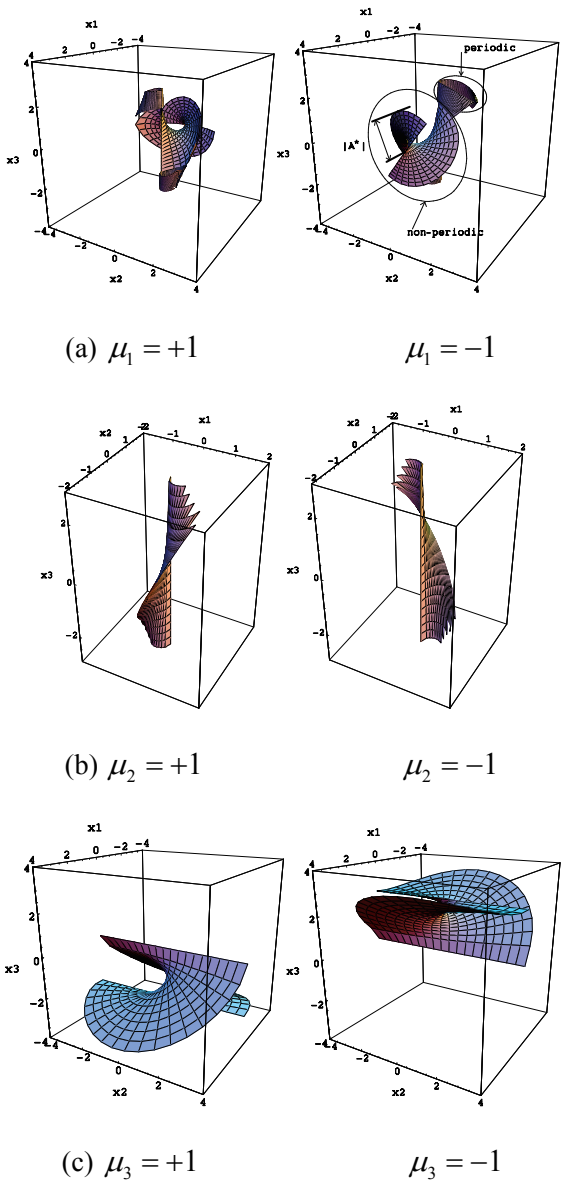

Fig. 7 Scaled constant-control manifold for case (I) (a), for case (III) (b), and for case (VI)(c).

uncontrolled angular velocity ω_3 and the one of the controlled angular velocity ω_1 converge to zero. The time required to reach the transient goal from the intersection point is found to be 1.1003[sec]. After the two angular velocities become zero, the angular velocity of the remaining controllable axis ω_2 is controlled until reaching the origin by a negative constant torque along the middle principal moment of inertia. The time required to converge to the origin from the transient goal is found to be 1.0222[sec]. The total time required to converge from the initial angular velocity to the origin is, therefore, given by

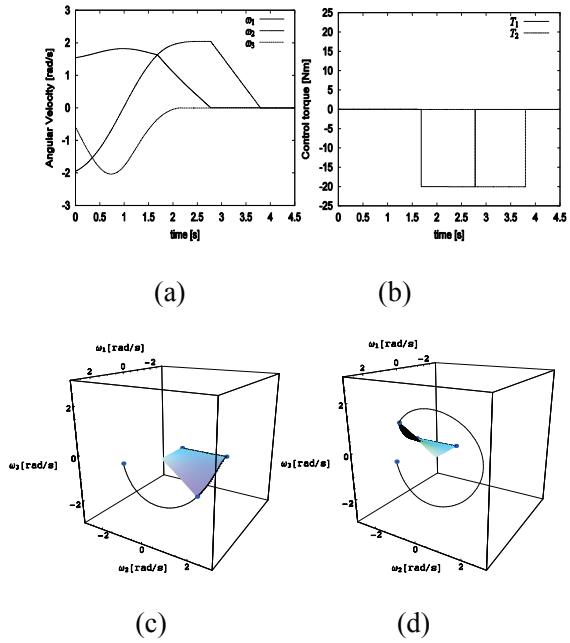

Fig.8 Time response of the angular velocities (a), time histories of the constant control torques (b), the time and energy optimal trajectory along with the intersected manifold (c), and the energy optimal but not time optimal trajectory along with the intersected manifold (d) (The start and endpoints of each segment of the trajectory are indicated by the markers).

approximately 3.8073 (1.6848 +1.1003+1.0222)[sec].

IV. Conclusion

In this paper, sliding-mode controllers have been studied for two topics related with the space debris elimination: fly-around motion control, and angular velocity stabilization by means of two-control-torque.

For the fly-around motion, a linearization feedback controller based on an exact-linearization method has been introduced in order to control the position and attitude of a chaser satellite for the purpose of constellation flight with a target satellite in the absence of a gravitational field and other disturbances. The derived controller is basically a sliding-mode controller, including the potential control inputs to avoid the singularities that take place when the line of sight is lost and the target escapes the on-board camera screen on the chaser satellite, or the attitude of the chaser satellite is opposite to that of the target satellite. In order to improve the performance of the proposed exact-linearization controller, an adaptive law has been provided for the presence of the inertia ratios uncertainty of the target. Numerical simulations have been conducted to demonstrate the effectiveness of the proposed method. The results of numerical simulations show that the proposed exact-linearization method with the adaptive law can precisely

control the position and attitude of the chaser satellite in order to track those of the target satellite by estimating the inertia ratio of the target, even if the inertia ratios uncertainty of the target satellite are included in modeling at the initial time.

For the two-control torque problem, a constant control torque method has been proposed for attenuating the rotational motion of an asymmetric rigid body. The manifold is defined as a set of the angular velocities of an asymmetrical rigid body that can approach the transient goal by employing a constant control torque, and can be obtained analytically by integrating the equations of motion backward in time from the transient goal, which is accessible from the origin by means of a single constant control torque. The obtained manifold can be used as the reference state for the sliding mode control. The trajectory resulting from the proposed method consists of three steps: First, a trajectory boosted around the maximum or minimum principal moments of inertia, and damped around the middle principal moment of inertia by control torques if necessary (if unnecessary, a trajectory of torque-free motion (polhode)) until an intersection point with the manifold is reached. Second, a trajectory sliding on the manifold, and finally a trajectory along the one controllable axis until the origin is reached. Thanks to the analytically obtained manifolds and polhode, the time required for convergence to the origin can be obtained numerically by calculating the intersection point between the manifolds and trajectories. To delete ambiguities of multiple solutions, the energy optimality and settling time is considered. The results of an example numerical simulation showed that the complete attenuation of the angular velocities of an asymmetrical rigid body can be achieved by the proposed method, provided that internal and external disturbances and modeling uncertainties are absent, and the intersection point between the trajectory and the manifold is completely obtained.

References

[1] Wie, B., Weis, H., and Arapostathis, A., "Quaternion Feedback Regulation for Spacecraft Eigenaxis Rotations", *Journal of Guidance, Control, and Dynamics*, Vol.12, No.3, 1989, pp.37-380.

[2] Bilimoria, K. D., and Wie, B., "Time-Optimal Three-Axis Reorientation of a Rigid Spacecraft", *Journal of Guidance, Control, and Dynamics*, Vol.16, No.3, 1993, pp.446-452.

[3] Steyn, W.H., "Near-Minimum-Time Eigenaxis Rotation Maneuvers Using Reaction Wheels", *Journal of Guidance, Control, and Dynamics*, Vol.18, No.5, 1995, pp.1184-1189.

[4] Hwa-Suk Oh, Young-Deuk Yoon, Young-Ken Change, Jai-Hyuk Hwang, and Sang Seok Lim, "Near-Eigenaxis Rotation Control Law Design for Moving-to-Rest Maneuver", *Journal of Guidance, Control, and Dynamics*, Vol.24, No.6, pp.1228-1231, 2001.

[5] Yuan, J.S.C., "Closed-Loop Manipulator Control Using Quaternion Feedback", *IEEE Transactions on Robotics and Automation*, Vol.4, No.4, 1988, pp.434-440.

[6] Vadali, S. R., "Variable-Structure Control of Spacecraft Large-Angle Maneuvers", *Journal of Guidance, Control and Dynamics*, Vol.9, No.2, 1986, pp.235-239.

[7] Crassidis, J. L., and Markley, F. L., "Sliding Mode Control Using Modified Rodrigues Parameters", *Journal of Guidance, Control and Dynamics*, Vol.9, No.6, 1996, pp.1381-1383.

[8] Robinett, R. D., and Parker, G. G., "Spacecraft Euler Parameter Tracking of Large-Angle Maneuvers via Sliding Mode Control", *Journal of Guidance, Control and Dynamics*, Vol.19, No.3, 1996, pp.702-703.

[9] Chen, Y. P., and Lo, S. C., "Sliding-Mode Controller Design for Spacecraft Attitude Tracking Maneuvers", *IEEE Transactions on Aerospace and Electronic Systems*, Vol.29, No.4, 1993, pp.1328-1333.

[10] Lo, S. C., and Chen, Y. P., "Smooth Sliding-Mode Control for Spacecraft Attitude Tracking Maneuvers", *Journal of Guidance, Control, and Dynamics*, Vol.18, No.6, 1995, pp.1345-1349. , 1996, pp. 1206-1211 (in Japanese).

[11] Terui, F., "Position and Attitude Control of a Spacecraft by Sliding Mode Control", *Transactions of the Japan Society of Mechanical Engineers (C)*, Vol.64, No.621, 1998, pp.215-222 (in Japanese).

[12] Isidori, A., "Nonlinear Control Systems(second edition)", Springer-Verlag, 1995.

[13] Dwyer III, T.A.W., "Exact Nonlinear Control of Spacecraft Slewing Maneuvers with Inertial Moment Transfer", *Journal of Guidance, Control and Dynamics*, Vol.9, No.2, 1986, pp. 240-247.

[14] Kida, K. and Yamaguchi, T., "On Linearization of Nonlinear Spacecraft Motion", *Transactions of the Society of Instruments and Control Engineers*, Vol.27, No.8, 1991, pp.1073-1075 (in Japanese).

[15] Yamada, K., Yoshikawa, S., Yoshida, N., and Koyama, H., "Relative Motion Control Between Spacecraft", *Transactions of the Society of Instruments and Control Engineers*, Vol.30, No.10, 1994, pp. 1225-1233 (in Japanese).

[16] Crouch, P.E., "Spacecraft Attitude Control and Stablilization: Application of Geometric Control Theory to Rigid Body Model," IEEE Transactions on Automatic Control, Vol.29, No.4, 1984, pp.321-331.

[17] Brockett, R.W., "Asymptotic Stability and Feedback Stabilization," Differential Geometric Control Theory, Birkhauser, Boston, 1983, pp.181-208.

[18] Aeyels, D., "Stabilization by Smooth Feedback Control of the Angular Velocity of a Rigid Body," Systems and Control Letters, Vol.6, No. 1, 1985, pp.59-63.

[19] Aeyels, D., and Szafransski, M., "Comments on the Stabilizability of the Angular Velocity of a Rigid Body", Systems and Control Letters, Vol.10, No.1, 1988, pp.35-39.

[20] Sontag, E.D., and Sussman, H.J., "Futher Comments on the Stabilizability of the Angular Velocity of a Rigid Body," Systems and Control Letters, Vol.12, No. 3, 1988, pp.213-217.

[21] Outbib, R. and Sallet, G., "Stabilizability of the Angular Velocity of a Rigid Body Revisited," Systems & Control Letters, Vol. 18, No. 2, 1992, pp.93-98.

[22] Andriano, A., "Global Feedback Stabilization of the Angular Velocity of a Symmetric Rigid Body," Systems and Control Letters, Vol. 20, No.5, 1993, pp.361-364.

[23] Tsiotras, P., and Schleicher, A. "Detumbling and Partial Attitude Stabilization of a Rigid Spacecraft under Actuator Failure," AIAA Paper 00-4044, 2000.

[24] Astolfi, A. and Rapaport, A., "Robust Stabilization of the Angular Velocity of a Rigid Body," Systems & Control Letters, Vol.34, No. 5, 1998, pp.257-264.

[25] Astolfi, A., "Output Feedback Stabilization of the Angular Velocity of a Rigid Body," Systems & Control Letters, Vol. 36, No.3, 1999, pp.181-192.

[26] Mazenc, F. and Astolfi, A., "Robust Output Feedback Stabilization of the Angular Velocity of a Rigid Body," Systems & Control Letters, Vol. 39, No. 3, 2000, pp.203-210.

[27] Livnch, R., and Wie, B., "New Results for an Asymmetric Rigid Body with Constant Body-Fixed Torques," AIAA Journal of Guidance, Control, and Dynamics, Vol.20, No.5, 1997, pp.873-881.

Nonlinearity of the unsteady aerodynamics of the viscous flow on supercritical wing in transonic regime

Kenichi Saitoh

Japan Aerospace Exploration Agency, Japan

Keywords: Limit Cycle Oscillation, Transonic, Unsteady aerodynamics

Abstract. Unsteady aerodynamics of two dimensional supercritical wing profile in transonic regime was investigated by Navier-Stokes code. First harmonic components of the unsteady aerodynamics obtained by simulation for forced oscillations of heaving and pitching mode were plotted to the amplitude of oscillations and it shows nonlinearity of the unsteady aerodynamics in small amplitude region. Stability analysis based on the first harmonic components of the unsteady aerodynamics also shows nonlinear trend. Limit Cycle Oscillation (LCO) of small amplitude about 0.1 *deg.* could exist from the stability analysis and simulation was carried out. Nonlinearity of unsteady aerodynamics in small amplitude range is affected by transition point, which interferes with unsteady pressure distribution in local supersonic region on upper surface. These computational results are described in this paper.

1 INTRODUCTION

Schewe et al. found small amplitude LCO which has about 0.2 *deg.* of pitching oscillation in transonic wind tunnel test with two dimensional elastic support system[1]. This implies it has nonlinearity in small amplitude region, but the LCO is thought different from a typical one which is induced by the shock wave motion on the wing surface and limited the amplitude by the flow separation. Castro showed to simulate small amplitude LCO by considering perforated wind tunnel wall effect in his CFD analysis[2]. Thomas showed a relation between amplitude of the pitching oscillation of the LCO and flutter speed using Harmonic Balance method[3], but no small amplitude LCO was shown.

Characteristics of the transonic unsteady aerodynamics especially in small amplitude oscillation are investigated by the CFD analysis for NLR-7301 supercritical wing profile in this paper.

2 ANALYSIS METHOD

2.1 Equation of binary aeroeastic system

Schematic binary aeroelastic system is shown in Figure 1, and equation of the system is as follows.

$$\begin{bmatrix} 1 & x_a \\ x_a & r_a^2 \end{bmatrix}\begin{bmatrix} \ddot{\bar{h}}^* \\ \ddot{\alpha}^* \end{bmatrix}+\begin{bmatrix} 2\zeta_h\omega_h^* & 0 \\ 0 & r_a^2 2\zeta_\alpha\omega_\alpha^* \end{bmatrix}\begin{bmatrix} \dot{\bar{h}}^* \\ \dot{\alpha}^* \end{bmatrix}+\begin{bmatrix} \omega_h^{*2} & 0 \\ 0 & r_a^2\omega_\alpha^{*2} \end{bmatrix}\begin{bmatrix} \bar{h} \\ \alpha \end{bmatrix}=\frac{1}{\mu\pi}\begin{bmatrix} -C_l \\ 2C_m \end{bmatrix} \quad (1)$$

The equation is nondimensionalized by half chord length b for length, total mass m for mass and b/U for time, where U is uniform speed of flow. Asterisk means values based on non-dimensional time. Structural parameters of reference [1] are converted for Eq. (1) and listed in table 1. Eq. (1) is also expressed as Eq. (2) in this paper.

$$M\ddot{q} + C\dot{q} + Kq = f \quad (2)$$

2.2 Numerical analysis

Navier-Stokes code used for the analysis is based on the thin layer NS equation and Baldwin-Lomax turbulence model is adopted[4]. Structural mode equation combined with the aerodynamics is integrated by Wilson's implicit θ method. Structured C type grid of which size is 313x79 is generated and 247 grid points are placed on the wing surface. Thickness of the grid on the wing is $6\times10^{-5}b$ and far field boundary is $40b$. Time step size for unsteady analyses is about 0.002 in non-dimensional time. Courant number is about 30. In LCO simulations, 0.001 is taken as time step size to converge results.

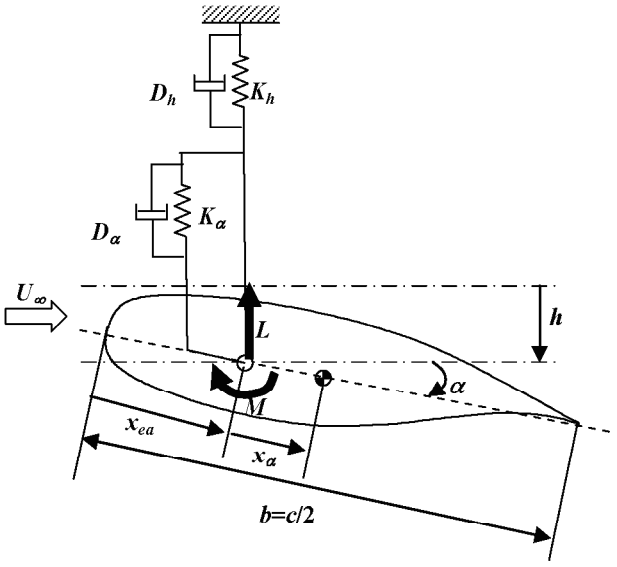

Figure 1 : Two dimensional aeroelastic system

Wing profile data of reference [5] is used. The trailing edge of the data is at x/c=1.015, but in this analysis the profile is cut at x/c =1.0 to combine upper and lower surface at the center in thickness. So the line between leading and trailing edge has −0.16 *deg.* inclination.

Table 1 : Structural parameters

reference length (half chord length)	b	= 0.15 [m]	
center of rotation	x_{ea}	= 0.50	
static unbalance	x_α	= 0.0968	
radius of gyration	r_α	= 0.394	
pitching frequency	ω_α^*	= 0.1584	= $\sqrt{K_\alpha / I_\alpha}b/U_\infty$
heaving frequency	ω_h^*	= 0.1204	= $\sqrt{K_h / m}b/U_\infty$
damping of pitching	ζ_α	= 0.0043	= $D_\alpha/(2\sqrt{K_\alpha I_\alpha})$
damping of heaving	ζ_h	= 0.0071	= $D_h/(2\sqrt{K_h m})$

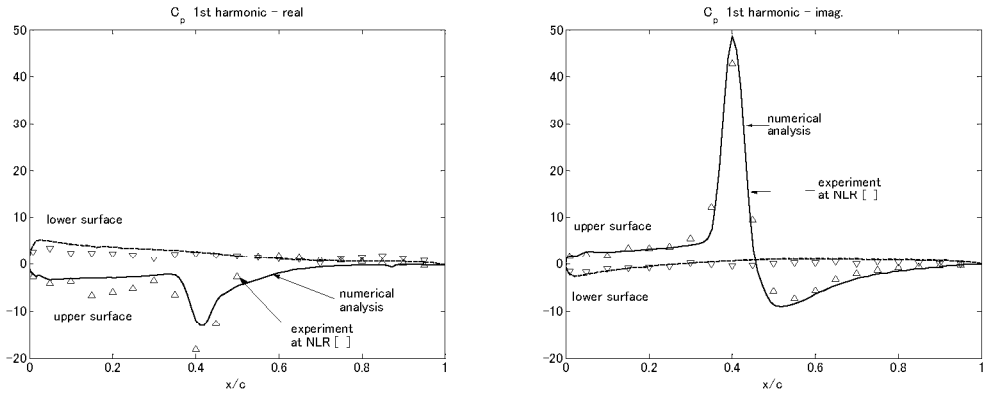

Figure 2 : Comparison of CFD with experiment; case CT-5[5]

The code is validated by comparing to the AGARD test case[5][6] of the same wing profile. The experimental data of which Mach number is 0.70 and mean angle of attack is 2.0 *deg.* has well developed shock. The numerical result shows reasonable results compared with the data (Figure 2).

2.3 Fourier series expansion of unsteady aerodynamics

To evaluate unsteady aerodynamics and analyze the stability of the aeroelastic system, numerical simulation was performed for 5 periods with heaving and/or pitching forced oscillation and Fourier coefficients were obtained from time histories of the aerodynamics. When a forced oscillation mode is $q = (q_{1,r} + iq_{1,i})e^{i\omega t}$, first harmonic component of generated unsteady aerodynamics is $f_1 = (f_{1,r} + if_{1,i})e^{i\omega t}$, where $f_{1,r}$ and $f_{1,i}$ are in and out of phase with the oscillation. Unsteady aerodynamics including 0th and higher order is expressed as followings.

$$f - f_0 + \sum_{m=1}^{\infty} (f_{m,r} + if_{m,i})e^{im\omega t} \tag{3}$$

Effect of harmonic components of unsteady aerodynamics on the system stability is considered here. When the system is in harmonic oscillation, the energy of the system given by the flow is

$$\oint_{S_H} f^T \frac{dq}{dt} dt \tag{4}$$

where f is unsteady aerodynamics and S_H is trajectory of the system. According to the Eq.(1) the energy given by flow in one period is

$$\frac{1}{\mu\pi}\int_0^{2\pi/\omega^*}(-C_l\dot{\bar{h}}^* + 2C_m\dot{\alpha}^*)dt^* \tag{5}$$

Substituting the complex Fourier series expansion

$$q = q_0 + \sum_{l=1}^{\infty}(q_l e^{il\omega t} + \bar{q}_l e^{-il\omega t}),\quad f = f_0 + \sum_{m=1}^{\infty}(f_m e^{im\omega t} + \bar{f}_m e^{-im\omega t}) \tag{6}$$

into Eq. (4), it become 0 when $m \neq l$ because of orthogonality of Fourier series expansion. Where $\bar{q}$, $\bar{f}$ are complex conjugate of q, f respectively. When the system oscillates on first harmonic trajectory, the energy of the system given by flow can be specified by the first harmonic components of the unsteady aerodynamics. Subtracting energy dissipation of structural damping from Eq. (4), we can tell whether the system in sinusoidal oscillation is getting energy or not.

When the trajectory of LCO is S_L, the system energy getting from the flow is

$$\oint_{S_L} f^T \frac{dq}{dt} - e_d \tag{7}$$

where e_d means energy dissipation by structural damping. The difference of energy flux between sinusoidal oscillation and LCO is higher order components of the trajectory of the LCO. This means, if the LCO trajectory is close to sinusoidal motion, the stability of the LCO can be specified by the first harmonic component of the aerodynamics.

Furthermore, superposing of unsteady aerodynamics is valid if its amplitude is infinitesimally small, otherwise it always has an error to the nonlinear system.

2.4 Stability analysis

The unsteady aerodynamics will be evaluated according to the amplitude of oscillation and the dependency of the system stability to the amplitude will be investigated. Unsteady aerodynamic coefficients such as C_l and C_m are calculated for various amplitude and reduced frequency of forced heaving and pitching oscillation mode. Superposing those C_l and C_m, stability analysis can be performed out by *p-k* method. The experiment[1] indicated reduced frequency at LCO was nearly 0.12, therefore unsteady aerodynamics are calculated for k=0.10, 0.12 and 0.15. For the *p-k* method, those are interpolated like linear manner. Although the amplitude ratio between heaving and pitching mode for the unsteady aerodynamics should be the same to that of the unstable mode vector, $\bar{h}/\alpha$ =1.32 was used for all cases, which was evaluated by experiment and some analysis previously done.

To exclude the superposing effect of the unsteady aerodynamics, Newton-Raphson method[3] solving Eq.(1) is used. Sinusoidal oscillation representing LCO can be expressed as $q_1 e^{i\omega t}$, where $q_1 = \begin{bmatrix} h_r + ih_i & \alpha_1 \end{bmatrix}^T$, based on the pitching oscillation. If unsteady aerodynamics is expressed as $f_1 e^{i\omega t}$, Eq. (2) become

$$\left\{\omega^2 M + i\omega C + K\right\} q_1 e^{i\omega t} = f_1 e^{i\omega t} \tag{8}$$

Unknown parameters $L = \begin{bmatrix} \omega & \mu & h_r & h_i \end{bmatrix}^T$ can be solved based on

$$R = \left\{\omega^2 M + i\omega C + K\right\} q_1 - f_1 = 0 \tag{9}$$

By Newton-Raphson method, L can be solved iteratively as

$$L^{n+1} = L^n - \left(\frac{\partial R^n}{\partial L^n}\right)^{-1} R^n \tag{10}$$

$\partial R^n / \partial L^n$ can be solved analytically because it is explicit function of L. Iteration will be continued until difference between L^{n+1} and L^n become small enough, in this case relative error become 10^{-6}. Results of *p-k* analysis was taken as initial value of L. Reference [3] indicate linear solution could bring good convergence. Based on the converged value of $h_r + ih_i$ and ω, unsteady aerodynamics should be calculated again. In this paper, this iteration was done twice and difference of flutter index between before and after iteration 1% at maximum.

Although mean value of α should be taken into account because it has important role for unsteady aerodynamics, in this paper it is fixed for the analysis to avoid complexity.

3. RESULTS

3.1 Influence of amplitude on unsteady aerodynamics

Unsteady C_l and C_m for each heaving and pitching amplitude are shown in Figure 3. Magnitude of unsteady aerodynamics is normalized by the amplitude of forced oscillation, therefore the magnitude and also phase would be constant to any amplitude if it is linear.

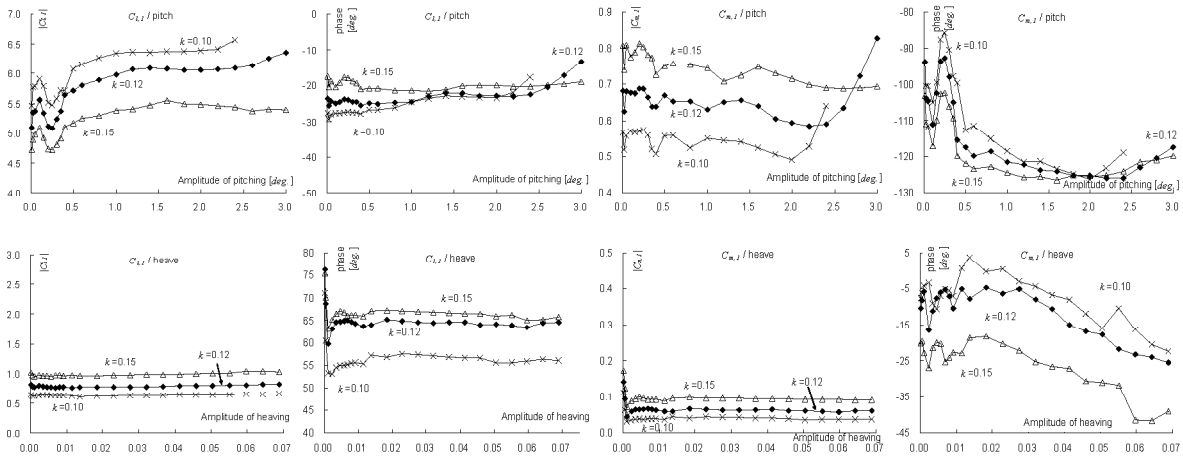

Figure 3 : Unsteady C_l and C_m for heaving and pitching mode

Figure 3 shows variation of the unsteady aerodynamics with smaller than amplitude 0.5 *deg.*, besides the large amplitude. In the calculation of pitching oscillation with k=0.10, those were not converged over amplitude 2.4*deg.*

3.2 Influence of unsteady aerodynamics variation on stability boundary caused by amplitude

Stability boundary obtained by the *p-k* analysis with superposed aerodynamics is shown in Figure 4. Flutter index F_i is $F_i = 1/\omega_\alpha^* \sqrt{\mu} = (U/b\omega_\alpha)/\sqrt{\mu}$. Variation of stability boundary can be seen like the unsteady aerodynamics. High stability region where flutter index is large appears over 2.5 *deg.* and also around 0.2 *deg.* in pitching amplitude.

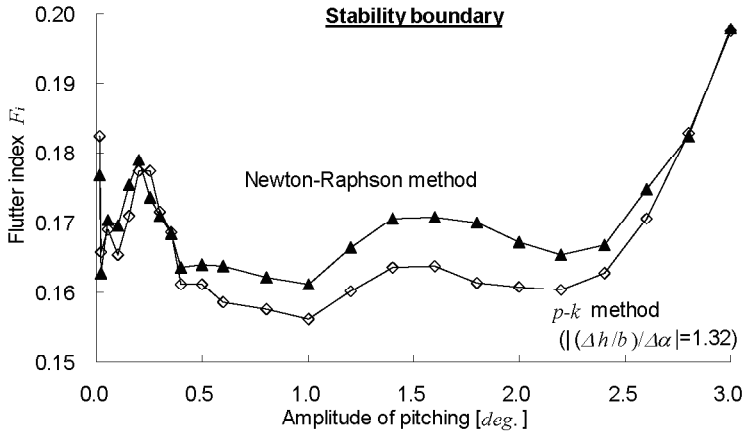

Figure 4 : Stability boundary

3.3 Evaluation of superposing unsteady aerodynamics

In transonic regime, linear stability analysis such as *U-g* method, *p-k* method, etc. can be more accurate using unsteady aerodynamics computed by transonic code. If unsteady aerodynamics is computed for each mode and those are superposed for the stability analysis, only infinitesimal small

amplitude is exact solution. Superposing effect is investigated and it is shown in Figure 5. Unsteady aerodynamics for the heaving and pitching mode which is h/α=1.32, phase lag $\angle(h\text{-}\alpha)$=10*deg.* and k=0.12. are calculated. Triangle marks are unsteady aerodynamics directly obtained by the mode and circles are obtained by superposing two unsteady aerodynamics separately computed for heaving and pitching mode. Though the difference is small in smaller amplitude than 0.5*deg.*, there is a certain difference in larger amplitude than that.

Stability boundary obtained by Newton-Raphson method is shown in Figure 4. It shows higher stability than *p-k* method between 0.5 and 2.5*deg.* of pitching amplitude. Although the difference of flutter index is 5% at maximum, the shape of the boundary looks similar.

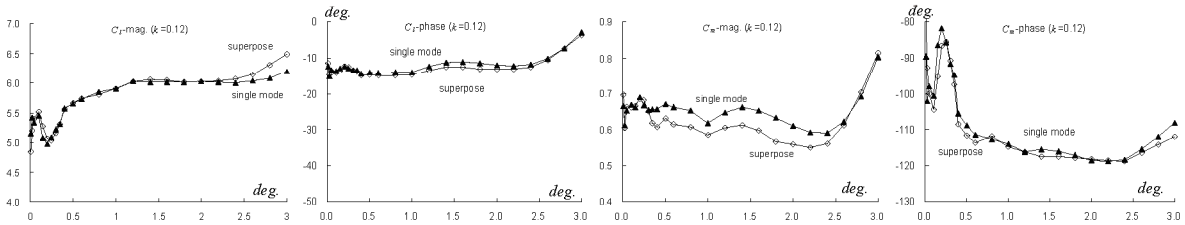

Figure 5 : Superposing effect (Unsteady C_l and C_m for pitching mode)

3.4 LCO amplitude related to the stability boundary

In Figure 4, stability boundary is shown and above the boundary the system is unstable and blow the line it is stable. Oscillation diverges with the condition above the boundary and converges below the boundary. On a part of the line where it has plus inclination, oscillations come to the point on the line at a constant F_i, which is stable equilibrium. Exchanging x and y axis, it looks familiar bifurcation diagram.

At F_i=0.175, two stable equilibria exist at pitching amplitude 0.13 and 2.6 *deg.* Simulation starting with large initial value which is velocity corresponding to the one *deg.* pitching amplitude results in the LCO with pitching amplitude 2.6 *deg.*(Figure 6 right). With smaller initial value, resulting LCO amplitude is about 0.9 *deg.* (Figure 6 left). The bifurcation diagram is confirmed by LCO simulations. Phase graph in LCO oscillation is shown in Figure 7. Higher harmonic component is

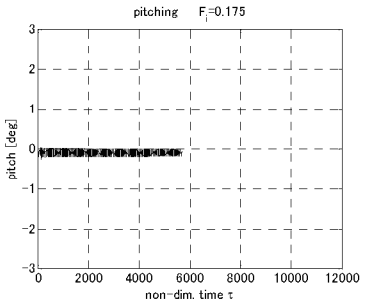

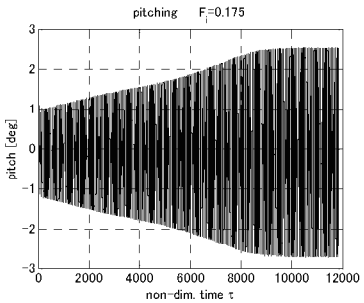

Figure 6 : LCO simulation

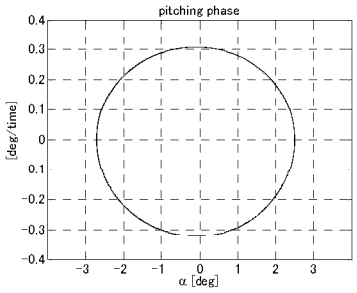

Figure 7 : Phase graph on LCO

small and taking first harmonic component of unsteady aerodynamics seems to be valid.

3.5 Considering nonlinearity in small amplitude oscillation

Variation of unsteady aerodynamics and stability boundary in small amplitude of oscillation has been observed by numerical analysis. In this section, we see what is happening in that region.

More than 2 *deg.* of pitching amplitude breaks the sinusoidal motion of the shock wave. Though shock wave propagates upstream as pitch goes up, the shock does not come back downstream and new shock appears after pitch goes down. Massive flow separation is generated and BL turbulence model may not calculate correctly.

On the other hand in less than amplitude 0.5 *deg.*, peak of the unsteady pressure distribution can be observed around $0.2c$ besides around $0.65c$. This wing profile shows that as the incidence decreases the pressure sinks at the center of the supersonic region on the upper surface, at which the peak appears in unsteady pressure distribution.

To see what is happening to the unsteady aerodynamics with small amplitude oscillation, effect of the transition point was investigated. In all of the calculations described above, transition points are automatically obtained, where turbulence viscosity coefficients μ_{tur} become 14. In this case the transition point is about 18%c. In Figure 9, unsteady pressure distributions and unsteady C_l are shown with the transition points automatically calculated, fixed at leading edge and 18%c. The peak of the unsteady pressure distribution moves upstream with the leading edge transition. Variation of the unsteady C_l becomes small with leading edge transition in small amplitude (Figure 8). So it can be said that the small amplitude LCO is affected by transition point or Reynolds number.

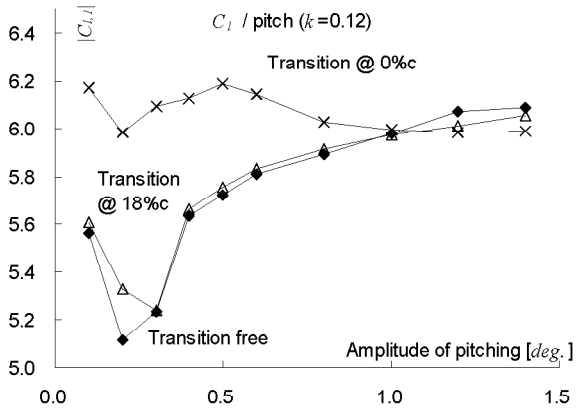

Figure 8 : Transition effect on unsteady C_l

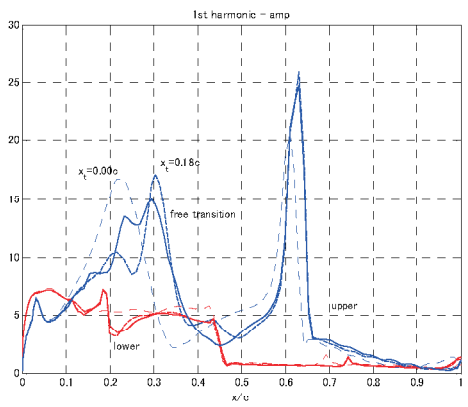

Figure 9 : Transition effect on Unsteady C_p distribution

4. CONCLUSION

NS analysis with free transition shows variation of unsteady aerodynamics in small amplitude range that is smaller than 0.5 *deg.* in pitching oscillation. This also affects stability boundary. Nonlinear phenomena such as LCO can be estimated by stability analysis with linear approximation. The *p-k* method with superposed unsteady aerodynamic coefficients can also specify the stability boundary, although it has a little error, in this case it is 5% of flutter index. Small amplitude LCO had been observed in the experiment might be the effect of transition point near the center of the supersonic region on the upper surface of the supercritical wing. If it can be confirmed by the experiment, supercritical wing with natural laminar flow might be exposed to small amplitude oscillation.

5. REFERENCES

[1] G. Schewe, A. Knipfer, H. Mai, G. Dietz, "Experimental and Numerical Investigation of Nonlinear Effects in Transonic Flutter", DLR IB 232-2002J01

[2] B. M. Castro, K. D. Jones, J. A. Ekaterinaris and M. F. Platzer, "Navier-Stokes Analysis of Wind-Tunnel Interference on Transonic Airfoil Flutter", AIAA Journal, Vol. 40, No. 7, July 2002, pp.1269-1276

[3] J. P. Thomas, E. H. Dowell and K. C. Hall, "Modeling Viscous Transonic Limit-Cycle Oscillation Behavior Using a Harmonic Balance Approach", Journal of Aircraft, Vol. 41, No. 6, Nov.-Dec., 2004, pp.1266-1274

[4] H. Kheirandish, G. Beppu and J. Nakamichi, "Numerical Flutter Simulation of a Binary System in Transonic Region", Aircraft Symposium, Hiroshima, Japan, 1995

[5] R. J. Zwaan, "DATA SET 4, NLR 7301 Supercritical Airfoil Oscillatory Pitching and Oscillationg Flap", AGARD-R-702, 1982

[6] U. R. Mueller, H. Henke, "Computation of Transonic Steady and Unsteady Flow about the NLR7301 Airfoil", Notes on Numerical Fluid Mechanics, Vol. 5x, pp.397-416, Commission of the European Communities, 1996

Lectures and Workshop International
- Recent Advances in Multidisciplinary Technology and Modeling -
May 23rd-25th, 2007

Aeroelastic Control of Composite Plate Wings based on the Optimal Placement of Sensors and Actuators

Masaki KAMEYAMA

Department of Aerospace Engineering, Tohoku University
6-6-01, Aramaki-Aza-Aoba, Aoba-ku, Sendai 980-8579, JAPAN

Abstract

The present paper treats the flutter suppression of composite plate wings with segmented piezoelectric sensors and actuators. First, fundamental mechanism of flutter suppression based on the measurement and control of specific vibration modes is examined for composite plate wings. Aeroelastic analysis of composite plates is based on the finite element method and the subsonic unsteady lifting surface theory. Polyvinylidene fluoride (PVDF) sensors are used as a modal sensor for measurement of specific modal displacements, which is constructed by optimizing the sensor gain distribution. Lead zirconate titanate (PZT) actuators are also used as actuators for flutter suppression, which generate the modal forces for specific modes with the pseudo-optimal output feedback control law based on the linear quadratic regulator (LQR) control theory. The importance of the measurement and control of the first torsional vibration mode for the flutter suppression is clarified through the numerical examples.

Next, validity of the flutter suppression based on the optimal placement of a limited number of sensors and actuators is examined for composite plate wings. Modal sensor for measurement of the modal displacement of the first torsional vibration mode is designed by the optimal placement of PVDF sensors based on the minimization criterion of observation spillover. Actuation system to generate the modal force for the first torsional vibration mode is designed by the optimal placement of PZT actuators based on the minimization criterion of control spillover. The effectiveness of optimal placement of sensors and actuators in the flutter suppression is clarified through the numerical examples.

I. Introduction

Aeroelastic characteristics have played the significant role in structural design of aircraft wing. Flutter is one of the representative dynamic phenomena of aeroelastic instability, which results in catastrophic destruction of wing structures. For the improvement of flutter property, active control technology with respect to aeroelastic response by using sensors and actuators has also been studied [1-3] since a flutter suppression system was demonstrated by using B-52E airplane in 1970s. Recently, it has been widely accepted that active aeroelastic control technology is the important one related to safety and weight reduction of aircraft structures for future research and development on aircraft in Japan [4]. On the other side, numerous research and development on the active control technology have been carried out as the fundamental one in order to realize so-called morphing aircraft in the United States, for example the Smart Wing program by Defense Advanced Research Projects Agency (DARPA) and the Active Aeroelastic Wing flight research program by the U.S. Air Force Research Laboratory (AFRL), NASA Dryden Flight Research Center (DFRC), and Boeing Phantom Works.

Studies on aeroelastic control technology have been carried out by adopting several kinds of structural, aerodynamic and control models, although, they can be classified into two groups by sort of sensors and actuators to be used for measurement and control; aeroelastic control with control surfaces and with smart materials. Smart structures that control their aeroelastic response by using built-in sensors and actuators have drawn attention of many researchers [5,6]. Especially, a lot of research on the application of piezoelectric materials [7] to flutter control has been carried out, since piezoelectric materials are effective on active control in

high frequency region from the viewpoint of quick response. It should be noted that the present study has focused on piezoelectric materials as smart materials for a control device, not shape memory materials from the same point of view mentioned above.

The unsettled problems of current research in these fields can be classified in accordance with the following aspects: it is indicated that feedback control based on the measurement and control of torsional vibration is effective on flutter suppression of two-dimensional airfoil with trailing-edge control surface through the previous numerical investigations on fundamental mechanism of flutter suppression. To the authors' best knowledge, however, all of the previous studies have not yet investigated the effects of feedback control with respect to specific vibration modes on flutter suppression of three-dimensional wings, like a plate wing, in detail. On the other side, various kinds of more sophisticated robust control rules have been mainly adopted for the flutter suppression of three-dimensional lifting surface, like a plate wing, and the validity of the proposed control methods has been examined through the numerical and experimental results. However, design methods of measurement and control system for flutter suppression considering the importance of the feedback control with respect to specific vibration modes have not yet been examined.

The present paper treats the flutter suppression of composite plate wings with segmented piezoelectric sensors and actuators. First, fundamental mechanism of flutter suppression based on the measurement and control of specific vibration modes is examined for unswept composite plate wings. Aeroelastic analysis of composite plates is based on the finite element method and the subsonic unsteady lifting surface theory. Piezoelectric sensors are used as a modal sensor for measurement of specific modal displacements, which is constructed by optimizing the sensor gain distribution. Piezoelectric actuators are also used as actuators for flutter suppression, which generate the modal forces for specific modes with the pseudo-optimal output feedback control law based on the LQR control theory. The importance of the measurement and control of the first torsional vibration mode for the flutter suppression is clarified through the numerical examples.

Next, validity of the flutter suppression based on the optimal placement of a limited number of piezoelectric sensors and actuators is examined for unswept composite plate wings. Modal sensor for measurement of the modal displacement of the first torsional vibration mode is designed by the optimal placement of piezoelectric sensors based on the minimization criterion of observation spillover. Actuation system to generate the modal force for the first torsional vibration mode is designed by the optimal placement of piezoelectric actuators based on the minimization criterion of control spillover. The effectiveness of optimal placement of sensors and actuators in the flutter suppression is clarified through the numerical examples.

II. Fundamental Equations

A. Aeroelastic Response of Composite Plate Wings with Segmented Piezoelectric Sensors and Actuators

The finite element equations for aeroelastic response of cantilevered laminated plates with piezoelectric patches can be described as follows:

$$\begin{aligned} &[M]\{\ddot{w}\}+[K]\{w\}=q[Q]\{w\}-[A]\{\phi_A\}, \\ &\{\phi_S\}=-[S]\{w\}, \end{aligned} \tag{1}$$

where the mass matrix is denoted by M, the displacement vector is denoted by w and the dynamic pressure is denoted by q. The aerodynamic influence matrix is denoted by Q. In this paper, the aerodynamic influence matrix Q, which represents the unsteady aerodynamic forces acting on the vibratory wing surface in subsonic flow, is evaluated based on the doublet-point method [8]. Besides, the matrices K, A and S can be described as follows:

$$\begin{aligned} &[K]=[K_{ww}]-[K_{w\phi}][K_{\phi\phi}]^{-1}[K_{\phi w}], \\ &[A]=[K_{w\phi}],\ [S]=[K_{\phi\phi}]^{-1}[K_{\phi w}], \end{aligned} \tag{2}$$

where the elastic stiffness matrix is denoted by K_{ww}, the mechanical-electric coupling stiffness matrices are denoted by $K_{w\phi}$ and $K_{\phi w}$, and the piezoelectric stiffness matrix is denoted by $K_{\phi\phi}$. The matrix A plays a role of computing actuator control force from the applied voltages ϕ_A to actuators, and the matrix S plays a role of computing electrical potentials ϕ_S on sensors from the displacements w.

It is necessary to transform the equations of motions into the state-space form for the aeroservoelastic analysis, and the unsteady aerodynamic forces should be approximated in terms of rational functions of Laplace variable. In this paper, the minimum state method [9] combined with optimization techniques is adopted for the rational function approximation. The minimum state method approximates the aerodynamic influence matrix by

$$\left[\tilde{Q}(\bar{s})\right]=[Q_0]+[Q_1]\bar{s}+[Q_2]\bar{s}^2+[D](\bar{s}[I]-[R])^{-1}[E]\bar{s}, \tag{3}$$

where the non-dimensional Laplace variables (=sb/V) is denoted by s, semi-chord length at the wing root, free stream velocity and the Laplace variable are denoted by b, V and s, respectively. The unknown coefficient matrices are denoted by Q_0, Q_1, Q_2, D, R and E. Physically, Q_0, Q_1 and Q_2 capture the dependence of the unsteady aerodynamics on displacement, velocity and acceleration, respectively. The last term in the right-hand side of Eq. (3) captures the lag in the construction of aerodynamic forces associated with the circulatory effects. As an optimizer, the DFP (Davidon-Fletcher-Powell) variable metric method is adopted with the golden section method in the ADS (Automated Design Synthesis) program [10].

When a modal approach is introduced, the following state-space equations that include the effects of piezoelectric control forces can be obtained from Eqs. (1)-(3):

$$\begin{aligned} \{\dot{x}\} &= [A_S]\{x\} + [B_S]\{\phi_A\}, \\ \{x\} &= \left\{ \{w_m\}^T \quad \{\dot{w}_m\}^T \quad \{p\}^T \right\}^T, \end{aligned} \tag{4}$$

where the system matrix is denoted by A_S and the input matrix is denoted by B_S, which depends on the location of piezoelectric actuators. The state vector is denoted by x, which consists of the modal displacements w_m, the modal velocities and the augmented aerodynamic states p.

B. Optimal Placement of Sensors and Actuators for Measurement and Control of Torsional Vibration

Flutter suppression of composite plate wings based on the measurement and control of torsional vibration with a limited number of sensors and actuators is examined in this research. Here, the measurement and control systems have been constructed by the optimal placement of sensors and actuators based on the minimization criteria of observation and control spillovers for the highly precise measurement and control of torsional vibration.

a) Design of modal transducer based on the optimal placement of sensors and the optimization of sensor gain distribution [11] In this paper, piezoelectric sensors are used as a modal transducer for identifying specific modes in measurement of dynamic aeroelastic response of cantilevered laminated plates. Total output voltage of all sensors Φ_S can be obtained as a sum of each sensor output voltage $\phi_{s,i}$ multiplied by the corresponding sensor gain g_i as follows:

$$\Phi_S(t) = \sum_{i=1}^{ns} \phi_{s,i}(t) g_i = \{\phi_s\}^T \{g\} = -\{w_m(t)\}^T [\Phi]^T [S]^T \{g\}, \tag{5}$$

where the modal matrix is denoted by Φ. Optimization of the sensor gain distribution g_{1T} to construct a modal transducer that estimates the modal displacement of the first torsional mode from electrical potentials on each sensor under a given sensor location can be represented in the following constrained optimization problem [11]:

$$\begin{aligned} &\text{maximize} \quad -\{\phi_{1T}\}^T [S]^T \{g_{1T}\}, \\ &\text{subject to} \quad [\Phi_{1T}]^T [S]^T \{g_{1T}\} = 0, \quad \{g_{1T}\}^T \{g_{1T}\} = 1, \end{aligned} \tag{6}$$

where the modal vector of the first torsional vibration mode is denoted by ϕ_{1T} and the modal matrix which consists of eigenvectors except those of the higher residual modes and that of the first torsional mode ϕ_{1T} is denoted by Φ_{1T}. The optimal sensor gain distribution can be obtained as the eigenvector corresponds to the maximal eigenvalue of the eigenvalue problem, which is equivalent to the optimization problem stated as above. In addition, a modal transducer for the first torsional vibration mode is constructed by the optimal placement of sensors based on the minimization criterion of observation spillover [12]. The optimization problem minimizing the observation spillover can be stated as follows:

$$\text{minimize} \ \lambda_{\max}\left(\{s_{sp}\}\{s_{sp}\}^T \right), \tag{7}$$

where $\lambda_{\max}$ is the maximal eigenvalue of the matrix and s_{sp} represents the relation between the higher residual modes and the observation spillover. From Eq. (7), the sensor locations minimizing the maximal eigenvalue of $\{s_{sp}\}\{s_{sp}\}^T$ become the optimal sensor locations, and then the specific modal displacement $w'_{m,1T}$ is estimated from the output of the sensors optimally placed as follows:

$$w'_{m,1T}(t) = -\frac{\Phi_s(t)}{\{\phi_{1T}\}^T [S]^T \{g_{1T}\}}. \tag{8}$$

b) Optimal placement of actuators for control of torsional vibration [12] In this paper, the LQR with output feedback is applied for a design of flutter suppression system of cantilevered laminated plates with segmented piezoelectric sensors and actuators.

The quadratic performance index is formulated based on the LQR control theory as follows:

$$J = \int_0^\infty \left(\{x\}^T [R_1] \{x\} + \{\phi_A\}^T [R_2] \{\phi_A\} \right) dt \tag{9}$$

where R_1=diag[Ω,I,I] and R_2=rI are the symmetric weighting matrices on states and control inputs, respectively. The matrix with free-vibration eigenvalues on the diagonal is denoted by Ω. The state feedback gain matrix minimizing the quadratic performance index described as Eq. (9) can be obtained by solving the algebraic Riccati equations [13]. An actuation system in order to control the first torsional vibration mode is constructed by the optimal placement of actuators based on the minimization criterion of control spillover [12]. The optimization problem minimizing the control spillover can be stated as follows:

$$\text{minimize } \lambda_{\max}\left([A_{sp}]^T [A_{sp}] \right), \tag{10}$$

where A_{sp} represents the relation between the higher residual modes and the control spillover. From Eq. (10), the actuator locations minimizing the maximal eigenvalue of $[A_{sp}]^T[A_{sp}]$ become the optimal actuator locations.

In the case of that all of the aerodynamic states p and all of the rest modal displacements/velocities except those of the first torsional vibration mode are excluded from the states for feedback purpose, the applied voltages to piezoelectric actuators are determined by the pseudo-optimal output feedback gain matrix K_{FO} obtained based on the minimum norm method [14] as follows:

$$\begin{aligned} \{\phi_A\} &= -[K_{FO}]\{y\} = -[\bar{K}_F][C_s]^T \left([C_s][C_s]^T \right)^{-1} \{y\}, \\ \{y\} &= [C_s]\{x\}, \end{aligned} \tag{11}$$

where the modified state feedback gain matrix to generate control force applied to only the first torsional mode is denoted by $\bar{K}_F$ and the output vector and the output matrix are denoted by y and C_S, respectively.

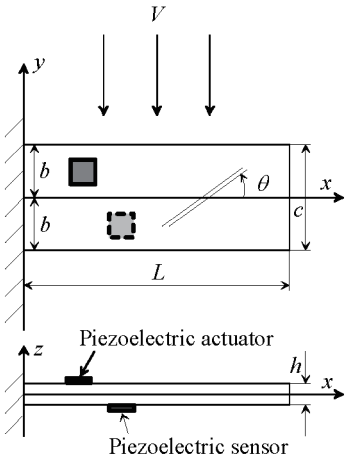

Figure 1 Cantilevered laminated plates (L=305mm,c=2b=76.2mm,h=0.804mm)

III. Numerical Results and Discussions

A. Numerical Model

In this paper, a cantilevered laminated plate $[0_2/90]_s$ with piezoelectric patches shown in Fig. 1 is employed. PVDF sensors and PZT actuators are placed on the bottom and top surfaces of the plate. The material properties of lamina of graphite/epoxy composite, PZT and PVDF patches are shown in Tables 1-3. Here, the in-plane stiffness and piezoelectric characteristics of piezoelectric materials are assumed to be isotropic in this research. The 12x6 and 8x6 elements are used for the structural and aerodynamic analyses, respectively, and the sizes of sensors and actuators are same as that of a finite element in the structural analysis. The eight-node rectangular isoparametric element is employed in the present structural analysis based on Mindlin plate theory. After the vibration analysis, a modal reduction is performed using the lowest eight modes to solve Eq. (1), as shown in Eq. (4), and then the Runge-Kutta method of the fourth order is adopted to integrate the state-space equations described as Eq. (4).

To validate the present aeroelastic analysis, the flutter velocity of cantilevered laminated plates without piezoelectric patches is compared with the reported results [15] in Table 4. This table shows that the present results agree well with the reported experimental results and computational results obtained by the frequency-domain analysis. These

Table 1 Material properties of CFRP

E_{11} [GPa]	E_{22} [GPa]	G_{12}=G_{13}=G_{23} [GPa]	ν_{12}	ρ [kg/m^3]
98.0	7.90	5.60	0.28	1520

Table 2 Material properties of PZT

d_{31}=d_{32} [pm/V]	ε_{33} [nF/m]	E_{11}=E_{22} [GPa]	ν_{12}	ρ [kg/m^3]	Thickness [mm]
254	15.0	63.0	0.30	7600	1.0

Table 3 Material properties of PVDF

d_{31}=d_{32} [pm/V]	ε_{33} [nF/m]	E_{11}=E_{22} [GPa]	ν_{12}	ρ [kg/m^3]	Thickness [mm]
22.0	0.1062	2.00	0.29	1800	0.1

Table 4 Comparison of flutter velocities

Laminate configurations	Flutter velocity [m/s]		
	Present	Ref. [15] Exp.	Ref. [15] Comp.
$[0_2/90]_s$	22.9	25	21.0
$[+45_2/0]_s$	27.6	28	27.8
$[+30_2/0]_s$	27.1	27	27.8

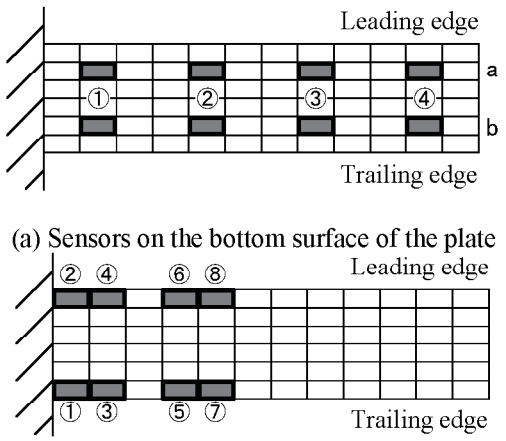

(a) Sensors on the bottom surface of the plate

(b) Actuators on the top surface of the plate

Figure 2 Locations of sensors/actuators

Table 5 Natural frequencies and flutter velocity for $[0_2/90]_s$ laminate (Fig. 2)

Natural frequencies [Hz]					Flutter velocity
First	Second	Third	Fourth	Fifth	[m/s]
14.9	52.4	71.4	124.7	194.0	31.1

results indicate that the present analysis can produce accurate results.

B. Critical Measured and Controlled Modes for Flutter Suppression

At first, critical measured and controlled modes for flutter suppression of a $[0_2/90]_s$ cantilevered laminated plate is examined. The eight sensors and the eight actuators are placed on the bottom and top surfaces of the plate, respectively, as shown in Fig. 2. The natural frequencies of the lowest five modes and the open-loop flutter velocity of a $[0_2/90]_s$ cantilevered laminated plate with sensors and actuators are shown in Table 5. As compared with Table 4, it can be found that the flutter velocity increases due to the mass and stiffness properties of piezoelectric actuators. For an active control design, the design velocity is set to be 34.2m/s and the value of the weighting coefficient r in Eq. (9) is set to be 10^1.

Flutter suppression based on the feedback control on the specific mode, which needs to be controlled among controlled modes and is named as critical controlled mode, and that, which needs to be measured among measured modes and is named as critical measured mode, is examined. Figure 3 shows the results of flutter control based on the second vibration mode, which corresponds to the first torsional vibration mode, at the design velocity. Here, the vibration of the plate is induced by sudden release of 0.1mm initial deflection of the center of the wing tip and the control is started after a lapse of 0.3s in this case. From this figure, it can be found that the divergent vibration can be suppressed by pseudo-optimal output feedback control based on the measurement and control of the first torsional vibration mode. On the contrary, Fig. 4 shows the results of flutter control based on the first or the third vibration modes, which correspond to the lower

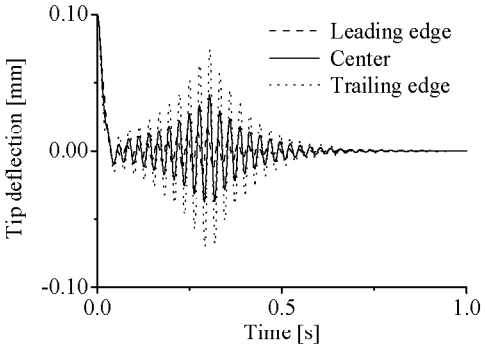

Figure 3 Result of control based on the 1T mode

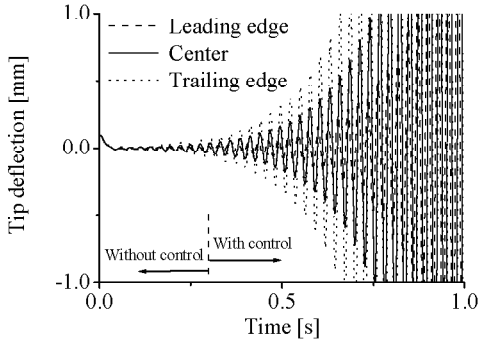

(a) Based on the 1B mode

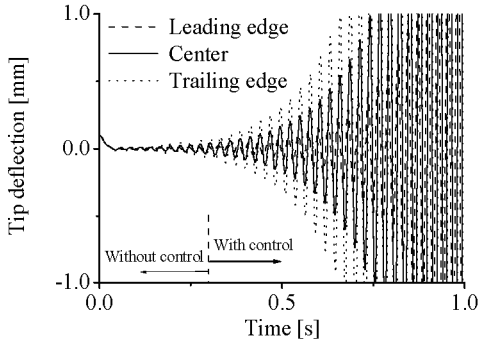

(b) Based on the 2B mode

Figure 4 Results of control

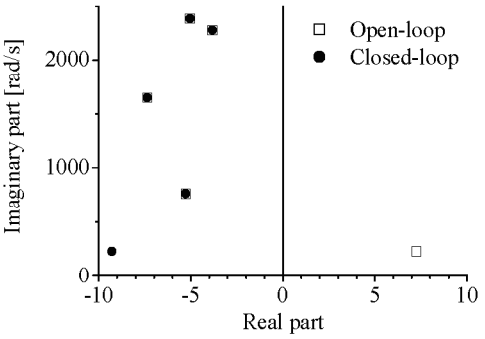

Figure 5 Comparison of open- and closed-loop eigenvalues at design velocity

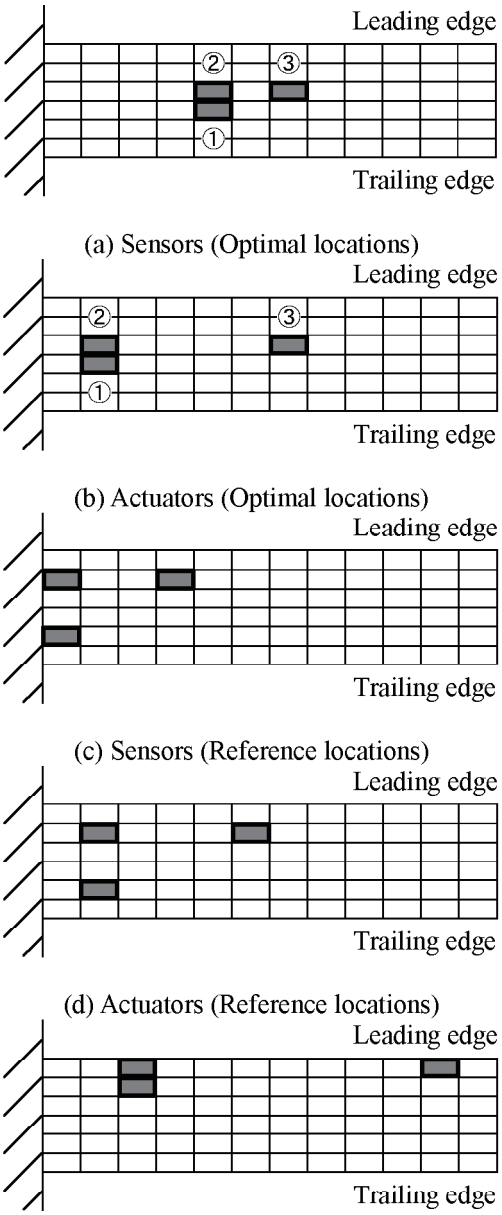

(a) Sensors (Optimal locations)

(b) Actuators (Optimal locations)

(c) Sensors (Reference locations)

(d) Actuators (Reference locations)

(e) Sensors (Optimum for reference locations of actuators)

Figure 6 Locations of sensors/actuators

Table 6 Natural frequencies and flutter velocity for $[0_2/90]_s$ laminate (Fig. 6(a) and 6(b))

Natural frequencies [Hz]					Flutter velocity
First	Second	Third	Fourth	Fifth	[m/s]
11.6	45.9	67.6	144.4	185.1	27.7

Table 7 Optimal values of sensor gain

①	②	③
0.7040	-0.6862	0.1829

bending vibration modes, at the design velocity. From this figure, it is also found that the divergent vibration cannot be suppressed by pseudo-optimal output feedback control based on the measurement and control of the bending vibration mode.

Figure 5 shows the changes in eigenvalues for the open-loop system and the closed-loop system by using feedback control based on the second vibration mode at the design velocity. From this figure, it is found that the present controller makes the open-loop system stable by moving unstable eigenvalue to stable region parallel to real axis, meanwhile the stable eigenvalues in the open-loop system keep their positions. The present controller, that is to say, has no effect on the increase of the fictitious torsional stiffness of plate, but has an effect on the increase of the damping of the first torsional mode of plate. This is also confirmed from the results that a divergent vibration can be similarly suppressed by using the present controller whether the modal displacement of the second vibration mode is included in the feedback variables or not.

These results show that the measurement and control of the torsional vibration mode is essential for flutter suppression of composite plate wings, and a feedback control based on the first torsional vibration mode can suppress the divergent vibration efficiently when using a single vibration mode feedback control scheme.

C. Flutter Suppression based on the Optimal Placement of Sensors and Actuators

In the next examples, a stable flutter suppression methodology of composite plate wings by using a limited number of sensors and actuators is studied. For the highly precise measurement and control of the torsional vibration mode, optimal location of piezoelectric sensors and actuators is searched by the minimization criteria of observation and control spillovers. Here, the optimal locations of sensors and actuators should be determined based on the simultaneous optimal placement, since the stiffness and mass properties of piezoelectric sensors/actuators are considered in the present structural analysis. However, the influence of the sensor locations on the vibration characteristics of composite plate wings can be neglected due to lightweight and high-flexibility of sensor chosen in numerical examples. Therefore, the optimal locations of sensors and actuators are determined successively in this paper.

When three sensors and three actuators are used, the optimal sensor and actuator locations obtained from the criteria in Eqs. (7) and (10) are shown in Fig. 6, respectively. The optimal locations can be determined by a round-robin calculation for all possible combinations of sensor and actuator locations in this paper. It is noted that Fig. 6(c) and 6(d) show a set of different sensor locations and that of different actuator locations, which are chosen arbitrarily and named as reference location. It is also noted that Fig. 6(e) shows the optimal sensor locations obtained from the criterion in Eq. (7) under the reference actuator locations shown in Fig. 6(d). Table 6 shows the natural frequencies and the open-loop flutter velocity for the

cantilevered laminate with sensors and actuators optimally placed as shown in Fig. 6(a) and 6(b). In addition, Table 7 shows the optimal values of the sensor gain for the second mode, which corresponds to the first torsional vibration mode. It should be noted that the fourth ~ eighth modes and the fourth ~ sixth modes are the residual modes in terms of observation and control spillovers in Eqs. (7) and (10), respectively. As for the modal transducer, an Infinite Impulse Response (IIR) low-pass filter of inverse-Chebyshev type with the cut-off frequency of 68Hz, which lies between the third and the fourth natural frequencies, is added in order to stabilize the flutter suppression in the present numerical examples. Here, a modal velocity can be estimated by a finite difference approximation for the values of the estimated modal displacements. For the active control design, the design velocity is set to be 30.5m/s, and the value of the weighting coefficient r in Eq. (9) is set to be 10^1.

Figure 7 shows the results of control at the design velocity. This figure shows the effect of the locations of sensors on the flutter suppression. Figures 7(a) and 7(b) correspond to the deflection of the plate tip controlled by actuators placed on the optimal location as shown in Fig. 6(b) based on the estimated modal displacement by optimal modal transducer and by sensors placed on reference locations as shown in Fig. 6(c), respectively. Besides, Fig. 7(c) shows the control voltages applied to the piezoelectric actuators, which corresponds to Fig. 7(a). In this paper, the vibration of the plate is induced by sudden release of 0.1mm initial deflection of the center of the wing tip and the control is started after a lapse of 0.3s in this case. From this figure, it is found that the optimal modal transducer can suppress the divergent vibration efficiently. On the contrary, it is also found that the vibration diverges quickly due to observation spillover caused by the reference modal transducer. Figure 8 shows the comparison of the power spectrums of the modal velocity of the first torsional vibration mode estimated by the optimal and reference modal transducers. Here, the free stream velocity is the same as the flutter velocity and a low-pass filter is also added. The vibration of the plate is induced by sudden release of 0.1mm initial deflection of the center of the wing tip. From this figure, it can be found that the amplitudes in the fourth ~ sixth vibration modes show remarkable reduction although those in the seventh ~ eighth modes show some increases due to the optimal sensor placement. On one side, the optimal sensor gain distribution plays a role as a kind of modal band-pass filter that passes the first torsional vibration mode in the lowest three vibration modes. On the other side, the optimally located sensors play a role as a kind of modal low-pass filter that passes the lowest three modes, that is to say, the performance of this low-pass filter depends heavily on the sensor location. Since a highly-accurate modal measurement of the

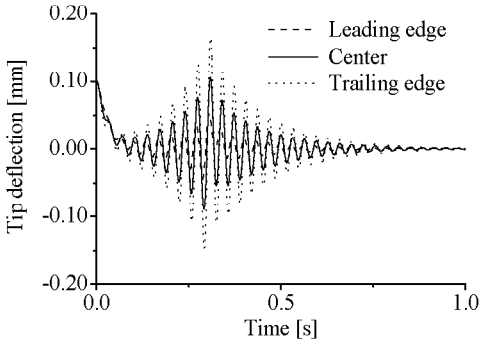

(a) Time histories of tip deflections (Optimal locations of sensors)

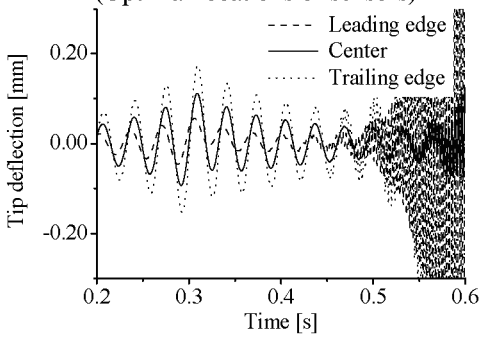

(b) Time histories of tip deflections (Reference locations of sensors)

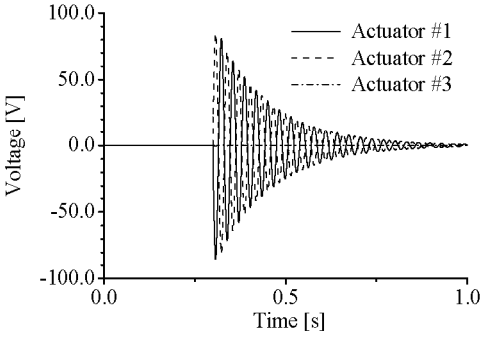

(c) Time histories of control voltages (Optimal locations of sensors)

Figure 7 Results of control

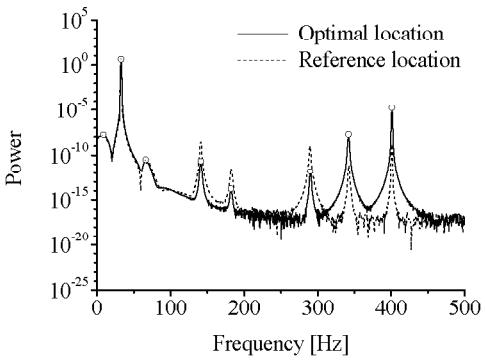

Figure 8 Effect of location of sensors on power spectrum of the modal velocity of 1T mode (V=27.7m/s, with filtering)

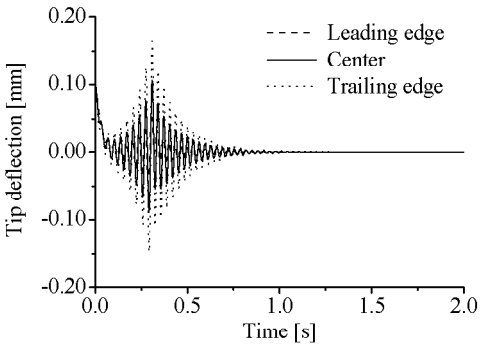

(a) Time histories of tip deflections (Optimal locations of actuators)

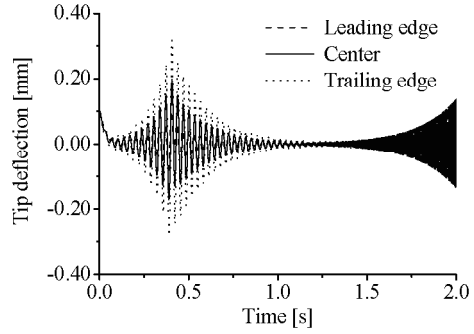

(b) Time histories of tip deflections (Reference locations of actuators)

Figure 9 Results of control

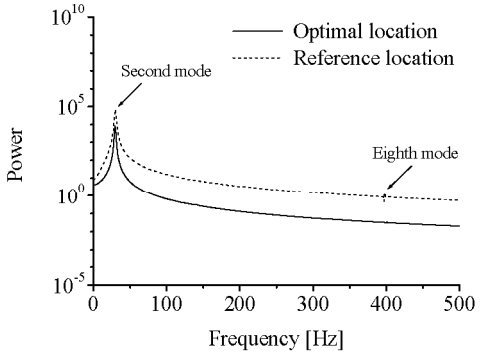

Figure 10 Effect of location of actuator on power spectrum of the modal control force of 1T mode (V=30.5m/s)

modal displacement of the first torsional vibration mode can be realized by a pair of these filter-like elements, it is clarified that the optimal placement of sensors is indispensable to the flutter suppression based on the estimated modal displacement for suppressing observation spillover.

Figure 9 shows the results of control at the design velocity. This figure shows the effect of the locations of actuators on the flutter suppression. Figures 9(a) and 9(b) correspond to the deflection of the plate tip controlled by actuators placed on the optimal location and on the reference locations as shown in Fig. 6(d), respectively, based on the estimated modal displacement by optimal modal transducer. In this case, the vibration of the plate is induced by sudden release of 0.1mm initial deflection of the center of the wing tip and the control is started after a lapse of 0.4s. From this figure, it is found that the vibration converges by control in both cases. The actuators placed on the reference locations, however, cause divergent vibration again due to control spillover after a lapse of about 1.0s. Figure 10 shows the comparison of the power spectrums of the modal control force applied to the first torsional vibration mode in the cases of the optimal and reference actuator locations. Here, the free stream velocity is the same as the design velocity and the exact modal displacement and modal velocity of the first torsional mode calculated by the finite element analysis are used for feedback purpose. From this figure, it can be found that the amplitude in the eighth vibration mode shows considerable reduction due to a highly-accurate modal control for the controlled modes based on the optimal actuator placement. On one side, the output feedback gains play a role as a kind of modal band-pass filter that passes the first torsional vibration mode in the lowest three vibration modes. On the other side, the optimally located actuators play a role as a kind of modal low-pass filter that passes the lowest three modes, that is to say, the performance of this low-pass filter depends heavily on the actuator location, same as modal transducer design. Since a highly-accurate modal control for the first torsional vibration mode can be realized by a pair of these filter-like elements, it is clarified that optimal placement of actuators is indispensable to the flutter suppression based on the estimated modal displacement for suppressing control spillover.

Figure 11 shows the time histories of the deflection of the plate tip controlled by actuators placed on the reference locations as shown in Fig. 6(d) based on the estimated modal displacement by sensors placed on the optimal locations as shown in Fig. 6(e). From this figure, it is indicated that the divergent vibration does not occur immediately after control starts, like that shown in Fig. 9(a). Figures 12 and 13 show the time histories of the measured modal displacement of the second vibration mode and those of the modal control force applied to the fourth vibration mode, respectively. In Fig. 12, it is found that the higher residual modes have an effect on the modal displacement of the second vibration mode after a lapse of about 1.6s in the case of the reference actuator locations. In Fig. 13, it is also found that the higher residual modes affect the modal control force applied to the fourth vibration mode after a lapse of about 1.6s in the case of the reference actuator locations, and makes it diverge gradually, unlike the case of the optimal locations. Therefore, it is clarified again that optimal placement of actuators is indispensable to the flutter suppression based on the estimated modal displacement for suppressing control spillover.

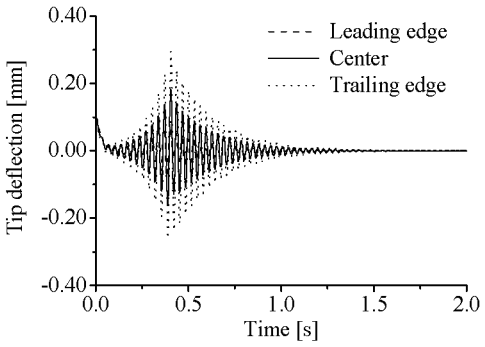

Figure 11 Result of control
(Reference locations of actuators)

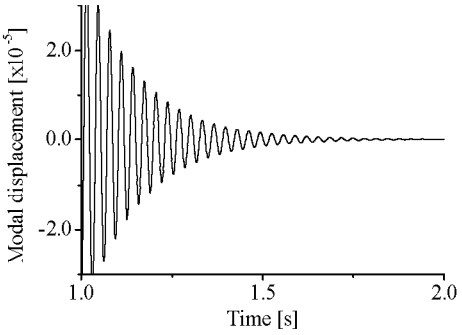

(a) Optimal locations of actuators

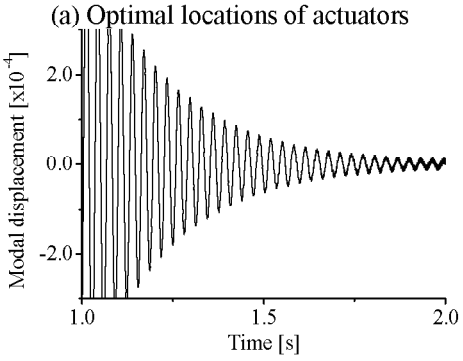

(b) Reference locations of actuators

Figure 12 Time histories of modal displacement of the second vibration mode

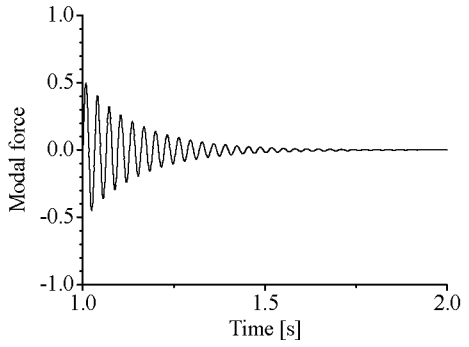

(a) Optimal locations of actuators

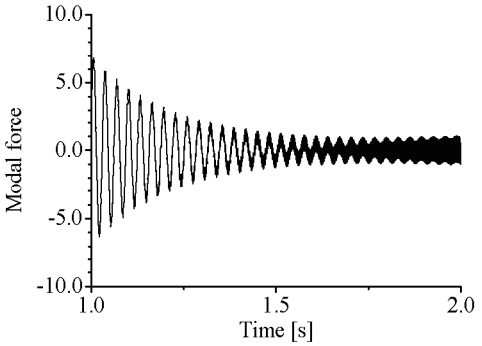

(b) Reference locations of actuators

Figure 13 Time histories of modal control force of the fourth vibration mode

These results show the importance of the locations of sensors and actuators for flutter suppression and that the present method can realize the flutter suppression based on the measurement and control of the first torsional vibration mode by using a limited number of segmented piezoelectric sensors and actuators.

IV. Conclusions

Flutter suppression methodology of cantilevered laminated plates with segmented piezoelectric sensors and actuators has been studied in this paper. Modal transducer for measurement of the modal displacement of the first torsional vibration mode is designed by the optimal placement of PVDF sensors based on the minimization criterion of observation spillover. Actuation system to generate the modal force for the first torsional vibration mode is designed by the optimal placement of PZT actuators based on the minimization criterion of control spillover. It is clarified from the numerical results that flutter suppression of composite plate wings based on the measurement/control of the first torsional vibration mode becomes possible by optimal placement of a limited number of sensors and actuators. In addition, the experimental verification should be needed in the future work.

Acknowledgement

The author would like to thank Dr. Hisao Fukunaga for a valuable discussion.

References

[1] Livne E. Future of airplace aeroelasticity. Journal of Aircraft 2003; 40(6): 1066-1092.

[2] Mukhopadhyay V. Historical perspective on analysis and control of aeroelastic responses. Journal of Guidance, Control, and Dynamics 2003; 26(5): 673-684.

[3] Horikawa H, Dowell EH. An elementary explanation of the flutter mechanism with active feedback controls. Journal of Aircraft 1979; 16(4): 225-232.

[4] Nakamichi J, Yamamoto K, Nakamura T, Ishikawa K, Enomoto S. Research activities in JAXA. Aeronautical and Space Sciences Japan 2006; 54(624): 17-19 (in Japanese).

[5] Giurgiutiu V. Review of smart-materials actuation solutions for aeroelastic and vibration control. Journal of Intelligent Material Systems and Structures 2000: 11(7); 525-544.

[6] Lazarus KB, Crawley EF, Lin CY. Fundamental mechanisms of aeroelastic control with control surface and strain actuation. Journal of Guidance, Control, and Dynamics 1995; 18(1): 10-17.

[7] Crawley EF, de Luis J. Use of piezoelectric actuators as elements of intelligent structures. AIAA Journal 1987; 25(10): 1373-1385.

[8] Ueda T, Dowell EH. A new solution method for lifting surfaces in subsonic flow. AIAA Journal 1982; 20(3): 348-355.

[9] Karpel M. Time-domain aeroservoelastic modeling using weighted unsteady aerodynamic forces. Journal of Guidance, Control, and Dynamics 1990; 13(1): 30-37.

[10] Vanderplaats GN, Sugimoto H. A general-purpose optimization program for engineering design. Computers and Structures 1986; 24(1): 13-21.

[11] Kim J, Hwang JS, Kim SJ. Design of modal transducers by optimizing spatial distribution of discrete gain weights. AIAA Journal 2001; 39(10): 1969-1976.

[12] Sun D, Tong L, Wang D. Vibration control of plates using discretely distributed piezoelectric quasi-modal actuators/sensors. AIAA Journal 2001; 39(9): 1766-1772.

[13] Potter JE. Matrix quadratic solution. SIAM Journal on Applied Mathematics 1966; 14(3), 496-501.

[14] Kosut RL. Suboptimal control of linear time-invariant systems subjected to control structure constraints. IEEE Transactions on Automatic Control 1970; AC15(5): 557-563.

[15] Hollowell SJ, Dugundji J. Aeroelastic flutter and divergence of stiffness coupled, graphite/epoxy cantilevered plates. Journal of Aircraft 1984; 21(1): 69-76.

Dynamic Structural Response Analysis of Flexible Rolled-Up Solar Array Subjected to Deformation-Dependent Thermal Loading

Masahiko Murozono
Kyushu University, Fukuoka 819-0395, Japan

Key Words : Thermoelasticity, Solar array, Dynamic response, Radiant heating, Self-excited vibration

Abstract

Theoretical studies in the thermally induced dynamic structural response of an asymmetric rolled-up solar array and its stability are presented. Structural response analysis of the solar array subjected to deformation-dependent thermal loading was conducted considering with the thermoelastic coupling effect. The governing equations and the time dependent boundary conditions are formulated assuming that the solar array is heated by the unidirectional radiation and that net heat input depends on the angle of incidence of radiation with respect to the array axis. Quasi-static responses of the solar array induced by external radiant heating were calculated, and it was shown that the difference of several percent arose in the steady-state value of the tip deflection between the case of coupled analysis and the case of uncoupled analysis. Dynamic responses of the solar array induced by sudden radiation heating for a typical night-day orbital transition were determined and the stability of the system was discussed. Variations of the dynamic response are examined. The response becomes either a self-excited vibration or a damped vibration with the system parameters such as radiation incident angle. Unstable boundary curves, which divide the parameter plane into regions of stability and instability according to the direction of radiation and system damping ratio, are also presented.

1. Introduction

The problem of structural vibration due to thermal effects was introduced by Boley[1)], who has taken structural inertia effects into account but no notice of influences of deformations upon temperature distributions. A number of review articles[2),3)] about thermally induced vibrations in aerospace applications have appeared.

A series of research has been done starting with the failure of the Hubble Space Telescope solar array with a kink about midway along its length. Thornton and Kim[4)] describe an analysis of the thermally induced bending vibrations of a symmetric flexible rolled-up solar array model. Uncoupled and coupled thermal-structural dynamics responses were studied using an analytical model restricted to symmetric bending deformations of the solar array. Chung and Thornton[5)] focused on a torsional analysis of a symmetric FRUSA model. A torsional buckling analysis was conducted using an analytical model restricted to antisymmetric torsional deformations of the solar array. However, an HST solar array is not exactly symmetric about its centerline; its solar blanket is shifted slightly toward the outer BiSTEM. Even though the solar array was heated by uniform radiation, coupled bending-torsional deformations occur because of the asymmetry. Murozono and Thornton[6)] presented an theoretical analyses of the buckling characteristics and the quasistatic thermal-structural responses of an asymmetric FRUSA model. One of the results of the analyses considering the geometric asymmetry suggested that thermally induced quasistatic torsional deformation may have caused the failure of the HST solar array BiSTEM. Dynamic thermal-structural responses of the same asymmetric solar array model were also studied by the authors. Although the analyses showed quasistatic and dynamic thermally induced structural responses, the analyses did not consider the coupling of temperature fields and deformations.

Thermally induced bending vibrations of thin-walled boom subjected to external radiant heating have been investigated[7),8)] considering the deformation-dependent thermal loading and the thermal-structural coupling effects. A theoretical analysis was carried out, in which the boom was modeled as an uniform thin-walled circular section cantilever beam or the same beam with a concentrated tip mass at the free end, and experimental verifications of the analysis executed under laboratory conditions both in air and in a vacuum chamber. The experiment showed that unstable bending vibrations can occur when the incident radiation is large.

This paper describes a coupled thermal-structural analysis of an asymmetric FRUSA model to determine a better understanding of the response of the solar array subjected to deformation-dependent thermal loading. Basic equations of the heat conduction and the quasistatic and the dynamic

structural responses of the solar array subjected to sudden radiant heating for a typical night-day orbital transition are formulated. Numerical calculations are presented for the HST solar array to show the difference quantitatively between coupled and uncoupled responses. Stability boundaries and the dynamic structural responses of the solar array both in stable and in unstable regions are also presented.

2. Solar Array Model

The Hubble Space Telescope solar array in-orbit configuration consists of two identical wing-like structures. Each wing has two flexible solar blankets that are deployed from a drum mounted on a shaft cantilevered from the spacecraft. Each solar blanket is unfurled by a rotating actuator mechanism that pushes the two BiSTEM booms from the drum. The deployed ends of the BiSTEMs are connected to a spreader bar to which the solar blanket is attached. A BiSTEM is made from thin stainless-steel tapes formed into circular open cross sections. In their stored configuration, each tape is flattened and stored on a spool within the drum mechanism. During deployment, the stored elastic energy in the flattened tape assists the unfurling mechanisms as each STEM extends and curls back to its original shape forming a BiSTEM with seams diametrically opposed. The spreader bar houses a mechanism that compensates for a slight difference in the BiSTEMs lengths. The storage drum houses a torque mechanism that maintains blanket tension. Thus, during orbital operations, the blanket tension on the spreader bar exerts a compressive force on each BiSTEM.

The mathematical model and coordinate system used in the subsequent analyses are shown in Fig.1. The solar array length and the half spreader bar length are denoted by L and b, respectively. The model assumes that 1) the solar blanket is an inextensible membrane whose thermal expansions and contractions are neglected, 2) the solar blanket is subjected to uniform tension in the x direction, and the membrane tensile force F_x per unit width is constant, 3) the inner and outer BiSTEM booms are identical cantilevered beams subjected to different axial compressive force P_1 and P_2, respectively, 4) torsional rotations are sufficiently small so that BiSTEM's bending displacements occur only in the x-z plane, 5) thermal expansions of the BiSTEMs are neglected, and 6) the spreader bar is a rigid member of length $2b$ and supports the membrane tensile force over a length b_1+b_2. For the determination of the temperature distributions, the BiSTEM booms are assumed to be one-piece thin-walled circular section beams.

When the solar blanket is subjected to uniform tensile force F_x per unit width, the inner and the outer BiSTEM booms are subjected to axial compressive forces P_1 and P_2, respectively. The compressive axial forces are determined by considering force equilibrium of the spreader bar in the x direction and moment equilibrium about the z axis. The results may be represented as

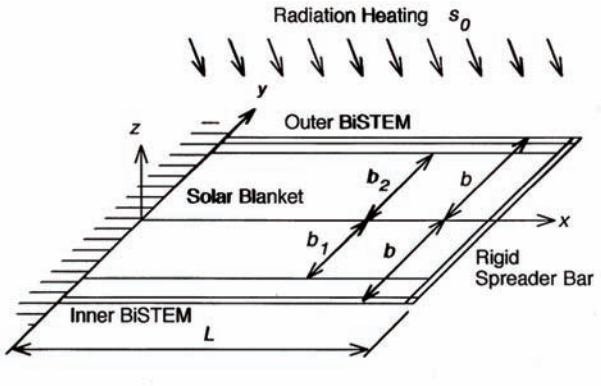

Fig. 1 Solar array analytical model.

$$P_i = P_{fi} P \quad , \quad i = 1, 2 \tag{1}$$

where

$$P_{f1} = 1 - \frac{b_2 - b_1}{2b} \quad , \quad P_{f2} = 1 + \frac{b_2 - b_1}{2b} \tag{2}$$

and the subscripts 1 and 2 denote the inner and the outer BiSTEMs, respectively. The average axial compressive force P of the BiSTEMs is defined by

$$P = (1/2) F_x (b_1 + b_2) \tag{3}$$

3. Formulations

3.1 Thermal Analysis

Here, a brief description of the perturbation temperature of the BiSTEM boom is given. Detailed discussions of the thermal analysis are found in Refs. 7 and 11. Coupled thermal-structural analyses will be presented based on the assumption that the absorbed heat flux is affected by the boom's deformation. A deformed boom with the incident heat flux s_0 is shown in Fig. 2. The solar array is subjected to an incident solar heat flux s_0 that varies as a step function with time from the direction inclined to the vertical by the angle θ. In writing the energy conservation equation, the heat flux absorbed by the boom is the component normal to the surface. Because of bending, a normal to the beam surface has rotated through a small angle equal to the beam slope. Then, the incident normal heat flux to the

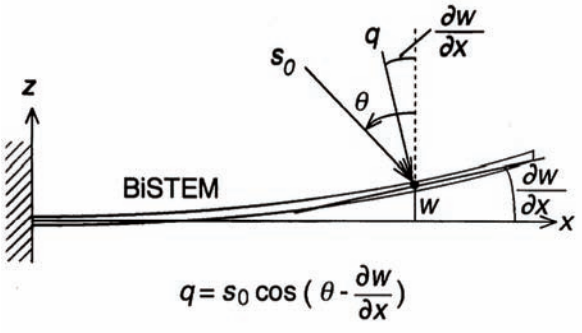

Fig.2 Heat flux for coupled thermal-structural analysis

surface can be expressed by

$$q = s_0 \cos(\theta - \frac{\partial w_i}{\partial x}) \tag{4}$$

where w_1 and w_2 are deflections of the inner and the outer BiSTEMs, respectively. After the thin walled circular boom is idealized by some heat transfer assumptions[7], conservation of energy including circumferential conduction and radiation from the external surface yields

$$\frac{\partial T_i}{\partial t} - \frac{k}{\rho c R^2}\frac{\partial^2 T_i}{\partial \phi^2} + \frac{\varepsilon_s \sigma}{\rho c h} T_i^{\,4} = \frac{\alpha_s q}{\rho c h}\delta \cos\phi \tag{5}$$

where k, ρ, and c are the thermal conductivity, the mass density, and the specific heat of the BiSTEM, respectively, R and h are the radius and the wall thickness of the BiSTEM cross section, ε_s and α_s are the thermal emissivity and the thermal absorptivity of the boom surface, and σ is the Stefan-Boltzmann constant. And where ϕ is the angular coordinate of the BiSTEM cross section and parameter δ indicates that only front half of the boom is heated.

$$\begin{cases} \delta = 1 & , \quad -\pi/2 \le \phi \le \pi/2 \\ \delta = 0 & , \quad \pi/2 < \phi < 3\pi/2 \end{cases} \tag{6}$$

The temperature distribution is represented as the sum of an average temperature $\overline{T_i}(x,t)$ and a perturbation temperature $T_{mi}(x,t)\cos\phi$, that is

$$T_i(x,\phi,t) = \overline{T_i}(x,t) + T_{mi}(x,t)\cos\phi \tag{7}$$

where the amplitude of the perturbation temperature is assumed small compared with the average temperature so that $T_{mi}/\overline{T_i} << 1$. In addition, the heat flux distribution is presented as a truncated Fourier series with higher order terms neglected. With these assumptions, substituting Eq.(7) into Eq.(5) yields an ordinary differential equation for the average temperature and an equation for the perturbation temperature.,

$$\frac{\partial \overline{T}_i}{\partial t} + \frac{\varepsilon_s \sigma}{\rho c h}\overline{T}_i^{\,4} = \frac{1}{\pi}\frac{\alpha_s s_0}{\rho c h}\cos(\theta - \frac{\partial w_i}{\partial x}) \ , \ i = 1,2 \tag{8}$$

$$\begin{aligned} &\frac{\partial T_{mi}}{\partial t} + (\frac{k}{\rho c R^2} + \frac{4\varepsilon_s \sigma}{\rho c h}\overline{T}_i^{\,3})T_{mi} \\ &= \frac{1}{2}\frac{\alpha_s s_0}{\rho c h}\cos(\theta - \frac{\partial w_i}{\partial x}) \ , \ i = 1,2 \end{aligned} \tag{9}$$

At steady state, the incident heat flux approaches a constant value which is approximated by neglecting the BiSTEM's slope. The steady-state average temperature is given from Eq.(8) as

$$T_{ss} = (\frac{1}{\pi}\frac{\alpha_s s_0}{\varepsilon_s \sigma}\cos\theta)^{1/4} \tag{10}$$

Assuming that the term $\overline{T}_i^{\,3}$ on the left-hand side of Eq.(9) may be approximated as $T_{ss}^{\,3}$ produce a linear differential equation for T_{mi}. The thermal bending moment M_{Ti} is defined as an integration over a cross section by

$$M_{Ti} = \int_A E\alpha \Delta T(x,\phi,t) z dA \tag{11}$$

where E is the Young's modulus, α is the coefficient of thermal expansion, and ΔT denotes a BiSTEM's cross-sectional temperature gradient. Linear equation is solved to yield T_{mi} and the thermal bending moment can then be obtained as

$$M_{Ti}(x,t) = \frac{EI\alpha T^*}{R\tau}\int_0^t \exp(-\frac{t-p}{\tau})\cos(\theta - \frac{\partial w_i}{\partial x})dp \tag{12}$$

where

$$T^* = \frac{1}{2}\frac{\alpha_s s_0}{\rho c h}\tau \tag{13}$$

$$\begin{aligned} \frac{1}{\tau} &= \frac{k}{\rho c R^2} + \frac{4\varepsilon_s \sigma}{\rho c h}T_{ss}^{\,3} \\ &= \frac{k}{\rho c R^2} + \frac{4\varepsilon_s \sigma}{\rho c h}(\frac{1}{\pi}\frac{\alpha_s s_0}{\varepsilon_s \sigma}\cos\theta)^{3/4} \end{aligned} \tag{14}$$

The temperature T^* denotes the steady-state value of the perturbation temperature, and the parameter τ is a characteristic thermal response time. The temperature distribution at a BiSTEM boom cross section is represented as the sum of the average temperature and the perturbation temperature. Among these terms, the perturbation temperature that varies over the cross-section induces a thermal bending moment that causes the BiSTEM boom to bend.

3.2 Structural Analysis

We now consider the coupled thermal-structural response of the solar array when both BiSTEM booms are subjected to the same uniform radiation heating. The structural analysis is performed using equations of motion for the boom bending, boom torsion, and the solar blanket. The equations are solved under the boundary conditions at the support and the interface conditions at the spreader bar. First, considering effects of the compressive axial forces, the partial differential equations and the boundary conditions for BiSTEM bending are

$$L_{1i}[w_i] = EI\frac{\partial^4 w_i}{\partial x^4} + P_i\frac{\partial^2 w_i}{\partial x^2} + \frac{\partial^2 M_{Ti}}{\partial x^2} + \rho A\frac{\partial^2 w_i}{\partial t^2} = 0 \quad , \quad i = 1,2 \tag{15}$$

$$w_i(0,t) = 0 \ , \ \frac{\partial w_i}{\partial x}(0,t) = 0 \ , \ M_{yi}(L,t) = 0 \ ; \ i = 1,2 \tag{16}$$

where $w_i(x,t)$ is the BiSTEM boom deflection, EI is the BiSTEM bending stiffness, ρA is the mass per unit length, and M_{yi} is the bending moment defined by

$$M_{yi} = -EI\frac{\partial^2 w_i}{\partial x^2} - M_{Ti} \ , \ i = 1,2 \tag{17}$$

and M_{Ti} is given in Eq.(11).

The partial differential equations and the corresponding boundary conditions for the BiSTEM boom torsional deformation including the axial compressive force effects are expressed as follows:

$$L_{2i}[w_i] = E\Gamma\frac{\partial^4 \theta_{xi}}{\partial x^4} - (GJ - \frac{P_i I_E}{A})\frac{\partial^2 \theta_{xi}}{\partial x^2} + I_x\frac{\partial^2 \theta_{xi}}{\partial t^2} = 0 \quad , \quad i = 1,2 \tag{18}$$

$$\theta_{xi}(0,t) = 0 \ , \ \frac{\partial \theta_{xi}}{\partial x}(0,t) = 0 \ , \ \frac{\partial \theta_{xi}}{\partial x}(L,t) = 0 \ ; \ i = 1,2 \tag{19}$$

where $\theta_{xi}(x,t)$ is the BiSTEM angle of twist, $E\Gamma$ is the BiSTEM warping stiffness, GJ is the torsional stiffness, I_E, A, I_x are the polar moment of inertia, cross-sectional area, and the mass moment of inertia per unit length, respectively. The latter two boundary condition means that the BiSTEM cross section is restrained from warping at both ends.

The solar blanket is modeled as a membrane with constant tension F_x per unit width. The tension F_y perpendicular to F_x is neglected since the membrane has a high aspect ratio and the tranverse edges of the membrane are free. The equation of motion and the boundary conditions for vibration of the membrane are expressed as

$$L_3[w_m] = -F_x\frac{\partial^2 w_m}{\partial x^2} + \sigma_m\frac{\partial^2 w_m}{\partial t^2} = 0 \tag{20}$$

$$w_m(0,y,t) = 0 \ , \ w_m(L,y,t) = w_{sd}(y,t) \tag{21}$$

where $w_m(x,y,t)$ is the solar blanket deflection, σ_m is the solar blanket mass per unit area, and w_{sd} is the spreader bar deflection. Because we assume that the spreader bar is rigid, w_{sd} may be written using the deflection of its center of mass, w_{s0}, and the rotation angle of the spreader bar θ_{s0}. For small rotations the deflection and the rotation of the spreader bar are presented using the tip deflections of the BiSTEMs as

$$\begin{aligned} w_{sd}(y,t) &= w_{s0}(t) + y\theta_{s0}(t) \\ &= \frac{1}{2}\{w_1(L,t) + w_2(L,t)\} \\ &\quad + \frac{y}{2b}\{w_2(L,t) - w_1(L,t)\} \end{aligned} \tag{22}$$

3.3 Approximate Solution

Because the thermal bending moment depends on the BiSTEM boom slope that appears in the integrand of Eq.(12), a modal representation of the solution could not be obtained. Then, an approximate solution based on the method of weighted residuals is developed. The solutions for the BiSTEM boom deflection and rotation and the solar blanket deflection are taken in the form

$$\begin{aligned} w_i(x,t) &= W_i(x)U(t) \ , \ i = 1,2 \\ \theta_{xi}(x,t) &= \Theta_i(x)U(t) \ , \ i = 1,2 \\ w_m(x,y,t) &= W_m(x,y)U(t) \end{aligned} \tag{23}$$

where the approximate functions $W_i(x)$, $\Theta_i(x)$, and $W_m(x,y)$ are assumed to satisfy the geometric boundary conditions. In the following calculations, functions that represent the deformation obtained in the quasistatic thermal-structural response analysis are used as the approximate functions. The method of weighted residuals is based on

$$\int_{\Omega} R(x,t)W(x)dx = 0 \tag{24}$$

where $R(x,t)$ is the residual obtained from substituting an approximate solution into a differential equation, and $W(x)$ is a weighting function. In the present analysis, the approximate functions are used as the weighting functions according to the Galerkin's method. Thus, residual form for the governing equation can be written as

$$\begin{aligned}&\int_0^L L_{11}[w_1]W_1(x)dx + \int_0^L L_{12}[w_2]W_2(x)dx \\ &+ \int_0^L L_{21}[\theta_{x1}]\Theta_1(x)dx + \int_0^L L_{22}[\theta_{x2}]\Theta_2(x)dx \\ &+ \int_0^L \int_{-b_1}^{b_2} L_3[w_m]W_m(x,y)\,dydx = 0\end{aligned} \tag{25}$$

To consider the mass M_s and mass moment of inertia I_s of the spreader bar, both the mass distribution ρA and distribution of the mass moment of inertia I_x are replaced as follows:

$$\begin{aligned}\rho A &\to \rho A + \frac{1}{2}M_s\,\delta(x-L) \\ I_x &\to I_x - I_s\,\delta(x-L)\end{aligned} \tag{26}$$

where $\delta(x)$ denotes the delta function.
Introducing the approximations for w_i, θ_{xi}, and w_m from Eq.(23) and integrating the special derivatives by parts, an ordinary differential equation for the unknown function $U(t)$ is obtained as

$$\ddot{U} + \omega_0{}^2 U = \frac{1}{M}F(t) \tag{27}$$

where ω_0 is an approximate value to the first mode natural frequency

$$\omega_0 = \sqrt{K/M} \tag{28}$$

And K, M, and $F(t)$ are the stiffness, mass, and force, respectively, for the equivalent single degree of freedom system and are written as follows:

$$\begin{aligned}K &= EI\int_0^L \{(W_1'')^2 + (W_2'')^2\}\,dx \\ &- \int_0^L \{P_1(W_1')^2 + P_2(W_2')^2\}\,dx \\ &+ E\Gamma\int_0^L \{(\Theta_1'')^2 + (\Theta_2'')^2\}\,dx \\ &+ \int_0^L \{(GJ - \frac{P_1 I_E}{A})(\Theta_1')^2 + (GJ - \frac{P_2 I_E}{A})(\Theta_2')^2\}\,dx \\ &+ F_x\int_0^L \int_{-b_1}^{b_2} (W_m')^2\,dydx\end{aligned} \tag{29}$$

$$\begin{aligned}M &= \rho A\int_0^L (W_1{}^2 + W_2{}^2)\,dx \\ &+ I_x\int_0^L (\Theta_1{}^2 + \Theta_2{}^2)dx + \sigma_m\int_0^L\int_{-b_1}^{b_2} W_m{}^2\,dydx \\ &+ M_s\{\frac{1}{2}[(W_1(L) + W_2(L)]\}^2 \\ &+ I_s\{\frac{1}{2b}[W_2(L) - W_1(L)]\}^2 \\ &+ \frac{1}{2}M_s\{W_1{}^2(L) + W_2{}^2(L)\} \\ &- I_s\{\Theta_1{}^2(L) + \Theta_2{}^2(L)\}\end{aligned} \tag{30}$$

$$\begin{aligned}F(t) &= -\int_0^L W_1''(x)M_{T1}(x,t)\,dx \\ &- \int_0^L W_2''(x)M_{T2}(x,t)\,dx\end{aligned} \tag{31}$$

Both the stiffness K and the mass M depend on the shapes of the approximate functions and the geometric and physical properties of the solar array, and independent from the thermal properties such as the heat flux s_0, characteristic thermal response time τ, and the incident angle θ. Approximate functions for the BiSTEM bending and torsion used here are written as follows:

$$\begin{aligned}W_i(x) &= \alpha_i\{\tan\lambda_i L(1-\cos\lambda_i x) - (\lambda_i x - \sin\lambda_i x)\} \\ &- \frac{1}{P_{fi}}\frac{1-\cos\lambda_i x}{\cos\lambda_i L}\end{aligned} \tag{32}$$

$$\Theta_i(x) = \gamma_i\{\sinh\beta_i L(\sinh\beta_i x - \beta_i x) - (1-\cosh\beta_i L)(1-\cosh\beta_i x)\} \tag{33}$$

For the solar blanket deflection, the approximate function is expressed as

$$W_m(x,y) = \frac{x}{L}(W_{s0} + y\Theta_{s0}) \tag{34}$$

where the deflection of the center of mass of the spreader bar W_{s0} is given

$$W_{s0} = \frac{1}{2}\{\alpha_1(\tan\lambda_1 L - \lambda_1 L) + \alpha_2(\tan\lambda_2 L - \lambda_2 L)\} - \frac{1}{2}\left(\frac{1}{P_{f1}}\frac{1-\cos\lambda_1 L}{\lambda_1 L} + \frac{1}{P_{f2}}\frac{1-\cos\lambda_2 L}{\lambda_2 L}\right) \tag{35}$$

and

$$\Theta_{s0} = \frac{1}{2b}\{\alpha_2(\tan\lambda_2 L - \lambda_2 L) - \alpha_1(\tan\lambda_1 L - \lambda_1 L)\} - \frac{1}{2b}\left(\frac{1}{P_{f2}}\frac{1-\cos\lambda_2 L}{\lambda_2 L} - \frac{1}{P_{f1}}\frac{1-\cos\lambda_1 L}{\lambda_1 L}\right) \tag{36}$$

Detailed discussions of the quasistatic thermal-structural response analysis are found in Ref.6. Parameters λ_i and β_i (i=1, 2) are defined in terms of the compressive axial force of the BiSTEM by

$$\lambda_i^{\,2} = \frac{P_i}{EI}\ , \quad \beta_i^{\,2} = \frac{1}{EI}\left(GJ - \frac{P_i I_E}{A}\right)\ ; \quad i = 1,2 \tag{37}$$

The parameter α_i (i=1, 2) , which determine the magnitude of the BiSTEM bending deflection, is obtained by solving the simultaneous equations given by

$$\begin{bmatrix} C_{11} & C_{12} \\ C_{21} & C_{22} \end{bmatrix}\begin{Bmatrix} \alpha_1 \\ \alpha_2 \end{Bmatrix} = \begin{Bmatrix} g_1 \\ g_2 \end{Bmatrix} \tag{38}$$

where each term of the coefficient matrix C_{ij} (i, j =1, 2) is determined by the BiSTEM compressive axial forces and properties of the solar array as

$$C_{11} = \frac{P_1}{L}\tan\lambda_1 L \tag{39a}$$

$$C_{12} = \frac{P_2}{L}\tan\lambda_2 L \tag{39b}$$

$$C_{21} = P_1 b\lambda_1 + Pb\frac{\tan\lambda_1 L - \lambda_1 L}{L} \times\left(\frac{b_2^{\,2} - b_1 b_2 + b_1^{\,2}}{3b^2} - \frac{b_2 - b_1}{2b}\right) + \frac{\tan\lambda_1 L - \lambda_1 L}{2b}\sum_{i=1}^{2}\left(GJ - \frac{P_i I_E}{A}\right) \times\frac{\beta_i \sinh\beta_i L}{\beta_i L\sinh\beta_i L + 2(1-\cosh\beta_i L)} \tag{39c}$$

$$C_{22} = -P_2 b\lambda_2 - Pb\frac{\tan\lambda_2 L - \lambda_2 L}{L} \times\left(\frac{b_2^{\,2} - b_1 b_2 + b_1^{\,2}}{3b^2} + \frac{b_2 - b_1}{2b}\right) - \frac{\tan\lambda_2 L - \lambda_2 L}{2b}\sum_{i=1}^{2}\left(GJ - \frac{P_i I_E}{A}\right) \times\frac{\beta_i \sinh\beta_i L}{\beta_i L\sinh\beta_i L + 2(1-\cosh\beta_i L)} \tag{39d}$$

The terms on the right-hand side of the equation are defined as

$$g_1 = \frac{1}{L}\left(\frac{1-\cos\lambda_1 L}{\cos\lambda_1 L} + \frac{1-\cos\lambda_2 L}{\cos\lambda_2 L}\right) \tag{40a}$$

$$g_2 = \frac{b}{L}\left\{\frac{1}{P_{f1}}\frac{1-\cos\lambda_1 L}{\cos\lambda_1 L}\left(\frac{b_2^{\,2} - b_1 b_2 + b_1^{\,2}}{3b^2} - \frac{b_2 - b_1}{2b}\right) - \frac{1}{P_{f2}}\frac{1-\cos\lambda_2 L}{\cos\lambda_2 L}\left(\frac{b_2^{\,2} - b_1 b_2 + b_1^{\,2}}{3b^2} + \frac{b_2 - b_1}{2b}\right)\right\} - \frac{1}{2Pb}\left(\frac{1}{P_{f2}}\frac{1-\cos\lambda_2 L}{\cos\lambda_2 L} - \frac{1}{P_{f1}}\frac{1-\cos\lambda_1 L}{\cos\lambda_1 L}\right) \times\sum_{i=1}^{2}\left(GJ - \frac{P_i I_E}{A}\right)\frac{\beta_i \sinh\beta_i L}{\beta_i L\sinh\beta_i L + 2(1-\cosh\beta_i L)} \tag{40b}$$

The magnitude parameter γ_i (i=1, 2) for the BiSTEM angle of twist is obtained as

$$\gamma_i = -\frac{\Theta_{s0}}{\beta_i L\sinh\beta_i L + 2(1-\cosh\beta_i L)}\ , \quad i = 1,2 \tag{41}$$

The numerator is the BiSTEM tip angle of twist. It is given by Eq.(36).

Because the thermal bending moments appearing in Eq.(31) contain the BiSTEM boom slope $\partial w_i / \partial x$ in the cosine term inside of an integral as shown in Eq.(12), which represents the coupling between the structural and the thermal responses, the equivalent single-degree-of-freedom equation remains difficult to solve analytically. Then, Eq.(31) can be linearized by approximating the cosine term inside of an integral based on the assumption that the BiSTEM boom's slope is small as

$$\cos(\theta - \frac{\partial w_i}{\partial x}) \cong \cos\theta + \frac{\partial w_i}{\partial x}\sin\theta \ , \ i = 1, 2 \quad (42)$$

Using the approximation and considering the system damping, the ordinary differential equation of the unknown function $U(t)$ becomes a linear equation as

$$\ddot{U} + 2\zeta\omega_0\dot{U} + {\omega_0}^2 U = \frac{1}{M}F(t) \quad (43)$$

where ζ is the damping ratio, and

$$\omega_0 = \sqrt{K/M}$$

The force $F(t)$ appearing in the right-hand side of Eq.(43) still contains the unknown function inside of integrals

$$\begin{aligned} F(t) = &-\frac{EI\alpha T^*}{R\tau}\{\int_0^L \int_0^t W_1''(x)\exp(-\frac{t-p}{\tau}) \\ &\times[\cos\theta + W_1'(x)U(p)\sin\theta]\,dpdx \\ &+ \int_0^L \int_0^t W_2''(x)\exp(-\frac{t-p}{\tau}) \\ &\times[\cos\theta + W_2'(x)U(p)\sin\theta]\,dpdx\} \end{aligned} \quad (44)$$

3.4 Quasistatic Responses

To evaluate the effect of thermo-elastic coupling quantitatively, quasistatic responses are obtained by neglecting the effect of inertia term. Equation for the unknown function $U(t)$ has the form as

$$KU = F(t) \quad (45)$$

With the Laplace transform for the convolution integrals and the inverse transform, a solution is obtained as

$$U(t) = -\frac{A\cos\theta}{K + B\sin\theta}(1 - e^{-Ct}) \quad (46)$$

Where K is the stiffness defined in Eq. (29), and parameters A, B, and C are defined as follows

$$\begin{aligned} A &= \frac{EI\alpha T^*}{R}(\int_0^L W_1''\,dx + \int_0^L W_2''\,dx) \\ B &= \frac{EI\alpha T^*}{R}(\int_0^L W_1''\,W_1'\,dx + \int_0^L W_2''\,W_2'\,dx) \end{aligned} \quad (47)$$

$$C = \frac{1}{\tau}(1 + \frac{B}{K})\sin\theta \quad (48)$$

Quasistatic structural responses of the solar array are calculated by using Eq.(23) with Eq. (46).

3.5 Dynamic Responses and Stability Criterion

The dynamic responses and the stability of them of the solar array are determined by obtaining the Laplace trancform of the differential equation.

$$\begin{aligned} &s^2\overline{U}(s) + 2\zeta\omega_0 s\overline{U}(s) + {\omega_0}^2\overline{U}(s) \\ &= -\frac{1}{M}\frac{1}{\tau s + 1}\{\frac{A\cos\theta}{s} + B\sin\theta\cdot\overline{U}(s)\} \end{aligned} \quad (49)$$

The dynamic response is calculated by inversion of the Laplace transform $\overline{U}(s)$ obtained by solving Eq. (49) to yield $U(t)$. The inverse transform can be practiced analytically by solving the cubic equation and using the inverse transform for convolution integrals. Approximate solutions are given by Eq. (23) with the $U(t)$. The characteristic equation can be written in the dimensionless form as

$$q(\bar{s}) = \bar{s}^3 + (2\zeta + \kappa)\bar{s}^2 + (1 + 2\zeta\kappa)\bar{s} + \kappa(1 + \eta) = 0 \quad (50)$$

where

$$\bar{s} = \frac{s}{\omega_0} \ , \ \kappa = \frac{1}{\omega_0\tau} \ , \ \eta = \frac{B}{K}\sin\theta \quad (51)$$

In the last equation, K is the stiffness by Eq. (29) and B is defined in Eq. (47). The parameter κ means the ratio of the characteristic mechanical response time to the characteristic thermal response time and its inverse number $1/\kappa$ is an equivalent to the nondimensional parameter used by Boley[12] in the analysis of thermally induced bending vibration of beams. The parameter η is in direct proportion to the

intensity of the heat flux s_0 and is also dependent on the direction of the radiation heating θ. From the Routh-Hurwitz stability criterion, following condition is required for a stable response.

$$\eta < \frac{2\zeta(\kappa^2 + 2\zeta\kappa + 1)}{\kappa} \tag{52}$$

Because ζ and κ are positive quantities, right-hand side of the equation is always positive. Thus, the stability criterion shows that negative or zero incident angles of solar radiation heating, $\theta \le 0$, produce stable responses.

4. Numerical Calculation Results

Numerical calculations presented hereafter use data[9), 10)] for the HST solar arrays as shown in Table 1. The BiSTEM material is stainless steel.

4.1 Quasistatic Thermal Structural Responses

Since it is expected that structural responses significantly vary with P, the average axial compressive force P is assumed to take the design value 14.75 N unless otherwise specified.. The quasistatic structural response of the BiSTEM tip deflection was calculated using Eq. (46) to evaluate the effect of thermo-elastic coupling quantitatively. Figure 3 shows time histories of the BiSTEM tip deflections and the distributions of the steady-state deflections when the solar array is heated from a direction within the fixed-end side, θ>0. Figure 4 shows the responses when the solar array is heated from a direction of the tip-end side, θ<0. Quasistatic responses calculated based on the uncoupled analysis, that the temperature is independent of the deflection or the slope of the BiSTEM boom, are also shown in these figures. Because the temperature difference between the heated and the unheated sides increases with time, the deflections also increase with time. Figures 3 and 4 show that deflections of the outer and the inner BiSTEMs are different in spite of the uniform heating, due to the coupled bending-torsional deformations because of the geometric asymmetry of the solar array. Figure 3 shows that coupled thermo-elastic responses are slightly smaller than the uncoupled calculation results when the incident angle θ is positive. Contrary to this, Fig. 4

Table 1 Solar array properties of the HST

Solar array length	L=5.91 m
Half width	b=1.428 m
Solar heat flux	s_0=1.350 x 10^3 W/m^2
Stefan-Boltzmann constant	σ=5.670 x 10^{-8} W/(m^2·K^4)
Solar blanket	
Width	b_1+b_2
	b_1=1.138 m
	b_2=1.249 m
Mass per unit area	σ_m=1.589 kg/m^2
Spreader bar	
Mass	M_s=1.734 kg
Mass moment of inertia	I_s=1.179 kgm^2
BiSTEM	
Cross-sectional area	A=1.613 x 10^{-5} m^2
Bending stiffness	EI=1.711 x 10^2 Nm^2
Warping stiffness	EI=4.991 x 10^{-1} Nm^4
Torsional stiffness	GJ=6.503 x 10^{-3} Nm^2
Polar moment of inertia	I_E=1.948 x 10^{-9} m^4
Mass moment of inertia per unit length	I_x=1.348 x 10^{-5} kgm^2/m
Density	ρ=7.010 x 10^3 kg/m^3
Wall thickness	h=2.35 x 10^{-4} m
Radius	R=1.092 x 10^{-2} m
Specific heat	c=5.020 x 10^2 J/(kgm)
Thermal conductivity	k=1.661 x 10^1 W/(mK)
Coefficient of thermal expansion	α=1.629 x 10^{-5} 1/K
Thermal absorptivity	α_s=0.5
Thermal emissivity	ε_s=0.13

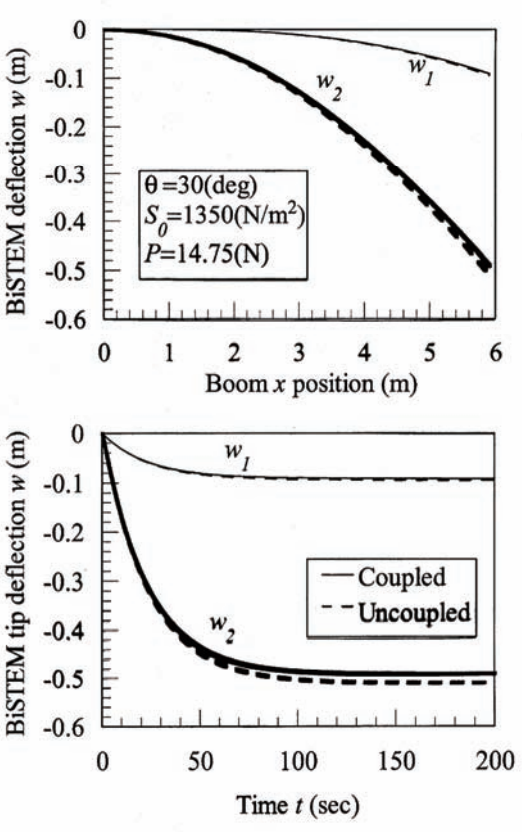

Fig.3 Quasistatic responses of the solar array subjected to uniform radiation heating from the direction θ=π/6.

shows that deflections calculated based on the coupled analysis are larger than that of the uncoupled analysis when the angle θ is negative. Variations of the steady-state tip deflections of the BiSTEM obtained by the coupled analysis with the solar incident angle θ are shown in Fig. 5 for several values of the axial force P. Because the deformations are almost pure bending when P is small, the curves are shown for $P > 12$ N. It is clearly shown that the largest value of the tip deflection occurs at the case of $\theta \cong 0$ in which the solar array is heated from the direction normal to the undeflected boom axis.

Next, we examine the variation of the effect of the thermoelastic coupling with the radiation heat incident angle θ. Because time histories are considered to be essentially similar to the results shown in Figs. 3 and 4, we only consider the steady-state deflections of the BiSTEM. The thermoelastic coupling effect on the quasistatic responses is determined quantitatively using the relative difference defined as

$$|\Delta| = \left| \frac{w_{coupled} - w_{uncoupled}}{w_{uncoupled}} \right| \tag{53}$$

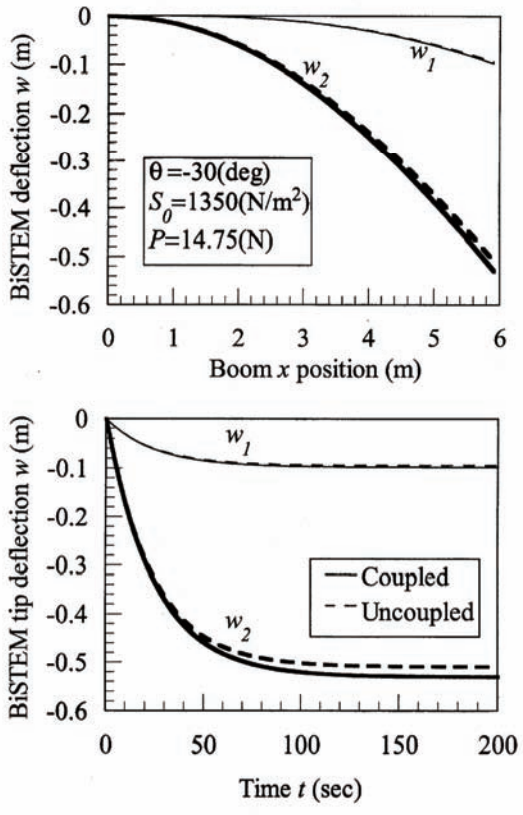

Fig.4 Quasistatic responses of the solar array subjected to uniform radiation heating from the direction θ=-π/6.

where $w_{coupled}$ and $w_{uncoupled}$ are the steady-state deflections calculated by the coupled and the uncoupled analyses, respectively. Figure 6 shows variation of $|\Delta|$ with the angle θ. The horizontal axis uses an absolute value of θ. When the heat incident angle θ approaches $\pm\pi/2$, the parameter of the effects of thermoelastic coupling $|\Delta|$ becomes large although the magnitudes of the deflections themselves become small.

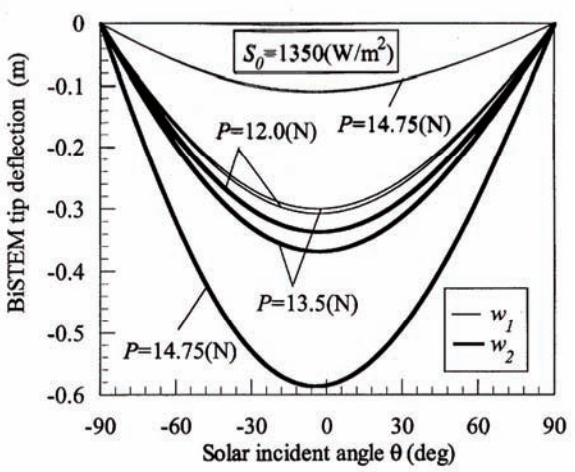

Fig.5 Variations of BiSTEM tip deflections with the solar incident angle θ.

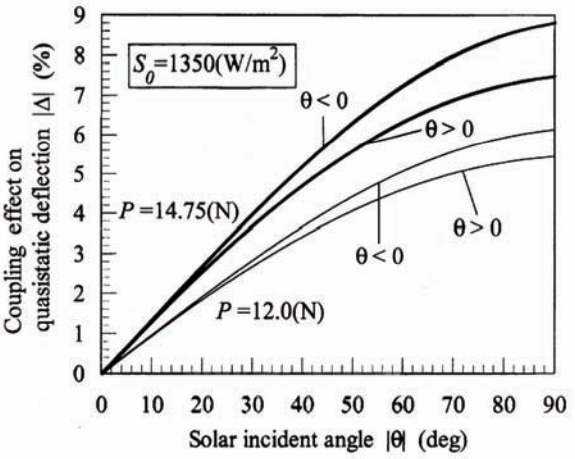

Fig.6 Quantitative effect of the thermoelastic coupling on quasistatic responses of the solar array.

4.2 Stability Boundaries and Dynamic Responses

According to the stability criterion given in Eq. (52), the stability boundary curves which divide the parameter plane into stable and unstable regions are shown in Fig. 7. The vertical axis of the figure is the

angle θ that measures the inclination of the radiant heat flux from the vertical and on the horizontal axis is the system damping ratio ζ. The stability criterion shows that the response is unconditionally stable for $\theta \le 0$. There exists the lower limit value of the damping ratio ζ that the system is stable, and if the damping ratio is lower than the critical value then the responses will be unstable. Boundary curves for the asymmetric and the symmetric solar array models are drawn in solid line and dotted line, respectively. It is shown that the unstable region is enlarged when the solar blanket moves toward the outer BiSTEM. Although the results are not shown, the stability boundary also depends on the axial compressive force P. Calculation for the asymmetric solar array model shows that the unstable region is enlarged as the axial force P becomes large.

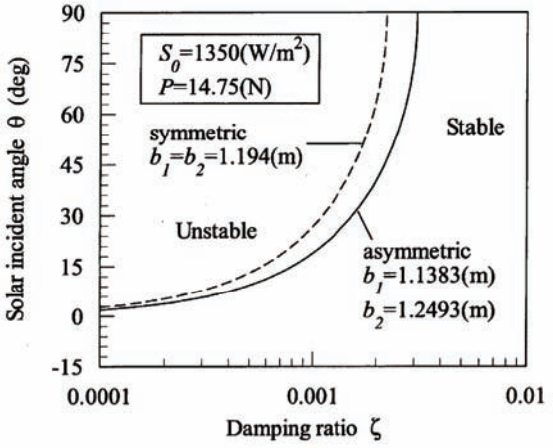

Fig.7 Stability boundaries in the θ-ζ parameter plane

The dynamic responses based on the coupled analyses can be determined from the inverse Laplace transform of $U(s)$ in Eq. (49) and substitution into Eq. (23). The procedure used in calculations of responses are as follows: solve the cubic characteristic equation to obtain three roots for the parameter s, expand $U(s)$ into a partial fraction decomposition, and practice inverse Laplace transform of $U(s)$ by using the convolution integrals. In order to demonstrate the thermoelastic coupled structural responses, deflection time histories for stable, unstable, and neutral cases were calculated. Figure 8 presents time histories of the BiSTEM tip deflections at the stability boundary. The steady-state vibrations with constant amplitude about the quasistatic deflections are shown. Because of bending-torsional coupling, torsional deformation causes the difference between quasistatic deflections of the inner and the outer BiSTEMs. Figure 9 presents time histories of the BiSTEM tip deflections both in stable and in unstable regions. Stable responses for a solar radiation incident angle θ=15 deg in the upper figure show that the quasistatic deflection of the outer BiSTEM is much larger than that of the inner BiSTEM and vibrations about the quasistatic deflections decay with time. In contrast, unstable responses for an incident angle θ=60 deg show that a self-excited vibration occurs. Because of the large incident angle θ, only a small amount of the radiant heat flux is absorbed by the BiSTEM boom, then the magnitude of the total response becomes relatively small in the case of θ=60 deg.

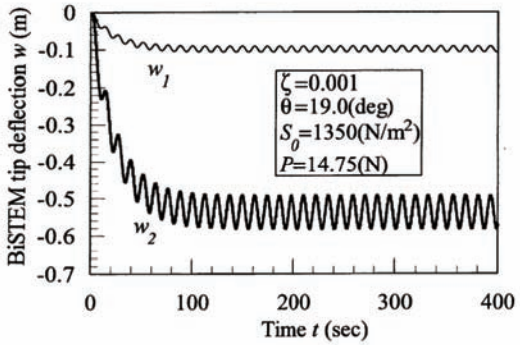

Fig.8 BiSTEM boom deflection time histories at the stability boundary

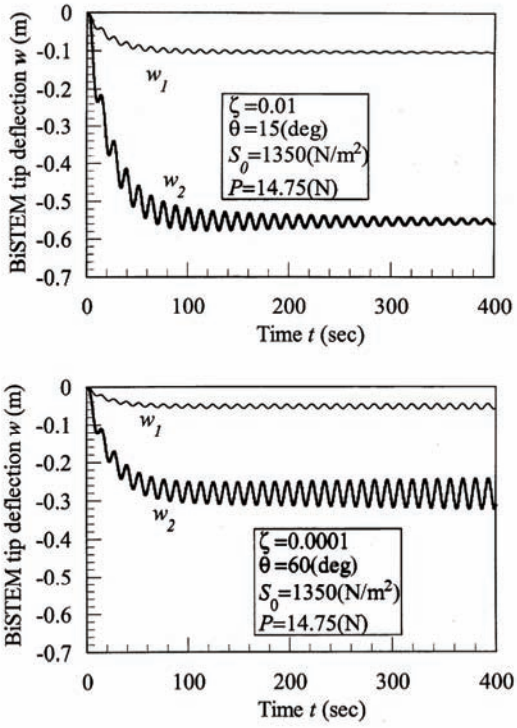

Fig. 9 Stable and unstable time histories of the BiSTEM boom tip deflection from the coupled analysis

The occurrence mechanism of the self-excited vibration or thermal flutter depends on the time-dependent radiation heat flux. The amount of heat flux absorbed by the BiSTEM boom is determined by the angle between the incident radiation heat flux and a normal to the boom surface. In the case of $\theta > 0$, when the boom deflects toward the radiant heat flux, the net incident angle decreases and the absorbed heat flux increases. When the boom deflects in the opposite direction, the net incident angle increases and the absorbed heat flux decreases. If the boom is vibrating, these variations of heat flux produce the time-dependent temperature gradient, and so time-varying thermal bending moment.

5. Conclusions

Theoretical analyses of the coupled thermal-structural responses of an asymmetric flexible rolled-up solar array were presented. The analyses were based on a generalized flexible rolled-up solar array model assuming asymmetric loading conditions because of geometric asymmetry. The coupled thermal-structural analysis includes the effects of structural deformation on external heating and temperature gradients. Numerical calculations were conducted using the data for the solar arrays of the HST.

An approximate solution was obtained by using the method of weighted residuals for the coupled thermal-structural responses of the solar array model. Effects of thermoelastic coupling were estimated quantitatively by calculating the quasistatic responses based on both the coupled and the uncoupled theories. The differences between the calculated results of the coupled and the uncoupled steady-state tip deflections of the BiSTEM booms are 9 % at the most.

Stability criterion and the dynamic coupled thermal-structural responses were also presented. According to the closed form stability criterion, the boundary curves which divide the parameter plane into stability and instability regions were shown. System parameters in determining the stability include the ratio of the structural and thermal response times, radiant heat incident angle, and the system damping. Dynamic structural responses of the solar array subjected to sudden radiation heating such as typical night-day transition in orbit were presented for stable, unstable, and the neutral cases. The time history of tip deflection in the unstable region shows the occurrence of thermal flutter.

References

1) Boley, B. A., “Thermally Induced Vibrations of Beams,” Journal of the Aeronautical Sciences, Vol.3, No.2, 1956, pp.179-181.

2) Malla, R. B. and Ghoshal, A., “Thermally Induced Vibrations of Structures in Space,” *Aerospace Thermal Structures and Materials for a New Era*, edited by E. A. Thornton, Progress in Astronautics and Aeronautics, Vol.168, 1995, pp.68-95.

3) Thornton, E. A., Thermal Structures for Aerospace Applications, AIAA, 1996, pp.343-396.

4) Thornton, E. A. and Kim, Y. A., “Thermally Induced Bending Vibrations of a Flexible Rolled-Up Solar Array,” *Journal of Spacecraft and Rockets*, Vol.30, No.4, 1993, pp.438-448.

5) Chung, P. W. and Thornton, E. A., “Torsional Buckling and Vibration of a Flexible Rolled-Up Solar Array,” AIAA Paper 95-1355, April 1995.

6) Murozono, M. and Thornton, E. A., “Buckling and Quasistatic Thermal-Structural Response of Asymmetric Rolled-Up Solar Array,” *Journal of Spacecraft and Rockets*, Vol.35, No.2, 1998, pp.147-155.

7) Murozono, M. and Sumi, S., “Thermally Induced Bending Vibrations of Thin-Walled Boom with Closed Section by Radiant Heating,” *Memoirs of the Faculty of Engineering, Kyushu University*, Vol.49, No.4, 1989, pp.273-290.

8) Murozono, M. and Sumi, S., “Thermal Flutter of Thin-Walled Circular Section Beams Subjected to Radiant Heating,” *Proceedings of the IV Conference of Asian-Pacific Congress on Strength Evaluation*, 1991, pp.676-681.

9) Reynolds, J.,”The Analysis of the Deployed Space Telescope Solar Array,” European Space Agency, ESA Doc. TN-SA-B142, British Aerospace, Bristol, England, UK, Jan. 1983.

10) “STEM Design Characteristics and Parameters,” Astro Aerospace Corp., TR AAC-B-006, Carpinteria, CA, Sept. 1985.

11) Rimrott, F. P. J. and Abdel-Sayed, R., “Flexural Thermal Flutter Under Laboratory Conditions,” *Transactions of the Canadian Society for Mechanical Engineering*, Vol.4, No.4, 1977, pp.189-196.

12) Boley, B. A., “Approximate Analyses of Thermally Induced Vibations of Beams and Plates,” Transactions of the ASME, Journal of Applied Mechanics, Vol.39, No.1, 1972, pp.212-216.

Minimization of Unsteady Thermal Deformation by Using Laminated Structures under the Stress Restrictions

Yuki ASANO, Takehiro KARIYAZAKI, and Masahiko MUROZONO
Department of Aeronautics and Astronautics, Kyushu University

Keywords: thermal deformation, thermal stress, laminated structure

Abstract

Laminated beam structures are designed in order to minimize thermal deformations in steady or unsteady temperature field. To suppress thermal deformation, composite materials that has negative longitudinal coefficient of thermal expansion are layered with material that has positive coefficient of thermal expansion (CTE). Assuming steady temperature fields, beam with no strain at central axis and no curvature can be designed. In unsteady temperature fields, it is possible to suppress thermal deformations while lowering thermal stresses. If it takes a long time until the temperature distribution get steady, the beam should be designed with considering unsteady temperature distributions because the beam that was designed with considering only steady temperature distribution could have large thermal deformations in its transitional period. For suppressing thermal deformations, interlaminar shearing stress, and interlaminar moment, materials with large Young's Modulus, CTE, and thermal conductivity are effective to use for low temperature side, oppositely, materials with small Young's Modulus, CTE, and thermal conductivity are effective to use for high temperature side.

1. Introduction

Many space structural components experience a non-uniform temperature variation because of solar radiant heating. Through-thickness temperature variation of thin structures may cause thermal deformations composed of in-plane expansion and out-of-plane curvature.

Nowadays, not only aluminum alloys but also carbon fiber composites are often used for space structures because of their lightweight, high strength and small coefficient of thermal expansion (CTE). Even if its CTE is small, however, large through-thickness temperature gradient in the structure may cause thermal deformations and that could lead undesirable problems to structures like space antennas because such kind of structure has to keep high accuracy of dimension.

By the way, there are some composite materials that possess a negative axial CTE and high stiffness. With the availability of such kind of materials, composite laminae that has negative axial CTE may be made. By laminating these composite laminae with other laminae that has positive CTE, thermal deformations can be suppressed.

Whetherhold and Wang investigated the way to eliminate both in-plane expansion and out-of-plane curvature of symmetric laminated beam or eliminate out-of-plane curvature while matching in-plane expansion in a desired value in steady temperature distributions[1][2].

In this paper, the methods to suppress thermal deformations by using asymmetric laminated beam in steady and unsteady temperature variations are investigated.

2. Analysis model

Figure 1 shows the model of this study. It is an asymmetric three-layer laminated beam. The upper side is kept in high temperature and the bottom side is kept in low temperature.

Where,

E : Young's Modulus

α : Coefficient of thermal expansion, CTE

λ : Thermal conductivity

c : Specific heat

ρ : Density

T : Temperature

h : Thickness

Thickness ratios ϕ_1 and ϕ_3 are respectively defined as follows.

$$\phi_1 = \frac{h_1}{h_2},\ \phi_3 = \frac{h_3}{h_2} \tag{1}$$

In this study $T - 0$ [°C] is defined as the reference temperature in which materials have no thermal deformation.

Table 1 shows the material properties used in this study. For composite materials, CTE means longitudinal CTE.

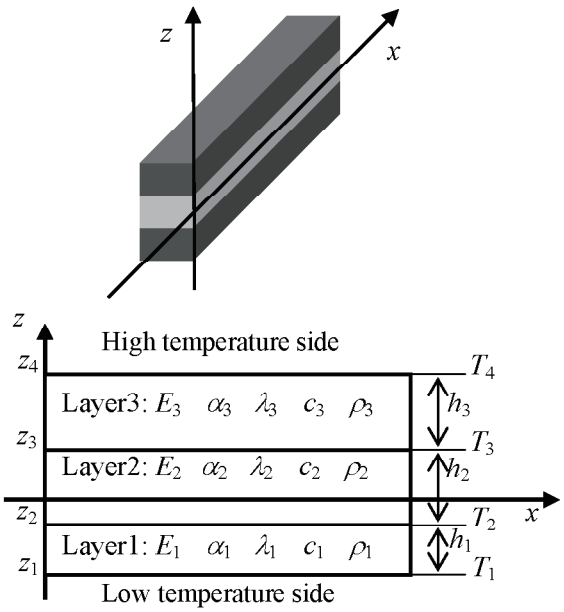

Fig. 1. Analysis Model

3. Designing laminated beam in steady temperature distribution

3.1. Temperature distribution

The temperature distributions are assumed linear for each layer, so they are represented as below.

$$T(z)=\begin{cases} T_1+\dfrac{T_2-T_1}{h_1}(z-z_1) & \text{for Layer 1} \\ T_2+\dfrac{T_3-T_2}{h_2}(z-z_2) & \text{for Layer 2} \\ T_3+\dfrac{T_4-T_3}{h_3}(z-z_3) & \text{for Layer 3} \end{cases} \quad (2)$$

Since the heat flux which pass through each layer is constant,

$$\frac{\lambda_1}{h_1}(T_2 - T_1)=\frac{\lambda_2}{h_2}(T_3 - T_2)=\frac{\lambda_3}{h_3}(T_4 - T_3) = \frac{T_4-T_1}{h_1/\lambda_1+h_2/\lambda_2+h_3/\lambda_3} \quad (3)$$

From these equations, T_2 and T_3 are represented respectively as,

$$T_2 = T_1 + \frac{(T_4-T_1)\phi_1}{\phi_1+(1+\phi_3/r_3)r_1}, \qquad T_3 = T_4 - \frac{(T_4-T_1)\phi_3}{\phi_3+(1+\phi_1/r_1)r_3} \quad (4)$$

Here,

$$r_1=\frac{\lambda_1}{\lambda_2},\ r_3=\frac{\lambda_3}{\lambda_2} \quad (5)$$

This means that temperature distribution depends on only bottom side temperature T_1 and upper side temperature T_4.

3.2. Thermal stress and thermal deformations

Thermal stress for any z is given as below.

$$\sigma_x(z)=E(z)\left[\varepsilon_x^0+\kappa_x z-\alpha(z)T(z)\right] \quad (6)$$

Using this equation and condition of equilibrium, thermal deformations are given as follows.

$$\begin{Bmatrix}\varepsilon_x^0 \\ \kappa_x\end{Bmatrix}=\begin{bmatrix}A & B \\ B & D\end{bmatrix}^{-1}\begin{Bmatrix}N_x^T \\ M_x^T\end{Bmatrix} \quad (7)$$

Here,

ε_x^0 : strain at the central axis of the beam

κ_x : curvature

N_x^T : thermal force

M_x^T : thermal moment

A : in - plane stiffness

B : coupling stiffness

D : out - of - plane stiffness

3.3. Optimization

3.3.1. Optimization theory

In this study, the barrier method is used for constraint conditions of parameters and the penalty method is used for constraint conditions of other functions. In the conjugate gradient method, unless the Hessian matrix of objective function is positive definite, descent direction vector dose not face toward

Table 1 Material Properties

Material	Young's Modulus E (GPa)	CTE (longitudinal) α (μ/°C)	Thermal conductivity λ (W/mK)	Specific heat c (J/kgK)	Density ρ (kg/m^3)
ASGr/Ep	138	-0.3	0.71	1.37	1.40
Kevlar/Ep	76	-4.0	0.16	1.10	1.60
P100Gr/Ep	480	-1.22	2.0	0.95	1.80
Aluminum	69	24	180	0.90	2.70

descent direction but saddle point of the objective function. Objective function in this study is composed of strain, curvature, and stress, and Hessian matrix of these are not always positive definite. So optimization problem is solved with the steepest descent method when descent direction vector does not face toward descent direction in the conjugate gradient method.
Three types of optimization were calculated. In all of them temperature at upper surface and bottom surface are given, and material properties for each layer are also given.

3.3.2. Minimizing thermal deformations

The purpose of the first optimization is to minimize both strain and curvature under the constraint that interlaminar stress must be under the desired value $\Delta\sigma_{max}$ [MPa]. Design parameters are thickness ratio ϕ_1 and ϕ_3. Table 2 shows the result of this optimization.

3.3.3. Minimizing interlaminar stress

The purpose of this optimization is to minimize interlaminar stress under the constraint that strain must be under the desired value ε_{max} [μ] and curvature is 0. Design parameters are also ϕ_1 and ϕ_2. The result is shown in table 3.

3.3.4. Eliminating both strain and curvature

In the previous optimization, if ε_{max} is set to 0, the beam with no strain and no curvature is designed. Table 4 shows some examples of the result. When the bottom side temperature T_1 is 0 [°C], thickness ratios in which strain and curvature become 0 are independent of the upper side temperature T_4. However, when T_1 is 50.0 [°C], thickness ratios depend on T_4. So, thickness ratio depends on both surface temperatures except the case T_1 is 0 [°C]. When T_1 is 0 [°C], interlaminar stresses $\Delta\sigma_1$ and $\Delta\sigma_2$ are proportional to T_4

Figure 2 shows the stress distribution and the temperature distribution of the beam [P100Gr/Ep -Al-Kevlar/Ep] with thickness ratios that eliminates both strain and curvature under the thermal boundary condition, T_1 is 0 [°C] and T_4 is 50[°C]. or 100 [°C]. Temperature in an aluminum layer is almost constant and composite material layers have large temperature gradients.

Table 2. Minimizing thermal deformations, T_1 = 0 [°C], T_4 = 100 [°C]

(a): Layer1-2-3 = Kevlar/Ep-Al- Kevlar/Ep

$\Delta\sigma_{max}$ [MPa]	ϕ_1	ϕ_3	ε [μ]	κ[μ/m]	$\Delta\sigma_1$ [MPa]	$\Delta\sigma_2$ [MPa]
100	2.879	2.771	-3.05	-52.07	100.00	99.67
50	0.951	2.866	-43.96	-144.85	50.00	49.03
30	0.453	2.653	-71.22	-170.22	30.00	28.86
10	0.086	1.843	-95.89	-195.74	10.00	8.72

(b): Layer1-2-3=P100Gr/Ep-Al-ASGr/Ep

$\Delta\sigma_{max}$ [MPa]	ϕ_1	ϕ_3	ε [μ]	κ[μ/m]	$\Delta\sigma_1$ [MPa]	$\Delta\sigma_2$ [MPa]
100	3.749	4.817	0.00	0.00	48.50	36.84
50	3.849	4.758	0.25	0.22	49.99	37.97
30	1.585	4.095	-0.51	-4.38	30.00	20.82
10	0.145	3.239	-7.14	-11.22	10.00	3.17

(c): Layer1-2-3=P100Gr/Ep-Al- Kevlar/Ep

$\Delta\sigma_{max}$ [MPa]	ϕ_1	ϕ_3	ε [μ]	κ[μ/m]	$\Delta\sigma_1$ [MPa]	$\Delta\sigma_2$ [MPa]
100	2.515	0.922	0.00	0.00	40.13	35.25
50	2.515	0.922	0.00	0.00	40.13	35.25
30	1.350	0.720	0.44	-8.04	30.00	25.71
10	0.590	0.839	-57.59	-84.71	10.00	10.00

Table 3. Minimizing interlaminar stress, $\kappa = 0$ [μ/m]
(a): Layer1-2-3 = Kevlar/Ep-Al- Kevlar/Ep

ε_{max} [μ]	T_1 [°C]	T_4 [°C]	ϕ_1	ϕ_3	ε [μ]	$\Delta\sigma_1$ [MPa]	$\Delta\sigma_2$ [MPa]
10.0	0.0	100.0	4.569	2.296	9.93	130.50	130.53
20.0	0.0	100.0	4.243	2.199	19.96	129.22	129.25
30.0	0.0	100.0	3.957	2.108	29.89	128.06	128.09
10.0	0.0	200.0	4.746	2.346	9.98	262.37	262.42
10.0	50.0	100.0	3.037	2.408	10.00	152.72	152.74

(b): Layer1-2-3 = P100Gr/Ep-Al-ASGr/Ep

ε_{max} [μ]	T_1 [°C]	T_4 [°C]	ϕ_1	ϕ_3	ε [μ]	$\Delta\sigma_1$ [MPa]	$\Delta\sigma_2$ [MPa]
10.0	0.0	100.0	1.856	2.896	9.99	45.61	32.31
20.0	0.0	100.0	1.126	1.977	19.98	45.86	30.17
30.0	0.0	100.0	1.124	1.974	20.01	45.86	30.16
10.0	0.0	200.0	2.548	3.663	10.00	92.83	68.17
10.0	50.0	100.0	2.762	10.722	-10.00	117.36	91.32

(c): Layer1-2-3 = P100Gr/Ep-Al- Kevlar/Ep

ε_{max} [μ]	T_1 [°C]	T_4 [°C]	ϕ_1	ϕ_3	ε [μ]	$\Delta\sigma_1$ [MPa]	$\Delta\sigma_2$ [MPa]
10.0	0.0	100.0	1.145	0.614	10.00	33.14	25.70
20.0	0.0	100.0	0.616	0.433	20.00	31.09	20.49
30.0	0.0	100.0	0.361	0.315	30.00	31.11	17.13
10.0	0.0	200.0	1.651	0.748	10.00	71.35	59.26
10.0	50.0	100.0	1.834	1.888	-10.00	116.05	105.04

Table 4. Eliminating strain and curvature, $\varepsilon = 0$ [μ], $\kappa = 0$ [μ/m]
(a): Layer1-2-3 = Kevlar/Ep-Al- Kevlar/Ep

T_1 [°C]	T_4 [°C]	ϕ_1	ϕ_3	$\Delta\sigma_1$ [MPa]	$\Delta\sigma_2$ [MPa]
0.0	50.0	4.936	2.397	66.0	66.0
0.0	100.0	4.936	2.397	131.9	131.9
0.0	200.0	4.936	2.397	263.8	263.8
50.0	100.0	3.169	2.495	152.8	152.8
50.0	150.0	3.492	2.439	213.4	213.4

(b): Layer1-2-3 = P100Gr/Ep-Al-ASGr/Ep

T_1 [°C]	T_4 [°C]	ϕ_1	ϕ_3	$\Delta\sigma_1$ [MPa]	$\Delta\sigma_2$ [MPa]
0.0	50.0	3.749	4.816	24.2	18.4
0.0	100.0	3.749	4.816	48.5	36.8
0.0	200.0	3.749	4.816	97.0	73.7
50.0	100.0	2.192	7.331	122.8	93.1
50.0	150.0	2.251	6.406	136.9	103.8

(c): Layer1-2-3 = P100Gr/Ep-Al- Kevlar/Ep

T_1 [°C]	T_4 [°C]	ϕ_1	ϕ_3	$\Delta\sigma_1$ [MPa]	$\Delta\sigma_2$ [MPa]
0.0	50.0	2.515	0.922	20.1	17.6
0.0	100.0	2.515	0.922	40.1	35.2
0.0	200.0	2.515	0.922	80.3	70.5
50.0	100.0	1.564	1.759	119.5	104.5
50.0	150.0	1.564	1.470	129.7	113.5

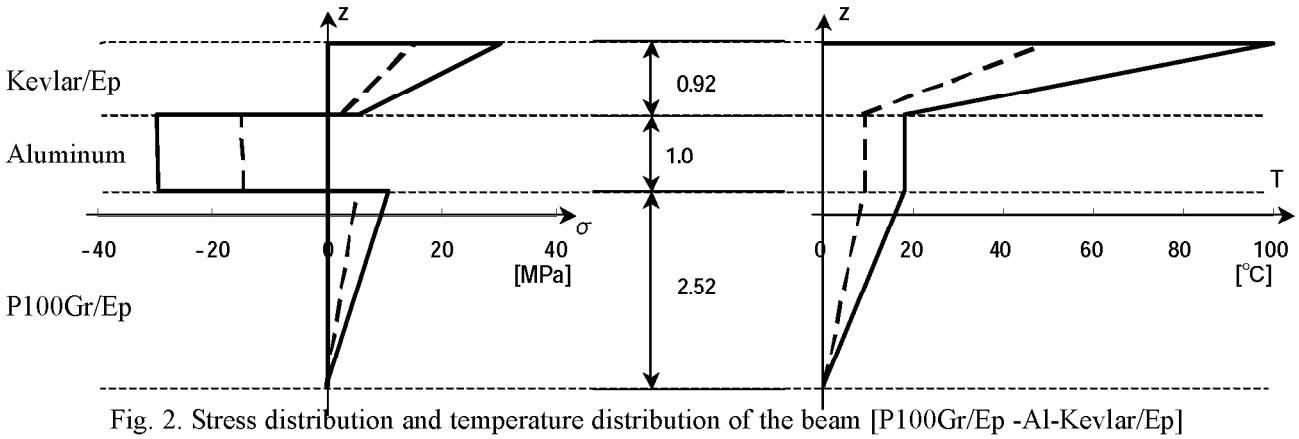

Fig. 2. Stress distribution and temperature distribution of the beam [P100Gr/Ep -Al-Kevlar/Ep] with thickness ratios that eliminates both strain and curvature under the thermal boundary condition, T_1 is 0 [°C] and T_4 is 50 [°C] or 100 [°C].

3.3.5. Matching thermal deformations in desired value

Figure 3 shows the normalized strain and curvature of the beam [P100Gr/Ep-Al-Kevlar/Ep] for thickness ratios from 0 to 10 under the thermal boundary condition, T_1 is 0 [°C] and T_4 is 100 [°C]. Thickness ratios with strain $\varepsilon = \xi$ and curvature $\kappa = \zeta$ are found out at the intersection of two curves, $\varepsilon = \eta$ and $\kappa = \zeta$. However, the solution for these requests does not always exist. For example, the curve for ε = -0.1 and the curve for $\kappa = 0$ have no intersection in first quadrant. So, requests for thermal deformations are not always satisfied.

4. Designing laminated beam in unsteady temperature distribution

Assuming that temperature distribution is steady, optimal laminated beam can be designed to satisfy a variety of requests for deformations or stress. In application to space structures, however, temperature distribution is not always steady. So, the laminated beam structure, some times, need to be designed with considering unsteady temperature distributions.

4.1. Unsteady temperature distributions

In this section, the beam is assumed to be heated uniformly. Then, a temperature distribution is calculated from Crank-Nicolson method based on one-dimensional heat conduction equation. Fig. 4 shows the thermal boundary conditions. The initial temperature in whole beam is 0 [°C]. And at time 0 [s], the upper side temperature increases to 100 [°C], T_1 = 100[°C], and is kept constant after that. The bottom side temperature is kept 0 [°C], T_1 = 0[°C]

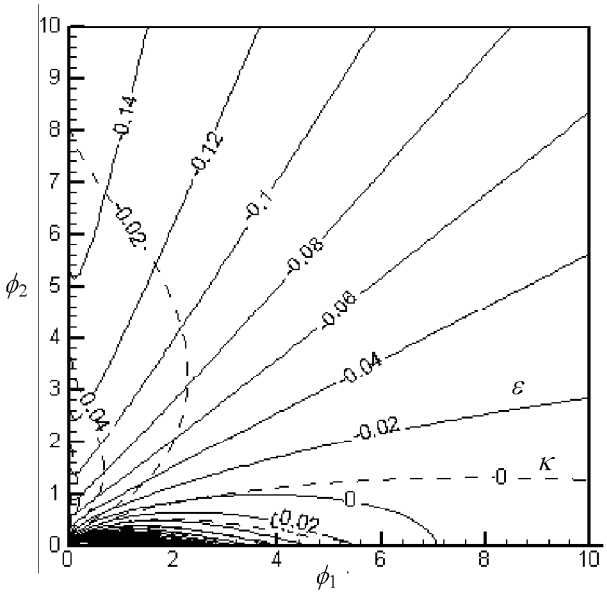

Fig. 3. Normalized strain and curvature of the beam [P100Gr/Ep -Al-Kevlar/Ep] T_1 = 0 [°C], T_4 = 100 [°C].

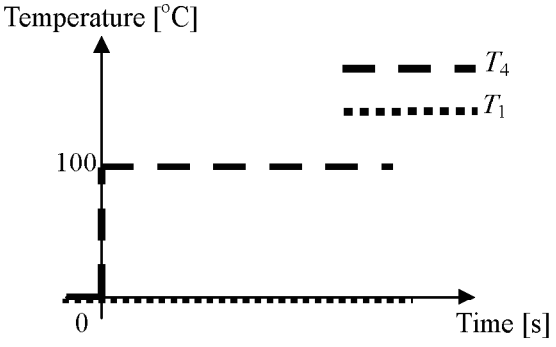

Fig.4. Surface Temperature

4.2. Interlaminar shearing stress and moment

To avoid delamination, interlaminar stress was considered as constraint in chapter 3. In this chapter, however, interlaminar moment and interlaminar shearing stress are considered as constraints to avoid delaminations of mode-1 and mode-2 at free edge because delamination is easy to happen at the free edge, Fig. 5. Fig. 6 is the image of interlaminar moment M_z and shearing stress F_{xz}. These are respectively defined as below.

$$M_z(z_i) = \int_{z_i}^{z_{i+1}} \sigma_x(z)(z - z_i)\mathrm{d}z \tag{8}$$

$$F_{xz}(z_i) = -\int_{z_i}^{z_{i+1}} \sigma_x(z)\mathrm{d}z \tag{9}$$

4.3. Optimization

Thermal deformations are represented by curvature and strain at the central axis of the beam (κ_x and ε_x^0). They are calculated with classical lamination theory and objective function consists of them.

$$f(x) = \max_{0\le t\le t_f}\left\{c_1\left[\varepsilon_x^0(t)/\varepsilon_0\right]^2 + c_2\left[\kappa_x(t)/\kappa_0\right]^2\right\} \tag{10}$$

Here, ε_0 and κ_0 are, respectively, strain at the central axis and curvature of the aluminum beam in the same condition. c_1 and c_2 are weighting factors. This equation means that the objective function is the maximum value of the weighted square sum of normalized strain and curvature from time 0 [s] to termination time t_f. And the purpose of this optimization is to find optimum design parameters such as thickness ratio and material properties that minimize objective function.

Optimization procedure is as follows, Fig. 7. At first, objective function, constraint conditions, design parameters, and thermal boundary conditions are set for initialization. Then, unsteady temperature distributions; temperature distributions for each time instant, are calculated by Crank-Nicolson method. Thermal deformations and thermal stresses for each time instant are calculated based on those temperature distributions. If the objective function satisfies the at-end condition, it will be an optimum solution. If not, the appropriate design parameters are chosen by using descend method and return to the calculation of temperature distributions.

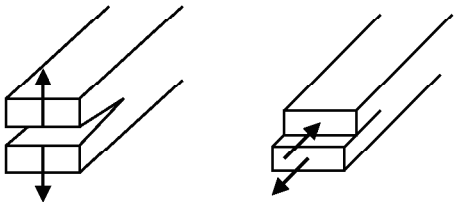

(a): Mode-1 (b): Mode-2

Fig. 5. 2 modes of delamination

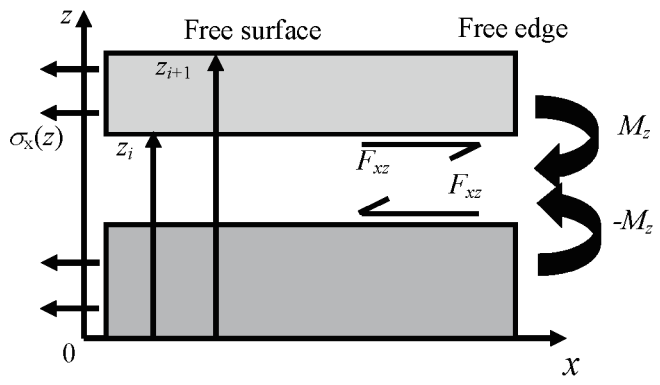

Fig. 6. Interlaminar shearing stress and interlaminar moment

4.3.1. Optimization about Material Properties

The purpose of this optimization is to find out the best material properties of the first and the third layers that minimize thermal deformation. The material in the second layer is assumed to be aluminum.

Design parameters are ratio of thickness and material properties of the first and the third layers. Table.5 shows optimization results. The strain and the curvature of an Aluminum beam in the same condition are $\varepsilon_0 = 1200\times10^{-6}$, $\kappa_0 = 48000\times10^{-6}$/m, respectively.

The material with small $|E\alpha|$ and λ is effective on the high temperature side. This has large temperature gradients and is not easy to transform at the high temperature. Oppositely, the material with large $|E\alpha|$ and λ is effective on the low temperature side. This has small temperature gradients and is easy to transform at the low temperature.

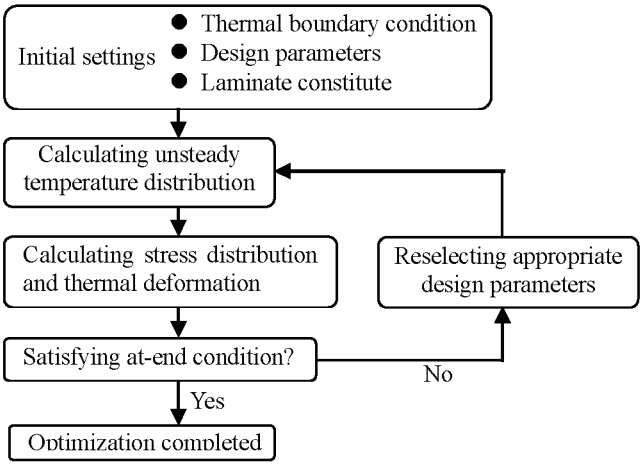

Fig. 7. Optimizing Procedure

Table.5. Optimization results about material properties

ϕ_1	E_1 (GPa)	α_1 ($\times 10^{-6}$/K)	λ_1 (W/mK)	$c_1\rho_1$ (MPa/K)	ε_{max} ($\times 10^{-6}$)	$f(x)$ ($\times 10^{-6}$)	$\lvert F_{xz}\rvert_{max}$ (kN/m)
0.741	500	-3.50	2.50	800	2.16	3.57	23.7
ϕ_3	E_3 (GPa)	α_3 ($\times 10^{-6}$/K)	λ_3 (W/mK)	$c_3\rho_3$ (MPa/K)	κ_{max} ($\times 10^{-6}$/m)	$\Delta\sigma_{max}$ (MPa)	$\lvert M_z\rvert_{max}$ (kNm/m)
1.04	107	-0.10	0.050	800	82.0	5.29	0.200

Table.6. Optimization results using actual materials

Layer1-2-3	ϕ_1	ϕ_3	ε_{max} ($\times 10^{-6}$)	κ_{max} ($\times 10^{-6}$/m)	$f(x)$ ($\times 10^{-6}$)	$\lvert F_{xz}\rvert_{max}$ (kN/m)	$\lvert M_z\rvert_{max}$ (kNm/m)	$\Delta\sigma_{max}$ (MPa)
Kevlar/Ep-Al-Kevlar/Ep	10.0	2.46	55.2	2990	3930	254	8.29	157
P100Gr/Ep-Al-ASGr/Ep	7.29	5.73	5.13	294	41.6	131	5.17	67.0
P100Gr/Ep-Al-Kevlar/Ep	8.89	1.13	12.7	520	118	186	7.39	82.3

4.3.2. Optimization Using Actual Materials

The optimization using actual materials shown in Table 1 is carried out. In this time, laminate constitution is given and only thickness ratios are the design parameters. Constraints for interlaminar shearing stress and moment are not considered.

Table.6 shows the optimization result. The laminate constitution [P100Gr/Ep-Al-ASGr/Ep] reduces thermal deformations most. This is because that laminate constitution has the closest material tendency to the tendency that was proved in the previous optimization. So optimization about material properties will be useful for deciding laminate constitution in designing process.

4.3.3. Constraints for interlaminar shearing stress and moment

For the laminate constitution [P100Gr/Ep-Al-ASGr /Ep], optimization about thickness ratios is carried out with considering constraints for inter laminar shear and moment in the same temperature condition. Interlaminar shearing stress and moment are restricted not to exceed 80% of the maximum values of the previous optimization, Table 6, $\lvert F_{xz}\rvert_{max} < 0.8\times131$ [kN/m], $\lvert M_z\rvert_{max} < 0.8\times5.17$[kNm/m]. Fig. 7 shows the time history of the objective functions. Line A shows the time history of objective function without considering constraints for interlaminar shearing stress and moment, and line B shows that with considering them. Instead of decreasing interlaminar shearing stress and moment, thermal deformations increase.

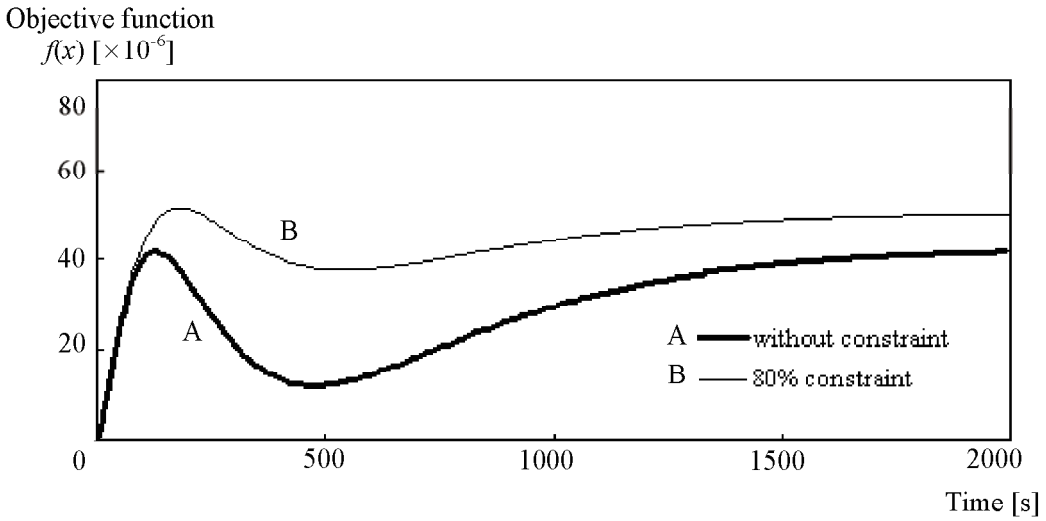

Fig. 7. Time histories of objective functions of the beam [P100Gr/Ep-Al-ASGr/Ep]
A: Optimization without any constraints for interlaminar shearing stress or moment
B: Optimization with constraints for interlaminar shearing stress and moment

4.3.4. Discussion on considering steady temperature distributions or unsteady ones

Optimum thickness ratios for laminate constitution [P100Gr/Ep-Al-ASGr/Ep] in steady temperature distribution, the bottom side temperature is 0 [°C], upper side temperature is 100 [°C], have been found out in section 3.3.4.

Line C in Fig. 8 shows how the time history of objective function changes if the beam with those thickness ratios experiences the unsteady temperature distribution shown in Fig. 4.

Comparing line C with the line A in Fig. 7; which is a time history of objective function for [P100Gr/Ep-Al-ASGr/Ep] in unsteady temperature distribution, line C is much larger than line A in transitional period. Since objective function represents thermal deformations, this means the beam, which was designed with considering steady temperature distribution, can be deformed much in transitional period. Oppositely, the beam, which was designed with considering unsteady temperature distribution, can suppress transitional thermal deformations, however deformations will remain after temperature distribution gets steady.

Conclusions

This paper showed that thermal deformation of the beam can be suppressed by using laminated structure composed of materials with negative longitudinal coefficient of thermal expansion (CTE) and materials with positive CTE. If temperature distribution is steady, thermal deformations; strain of the central axis and curvature, can be eliminated by laminating such materials in appropriate thickness ratios. It is impossible to eliminate both thermal deformations and interlaminar stress but it is possible to suppress both of them simultaneously. Even if temperature distribution is unsteady, thermal deformations can be suppressed while lowering thermal stresses by laminating material with small $|E\alpha|$ and λ on the high temperature side and material with large $|E\alpha|$ and λ on the low temperature side. Beam structure should be designed with considering unsteady temperature distribution if that structure experiences temperature changes because beam structure designed with considering steady temperature distribution could be deformed much when it experiences temperature changes.

References

[1] Robert C. Whetherhold and Jianzhong Wang, "Minimizing Thermal Deformation by Using Layered Structures", *Aerospace Thermal Structures and Materials for a New Era, Progress in Astronautics and Aeronautics*, Vol.168, pp.273-292

[2] Robert C. Whetherhold and Jianzhong Wang, "A Self-Correcting Thermal Curvature -Stable Bending Element", *Journal of Composite Materials*, Vol28, No.16, 1994, pp.1588-1597

[3] Robert C. Whetherhold and Jianzhong Wang, "Tailoring Thermal Deformation by using Layered Beams", *Composites Science and Technology*, Vol.53, 1995, pp.1-6.

[4] Hiroto Nagai and Masahiko Murozono, "Optimization for Thermal Deformation and Thermal Stress of Laminated Structures", *The 44th Proceeding of JSASS/JSME Structures Conference*, pp214-216

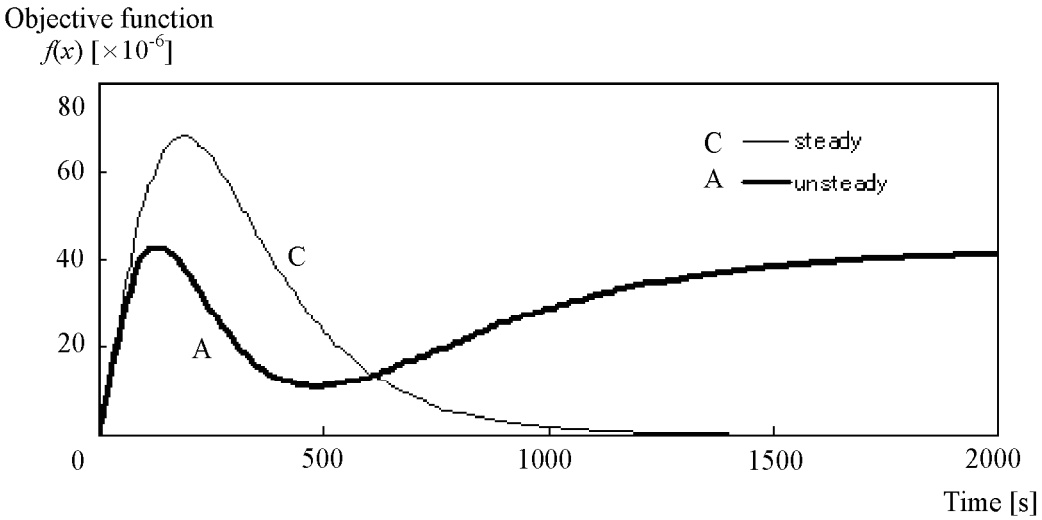

Fig. 8. Time histories of objective functions of the beam [P100Gr/Ep-Al-ASGr/Ep]
A: Considering unsteady temperature distributions
C: Considering steady temperature distributions

Experimental and Numerical Study of Surface Nitridation of Thermal Protection Material

Toshiyuki Suzuki* and Kazuhisa Fujita†
Japan Aerospace Exploration Agency, Tokyo, 182-0012, Japan

and

Takeharu Sakai‡
Nagoya University, Aichi, 464-8603, Japan

Nitridation of graphite is observed in the inductively coupled plasma heated wind tunnel. Probability values of nitridation reaction are determined from the amount of mass loss of graphite test piece and atomic nitrogen density in the test section. The amount of atomic nitrogen is determined by calculating the flowfield around the graphite test piece under wind tunnel freestream condition. The freestream condition at the entrance of test chamber is evaluated by calculating the flows in the plasma toarch fully theoretically. It is found from experimental and numerical results that the reaction probability is about 0.003 for the surface temperature of about 1900K. The uncertainties in the results are also described, and improvements are proposed.

Nomenclature

A	=	surface area of graphite test piece, 2.43×10^{-4} m^2
k	=	surface reaction velocity, m/s
M_s	=	molecular weight of species s, kg/mol
R	=	universal gas constant, 8.314 J/(mol-K)
r	=	mass loss rate, kg/s
T	=	temperature, K
α	=	reaction probability
ρ_s	=	density of species s, kg/m^3

I. Introduction

In Japan, there has been an increasing interest for planetary entry missions. Well known examples are sample return mission named HAYABUSA (MUSES-C)[1] and Unmanned Space Experiment Recovery System (USERS)[2]. When the entry capsule enters into Earth's atmosphere along the hyperbolic trajectory, the absolute velocity of the capsule exceeds about 12km/s. At such flight velocity, the flow temperature behind a detached shock wave becomes so high that air molecules can be vibrationally excited, dissociated, or ionized. In these missions, therefore, a carbon fiber reinforced plastic (CFRP) ablator that consists of a base carbon fiber matrix and a resin is employed as the material of a thermal protrection system (TPS). When the virgin material of the ablator is heated, the resin decomposes and a pyrolysis gas is formed within the ablator. The pyrolysis gas then flows toward a wall surface and is released into the boundary layer. In the boundary layer, atomic oxygen and nitrogen so dissociated will reach the ablating surface. Because the ablating surface becomes nearly pure carbon due to the pyrolysis process, the solid carbon on the surface is oxidized or is nitrided by the atomic species in the boundary layer resulting in surface recession of the TPS material. Therefore, an estimation of the amount of surface recession is one of main subjects to designing the TPS of entry capsules.

*Researcher, Institute of Aerospace Technology, 7-44-1 Jindaiji Higashi-machi, Chofu-shi, Tokyo 182-8522, E-Mail: suzuki.toshiyuki@jaxa.jp
† Senior Researcher, Institute of Aerospace Technology, 7-44-1 Jindaiji Higashi-machi, Chofu-shi, Tokyo 182-8522
‡ Assistant Professor, Department of Aerospace Engineering, Furo-cho, Chikusa-ku, Nagoya, Aichi 464-8603

A considerable amount of effort has been expended to determine how fast the material surface recedes at high temperature.[3-6] It is well known that the atomic oxygen reacts with solid carbon to form gaseous CO through the oxidation process,

$$O + C(s) \rightarrow CO + 3.74ev\,. \tag{1}$$

The speed of the oxidation is expressed by a reaction probability, which is defined as the ratio of the mass flux of oxygen contained in the reaction product to the mass flux of oxygen reaching the wall surface. In Refs. 3-5, the reaction probability of oxidation reaction has been measured in atomic beam experiments. In such experiments, a beam of atomic oxygen was made to hit a solid carbon surface, and the flux of the product of the surface reaction was measured. From these experiments, the reaction probability of oxidation was found to vary from 0.01 to 0.3 depending on the material temperature. The obtained data were approximated in Ref. 7 as following,

$$\alpha = 0.63\exp\left(-\frac{1160}{T}\right). \tag{2}$$

The expression of Eq. (2) has been widely used to estimate the mass loss and the amount of recession due to oxidation reaction.[8, 9]

Recently, the probability of reaction of nitrogen atoms with solid carbon to form gasceous CN,

$$N + C(s) \rightarrow CN + 0.35ev\,, \tag{3}$$

was experimentally determined by Park and Bogdanoff.[6] This process was so-called nitridation reaction. In the experiment, a stream of highly dissociated nitrogen was produced in a shock tube and passed over a grid of metal wire coated with carbon. The reaction probability of nitridation reaction was determined by comparing the number density of CN molecules, determined from the measured intensity of CN radiation, with the calculated number density of atomic nitrogen in the wake of a grid of metal. From the measurement, the reaction probability is deduced to be about 0.3. However, questions remain as to how well the reaction probability reproduce the amount of mass loss of the material in an actual heating environment of interest.

The aim of the present study is to observe the nitridation phenomenon in a high enthalpy wind tunnel facility. For this purpose, heating tests using a graphite test piece are conducted in a 110kW inductively coupled plasma (ICP) heated wind tunnel installed in the Institute of Aerospace Technology (IAT) of Japan Aerospace Exploration Agency (JAXA). In the heating tests, pure nitrogen is used as a working gas. The amount of mass loss of graphite test piecies due to the nitridation reaction is examined by comparing weights of test piece between before and after heating tests. In order to discuss the nitridation reaction occurred at the test piece surface in this study, and to determine the nitridation reaction probability from the obtained data, we need to know the properties of flowfield around the test piece in detail. For this purpose, the flowfield around the test piece is calculated using the thermo-chemical nonequilibrium CFD code under an wind tunnel freestream condition. The freestream condition is evaluated by calculating the flows in the ICP heater fully theoretically. Finally, we attempt to estimate the reaction probability of the nitridation. The obtained values are then compared with those obtaied by Park and Bogdanoff.

II. Experimental Configurations

The schematic diagram of the 110kW ICP heated wind tunnel facility in IAT of JAXA is given in Fig. 1. The facility consists mainly of a plasma torach and a test chamber. The plasma toarch consists of a cylindrical discharge chamber made of a quartz tube and an induction coil of three-turn. A working gas is introduced from upstream wall, and is then discharged by supplying a radio-frequency current to the induction coil. The hot gas then flows into a test chamber. The quarts tube has a diameter of 75 mm and a length of 250 mm. The radio-frequency generator can work at power between 70 and 110kW at a frequency of 1.78MIIz.

A pure nitrogen is used as a wotking gas in this study to observe the nitridation reaction occurred at graphite surface. As pointed out by Ref. 10, however, impurities such as oxygen and hydrogen may remain in the test section to some extent because the test chamber can not be completely evacuated. In that case, we can not tell the nitridation reaction occurred at test piece surface from another reactions. In order to avoid such situation, impurities in the test chamber was substituted by nitogen gas three times (pressure ratio=30) before ignition of the plasma toarch. By conducting this substitution, the amount of impurities in the test chamber becomes lower by about $(1/30)^3$=1/27000 than those without conducting the substitution.

A photograph of test piece used in this study is shown in Fig. 2. A flat-faced rodded graphite test piece has a diameter of 3 mm and has a length of 50 mm, and is mounted on a firebrick attachment. A length and area of the graphite test piece that exposed to hot nitrogen gas is 25 mm and 2.43×10^{-4} m^2, respectively. In the present study,

surface temperature of the graphite test piece is measured by a one-color optical pyrometer. Test conditions and the wind tunnel operational parameters are summarized in Table 1. The measurements were made at 566 mm from the quartz tube exit. The working power used in this study is 70 kW and the mass flow rate of working gas is 1.8 g/s, realizing a mass-averaged enthalpy of about 15 MJ/kg. The mass-averaged enthalpy values were determined by using an energy balance method. The heat flux measurements were made using a Gardon gauge.

In this study, the reaction probability of nitridation is estimated by using the amount of mass loss of graphite test piece after the heating test. The methodology used in this study is as follows. The surface reaction velocity is given by kinetic theory as

$$k = \frac{\alpha}{4}\sqrt{\frac{8RT}{\pi M_N}} \,. \tag{4}$$

Thus, the mass loss rate of graphite test piece due to nitridation reaction is given by

$$r = \frac{M_C}{M_N} A \rho_N \frac{\alpha}{4}\sqrt{\frac{8RT}{\pi M_N}} \,. \tag{5}$$

Because there is no other experimental information for the atomic nitrogen density ρ_N at this time, the solution obtained by numerical analysis is used in this study. It should be noted in Eq. (5) that constant surface temperature and surface area of test piece are assumed during the heating tests. This point will be discussed later.

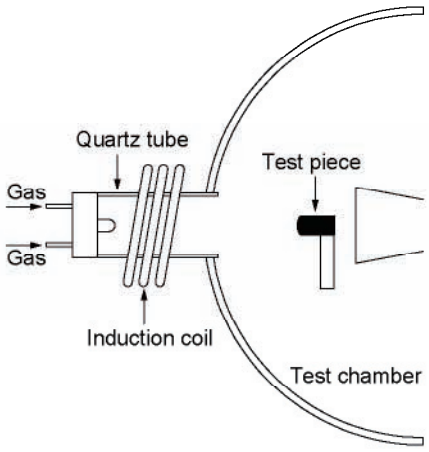

Fig. 1 Schematic of 110kW ICP heated wind tunnel facility installed in ISAS of JAXA.

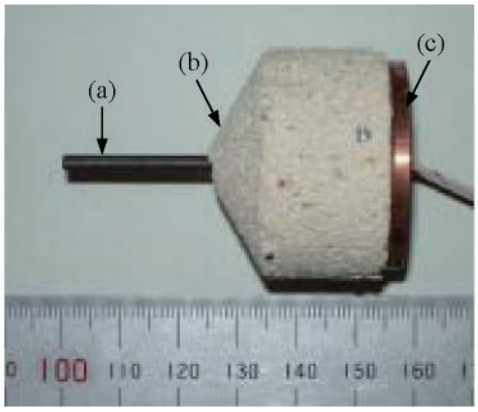

Fig. 2 Photograph of test piece used in this study; (a) graphite, (b) firebrick attachment, and (c) interface plate made of copper.

Table 1 Wind tunnel test conditions

Test piece No.	1	2	3	4
Working gas	N_2	N_2	N_2	N_2
Input power, [kW]	70	70	70	70
Mass flow rate, [g/s]	1.8	1.8	1.8	1.8
Ambient pressure, [kPa]	10	10	10	10
Heat flux, [MW/m^2]	0.7	0.7	0.7	0.7
Mass-averaged enthalpy, [MJ/kg]	15	15	15	15
Exposure time, [s]	600	900	900	1200

III. Numerical Methods

Two computational blocks are built to calculate the flowfield in the ICP heated wind tunnel: (1) simulation of the entire flowfield in the plasma toarch; and (2) simulation of flowfield over a graphite test piece in the test chamber.

A. Plasma Toarch Analysis Code

The inductively coupled plasma wind tunnel flowfield is calculated using a computational fluid dynamic(CFD) technique. An axisymmetric viscous flow is assumed to be thermochemical equilibrium, because pressure is 10kPa for typical operating conditions. Nitrogen is used as a test gas in the present study, and 5 chemical species model (N, N^+, N_2, N_2^+ and e-) is employed to account for high temperature phenomena. Mass, Momentum, and total energy conservation equations are solved using a finite volume method. Solutions are obtained by numerically integrating the equations in time to steady state by using mass flow rate, input power and operating frequency as the code input.

In the right hand side of the momentum and energy equations, the Lorentz force and Joule heating terms are included. The axisymmetric electromagnetic field is assumed as in the flowfeild calculation. Time-averaged values of Lorentz force and Joule heating are calculated by solving Maxwell equations. Technical details are given in Ref. 11. These terms are evaluated at every 1000 times in the CFD calculation by solving the electromagnetic field equations.

Two computational meshes are used to calculate the inductively coupled plasma flowfield: one for the flowfield calculation, and the other for the electromagnetic field. Figure 3 shows the computational grids used in the present study. In the figure, the zone 1 is used for the calculation of the plasma toarch flowfield with 90 x 44 grid points. The farfield boundary for the computational mesh of the electromagnetic field is extended appropriately to impose the boundary condition that electrical and magnetic field is taken to be zero.

B. Boundary Layer Analysis Code

The thermo-chemical nonequilibrium CFD code developed earlier[12] is used for the computation of flowfield over the graphite test piece. The governing equations are the Navier-Stokes equations for axisymmetric flowfield, consisting of species mass, momentum, total energy and vibronic energy conservation equations. The equations are discretized by the cell-centered finite volume scheme utilizing AUSM-DV numerical flux[13] and MUSCL approach for attaining higher order spatial accuracy. Solutions are obtained by integrating the equations in time to steady state using the LU-SGS algorithm.

For high temperature airflow, we employ the following five chemical species, i.e., N, N_2, N^+, N_2^+ and e-. Park's two-temperature model is employed to determine the thermo-chemical nonequilibrium states. The vibronic energy conservation equation accounts for 1) vibrational energy excitation of molecules through collisions between heavy particles, 2) elastic energy transfer between electrons and heavy particles, 3) gains or losses of energy by electron impact ionization, and 4) gains or losses of vibronic energy of heavy particles in chemical reactions.[14] Vibrational relaxation parameters, such as a vibrational relaxation time, are taken from Refs. 15 and 16. The relaxation time is accounted for Park's limiting cross section at high temperature. The values of reaction rate coefficients are taken from Refs. 8 and 15.

A typical example of computational mesh for the flowfield over the test piece is also shown in Fig. 3. The zone 2 with 113 x 69 grid points is used for the calculation. It should be noted that the inlet boundary condition at the entrance of test chamber is given by the solution obtained by the plasma toarch flowfield analysis. As to wall boundary condition at the wall surface of test piece, the constant wall temperature is arbitrary chosen as 500 K. In the present study, the thermo-chemical nonequilibrium CFD code is parallelized with OpenMP directives. All the flowfield calculations are performed using the CFD code on four processors of DELL PRECISION 690. Approximately 100,000 iteration steps are needed to drop the L2-norm of the residual 3 orders of magnitude, requiring about 8 hours of CPU time.

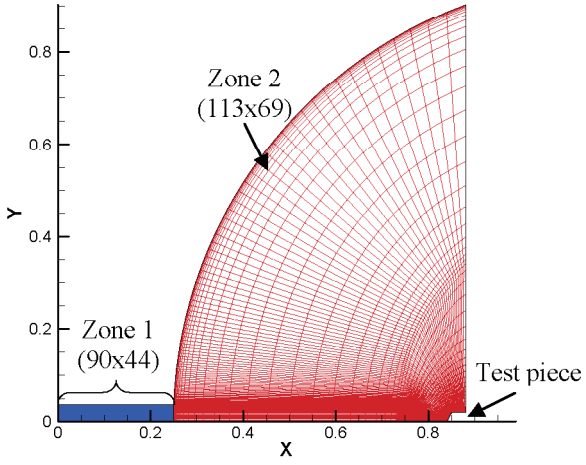

Fig. 3 Computational meshes for 110kW ICP heated wind tunnel facility installed in IAT of JAXA.

IV. Results and Discussions

A. Experimental Results

The heating tests using a graphite test piece are conducted in the 110 kW ICP heated wind tunnel for the wind tunnel test conditions shown in Table 1. Measured surface temperature variations for all test pieces are plotted against time in Fig. 4. As shown in this figure, all temperature variations are within a range between 1700 K and 2000 K, and they are found to be almost constant while heating. The heat up rate is very small, and is approximately 4.8 K/min. Average temperatures are 1953, 1930, 1853 and 1822 K, respectively. For the purpose of simplicity, we hereafter regard the average temperature as temperature of test piece during the heating test.

After the heating tests, graphite test pieces were removed from firebrick attachments, and were weighed to obtain the amount of mass loss of graphite test piece. Obtained weights and mass loss rates of test pieces are summarized in Table 2. A maximum mass loss of about 34% is obtained for the exposure

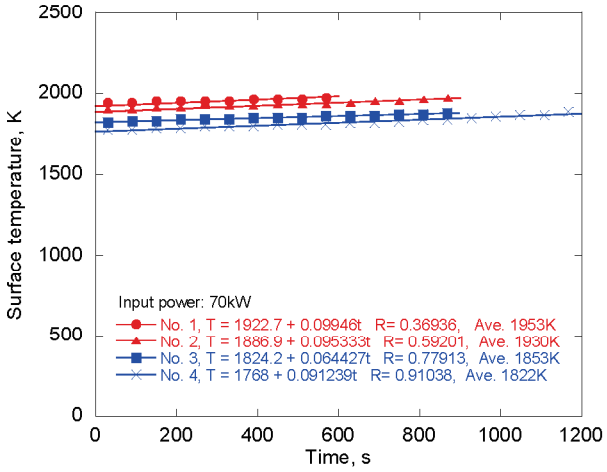

Fig. 4 Time history of surface temperature at the stagnation point.

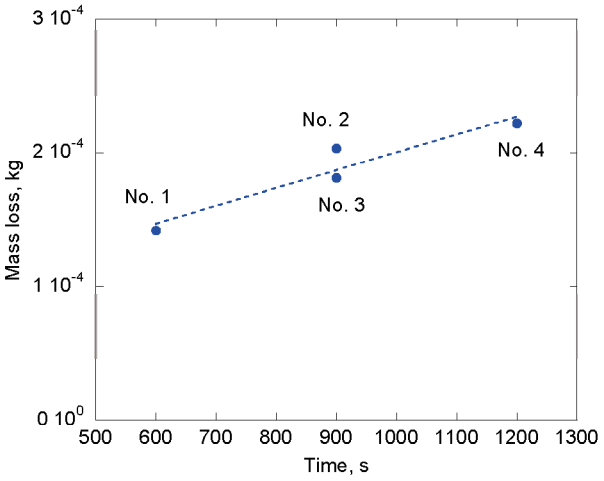

Fig. 5 Comparison of mass loss of graphite test piece.

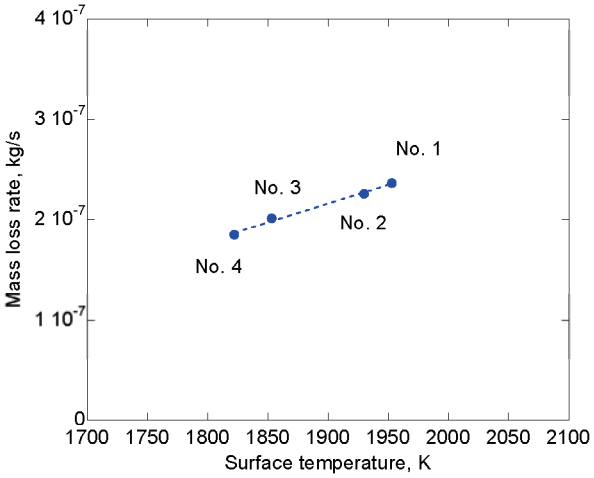

Fig. 6 Mass loss rate plotted against temperature.

Table 2 Mass loss rate of graphite test piecies

Test piece No.	1	2	3	4
Exposure time, [s]	600	900	900	1200
Average temperature, [K]	1953	1930	1853	1822
Mass before heating, [g]	0.6475	0.6478	0.6419	0.6459
Mass after heating, [g]	0.5058	0.4447	0.4609	0.4240
Mass loss [%]	21.88	31.35	28.20	34.36
Mass loss, [kg]	1.417E-4	2.031E-4	1.810E-4	2.219E-4
Mass loss rate, [kg/s]	2.362E-7	2.257E-7	2.011E-7	1.849E-7
Reaction probability	0.00378	0.00363	0.00330	0.00306

time of 1200s. Figure 5 shows the amount of mass loss as a function of exposure time. As shown in Fig. 5, the amount of mass loss of graphite test piece increases with time as expected. Note that the amount of mass loss for the case of test piece No. 2 is larger than that for the case of No. 3 though both of test piecies are heated with same exposure time of 900 s. This difference is due to the fact that the surface temperature for the case of No. 2 is higher than that for the case of No. 3, as shown in Fig. 4. As a result, the mass loss rate for the case of No. 2 becomes larger than that for the case of No. 3. The mass loss rate of graphite test piece obtained in this study are plotted against surface temperature in Fig. 6. From the figure, one can see that mass loss rate of graphite increases as temperature increases.

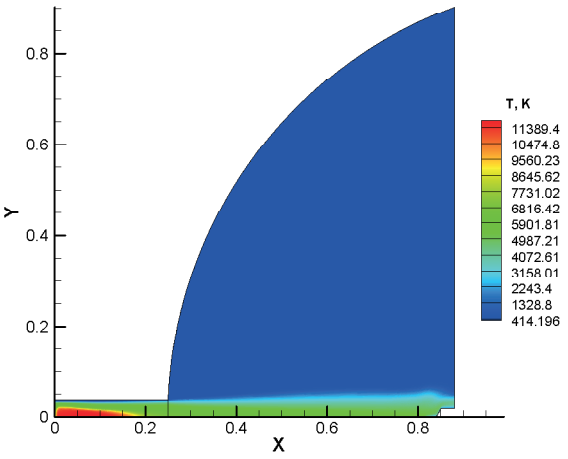

Fig. 7 Computational meshes for 110kW ICP heated wind tunnel facility installed in IAT of JAXA.

B. Numerical Results

In order to evaluate atomic nitrogen density in the test section, numerical analysis around the test piece is made under the ICP wind tunnel test condition. Inlet boundary condition at the entrance of the test chamber is given by the solution obtained by the plasma toarch flowfield analysis. Figure 7 shows typical example of temperature contours for the converged solution. Because of significant heating in the plasma toarch, the temperature becomes larger than 10,000 K, and then gradually decreases toward the test piece.

Calculated temperature, density and species concentrations along the stagnation line in the test chamber are shown in Figs. 8(a)-8(c), respectively. For the purpose of comparison, measured values using radiation spectroscopy by Fujita et al.[10] are given in the same figures. In the work by Fujita et al., radiation spectroccopy of flows in the ICP heated wind tunnel is conducted to evaluate the flow properties in the test section. The measurements are made at 372mm from the coil center (at 364mm from the test piece). By comparing the measured spectrum with that calculated by using the computer code named SPRADIAN2, molecular temperature and species concentrations are determined for nitrogen test flow at the wind tunnel test condition of 90 kW. Although the measured values were obtained for different input power condition from the present study, it is found from Figs. 8(a)-8(c) that the agreement between the calculation and the measurement is fairly good.

As shown in Fig. 8(a), a maximum temperature value of about 6800 K is obtained at the entrance of test chamber, and then gradually decreases toward the test piece. One can also see from Fig. 8(a) that thermal equilibrium is

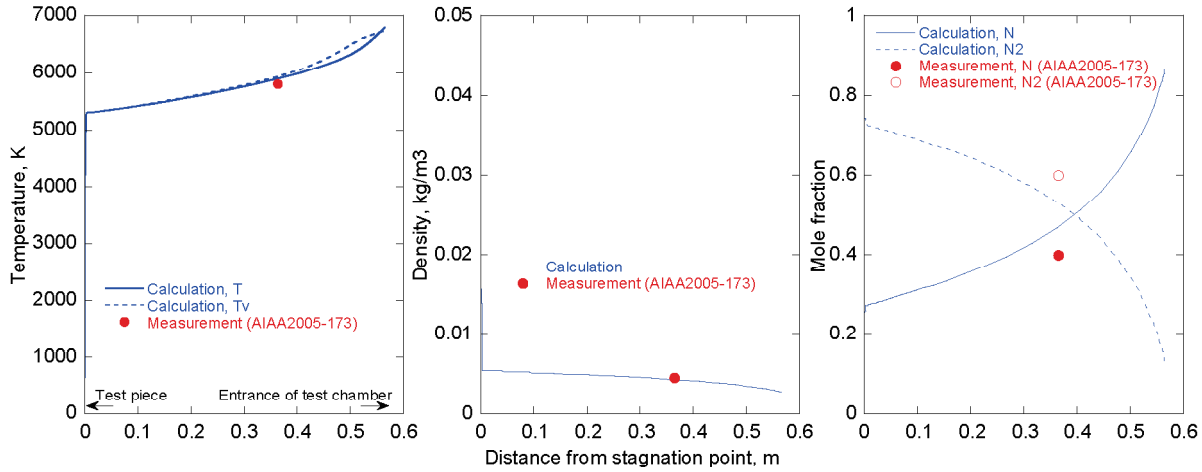

(a) Temperature **(b) Density** **(c) Mass concentration**

Fig. 8 Flow properties along stagnation line.

reached in the entire region. Figure 8(c) represents the mole fraction of atomic and molecular nitrogen. From this figure, one can see that recombination of atomic nitrogen occurs along the stagnation line. The mole fraction of atomic nitrogen at the test piece surface is about 0.25. From Figs. 8(b) and 8(c), atomic nitrogen density at the test piece surface for the present heating condition is estimated, and is found to be 7.0×10^{-4} kg/m^3.

C. Probability of Nitridation Reaction

We first consider the reaction probabirity of nitridation reaction for the case of test piece No. 1. In Fig. 9, Eq. (5) is plotted as a function of reaction probability with the surface temperature of 1953 K and the atomic nitrogen density of 7.0×10^{-4} kg/m^3. For the purpose of comparison, Eq. (5) with the atomic nitrogen densities of 7.0×10^{-3} and 7.0×10^{-5} kg/m^3 is also shown in the same figure. As shown in this figure, the smaller density we assume, the larger reaction probability becomes. The reaction probability is then found to be 0.00378 with the density value calculated in this study.

The reaction probability values for all test piecies are plotted against reciprocal temperature in Fig. 10. The results obtained by Park and Bogdanoff[6] and the reaction probability for the oxidation reaction in Eq. (1), taken from Ref. 7, are also shown for comparison. The reaction probability values obtained in this study are 0.00378, 0.00363, 0.00330 and 0.00306, respectively. Those values are also shown in Table 2. From the figure, one can see that the probability values of nitridation reaction are smaller that those of oxidation reaction.

As Fig. 10 shows, the reaction probability obtained in this study is substantially smaller than that obtained by Park and Bogdanoff. The exact reason for this distinction remains uncertain. However, in order to examine the reaction probability in the course of the present study, more work will be needed. Because the thermochemical state in the boundary layer is affected by the surface reaction product, CN, the amount of atomic nitrogen around the test piece will be changed. This modification in turn affects the amount of mass loss of test piece. Such effects are not included in the calculation made in this study. In addition, because surface shape of test piecies changes due to the nitridation reaction during the heating tests, constant surface area assumption made in this study will be no more reasonable. In order to examine these effects, and to estimate the flow density more accurately, the flowfield around the test piece need to be calculated by coupling with the thermal response calculation of the test piece. Such coupled calculation will be made in the future.

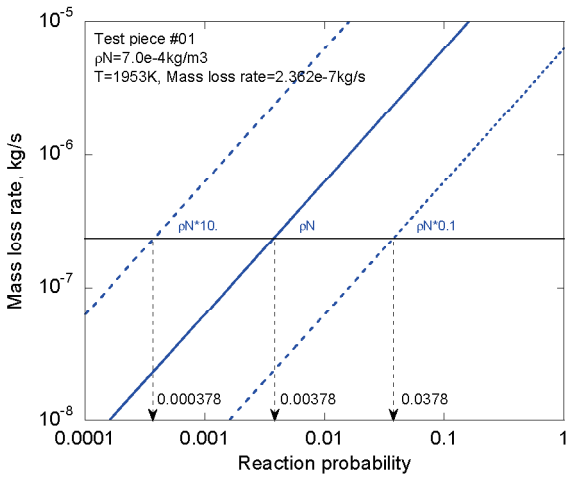

Fig. 9 Mass loss rate obtained in this study for the case of test piece No. 1.

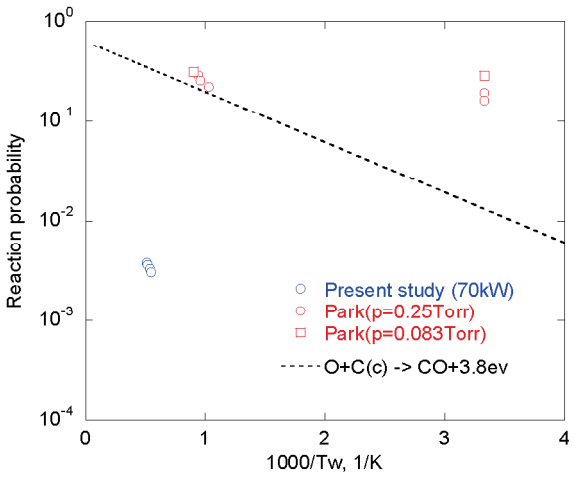

Fig. 10 Nitridation reaction probability values plotted against reciprocal temperature.

V. Conclusions

Heating tests are conducted in the 110kW ICP heated wind tunnel in IAT of JAXA. In the tests, graphite test piecies are exposed to nitrogen test flow. Mass loss of test piecies due to nitridation reaction are measured after the heating tests. A maximum mass loss of about 34% is obtained for the exposure time of 1200s. In order to evaluate the flow properties in the test section, the flowfield around the test piece is calculated under wind tunnel freestream condition. The freestream condition is evaluated by calculating the flows in the ICP heater fully theoretically. From

the study, the atomic nitrogen density at the stagnation point is found to be 7.0×10^{-4} kg/m^3. Using the amount of mass loss of test piece and atomic nitrogen density so evaluated, the reaction probability of nitridation is determined. The obtained probability value is about 0.003 for the temperature of about 1900K. It is found out that probability obtained in this study is about 1/100 smaller than that obtained by Park and Bogdanoff.

The present work relies partly on the accuracy of estimated flow density. More work will be needed to evaluate the amount of the atomic nitrogen around the test piece. It is desiable that the flowfield in the test section is calculated by accounting for the surface reaction product and shape change of test piece during the heating tests.

Acknowledgments

The first author appreciates various technical suggestions for the experiment given by Messrs. Kiyomichi Ishida, Junsei Nagai and Masashi Taniguchi of the Wind Tunnel Technology Center of JAXA. This work was partly supported by the Grant-in-Aid for Young Scientists (B) (No. 18760613) from the Ministry of Education, Culture, Sports, Science and Technology in Japan.

References

[1]Working Group of Asteroid Sample Return Mission, "A Program of Exploring an Asteroid (MUSES-C), The Proposal," Institute of Space and Astronautical Science, Kanagawa, Japan, March 1995.

[2]Institute for Unmanned Space Experiment Free Flyer, "Unmanned Space Experiment Recovery System," URL: http://www.usef.or.jp/English/f3_project/users/f3_users.html [cited 12 March 2006].

[3]Rosner, D. G., and Allendorf, H. D., "Comparative Studies of the Attack of Pyrolytic and Isotropic Graphite by Atomic and Molecular Oxygen at High Temperatures," *AIAA Journal*, Vol. 6, April 1965, pp. 650-654.

[4]Marsh, H., O'Hair, T. E., and Wynnes-Jones, L., "The Carbon-Atomic Oxygen Reaction Surface-Oxide Formation on Paracrystalline Carbon and Graphite," *Carbon*, Vol. 7, May 1969, pp. 555-566.

[5]Lundell, J. H., and Dickey, R. R., "Ablation of ATJ Graphite at High Temperatures," *AIAA Journal*, Vol. 11, Feb. 1973, pp. 216-222.

[6]Park, C., and Bogdanoff, D. W., "Shock-Tube Measurement of Nitridation Coefficient of Solid Carbon," *Journal of Thermophysics and Heat Transfer*, Vol. 20, No. 3, 2006, pp. 487-492.

[7]Park, C., "Effect of Atomic Oxygen in Graphite Ablation," *AIAA Journal*, Vol. 14, No. 11, 1976, pp. 1640-1642.

[8]Park, C., Jaffe, R. L., and Partridge, H., "Chemical-Kinetic Parameters of Hyperbolic Earth Entry," *Journal of Thermophysics and Heat Transfer*, Vol. 15, No. 1, 2001, pp. 76-90.

[9]Suzuki, T., Sakai, T., and Yamada, T., "Calculation of Thermal Response of Ablator Under Arc-Jet Flow Condition," *Journal of Thermophysics and Heat Transfer*, Vol. 21, No. 2, 2007, pp. 257-266.

[10]Fujita, K., Mizuno, M., Ishida, K., Ito, T., Sumi, T., and Kurotaki, T., "Spectroscopic Diagnostics of Electrically Heated High Enthalpy Wind Tunnels," AIAA Paper 2005-173, 43rd AIAA Aerospace Sciences Meeting and Exhibit, Reno, NV, Jan. 10-13, 2005.

[11]Ando,K., Sakai, T., and Yamada, T., "Calculation of Flows in an Inductively Coupled CO_2 Plasma Wind Tunnel," Symposium on Flight Mechanics and Astrodynamics, 2006, in Japanese

[12]Suzuki, T., Furudate, M., and Sawada, K., "Unified Calculation of Hypersonic Flowfield for a Reentry Vehicle," *Journal of Thermophysics and Heat Transfer*, Vol. 16, No. 1, 2002, pp. 94-100.

[13]Wada, Y., and Liu, M. S., "A Flux Splitting Scheme with High Resolution and Robustness for Discontinuities," AIAA Paper 94-0083, Jan. 1994.

[14]Park, C., *Nonequilibrium Hypersonic Aerothermodynamics*, John Wiley and Sons Inc., New York, 1989

[15]Park, C., "Review of Chemical-Kinetic Problems of Future NASA Missions. I: Earth Entries," *Journal of Thermophysics and Heat Transfer*, Vol. 7, No. 3, 1993, pp. 385-398.

[16]Park, C., Howe, J. T., Jaffe, R. L., and Candler, G. V., "Chemical-Kinetic Problems of Future NASA Missions. II. Mars Entries: A Review," *Journal of Thermophysics and Heat Transfer*, Vol. 8, No. 1, 1994, pp. 9-23.

Computational Analysis of Impulse Generation Mechanisms in Intense Laser-Solid Interaction

Takeharu Sakai*
Nagoya University, Nagoya, 464-8603, Japan
Kohei Anju†, Kensuke Sawada‡,
Tohoku University, Sendai, 980-8579, Japan
Koichi Mori§, and Akihiro Sasoh¶
Nagoya University, Nagoya, 464-8603, Japan

A computational technique is developed to study the impulse generation mechanisms with the laser ablation of a solid material. One-dimensional heat conduction equation of a solid material is solved to calculate vaporizing, melting, and heat-conducting process of the material irradiated by a laser beam. Vaporized plume expansion process into a background gaseous environment is calculated by solving one-dimensional Euler equations. The plume of the ablated material is assumed to be a local thermal equilibrium plasma, and the emission and laser beam absorption of the plasma are accounted for in the calculation of the plume expansion process. The flow calculation is coupled with the heat conduction calculation. The technique is applied to compute the time variation of the impulse data for the ablation of an aluminum target using Nd:YAG laser. The computed results are compared with the measurement conducted using the Velocity Interferometer System for Any Reflector(VISAR).

Nomenclature

C_{pl} = specific heat of liquid aluminum , 901 J/(kg K)
C_{ps} = specific heat of solid aluminum , 2229 J/(kg K)
c = velocity of light, 2.998×10^8 m/s
e = elementary electrical charge, 1.602×10^{-19} C
E_L = incident laser specific intensity, W/m^2
h = Planck constant, 6.626×10^{-34} J·s
I_{ion} = First ionization energy, 48,318 cm^{-1}
k = Boltzmann constant, 1.381×10^{-23} J/k
m = mass, kg
n = number density, m^{-3}
p = pressure, Pa
Q = partition function
R_f = reflectivity
R_u = universal gas constant, 8.314 J/(mol K)
x = coordinate in flowfield, m
T = temperature, K
T_m = melting temperature, 933.5 K
T_{bp} = normal boiling temperature, 2740 K

*Associate Professor, Department of Aerospace Engineering
†Graduate Student, Department of Aeronautics and Space Engineering
‡Professor, Department of Aeronautics and Space Engineering
§Associate Professor, Department of Aerospace Engineering
¶Professor, Department of Aerospace Engineering

t = time, sec
u = velocity, m/s
z = coordinate within solid, m
ΔH_m = latent heat of fusion, 10.3 kJ/mol
ΔH_v = latent heat of fusion at normal boiling point, 288.3 kJ/mol
ϵ = emission energy density, W/m^3
$\tilde{\epsilon}$ = internal energy, J/m^3
κ = thermal conductivity, W/(m K)
κ_l = thermal conductivity of liquid alminum, 100 W/(m K)
κ_s = thermal conductivity of solid alminum, 225 W/(m K)
λ = laser wavelength, m
ρ = density, kg/m^3
ρ_l = density of liquid alminum, 2700 kg/m^3
ρ_s = density of solid alminum, 2700 kg/m^3
η = degree of ionization

Subscripts

a = atom
B = Bremsstrahlung
b = background ambient gas
bp = boiling point
e = electron
IB = Inverse Bremsstrahlung
i = ion
int = liquid-vapor interface
l = liquid
m = melt
s = solid
sf = surface of a solid
t = target
v = vapor

I. Introduction

The impulse generated by the interaction of pulsed laser with a solid target is expected to be used for a number of space technology applications such as propulsion in space and a removal method of space debris, and a launch system to space.[1] A key issue to develop such space technologies by using laser power is to understand the impulse generation mechanisms during the ablation of the solid by the pulsed laser heating. Because laser ablation phenomenon is affected by a number of physical parameters such as target thermophysical characteristics, laser wavelength, laser intensity and pulse duration, and an ambient gas pressure, and so on, we must examine the impact of these parameters on the generation of the impulse and must know how efficiently the impulse can be produced by changing these physical parameters.

Recently, the time variation of the surface pressure of a solid target irradiated pulsed-laser beam is measured using a velocity interferometer called VISAR (Velocity Interferometer System for Any Reflector).[1,2] Figure 1 shows the schematic diagram of the laser ablation measurement using VISAR system. In VISAR, the velocity of the back-surface target in motion is measured based on a velocity interferometer using an optical detecting system. The impulse is evaluated by integrating the pressure on the local surface of the target. Further details are given in the papers,[1,2] and are omitted here. Measurements are carried out using Nd:YAG laser with the laser wavelength of 1064 nm or CO_2 laser with 10.6 μm. Aluminum and polyacetal are used as the target material. The ambient environment is filled with air. The measurement are made under the different ambient pressure ranging 10^{-2} to 10^5 Pa.

Laser ablation phenomenon is not well understood yet. Extensive efforts have been made to numerically simulate laser ablation phenomenon for various purposes.[3] The real-time impulse data measured by Sasoh et al. offer an opportunity to validate the current computational capabilities. It is the purpose of the present work to develop a computational method to calculate laser ablation phenomenon. The method will be used

to analyze the impulse generation mechanism during laser ablation.

The present paper is a progress report. A preliminary result is presented for the case of laser ablation of alminum target using Nd:YAG laser. Calculation is made for the case of the ambient pressure of 10^{-2} Pa. Calculated impulse data is compared with the measured real-time impulse data for the validation of the numerical method developed in the present work.

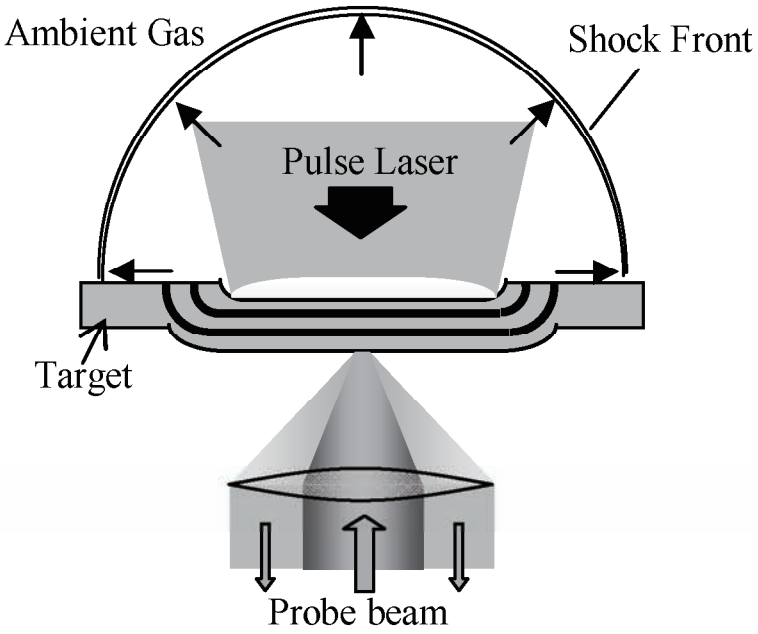

Figure 1. Schematic diagram of laser-ablative impulse measurement using VISAR

II. Numerical and Physical Modeling

In order to simulate laser ablation phenomenon, the flowfield that vaporized material expands and the heat conduction within aluminum solid target irradiated laser beam are calculated simultaneously. Various analytical models for the simulation of laser ablation are reviewed by Bogaerts et al.[3] Although a detailed explanation for the models is given therein, the present method is briefly explained next.

A. Flowfield

The expansion process of the metallic vapor produced by the ablation of solid aluminum is calculated using a computational fluid dynamics technique. The one-dimensional inviscid flow is assumed to be perfect gas. Mass, momentum, and energy conservation equations are solved using a finite volume method. The conservation equations can be written as

$$\frac{\partial \mathbf{Q}}{\partial t} + \frac{\partial \mathbf{F}}{\partial x} = \mathbf{S}$$

$$\mathbf{Q} = \begin{pmatrix} \rho_v \\ \rho_b \\ \rho u \\ e \end{pmatrix} \mathbf{F} = \begin{pmatrix} \rho_v u \\ \rho_b u \\ \rho u^2 + p \\ (e+p)u \end{pmatrix} \mathbf{S} = \begin{pmatrix} 0 \\ 0 \\ 0 \\ \kappa^{IB} E_L - \epsilon_B \end{pmatrix}$$

where $\rho = \rho_v + \rho_b$. ρ_b denotes the background ambient gas, and air is used as was in the experiment.[1,2] The air is represented by a perfect gas with the specific heat of 1.4. The gas pressure is given by the equation of state for perfect gas

$$p - (1+\eta) n_v kT + n_b kT.$$

Unsteady solutions are obtained by numerically integrating the equations using an Euler explicit method. Computed flow properties are second order accurate in space using the MUSCL approach. the primitive variables (ρ, u, p) are interpolated in the MUSCL approach. The numerical flux function is evaluated using the AUSM-DV scheme.[4] For the boundary condition at the vaporizing surface, the numerical flux function is calculated similarly by specifying the vapor properties such as density, velocity and pressure in a ghost cell. These properties will be explained in a later subsection. The source term $\mathbf{S}$ represents the loss and gain of the internal energy by radiation emission and absorption. The first term in the radiative source term stands for the absorption of laser intensity, and the second one represents the emission from the high temperature vaporized gas. These terms will be explained more details next.

Because the temperature of the metallic vapor plasma becomes the order of 10^4 K, the vapor is ionized and strong emission occurs. In addition, incident laser energy is absorbed by the ionized plasma, resulting that the laser beam incident onto the material target would be weaken. The thermal radiation process is represented by the continuum radiation which consists mainly of free-free transition. In the present study, the absorption and emission characteristics in the free-free transition is calculated assuming that local thermodynamic equilibrium is established.[3]

The total amount of energy emitted by the free-free transition can be written as follows[5]

$$c_B = \left(\frac{2\pi kT}{3m_e}\right)^{\frac{1}{2}} \frac{32\pi e^6}{3hm_e c^3} n_e n_i$$

The absorption coefficient is given by the sum of the contributions between electron and atom, and between electron and ion, as follows:[6]

$$\begin{aligned}
\kappa^{IB} &= \kappa^{IB}_{e-i} + \kappa^{IB}_{e-i} \\
\kappa^{IB}_{e-a} &= \left\{1 - \exp\left(-\frac{hc}{\lambda kT}\right)\right\} Q n_e n_i \\
\kappa^{IB}_{e-i} &= \left\{1 - \exp\left(-\frac{hc}{\lambda kT}\right)\right\} \frac{4e^6\lambda^3}{3hcm_e} \left(\frac{2\pi}{3m_e kT}\right)^{\frac{1}{2}}
\end{aligned}$$

The ionized state of the plasma vapor in the local thermodynamic equilibrium state is calculated by using the Saha equation

$$\frac{\eta^2}{1-\eta} = 2\frac{Q_i}{Q_a}\frac{1}{n_v}\left(\frac{2\pi m_e kT}{h^2}\right)^{\frac{3}{2}} \exp\left(-\frac{1.439 I_{ion}}{T}\right) \tag{1}$$

At present, we consider only a singly ionization reaction in the present study. The internal energy is given by

$$\bar{\epsilon} = \left\{\frac{3}{2}(1+\eta)kT + b_1 I_{ion}\eta\right\} n_v \tag{2}$$

where the symbol b_1 stands for an energy conversion factor from cm^{-1} to Joule. In order to calculate the ionization fraction η, and temperature T, Eqs.(1) and (2) are solved by an iterative procedure.

The laser beam intensity incident on the target, E_L, could be attenuated by the absorption of the plasma. This process is calculated by using Beer-Lambert law in the present study.

B. Heat conduction in solid target and vaporization

In order to calculate the pulsed laser heating of aluminum solid including melting and evaporation, one-dimensional heat diffusion equation is solved. Because the absorption length of the laser radiation is of the order of 10^{-7} m, the penetration of the laser radiation into the target is neglected and the laser radiation is assumed to be completely absorbed at the surface of the target.[7] The heat diffusion equation can be written as

$$\frac{\partial H_t}{\partial t} - v_{int}\frac{\partial H_t}{\partial z} = \frac{\partial}{\partial z}\left(\kappa_t \frac{\partial T_t}{\partial z}\right)$$

where z is the moving coordinate attached with the liquid-vapor interface. By assuming that the enthalpy H_t is a function of temperature, the temperature within the target is evaluated as follows:

$$T = \begin{cases} {H_t}/{\rho_s C_{p_s}} & H_t \leqslant \rho C_{p_s} T \\ T_{melt} & \rho_s C_{p_s} T < H_t \leqslant \rho_s C_{p_s} T_{melt} + Q_{melt} \\ T_{melt} + {(H_t - \rho_s C_{p_s} T_{melt} - \Delta H_m)}/{\rho_l C_{p_l}} & H_t > \rho_s C_{p_s} T_{melt} + \Delta H_m \end{cases}$$

The equation is discretized using the finite volume method, and solutions are obtained by integrating the discretized using an explicit method. The adiabatic condition is specified at $z = \infty$. The boundary condition at $z = 0$ is given by

$$\left(\kappa_t \frac{\partial T_t}{\partial z}\right)_{z=0} = \rho_l \Delta H_v v_{int} - (1 - R_f) E_L$$

Although the surface reflectivity R_f is believed to be reduced as the surface temperature increases, the surface reflectivity is taken to be a constant value of 0.83 in the present study. This value is determined iteratively to replicate the experimental impulse value for the case of the background ambient pressure of $10{-}2$ Pa.

The velocity of the liquid-vapor interface is determined from the flux of atoms leaving from the interface as follows:

$$v_{int} = \frac{p_v}{\rho_l \left(2\pi k T/m\right)} \tag{3}$$

where the sticking coefficient is taken to be unity in Eq. (3). The vapor pressure p_v can be calculated by using the Clasius-Clapeyron equation with the surface temperature T:

$$p_v = p_0 \exp\left\{\frac{\Delta H_v (T_{sf} - T_{bp})}{R_g T_{sf} T_{bp}}\right\} \tag{4}$$

where p_0 is 1 atm.

The vapor density, velocity, and pressure values at the evaporating surface are necessary in order to calculate the expansion of the ablated material. These values are used as the boundary condition in the CFD calculations explained earlier. The vapor pressure is given by Eq.4. The vapor density is calculated by using the vapor pressure

$$\rho_v = \frac{p_v m}{k T_{sf}}$$

The velocity of vapor leaving from the surface is given by assuming that the particles have a Maxwellian distribution

$$v_v = \left(\frac{2kT_{sf}}{\pi m}\right)^{\frac{1}{2}}.$$

Initial conditions are as follows: the ambient pressure and temperature in flowfield are taken to be $10^{\ -2}$ Pa and 300 K, respectively. The temperature within the target is taken to be 300 K. The 201 grid points (200 computational cells) are used for the flowfield. The non-uniform spacing grid is used and the minimum spacing adjacent to the target boundary is taken to be 10 nm. For the heat conduction equation, the 1001 grid points with the uniform spacing of 20 nm. The global time step is determined by comparing the minimum time step between for the heat conduction calculation and for the flowfield calculation. The value of the time step size is typically of the order of 10^{-14} s in the present study. Thermophysical parameters of aluminum are summarized in Nomenclature.

III. Results and Discussion

The present numerical method is applied to calculate the pulse laser ablation experiment using aluminum target for the case of the background ambient gas pressure of 10^{-2} Pa. Figure 2 shows the time variation of the incident laser intensity. Two laser intensity profiles are given in the figure for the cases with and

without the laser beam attenuation by the vapor plasma. The profile with attenuation stands for the laser intensity reaching at the target surface after passing through the plume of the vaporized material. Note that the intensity profile without attenuation is taken from the experimental laser output measured using a photon detector and is here given for the purpose of comparison. The duration time of the laser pulse is approximately 18 ns. From the intensity profile with attenuation, one can see that the intensity is abruptly reduced at the time of about 10 ns. This is due to the absorption of the original laser beam by the expanding plasma produced by the ablation of the target. After this reduction, the laser intensity increases again. Because the vapor plasma emits strong radiation, the internal energy of the vapor plasma is reduced and the temperature is decreased. As a result, the absorption by the vapor plasma is weaken.

In Fig. 3, the calculated surface temperature is plotted against time. The target begins to melt at about 1 ns after the pulsed laser heating. The evaporation starts at about 5 ns, and the total evaporated depth is approximately 50 nm, though the results are not shown here. The surface temperature reaches the maximum value of 5,650 K at about 10 ns. This time is correspond to the moment that the laser beam is attenuated as was explained in Fig. 2. After reaching the maximum temperature, the surface temperature gradually decreases. It should be noted that a small increase in the temperature profile after the maximum point is correspond to the second increase in the laser intensity profile seen in Fig. 2, as was described earlier.

Figures 4(a)-4(d) show the spatial distribution of the calculated temperature, pressure, velocity, and density of the expanding vapor plasma, respectively. In the figure, the results are presented for three different times, 5 ns, 10 ns, and 20 ns, respectively. It is seen from Fig. 4(a) that the vapor temperature in the thinner region near the wall increases rapidly up to 10 ns. This increase is due partly to the pulsed laser heating mainly to the absorption of the pulsed laser light by the vapor plasma. The temperature becomes the order of 10,000 to 60,000 K. The vapor temperature is decreased after 10 ns as the plume expands. The plateau of the temperature profile at 20 ns is seen from x=0.00025 to 0.00035 m. This relatively low temperature region is the result of the internal energy loss by the emission of radiation. From Fig. 4(b), the vapor pressure gradually drops apart from the target surface, and the pressure profile has its highest value near the target surface. One can see that the pressure value at 10 ns is rapidly increased as compared with the value at 5 ns. This increase will be also due to the absorption of the laser beam energy by the plasma, as is seen in Fig 4(a). One can see from Fig. 4(c) that the plume velocity reaches the maximum value of about 20,000 m/s. At 10 ns, the velocity has a strong peak near the target. This excess kinetic energy is believed to be delivered by the absorption of the pulsed laser energy. In the calculated results for the case without plasma shielding effect, this feature was not seen, though the result is not presented here. The calculated profile of vapor density at each time is similar to the one for the vapor pressure given in Fig. 4(b). In the present calculation, because the vapor plume expands into vacuum, the contact surface between air and metallic vapor could not be recognized.

In Fig. 5, the temporal variation of the impulse value is compared between measurement and calculation. The calculated impulse data is given by integrating the computed pressure at the computational cell adjacent to the target surface. The time variation of the computed profile is plotted in Fig. 6. The time variation of the experimental pressure is deduced from the impulse data given in Fig. 5, and is presented also in Fig. 6. From Fig. 5, the measured and calculated impulse values are increased as time evolves. The calculated impulse profile reaches its plateau value of about 1.5. The present calculation replicates the measured impulse value after 20 ns. However, the calculation could not predict the onset of the impulse rise in the experiment; the calculated impulse generation is delayed in comparison to the measurement. In addition, the slope in the impulse profile given by calculation is steeper than the measured one.

This result can be explained by the pressure profile presented in Fig. 6. From the figure, one can see that the pressure begins to increase after 5 ns in the present calculation. The computed pressure is quickly increased up to about 200 MPa. After the pressure profile has its maximum value, the pressure is rapidly decreased. Contrary to the calculated result, the pressure starts increasing at least at 2 ns in the experiment after the target begins to be heated. In addition, the pressure is slowly decreased compared with the calculation, keeping the higher pressure compared with the calculated pressure.

It is found from the present computation that the measured impulse value can be obtained by selecting an appropriate value of the surface reflectivity, R_f. However, qualitative nature of the impulse generation characteristics was different between calculation and measurement. A possible cause for this difference may be due to neglecting other detailed physics such as Knudsen layer effect, or the penetration of the laser intensity into the target. Whether such more detailed modeling could explain the discrepancy seen in the present study remains to be investigated in the future.

IV. Concluding Remarks

A computational method is developed to calculate the laser ablation phenomena during pulsed laser heating. The method can be used to simulate the impulse generation during the laser-solid interaction. The calculated results indicate that the effect of the plasma shielding has a strong impact on the impulse generation for the case of the low background ambient pressure. In order to fully understand the impulse generation mechanisms by laser ablation, more detailed physical modeling is needed.

References

[1]Sasoh A., Mori K., Anju K., Shimono M., Sawada K., and Zaretsky E. "Laser-Ablative Propulsion Using Polyacetal at Low Ambient Pressures," AIAA Paper 2007-1185, January, 2007.

[2]Mori K., Anju K., Sasoh A., and Zaretsky E., "Impulse generation by ND:YAG laser ablation of aluminum," AIAA Paper 2007-1187, January, 2007.

[3]Bogaerts A., Chen Z., Renaat G., and Akos V. "Laser ablation for analytical sampling: what can we learn from modeling?," *Spectrochimica Acta*, Part B Vol.58, 2003, pp.1867-1893.

[4]Wada, Y., and Liou, M. S., "A Flux Splitting Scheme with High-Resolution and Robustness for Discontinuities," AIAA paper 94-0083, January, 1994.

[5]Spitzer, L., *Physics of Fully Ionized Gases*, Interscience Publishers, London, 1956, pp.147-149.

[6]Root, R. G., "Modeling of Post-Breakdown Phenomena," in *Laser-Induced-Plasmas and Applications*, Rakziemski, L. J., and Cremers, D. A. Eds, Marcel Dekker, Inc., New York, 1989, pp.69-103.

[7]Jeong S. H., Greif R., and Rosso R. E., "Numerical modeling of pulsed laser evaporation of aluminum targets," *Applied Surface Science*, Vol. 129, May 1998, pp.177-183.

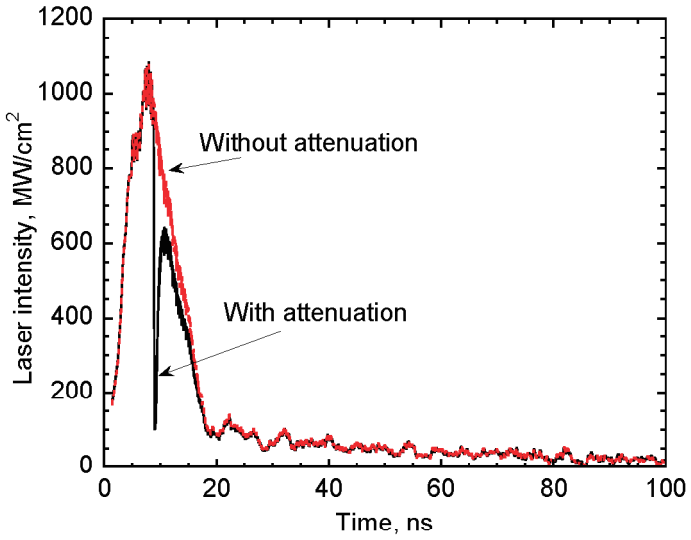

Figure 2. Comparison of time variation of incident laser intensity between with and without laser beam attenuation.

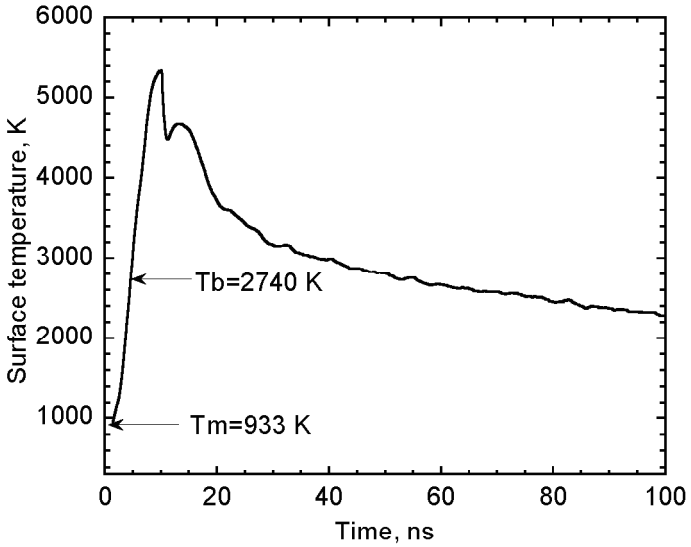

Figure 3. Time variation of calculated surface temperature

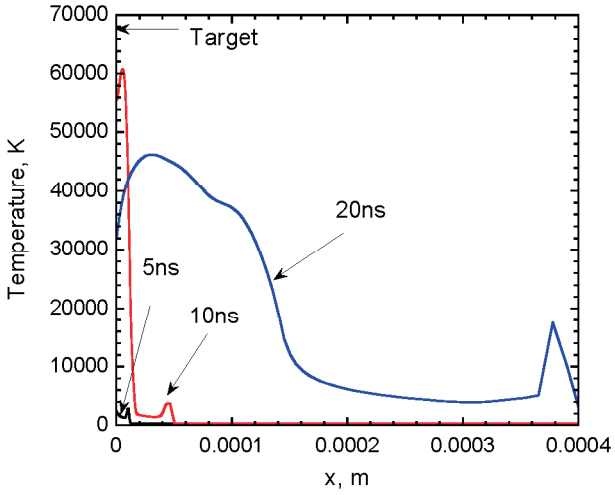

(a) Temperature

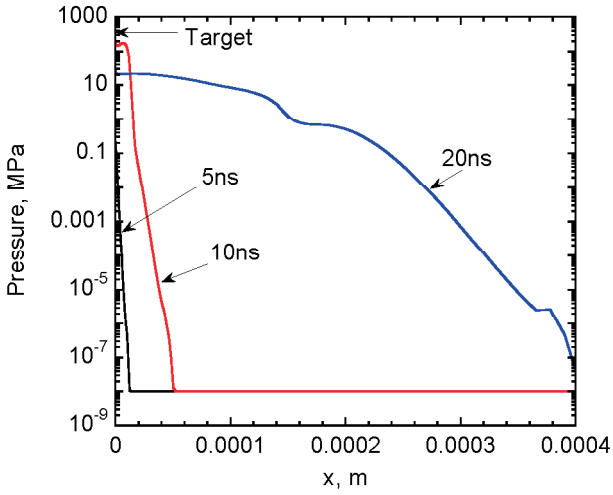

(b) Pressure

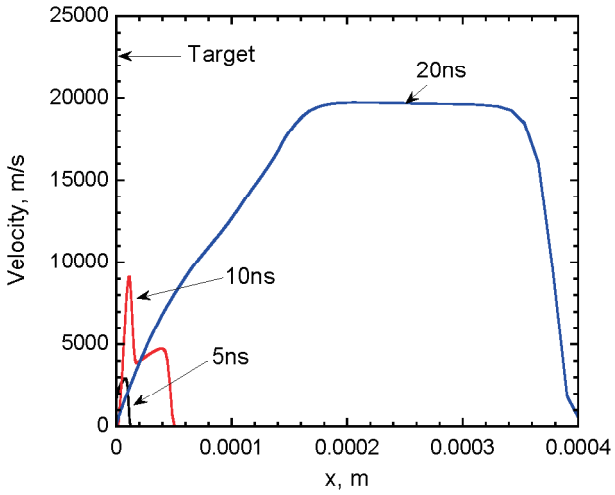

(a) Velocity

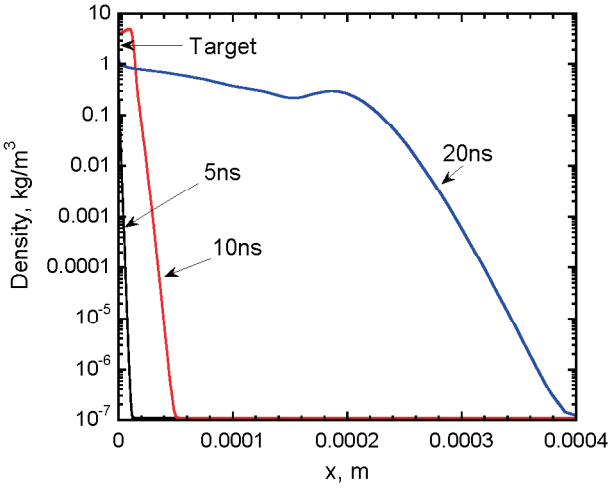

(b) Density

Figure 4. Calculated flow properties during pulsed laser heating

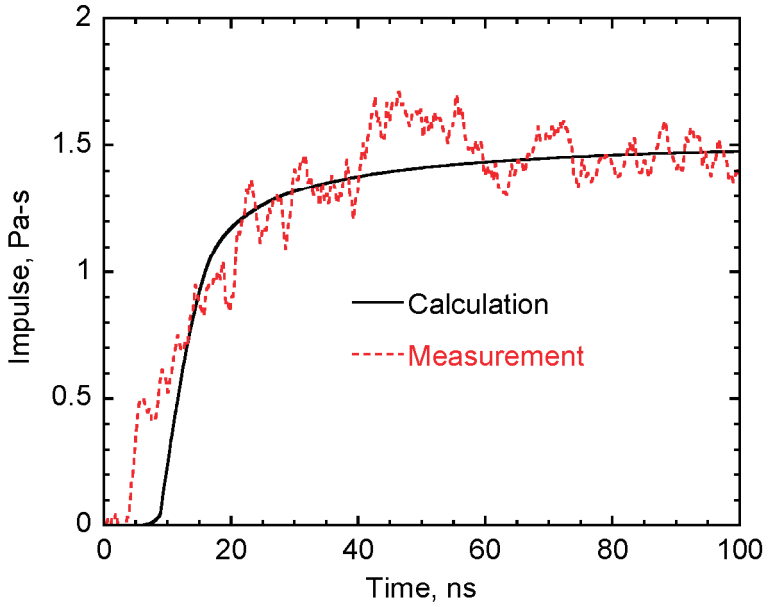

Figure 5. Comparison of impulse between measurement and calculation

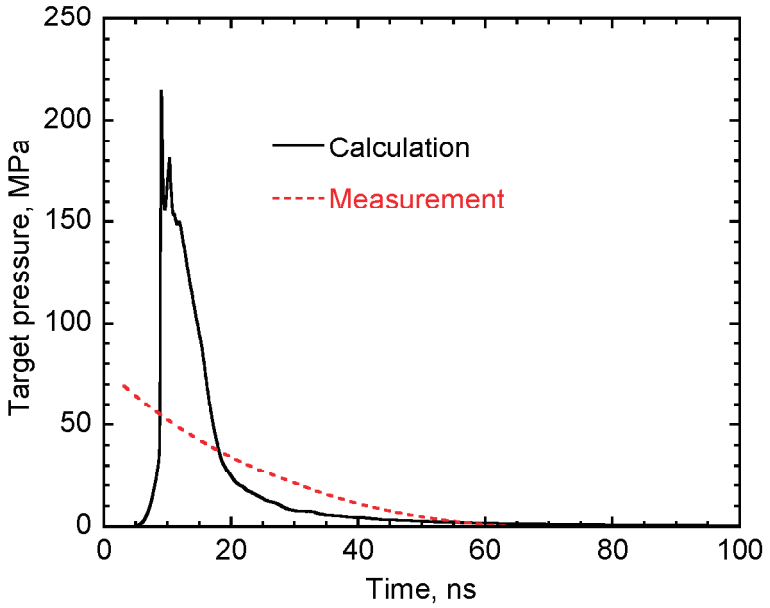

Figure 6. Comparison of target pressure between measurement and calculation

Analytical Evaluation of the Solid Rocket Motor Nozzle Surface Recession by the Alumina-Carbon Reaction

Yutaka Matsukawa and Yutaka Sato
JAXA Institute of Aerospace Technology

Abstract

A theoretical model describing the chemical ablation of a solid rocket motor nozzle ablator by the alumina-carbon reaction is presented. An application of it to a typical solid rocket motor with a graphite nozzle ablator indicates a large influence of the reaction on the nozzle surface recession.

1. Introduction

The nozzle inside of a Solid Rocket Motor (SRM) is exposed to the high enthalpy flow of the combustion gas, and hence the nozzle inside is composed of thermal protection materials, which are mainly carbonous ones. Improving the performance and reliability of the thermal protection materials for SRM nozzles is one of the issues in SRM technology, and has been addressed positively. At present, however, SRM failures are still frequently reported in the world. The number of demands for space applications using SRMs is expected to increase more and more in future years. Therefore, improving the performance and reliability of the thermal protection materials for SRM nozzles is still required.

Thermal protection materials ablate by the action of the flow of combustion gas, and consequently, the nozzle surface recesses. The recession influences on the elementary performances of a SRM and the thermal-structural performances of the nozzle since it changes the nozzle flow. Therefore, it is important in SRM technology to well evaluate the nozzle surface recession.

A variety of processes on the ablation of thermal protection materials have been proposed. Although thermal protection materials are applied not only to SRMs but also to atmospheric entry vehicles, one of the main differences between them is that SRM nozzle flow is a multiphase flow containing combustion products of condensed phase. The existence of this condensed phase in the flow complicates analyses on SRMs compared with those on atmospheric entry vehicles.

In order to evaluate the performance of thermal protection materials in high enthalpy flow, theoretical methods developed by NASA in the 1960s for atmospheric entry vehicles [1, 2] are in standard use involving applications on

SRMs. However, no standard method taking into account the influence of condensed phases in SRM nozzle flow has been developed: there are just a few particular models.

Two processes can be considered that the condensed phase directly contributes to the ablation of thermal protection materials: mechanical ablation by the collision of particles of the condensed phase, and chemical ablation by chemical reaction with the particles. As the authors know, there has been no study on the latter except Chiba's study [3]. In that study, experiments to collide alumina particles and carbon particles (as chemically inert particles) with plates of a thermal protection material were performed, and he asserted that the difference between those results is the contribution by chemical reaction.

The chemical reactivity between carbon and alumina has been discussed in metallurgy in view of technology on the carbothermal reduction of aluminum (e.g. [4]). And it could be noted that a model developed by Chiba is an empirical one which is not well discussed from chemical viewpoint.

This study presents a theoretical model describing the chemical ablation of a SRM nozzle ablator by the alumina-carbon reaction in terms of chemical viewpoint. And applying it to a typical SRM, an evaluation of the influence of this process on the SRM nozzle surface recession is performed.

2. Model

In this study, graphite is taken up as a nozzle ablator material, and hence an ablation model described here is for a non-charring material.

In neighborhood of the boundary between the combustion gas (including the condensed phase) and the nozzle ablator, gas phase, solid phase (graphite), and liquid phase (alumina) exist. It is assumed that the solid and liquid phases consist of single chemical species each, and that the gas phase consists of multiple chemical species. The balance of chemical element on the boundary is described as

$$Y_{(k)g}\dot{m}_g + J_{(k)g} - \alpha_{(k)s}\dot{m}_s + \alpha_{(k)l}\dot{m}_{(l)} = \alpha_{(k)l}\dot{m}'_{(l)} . \qquad (1)$$

Here, g, s, and l stand for gas, solid, and liquid phases, respectively. $\dot{m}$ is a mass flux relative to the speed of the nozzle surface recession. $\dot{m}_l$ is the mass flux of alumina impinging to the nozzle surface, and $\dot{m}'_l$ is the net accumulation rate of alumina on the boundary of unit area. $Y_{(k)g}$ is the mass fraction of chemical

element k in the gas phase , and $\alpha_{(k)}$ is the mass fraction of chemical element k in one mole of each phase. $J_{(k)g}$ is the diffusional mass flux of chemical element k in the gas phase, and it is described by the mass transfer correlation

$$J_{(k)g} = g_m\left(Y^w_{(k)g} - Y^e_{(k)g}\right), \quad (2)$$

where g_m is a mass transfer coefficient, and w and e represent for wall and boundary layer edge, respectively. Applying Eq. (2) into (1) derives the relation on the boundary

$$Y^w_{(k)g} = \frac{Y^e_{(k)g} + \alpha_{(k)s}B_s + \alpha_{(k)l}B''_l}{1 + B_s + B''_l}. \quad (3)$$

Here,

$$B = \frac{\dot{m}}{g_m}, \quad B' = \frac{\dot{m}'}{g_m},$$

and

$$B''_l = B'_l + B^{in}_l, \quad B^{in}_l = -B_l.$$

B^{in}_l takes positive values for the impinging flux of alumina to the surface. B_s appearing in this equations is the ablation rate of the nozzle ablator. It is noted that setting B''_l to zero reduces this formulation to the case of no alumina impingement.

The chemical composition of the gas phase on the boundary is determined on an assumption that the gas phase is in chemical equilibrium with the solid phase (graphite) at the wall temperature and pressure. B'_l is set to zero, which means no net alumina accumulation on the nozzle wall.

3. Application

3.1 SRM Model

A typical SRM of a propellant composition of AP/HTPB/AL=65/15/20 and a throat radius of 0.3 m is considered. The combustion pressure is set to 10 MPa. The chemical composition of the combustion products in the combustion chamber is calculated using the CEA2 code [5], and the resultant adiabatic flame temperature is 3300 K. The nozzle station where the Mach number of the main stream of the

nozzle flow is 2.0 is picked up here, and the ablation rate and the surface recession at this point is calculated. The nozzle main stream is calculated assuming to be a quasi one-dimensional, chemically equilibrium, and homogeneous flow. The resulting static pressure at this station is 1.5 MPa.

3.2 Ablation Rate

The calculated ablation rate with respect to the wall temperature is shown in Figure 1. The curve with $B_l^{in}=0$ is for the case of no-alumina impingement. This figure shows that the ablation rate increases with alumina impingement above about 1500 K.

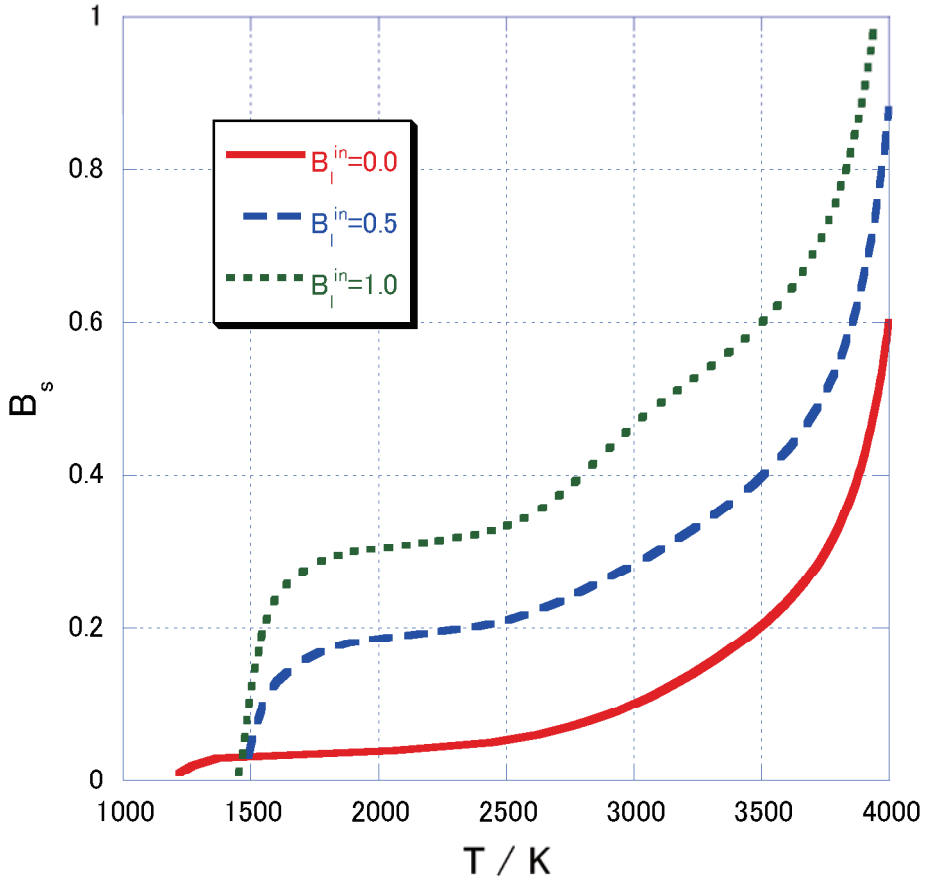

Figure 1 Ablation rate

3.3 Nozzle Surface Recession

The surface recession of the nozzle ablator is calculated by solving a heat conduction equation in the solid phase coupled with an energy balance equation on the surface using the above ablation rate. The wall temperature is determined in

this calculation. The heat transfer coefficient in the energy balance equation is calculated by the Bartz formula [6].

Figure 2 shows the temporal history of the surface recession. The recession rate increases with alumina impingement. This increase in the surface recession rate with alumina impingement is attributed to the increase in the ablation rate with that shown in Fig. 1 because, from the temporal history of the wall temperature, the wall temperature exceeds 1500 K already after 5 s for each case.

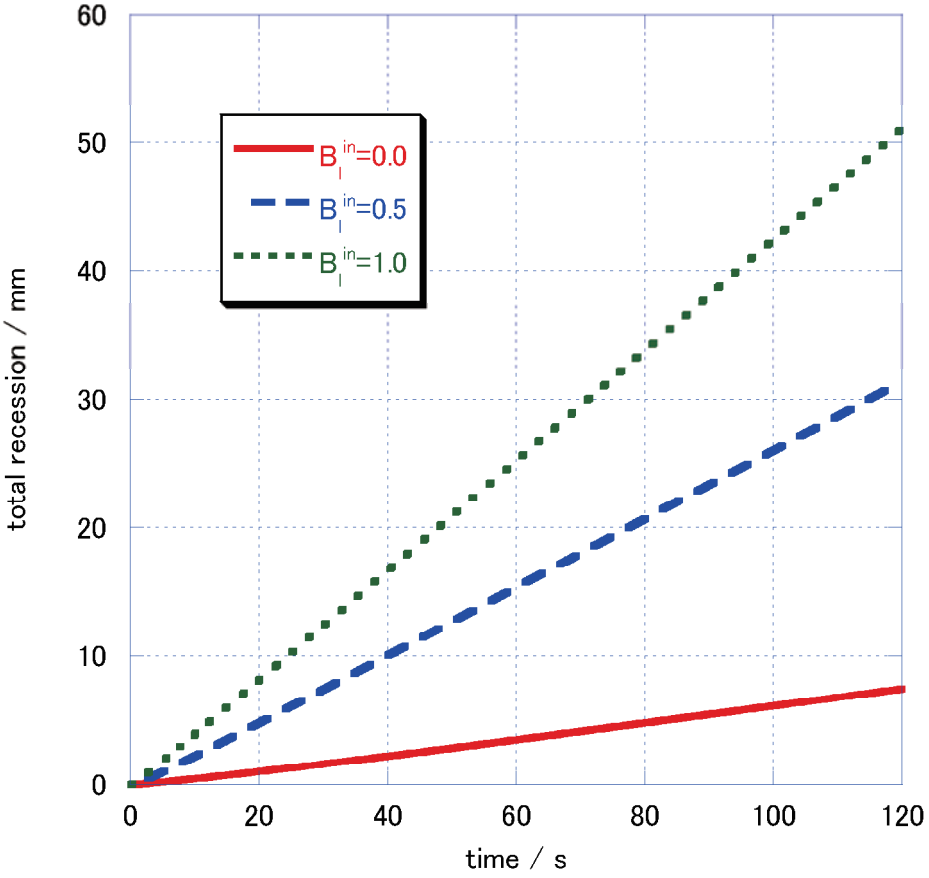

Figure 2 Surface recession

Figure 3 shows the ratio of the surface recession rate to that without alumina impingement (the rate with $B_l^{in}=0$). The ratio increases almost linearly with B_l^{in}. For the case of the SRM condition considered here, $B_l^{in}=1$ corresponds to an alumina impingement rate of about 3 kg/m^2·s, and it can be seen from this figure that the recession rate increases by a factor of about seven at this impingement rate. Although this study is not concerned with evaluating how much alumina

impinges into the surface, it seems that this value of 3 kg/m^2·s is not so large since the total mass flux at the nozzle throat is about 3000 kg/m^2·s. These results show that the model presented in this study indicates a large influence of the alumina-carbon reaction on the nozzle surface recession.

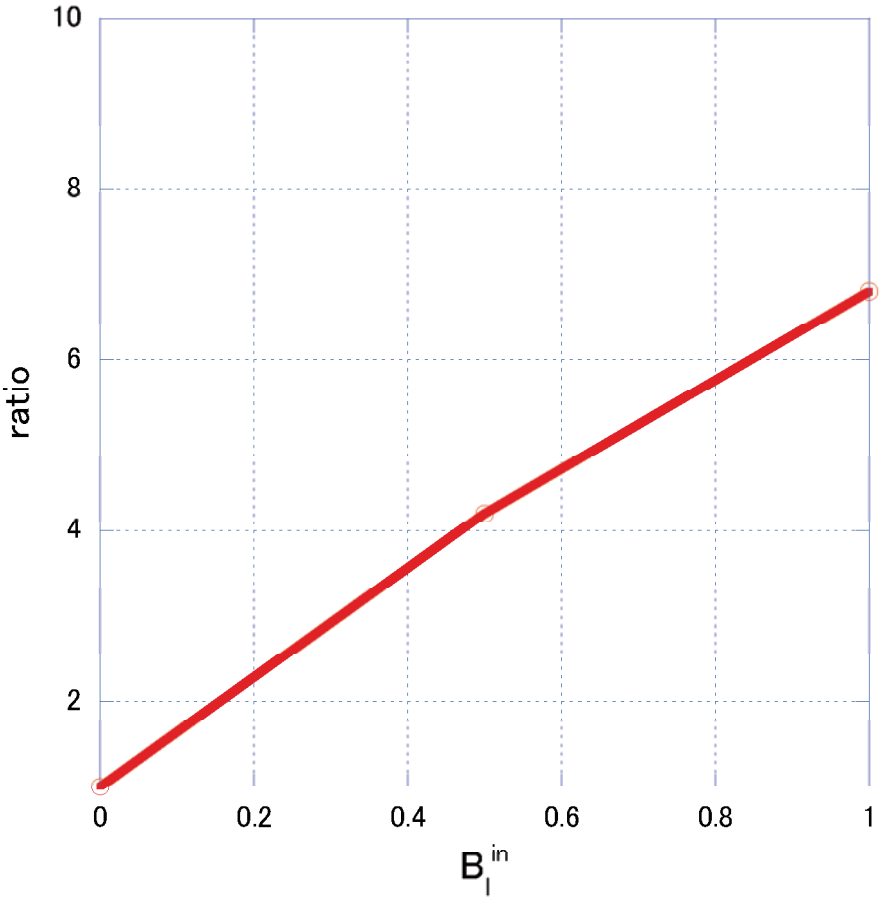

Figure 3 Ratio of the recession rate

4. Conclusion

A theoretical model describing the chemical ablation of a SRM nozzle ablator by the alumina-carbon reaction was presented. An application of it to a typical SRM with a graphite nozzle ablator indicated a large influence of the reaction on the nozzle surface recession.

References

1. Kendall *et al.*, AIAA J, 5(1967)1063.
2. Kendall *et al.*, NASA CR-1060 (1968).

3. Chiba, 1981 JANNAF Propulsion Meeting (1981)175.
4. Welch, JOM 51(1999)24.
5. Gordon and Mcbride, NASA RP-1311 (1994).
6. Bartz, Jet Propulsion 27(1957)49.

Consistency between continuous and discrete models – Another modeling problem in numerical simulation procedure –

AISO, Hideaki *

In the procedure of numerical simulation, which is widely used in science and engineering research and development activities, there are two stages of modeling. First we describe the phenomenon that we simulate by mathematical equations. It is called mathematical modeling. The mathematical description is usually a kind of continuous model including the concept of infinity or limiting etc., *i.e.* differentiation, integral and so on. Then we need the second modeling that approximates the continuous model by some discrete model that can be directly made into a computer program and computed by digital computers.

While the word "modeling" usually means the mathematical modeling, the second modeling is also an important factor in establishing the reliability of numerical methods and it is expected to realize some enough consistency between the continuous and discrete models. The lack of consistency between both models might even do harm with the discussion on the mathematical modeling.

We are concerned with the second modeling. We here discuss a few consistency (and inconsistency) problems that happen when the compressible Euler equations are discretized by differencing

1. Introduction

From the word of modeling almost all the people may imagine how to describe by mathematical equations the target phenomenon or machinery that we aim to analyze or optimize. Such mathematical description is called mathematical model and the procedure to obtain the equations is called mathematical modeling.

But in numerical simulation technology using digital computers we usually need another kind of modeling. The equations obtained through the mathematical modeling are usually continuous models like partial differential equations, which includes mathematical concepts of differentiation, integral and so on. The equations of continuous models can not be directly translated into the computer programs. Therefore we approximate the equation of continuous models by discrete equation using finite difference method, finite element method or other discretization methods and compute the discrete equation by digital computer. The obtained discrete equation is called discrete model and the discretization is another modeling to obtain the discrete models from then continuous ones.

Between the both models we naturally expect the consistency which means that the discrete model should inherit the property of the original continuous model. But it sometimes happens that the discrete model includes some fake property that does not come from the continuous model or that some essential property of continuous model is missed in the discrete model. Such inconvenience is called inconsistency between the both models. The complete consistency is usually impossible and some inconsistency is inevitable because the continuous and discrete models are different things that belongs to different categories. Then we require the discrete models' inheritance of essential property to establish reli-

*IAT (Institute of Aerospace Technology), JAXA (Japan Aerospace eXploration Agency) Jindaiji-Higashi-machi 7-44-1 Chofu TOKYO 182-8522 JAPAN, aiso@chofu.jaxa.jp

able numerical simulation. What is essential may vary according to the purpose of numerical simulation even if the same continuous model is used, and the required consistency may vary as well.

Such consistency-inconsistency problems as above are usually mathematical problems. Conventional viewpoint is that how well the discrete model approximates the continuous model, but it is also important to analyze the property or behavior of both models in parallel and compare them. In the case of partial differential equations for the motion of fluid, where the theory of exact solution is not enough, we especially need to discuss the property of discrete model from the viewpoint of consistency and inconsistency with the continuous model to improve the reliability of numerical simulation.

In this article we show and discuss a few inconsistency problems when the compressible Euler equations are discretized by Godunov method.

2. Compressible Euler Equations.

We are here concerned with difference approximation for the compressible Euler equations. We restrict ourselves into the one and two dimensional cases.

The one dimensional compressible Euler equations is written as follows.

$$U_t + F(U)_x = 0, -\infty < x < \infty, t > 0 \quad (1)$$

where $U = U(x,t)$, a function of space variable x and time t, is the vector of conservative variables

$$U = \begin{bmatrix} \rho \\ \rho u \\ e \end{bmatrix}$$

with the density ρ, the velocity u, the total energy e per unit, and F is the flux

$$F = \begin{bmatrix} \rho u \\ \rho u^2 + p \\ u(e+p) \end{bmatrix}$$

with the pressure p. U_0 is the initial value.

Similarly, the two dimensional problem is written in the form

$$U_t + F(U)_x + G(U)_y = 0, \quad -\infty < x, y < \infty, t > 0 \quad (2)$$

where the vector $U = U(x,y,t)$ of conservative variables and the fluxes F and G in x- and y-directions, respectively, are

$$U = \begin{bmatrix} \rho \\ \rho u \\ \rho v \\ e \end{bmatrix}, \; F = \begin{bmatrix} \rho u \\ \rho u^2 + p \\ \rho uv \\ u(e+p) \end{bmatrix}, \; G = \begin{bmatrix} \rho v \\ \rho uv \\ \rho v^2 + p \\ v(e+p) \end{bmatrix}.$$

u and v are velocity components in x- and y-directions, respectively.

We also assume the equation of state for ideal gas,

$$e = \frac{p}{\gamma - 1} + \frac{\rho u^2}{2} \text{ or } e = \frac{p}{\gamma - 1} + \frac{1}{2}\rho(u^2 + v^2), \quad (3)$$

where γ is the adiabatic constant.

3. Godunov method

While various methods of differencing the compressible Euler equations are proposed and each of them has its own advantage and disadvantage, we restrict our interest into Godunov method. It is one of the most naturally constructed difference methods with the use of finite volume concept and Riemann problem, although the cost of computation is not so cheap. Therefore it is a aimple and basic method in the theoretical sense and it is an appropriate discrete model to discuss the consistency problem between the continuous and discrete models.

Godunov method is finite volume scheme. First we discretize the space. We assume a discretization of uniform mesh. In one dimensional case $(-\infty, \infty)$ is discretized by the family $\{I_i\}_{i:\text{all the integers}}$ of finite volumes, where

$$I_i = (x_{i-\frac{1}{2}}, x_{i+\frac{1}{2}}),$$

$x_{i+\frac{1}{2}} = (i + \frac{1}{2})\Delta x$ with a space discretization increment Δx. In the two dimensional case $(-\infty, \infty) \times (-\infty, \infty)$ is discretized by $\{I_{i,j}\}_{i,j:\text{all the integers}}$, where

$$I_{i,j} = ((i-\frac{1}{2})\Delta x, (i+\frac{1}{2})\Delta x) \times ((j-\frac{1}{2})\Delta y, (j+\frac{1}{2})\Delta y),$$

$x_{i+\frac{1}{2}} = (i + \frac{1}{2})\Delta x$, $y_{j+\frac{1}{2}} = (j + \frac{1}{2})\Delta y$ with space discretization increments Δx and Δy in x- and y-

directions, respectively. The temporal discretization is given by $\{t^n\}_{n:\text{integers},n\geq 0}$, $t^n = n\Delta t$. Let U_i^n or $U_{i,j}^n$ an approximate value of the avarage of U

$$U_*^n = \frac{1}{I_*}\int_{I_*} U$$

over each finite volume I_i or $I_{i,j}$ at the time t^n. Using the law of conservation, the temporal evolution of integral of U over each volume I_i or $I_{i,j}$ is calculated as the sum of fluxes going across the boundary of the volume I_i or $I_{i,j}$ during the considered time. Then the finite volume scheme of difference is written in the following general form,

$$U_i^{n+1} = U_i^n - \frac{\Delta t}{\Delta x_i}\left\{\bar{F}^n_{i+\frac{1}{2}} - \bar{F}^n_{i-\frac{1}{2}}\right\} \tag{4}$$

in the one dimensional case, or

$$\begin{aligned} U_{i,j}^{n+1} = U_{i,j}^n - \tfrac{\Delta t}{\Delta x_i}\left\{\bar{F}^n_{i+\frac{1}{2},j} - \bar{F}^n_{i-\frac{1}{2},j}\right\} \\ - \tfrac{\Delta t}{\Delta y_j}\left\{\bar{G}^n_{i,j+\frac{1}{2}} - \bar{G}^n_{i,j-\frac{1}{2}}\right\}, \end{aligned} \tag{5}$$

in the two dimensional case, where $\bar{F}^n_{i+\frac{1}{2}}$, $\bar{F}^n_{i+\frac{1}{2},j}$, $G^n_{i,j+\frac{1}{2}}$ are numerical fluxes crossing the boundaries between I_i and I_{i+1}, $I_{i,j}$ and $I_{i+1,j}$, $I_{i,j}$ and $I_{i,j+1}$, respectively.

Godunov method employs the exact solution of Riemann problem naturally given at each boundary between neighboring finite volumes at each time step. In the one dimensional case a Riemann problem

$$\left\{\begin{array}{l} U_t + F(U)_x = 0 \\ U(x,0) = \left\{\begin{array}{l} U_i^n, x<0 \\ U_{i+1}^n, x>0 \end{array}\right. \end{array}\right. \tag{6}$$

is given. The problem has a self-similar exact solution $U = U(x,t;U_i^n,U_{i+1}^n) = U(x/t;U_i^n,U_{i+1}^n)$. In Godunov method the numerical flux crossing the boundary between I_i and I_{i+1} during the time interval $[t^n,t^{n+1})$ is given by

$$\bar{F}^n_{i+\frac{1}{2}} = F(U(0;U_i^n,U_i^n)) \tag{7}$$

and (4) and (7) determine the scheme of temporal evolution. In the two dimensional case, the numerical flux $\bar{F}^n_{i+\frac{1}{2},j}$ and $\bar{G}^n_{i,j+\frac{1}{2}}$ are given by

$$\bar{F}^n_{i+\frac{1}{2},j} = F(U(0;U_{i,j}^n;U_{i+1,j}^n)), \tag{8}$$

$$\bar{G}^n_{i,j+\frac{1}{2}} = G(U(0;U_{i,j}^n;U_{i,j+1}^n)) \tag{9}$$

using the solution to Riemann problems

$$\left\{\begin{array}{l} U_t + F(U)_x = 0 \\ U(x,0) = \left\{\begin{array}{l} U_i^n, x<0, \\ U_{i+1}^n, x>0, \end{array}\right. \end{array}\right. \tag{10}$$

$$\left\{\begin{array}{l} U_t + F(U)_x = 0 \\ U(x,0) = \left\{\begin{array}{l} U_i^n, x<0, \\ U_{i+1}^n, x>0, \end{array}\right. \end{array}\right. \tag{11}$$

respectively.

Unfortunately, in the case of compressible Euler equations the existence and uniqueness of exat solution is still an open problem, and any difference scheme is not proved to converge to the exact solution in any sense. But it might be expected that Godunov method would be one of the converging difference schemes if some difference schemes could be proved to converge to the exact solution.

In the following sections, we discuss a few inconvenient numerical behaviors of Godunov method. They may happen regardless with the sizes of difference increments. But the behaviors are those of discrete model and they do not necessarily prevent the scheme from convergencs as the difference increments tend to zero. On the contrary a difference scheme may still admit such kind of inconveniences even if its convergence proof is given.

4. Numerical instability around a strong shock wave.

It has been recognized from a time even before the article [2)] that mentions it first that some strange instability may occur in the numerical computation for compressible Euler equations when strong shock waves are formed. The instability is called *carbuncle phenomenon* or *carbuncle instability.* [2)] gives discussion from the viewpoint that the instability is from difference schemes.

From the experience, we already know some facts on the carbuncle instability. The instability occurs only in the case of multidimensional computation, even though the flow phenomenon

is sometimes only one-dimensional. The instability occurs when the shock surface is almost parallel to some axis of computational coordinate, but it seldom occurs when the shock surface is oblique enough to any of the axes. The stronger the shock, the more likely the instability occurs. The scale of instability has similarity to the size of computational grids, which implies that the instability comes from discrete models used in numerical computation but not from the original PDE.[1]

In [3], Moschetta et al. try to analyze the instability by comparing the linear stability of "large" system including all the variables in the computation and the occurrence of carbuncle instability in the real computation that is nonlinear. They do it in the case of stable shock that does not move in physical phenomenon, and they test a few kinds of difference schemes by using numerical derivative method to obtain each element of matrix of the "large" linear system.

In this section we observe the correspondence between some linearlized analysis and the occurrence of carbuncle instability in the case of progressing shock wave.

4.1. Numerical computation of progressing shock wave

We are concerned with the numerical computation of progressing shock wave.

We consider the initial value problem (2) with the initial value

$$U(x,0) = \begin{cases} U_L =^t [\rho_L, \rho_L u_L, 0, e_L], & x < 0, \\ U_R =^t [\rho_R, \rho_R u_R, 0, e_R], & x > 0 \end{cases} \tag{12}$$

that satisfies the Rankine-Hugoniot condition

$$F(U_R) - F(U_L) = s(U_R - U_L). \tag{13}$$

U_L and U_R are the states of both sides of planar shock parallel to y-axis progressing at the velocity s. For the physical relevancy of shock we assume the following entropy condition

$$u_L - c_L > s > u_R - c_R \text{ or } u_L + c_L > s > u_R + c_R \tag{14}$$

where $c_L = \sqrt{\gamma p_L/\rho_L}$ and $c_R = \sqrt{\gamma p_R/\rho_R}$ are the sound speeds of both side. We also assume the situation is always "fully upwind enough ";

$$u \pm c, u >> 0, c = \sqrt{\gamma p/\rho} \tag{15}$$

everywhere. Then the initial value problem (2), (12) has an entropy solution;

$$U(x,y,t) = U(x - st, y, 0) = \begin{cases} U_L, & x < st, \\ U_R, & x > st. \end{cases} \tag{16}$$

It means a progressing planar shock.

This solution is numerically calculated by Gudonov method. We impose the following CFL restriction

$$\frac{|u| + c}{\Delta x} + \frac{|v| + c}{\Delta y} \leq \frac{1}{\Delta t}. \tag{17}$$

4.2. Analysis on practical model of computation

We analyze the discrete temporal evolution (**??**) by Godunov method to examine the machinery that causes the carbuncle.

No carbuncle occurs if the initial data $\left\{U^0_{i,j}\right\}_{i,j}$ never depends on j and the discrete temporal evolution (**??**) is exactly calculated without any error. Even with errors, no carbuncle should not occur if the error at each cell $I_{i,j}$ does not depend on j.

In practical computation the errors at cells I_{i,j_1} and I_{i,j_2} might be different if $j_1 \neq j_2$.[2]

But the simple accumulation of such error is not enough to cause the carbuncle of our interest because, once any small carbuncle is recognized, it grows much faster than expected from the simple accumulation of error. Therefore it

[1] There are several different kinds of phenomena called "carbuncle". We restrict the statement only into the case of carbuncle mentioned above.

[2] It might come from the round off error in the digital representation of $\Delta y = y_{j+\frac{1}{2}} - y_{j-\frac{1}{2}}$. In fact, if we take $y_j + \frac{1}{2} = j$ as variables of "integer"-type, there is no difference of round off error at the cells $I_{i,j}$ of the same i and no carbuncle occurs. It is easily observed. But, also in this case, the instability may occur once a very small perturbation is artificially given.

is thought that the discrete temporal evolurion includes some machinery to amplify the error. Some other articles, for example, [3,1)] etc. also give discussion from a similar viewpoint.

For simplicity of analysis, we restrict the error into the exact odd-even mode;

$$\begin{aligned} &U^n_{i,j} = U^n_i + (-1)^j \hat{U}^n_i, \\ &U^n_i =^t [\rho^n_i, (\rho u)^n_i, 0, e^n_i], \\ &\hat{U}^n_i =^t [\hat{\rho}^n_i, \widehat{(\rho u)}^n_i, \widehat{(\rho v)}^n_i, \hat{e}^n_i]. \end{aligned} \tag{18}$$

The assumption is not so artificial. As mentioned in [2)], the carbuncle is almost odd-even. Furthermore, when the calculation is controlled like the footnote 2, a perturbation of the exact odd-even mode triggers the instability satisfying (18). But such control changes the property of instability very little.

The following theorem is basic in the analysis.

Theorem 1. *Asume the Godunov method. We obtain*

$$\begin{aligned} &\hat{U}^{n+1}_i \\ &= \hat{U}^n_i - \tfrac{\Delta t}{\Delta x}\left\{\tfrac{\partial F}{\partial U}(U^n_i)\hat{U}^n_i - \tfrac{\partial F}{\partial U}(U^n_{i-1})\hat{U}^n_{i-1}\right\} \\ &\quad -\tfrac{\Delta t}{\Delta y}\cdot 2\left|\tfrac{\partial G}{\partial U}(U^n_i)\right|\hat{U}^n_i + o(\delta) \\ &= \left\{I - \tfrac{\Delta t}{\Delta x}\tfrac{\partial F}{\partial U}(U^n_i) - 2\tfrac{\Delta t}{\Delta y}\left|\tfrac{\partial G}{\partial U}(U^n_i)\right|\right\}\hat{U}^n_i \\ &\quad +\tfrac{\Delta t}{\Delta x}\tfrac{\partial F}{\partial U}(U^n_{i-1})\hat{U}^n_{i-1} + o(\delta), \end{aligned} \tag{19}$$

or, in another expression,

$$\begin{aligned} &\tfrac{\partial U^{n+1}_i}{\partial U^n_i} = \left\{I - \tfrac{\Delta t}{\Delta x}\tfrac{\partial F}{\partial U}(U^n_i) - 2\tfrac{\Delta t}{\Delta y}\left|\tfrac{\partial G}{\partial U}(U^n_i)\right|\right\}, \\ &\tfrac{\partial U^{n+1}_i}{\partial U^n_{i-1}} = \tfrac{\Delta t}{\Delta x}\tfrac{\partial F}{\partial U}(U^n_{i-1}), \\ &\tfrac{\partial U^{n+1}_i}{\partial U^n_k} = O,\ i-k \neq 0, 1 \end{aligned} \tag{20}$$

where $|A|$ is determined for a diagonalizable matrix A by

$$\begin{aligned} |A| &= P\cdot diag(|\lambda_1|, |\lambda_2|, \cdots, |\lambda_n|)\cdot P^{-1} \\ &= P\begin{bmatrix} |\lambda_1| & 0 & 0 & \cdots & 0 \\ 0 & |\lambda_2| & 0 & \cdots & 0 \\ & \cdots & \cdots & \cdots & \\ 0 & & \cdots & & |\lambda_n| \end{bmatrix} P^{-1} \end{aligned} \tag{21}$$

with the diagonalization $P^{-1}AP = diag(\lambda_1, \lambda_2, \cdots, \lambda_n)$ with some matrix P.[3]

The proof is straightforward by the following lemmas 1 and 2. They are from the assumption (15) of full upwindness in x-direction and the fact that the flow in y-direction is almost acoustic.

Lemma 1.

$$\bar{F}^n_{i+\frac{1}{2},j} = F(U^n_{i,j}). \tag{22}$$

Lemma 2.

$$\begin{aligned} \bar{G}^n_{i,j+\frac{1}{2}} &= \tfrac{1}{2}\{G(U^n_{i,j}) + G(U^n_{i,j+1})\} \\ &\quad -\tfrac{1}{2}\left|\tfrac{\partial G}{\partial U}(U^n_i)\right|(U^n_{j+1} - U^n_j) + o(\delta). \end{aligned} \tag{23}$$

The both lemmas are easily proved by observing the observation of Riemann problem (**??**) or (**??**) to determine the numerical flux $\bar{F}^n_{i+\frac{1}{2},j}$ or $\bar{G}^n_{i,j+\frac{1}{2}}$, respectively.

Let $\hat{U}^n =^t [\cdots, \hat{\rho}^n_i, \widehat{(\rho u)}^n_i, \widehat{(\rho v)}^n_i, \hat{e}^n_i, \hat{\rho}^n_{i+1}, \widehat{(\rho u)}^n_{i+1}, \widehat{(\rho v)}^n_{i+1}, \hat{e}^n_{i+1}, \cdots]$. Determine the infinite matrix E^{n+1}_n by $E^{n+1}_n = \left[\frac{\partial U^{n+1}_i}{\partial U^n_k}(U^n_k)\right]_{i,k:\text{integers}}$, where each $\frac{\partial U^{n+1}_i}{\partial U^n_k}(U^n_k)$ is submatrix of the size 4×4 and indices i, k move over all the integers. Then $\hat{U}^n \mapsto \hat{U}^{n+1}$ is described as $\hat{U}^{n+1} = E^{n+1}_n \cdot \hat{U}^n + o(\delta)$. With the matrix E^{n+r}_n determined by $E^{n+1}_n = \left[\frac{\partial U^{n+r}_i}{\partial U^n_k}(U^n_k)\right]_{i,k:\text{integers}}$, $\hat{U}^{n+r} = E^{n+r}_n \cdot \hat{U}^n + o(\delta)$. Note $E^{n+r}_n = E^{n+r}_{n+r-1}\times\cdots\times E^{n+1}_n$, $r \geq 1$ and $\frac{\partial U^{n+r}_i}{\partial U^n_k}(U^n_k) = 0$ unless $i - r \leq k \leq i$.

We discuss the relation between the carbuncle and the linear stability of the map $\hat{U}^n \mapsto \hat{U}^{n+r} = E^{n+r}_n$ using discrete stable profiles of progressing shocks[4], which is explained in the beginning of next section. Our main insist is the following.

Insist. *The occurrence of carbuncle instsbility coincides with the linear instability of the map $\hat{U}^n \mapsto \hat{U}^{n+r}$*

4.3. Numerical experiments

There are two parts; preparing the profile of shock and seeing the instability.

[3] $|A|$ does not depend on P,the matrix used for diagonalization.

[4] The existence of such discrete stable profile of progressing shock is still open in theory. But it seems possible to obtain such profile numerically. It is discussed further in the next section.

4.3.1. Computation of profile

First we prepare a discrete stable profile of progressing shock numerically.

1. We use Godunov method for one dimension;
$$U_i^{n+1} = U_i^n - \frac{\Delta t}{\Delta x}\left\{\bar{F}^n_{i+\frac{1}{2}} - \bar{F}^n_{i-\frac{1}{2}}\right\}. \quad (24)$$
U_i^n's are those assumed in (18). $\frac{\Delta t}{\Delta x}$ is the same as that in the two dimensional computation later.

2. The computation domain is given by $i_{\min} \le i \le i_{\max}$ so that $i_{\max} - i_{\min}$ is large enough, and the initial values U_i^0's are given by
$$U_i^0 = \begin{cases} U_L, & i_{\min} \le i \le i_s \\ U_R, & i_s < i \le i_{\max}, \end{cases} \quad (25)$$
where U_L and U_R satisfy (13), (14), (15) and (17), and the shock speed s has a rational ratio to $\frac{\Delta x}{\Delta t}$, *i.e.* $s = \frac{q}{r} \cdot \frac{\Delta x}{\Delta t}$, q, r are positive integers relatively prime. The boundary is treated by the inflow condition at $i_{\min}$ and by the outflow condition at $i_{\max}$.

3. Proceed the discrete temporal evolution by (24).

4. Our goal is to obtain some stable profile of progressing shock. To do it within a limited domain, we shift the data every r steps of discrete temporal evolution, *i.e.* when $n \equiv 0 (\mathrm{mod} r), n > 0$, we shift back the data $\{U_i^n\}$ by r spatial nodes;
```
do i = i_min, i_max - q
  U_i^n = U_{i+q}^n
enddo
do i = i_max - q + 1, i_max
  U_i^n = U_R
enddo
```

5. Obtain the "convergence" of profile. Thanks to the data shift, in practical computation we can do it by comparing U_i^{n+r}'s and U_i^n's, for example, monitoring
$$S(n) = \sum_{i=i_{\min}}^{i_{\max}-r} \Big\{ |\rho_i^{n+r} - \rho_i^n| + |(\rho u)_i^{n+r} - (\rho u)_i^n| + |e_i^{n+r} - e_i^n| \Big\}.$$
Usually the numerical convergence is rather good and the relative order of S finally goes to 10^{-13} or so in the case of double precision computation. The obtained profile is used as the initial data $\{U_i^0\}_i$ for the test of instability.

We choose $i_{\min} = 0, i_{\max} = 1000, i_s = 100$. The choice $i_{\min} = 0, i_{\max} = 2000, i_s = 200$ is also tested. Both gives essentially the same profile.

4.3.2. Test of instability

Second we conduct two tests of instability using the data obtained above.

We see the linear stability of $\hat{U}^n \mapsto \hat{U}^{n+r}$ using E_n^{n+r}. But we need to extract some essential finite submatrix from E_n^{n+r} and choose the value of n. We choose i_- and i_+[5] so that
$$\begin{aligned} &|\rho_i^0 - \rho_L| < 10^{-4}|\rho_R - \rho_L|, i < i_-, \\ &|\rho_R - \rho_i^0| < 10^{-4}|\rho_R - \rho_L|, i > i_+ - r. \end{aligned} \quad (26)$$
Then we determine $\{4(i_+ - i_- - r)\} \times \{4(i_+ - i_- - r)\}$ matrix $\bar{E}_0^r$ by $\bar{E}_0^r = [\frac{\partial U_i^r}{\partial U_k^0}]_{i_- + r \le i \le i_+, i_- \le k \le i_+ - r}$, and numerically obtain the eigenvalue that has the largest absolute value.

We also conduct the usual two dimensional calculation by Godunov method. We test two kinds of computational domain and error triggering.

1. Computational domain is $1 \le i \le 10000, 1 \le j \le 2m$, m is a positive integer.[6] To control the error (see the footnote 2), the type of values $y_{j+\frac{1}{2}}$ and Δy on the computer program are to be "integer". The initial data $\{U_{i,j}^0\}$ are given by $\{U_i^0\}$ if $1 \le i \le 1000$, otherwise U_R. The boundaries at $i = 1, 10000$ are treated in the inflow and outflow manner, respectively. The boundaries at $j = 1, 2m$ are treated by the cyclic manner. We trigger the error by odd-even random error at $50 \le i \le 100$ of the relative order 10^{-10} or so.

[5] Practically, there is no difference in the final result of eigenvalue even if we replace 10^{-4} in (26) by 10^{-5}.

[6] There is no essential difference even if m is different. $m = 1$ is enough.

2. Computational domain is $1 \leq i \leq 10000, 1 \leq j \leq 2$. The initial data and boundary treatment are the same as the previous. The value Δy is determined so as to cause the round off error, for example, `0.7D-1`.

As far as we examined, there is no difference in the occurrence of instability between the two cases above.

4.4. Result of numerical experiments

We test various cases changing the condition. As far as our numerical experiment, the occurrence of carbuncle instability well coincides with the existence of $\bar{E}_0^r$'s eigenvalue with its absolute value exceeding 1.

We show a part of experiments' result. The part are done in a following manner.

1. The 3-shock with the characteristic $u + c$ is calculated. The parametrization $p_R/p_L = e^{\xi}$ determines the pressure ratio. $\xi < 0$ gives a shock wave. For the parametrization see [4] etc.

2. The velocity (in x-direction) is modified at the both sides of shock so that all the six characteristic speeds ($u \pm c, u$ of both sides) are positive and the ratio of the largest of them to the smallest is 10.

3. Then for $\xi = -1.0, -1.1, \cdots, -2.0$ we obtain profiles numerically with $s = \frac{1}{2} \cdot \frac{\Delta x}{\Delta t}$, and examined the linear system and two dimensional computation.

The result is shown in the following table.

ξ	Density Ratio	$i_+ - i_-$	Eigenvalue (absolute value maximum)	Occurence of carbuncle
-1.0	0.5037	37	0.9708	No
-1.1	0.4733	35	0.9779	No
-1.2	0.4455	34	0.9849	No
-1.3	0.4201	32	0.9917	No
-1.4	0.3969	31	0.9982	No
-1.5	0.3758	30	1.0044	Yes
-1.6	0.3566	29	1.0104	Yes
-1.7	0.3390	29	1.0162	Yes
-1.8	0.3231	28	1.0217	Yes
-1.9	0.3085	28	1.0269	Yes
-2.0	0.2953	27	1.0319	Yes

The table shows a good coincidence between the linear stability based on our linearization and the usual numerical computation for compressible Euler equations.

4.5. Remarks

Although the insist is not mathematically proved, it seems that numerical validation of our insist is possible. Therefore we may conclude that the carbuncle instability is caused by some kind of linear instability included in the scheme of numerical computation.

We mention that in the numerical computation of nonlinear problem the instability of computation does not always coincide with linear instability included in the nonlinear system. For example, also in the case of one dimensional computation of progressing shock wave it is possible to consider the linear system to see the amplification of small perturbation in discrete temporal evolution, but the original numerical computation is still stable even if the linear system is not stable. It is understood that the nonlinearity works to suppress the growth of instability.

Our computational validation implies that the instability caused by linear machinery grows without being suppressed by the nonlinearity. It supports the understanding that the carbuncle phenomenon is caused by some machinery existing only in multidimensional cases. There have been a dispute whether the carbuncle phenomenon is linear instability or nonlinear insta-

bility. It would be very difficult to give an correct answer to the dispute, but our numerical study gives some suggestion "the carbuncle phenomenon is basically linear instability but the instability of linear system (or the values of entries of matrix representing linear system that result instability) is from the strong nonlinearity that comes with the shock".

5. Numerical singularity in the formation of waves.

Another kind of inconvenience may be observed when waves are formed from a gap in the initial value. A similar behavior may be observed when a collision of discontinuities makes a gap from which multiple waves evolve.

We are concerned with the numerical computation by Godunov method for the Riemann problem of one dimensional compressible Euler equations (1) with the initial value

$$U(x,0)=U_0(x)\equiv\begin{cases}{}^t(\rho_-,\rho_-u_-,e_-), x<0,\\ {}^t(\rho_+,\rho_+u_+,e_+), x>0.\end{cases} \quad (27)$$

As an example of the numerical singularity, we observe the following numerical computation. The initial value of Riemann problem is the following.

$$\begin{aligned}&\rho_-=\rho_+=17.411708063,\\ &u_-=-4.560084435, u_+=4.560084435,\\ &p_-=p_+=54.59815003.\end{aligned} \quad (28)$$

where $p_\pm=(\gamma-1)\left(e_\pm-\frac{\rho_\pm(u_\pm)^2}{2}\right)$. Let the adiabatic constant $\gamma=1.4$. The exact solution has three constant states, which are

$$\begin{aligned}&(S_-)\ \rho=\rho_-, u=u_-, p=p_-,\\ &(S_0)\ \rho=1, u=0, p=1,\\ &(S_+)\ \rho=\rho_+, u=u_+, p=p_+.\end{aligned}$$

The neighboring states (S_-) and (S_0) are connected by the 1-rarefaction wave and (S_0) and (S_+) by the 3-rarefaction wave. Then the numerical computation is made with Godunov method. The number of finite volumes are 1200, and the CFL-number is 0.9. The picture shows the numerical solution when the number of time steps reaches 600.

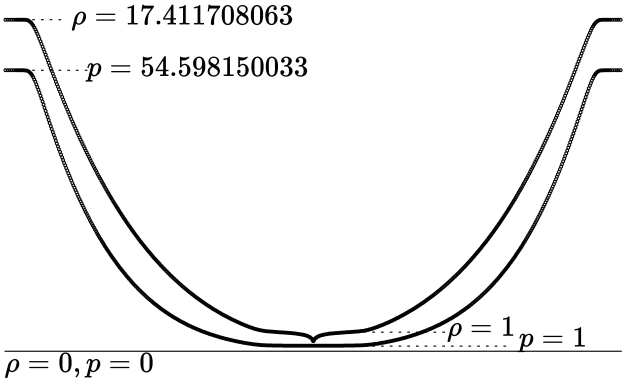

Roughly speaking the computational result has a good coincidence with the exact solution. But rather singular values are easily observed around the center. The singularity does not occur in the pressure but it clearly occurs in the density. The singularity is formed just a few steps after the start of computation. While it gets smaller until a few hundreds time steps, the singularity is completely stable at the time of picture and it never disappears nor declines.

If the convergence of scheme is discussed in the sense of L^p, the singularity does not harm with the discussion, because the nubmer of singularly valued points is uniformly finite regardless with the number of total points assumed in the discrete model. But the singularity really exists as far as we stay in the discrete model only where numerical calculation is conducted. The numerical calculation can proceed the limiting procedure only half the way but can not reach the final convergence target that is a solution of continuous model. The singular values, which are of course not physically relevant, may deteriorate the numerical result in the case of more complicated problems including reaction terms because the singular values would make the numerical estimate of reaction terms incorrect. In other words, the existence of a numerical singularity consisting of uniformly finite points could be neglected in the convergence discussion but the existence of singular value itself might do harm with the reliability of numerical computation.

Similar phenomena is observed in the case of more simple equations. We show a numerical ex-

ample for the p-system;

$$u_t + p(v)_x = 0, v_t - u_x = 0, -\infty < x < \infty, t > 0. \tag{29}$$

With $p(v) = k \cdot v^{-\gamma}$, $1 \leq \gamma \leq 3$, the p-system is a modeling of the motion of compressible gas using Lagrange coordinate. In this case, u and v mean the velocity and specific volume, respectively. Here let $k = 1, \gamma = 1.4$. We consider a Riemann problem of the following initial value.

Left state ($x < 0$): u=-3, v=1,
Right state ($x > 0$): u=3, v=1.

The following picture shows the both exact and numerical solutions of v at t=114.0958 (the number of time steps is 150). Godunov method is used to obtain the numerical solution.

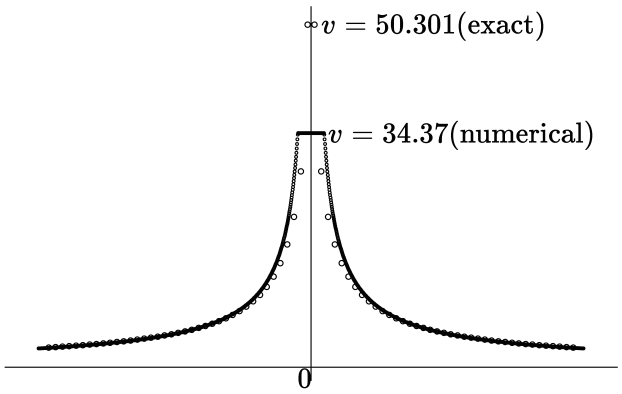

The computational region is $-40 < x < 40$, $\Delta x = 1$. The CFL-number is 0.9. In this case the analysis of discrete model is easier and it is possible to give a rough estimate of the behavior of singularity.

The both example seem alike, but there is a clear difference. This singularity disappears finally in the latter case. It seems that the main reason of this difference is that the p-system has two genuinely nonlinear characteristic fields but no linearly degenerate one. We note that three characteristic fields $u - c$, u, $u + c$ exist in the compressible Euler equations, and two $(u \pm c)$ of them are genuinely nonlinear and another (u) is linearly degenerate. On the other hand, it is easily analyzed that in the case of linear hyperbolic conservation law such a kind of singularity does not occur in the numerical calculation by Godunov method even though some smearing would be observed in a numerical result. Therefore we may conclude the following as for the numerical singularity discussed in this section.

(1) The nonlinearity of problem includes some machinery to cause numerical singularity and that it also has the machinery to erase it as the discrete temporal evolution is repeated.

(2) The coexistence of genuinely nonlinear fields and degenerated linear field in the compressible Euler equations causes some difficulty in constructing discrete models. (The nonlinearity initiates the singularity and the linearity reserves it.)

6. Conclusion

We discuss a few examples of consistency problems that lies between the continuous and discrete models. To improve the reliability of numerical simulation it is necessary to have more precise discussion on the consistency between the both models. We also need some different viewpoints of consistency other than conventional way of discussion like convergence, the order of accuracy so on.

From the viewpoint of mathematics, the coexistence of nonlinear and linear fields in the compressible Euler equations seems to give interesting problems to the numerical calculation as well as to theoretical analysis of exact solution.

References

1) H. Aiso, M. Abouziarov and T. Takahashi. Machinery of Numerical Instability in Conservative Difference Approximations for Compressible Euler Equations. . In S. Nishibata, editor, *Mathematical Analysis in Fluid and Gas Dynamics*, pages 178–191. Research Institute for Mathematical Sciences, Kyoto University, 2003.

2) J. Quirk. A contribution to the great Riemann solver debate. *International Journal*

for Numerical Methods in Fluids, 18:555–574, 1994.

3) J.-Ch. Robinet, J. Gressier, G. Casalis, and J.-M. Moschetta. Shock Wave Instability and Carbuncle Phenomenon: same intrinsic origin? . *J. Fluid Mechanics*, 417:237–263, 2000.

4) J. Smoller. *Shock waves and reaction-diffusion equations*. Springer-Verlag, NewYork, 1982.

Numerical Modeling for Supersonic Flow Analysis and Inverse Design

K. Matsushima.* D. Maruyama† and T. Matsuzawa‡
Department of Aerospace Engineering, Tohoku University, Sendai, Japan, 980-8579

For the aerodynamic wing design, the superior points of a inverse problem method are discussed as well as two mathematical models each of which is the core equation of each inverse problem are introduces. One mathematical model comes from three-dimensional potential flow equation and he thin wing theory, while the other is led from Busemann's 2nd order approximation based on the theory of oblique shock wave. The former yields the set of integral-differential equations and the latter does a quadratic equation in the corresponding inverse problem. Combining each inverse problem with residual-correction methodology and modern computational technology enables us to construct a low-cost and high-fidelity design method. To examine its capability and usefulness, several design problems have been done. Successful high-fidelity design results have been obtained for all cases. The computational cost is small. The inverse design needs about 20 time flow simulations which is much less than the cost of a general optimization.

Nomenclature

a = speed of sound
a_∞ = free-stream speed of sound
C_p = pressure coefficient
ΔC_p = difference between realized pressure coefficient and target one
c = chord length of an airfoil
c_1, c_2 = Busemann coefficients
$f(x)$, $f(x,y)$ = wing section/ airfoil geometry
Δf = amount of correction/ modification in wing section/ airfoil geometry
M_∞ = free-stream Mach number
P = pressure
P_∞ = free-stream pressure
Re = Reynolds number
t = airfoil thickness
x = airfoil-chord direction coordinate
y = span-wise direction coordinate
z = airfoil-thickness direction coordinate
α = angle of attack
β = $\sqrt{M_\infty^2 - 1}$
γ = ratio of specific heats
ρ = density
ρ_∞ = free-stream density
ϕ = velocity potential
θ = $df/dx - \alpha$ (flow deflection angle)

1 Introduction

Efficient design optimization methods are still sought after for use in aerodynamic design, though the computer performance and computational fluid dynamic (CFD) simulation technology have made great progress in these several decades. Therefore, engineers have become to desire higher-fidelity design as they have obtained more advanced simulation tools. Conventional design methods, such as gradient based one and Genetic algorithm (GA), perform optimizations using direct CFD computations. CFD computations sometimes mean Euler ones and sometimes Navier-Stokes (N-S). They, especially N-S computations still take much time to get results in sufficient detail. Usually the optimizations need a lot of number of CFD computations. Thus, the

* Associate Professor, Department of Aerospace Engineering, Email :kisam@ad.mech.tohoku.ac.jp
† Graduate Research assistant, Department of Aerospace Engineering,
‡ Graduate student, Department of Aerospace Engineering,

resulting process can be computationally very expensive. Then, designers have to limit design space or reduce the number of design parameters to save the computational cost. In this situation, could we regard the design as high-fidelity design? Flow analysis is of high fidelity, if N-S simulation with sufficient grid resolution is conducted. But, the design is not necessarily of high fidelity because they might examine only a small part of whole possible candidates.

There is another design methodology called as inverse design or (inverse problem methods). Inverse design determines the values of a set of design parameters by matching special target flow features given by a designer. They usually use mathematical models to find the solution for the set of design parameters that result in the target flow features. Inverse designs have proven valuable because once a solvable target flow feature is specified the required geometry can be obtained with fewer CFD valuations compared to a direct optimization. The refined knowledge of the target flow features allows rapid convergence towards the final design. Particularly, in the context of aerodynamic wing design, the flow feature should be surface Cp distribution. So the inverse problem provides wing geometry which realizes the target Cp distribution.

Classical inverse problem method was categorized as a low-fidelity design, since the method used mathematical models, which had been led from low-fidelity equations such as potential equation, linearized one and so on. With modern CFD technology, however, the method has attained high-fidelity design by combined with residual-correction methodology. We will discuss the methodology in Section 2. There, low-cost high-fidelity design method using inverse design and CFD computation is constructed. In Section 3, a mathematical model for three-dimensional supersonic flowfields will be discussed. An inverse design method using the model was already applied to a practical supersonic wing design [1,2] in JAXA's NEXST project [3,4]. The successful design results have been confirmed by the flight test on October 10 in 2005 [5,6]. In Section 4, another mathematical model will be discussed. The model originated from A. Busemann[7,8]. It was led by higher order approximation than the first one but is two- dimensional. The second one is being applied to the design of practical airfoils /wing-sections in a complicated flowfield. Its design applications will be also presented in the next paper. In Section 5, we will conclude the article.

At the end of the introduction, we mention additional favorable characteristic about the inverse design. In the design we can trace precise geometrical change of the wing surface because the number of geometrical control points used for the design is not strictly limited. In the case of setting 100 points in the chord direction on each of 100 span stations of the wing, which means the number of control points on the wing geometry is totally 10,000, the cost of solving a inverse problem is about 10 minutes with a 2.2Ghz PC.

2 Residual-Correction Methodology for Aerodynamic Inverse Design

The goal of the aerodynamic inverse design is to determine the surface geometry which realizes a specified target pressure distribution. The procedure is iterative. It can design a wing for not only a wing alone case but also any types of aircraft configuration.

Here the task sequence of a residual-correction method is illustrated. First, a baseline shape is to be defined. If one would like to design a wing for an airplane, the initial/ baseline shape is not a wing alone but a complete airplane where a wing is jointed with a fuselage. Then, the flowfield around a airplane is analyzed by CFD simulation to get the current pressure (Cp) distribution on the wing surface. Next the inverse problem is solved to obtain the geometrical correction value Δf corresponding to the difference between target and current pressure distributions ΔCp. Using Δf, the baseline shape is modified to be a new wing. Now, the current shape is updated. The next step is to go back to the flowfield analysis. The flow analysis is again conducted to see if the current shape realizes target pressure distribution. If the difference between target and current pressure distributions is negligible, the design is completed. Otherwise, the next step is once again to solve the inverse problem and iterate the design loop until the pressure difference becomes negligible. This iterative procedure of residual-correction concept expands the applicability of the inverse problem. Classically, the fidelity of the solution to an inverse problem method is within the extent of the basic equation to formulate the inverse problem. On the other hand, the solution can attain higher fidelity when the inverse problem is appropriately incorporated into a residual-correction method.

There are two primary parts in the design system; one is a flow analysis part which conducts grid generation and Navier-Stokes/Euler flow simulation. It evaluates the residual. The other is a design part where the inverse problem is solved to update the geometry. The design part determines the correction which is expected to compensate for the residual. Both parts are independent from each other in terms of their algorithms and basic equations as long as they are originated from flow physics. The accuracy of a design result depends on the analysis part. The flow analysis is done by a Navier-Stokes simulation code. Thus, designed geometry

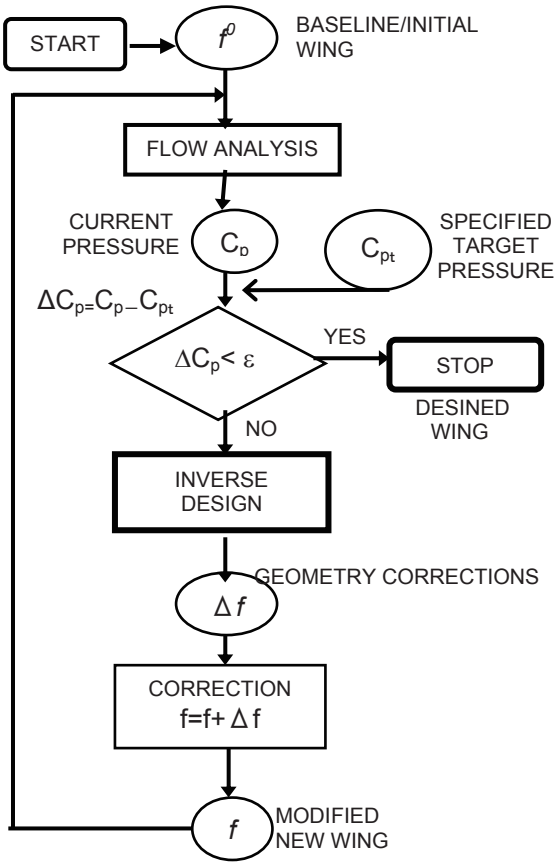

Figure 1. Residual-correction design concept

by the method will have the same fidelity as Navier-Stokes equations do.

3 An Supersonic Inverse Problem based on Three Dimensional Thin Wing Theory

3.1 Formulation of an Inverse Problem and Derived Mathematical Models

The basic equations of the first inverse problem that determines the aerodynamic geometry are

$$\left(1-M_{\infty}^{2}\right)\overline{\phi}_{\overline{x}\overline{x}}+\overline{\phi}_{\overline{y}\overline{y}}+\overline{\phi}_{\overline{z}\overline{z}}=0 \tag{3-1}$$

$$\overline{\phi}_{\overline{z}}\left(\overline{x},\overline{y},\pm 0\right)=\frac{\partial}{\partial\overline{x}}f_{\pm}\left(\overline{x},\overline{y}\right) \tag{3-2}$$

$$Cp_{\pm}\left(\overline{x},\overline{y}\right)=-2\overline{\phi}_{\overline{x}}\left(\overline{x},\overline{y},\pm 0\right) \tag{3-3}$$

where "¯" (over bar) indicates that values and functions are in the physical coordinate which has dimension.

Eq.(3-1) is the small disturbance velocity potential equation. Since M_{∞}>1.0 in supersonic flows, Eq.(3-1) is hyperbolic partial differential equation (PDE). Eq.(3-2) comes from thin wing theory and Eq.(3-3) is led by linearizng the Bernoulli equation in compressible flows [9]. The goal of the formulation is to obtain the mathematical function to relate ΔCp to geometrical correction of wing surface Δf. As stated in the previous section, the inverse problem of the residual-correction concept should handle the Δ-value, which is difference between two states of a flowfield. Thus, we take linear perturbation form of Eqs. (3-1) to (3-3) after the Prandtl-Glauert transformation Then, applying Green's theorem to the hyperbolic PDE and performing calculus on the resulted equation, we finally obtain following equations.

$$\Delta w_s(x,y)=-\Delta u_s(x,y)-\frac{1}{\pi}\iint_{\tau_+}\frac{(x-\xi)\Delta w_s(\xi,\eta)}{[(x-\xi)^2-(y-\eta)^2]^{3/2}}\,d\eta d\xi \tag{3-4}$$

$$where\quad \Delta u_s(x,y)=-\frac{1}{2\beta^2}(\Delta Cp_+ + \Delta Cp_-) \tag{3-5}$$

$$\Delta w_s(x,y)=\frac{1}{\beta^3}\frac{\partial}{\partial x}(\Delta f_+ - \Delta f_-) \tag{3-6}$$

$$\Delta w_a(x,y)=-\Delta u_a(x,y)-\frac{1}{\pi}\iint_{\tau_+}\frac{(x-\xi)\Delta u_a(\xi,\eta)}{(y-\eta)^2\sqrt{(x-\xi)^2-(y-\eta)^2}}\,d\eta d\xi \tag{3-7}$$

$$where\quad \Delta u_a(x,y)=-\frac{1}{2\beta^2}(\Delta Cp_+ - \Delta Cp_-) \tag{3-8}$$

$$\Delta w_a(x,y)=\frac{1}{\beta^3}\frac{\partial}{\partial x}(\Delta f_+ + \Delta f_-) \tag{3-9}$$

Equations. (3-4) and (3-7) are the mathematical models to relate pressure differences to geometrical correction. The x coordinate is chord-wise and the y coordinate is span-wise. It is illustrated in Fig. 2. In Eqs. (3-4) and (3-7), ξ and η are integral variables which correspond to x and y, respectively. The z coordinate is in the wing thickness direction. The models reduce three-dimensional problem to two-dimensional surface integrals. The subscript + indicates that the variable is on the upper surface of the wing while the subscript – indicates the lower surface. The area for integration, denoted by τ+, is the upper wing surface limited by the forwarded Mach cone from a point P(x,y) and leading edge line. The $y=\eta$ line (the singular cylinder in Fig. 2) is excluded from the integration area τ+. The Mach cone, P and τ+ are also shown in Fig. 2.

For design we use the models to determine the geometrical correction; Δw is unknown; Δu is given. Eq. (3-4) is a Volterra integral equation of the second kind for Δw_s. Δw_s is associated with the chord-wise thickness change at (x, y) on a wing. Eq. (3-7) is the integral expression for Δw_a, which is associated with the chord-wise curvature change of the wing section camber, at (x, y). The geometrical correction function, Δf, which is the z coordinate modification of the wing surface, is calculated using $\Delta w_s(x,y)$ and $\Delta w_a(x,y)$;

$$\Delta f_{\pm}(x,y/\beta)=\frac{1}{2\beta^3}\int_{L.E.}^{x}[\Delta w_s(\xi,y)\pm\Delta w_a(\xi,y)]d\xi \tag{3-10}$$

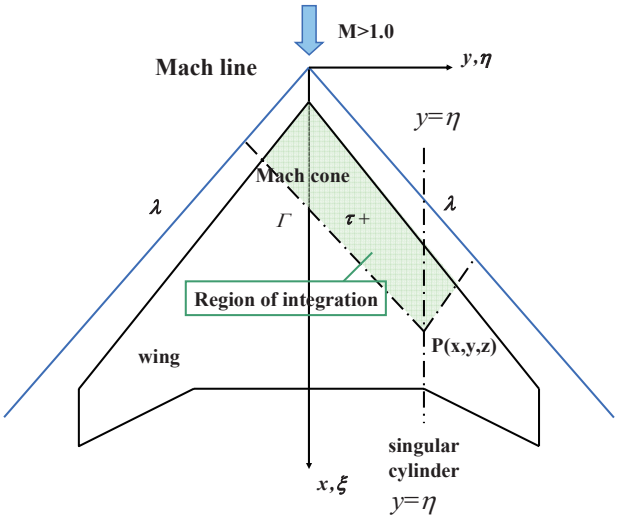

Figure 2 Flowfield and coordinate system for formulation.

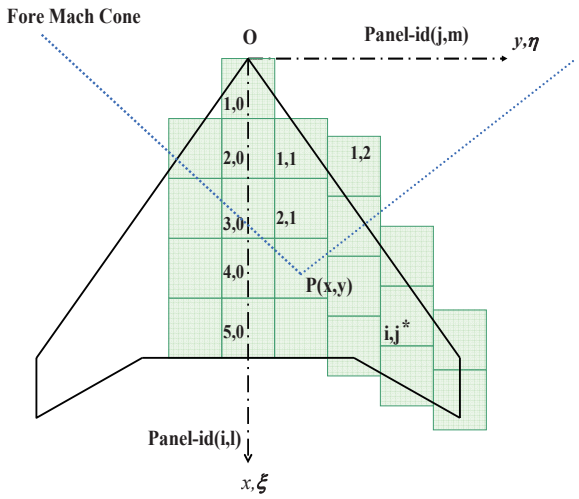

Figure 3 Panels on wing surface.

Discretization

To solve those integral equations presented in the previous subsection computationally, the wing surface is discretized into small rectangular panels as shown in Fig. 3. Then the double integrals of Eqs.(3-4) and (3-7) become the summation of piecewise integrals inside each panel. The piecewise integrals are evaluated at the center of each panel which is indicated as P(*i, j*) in Fig. 3. This lets us avoid the leading edge singularity. By assuming Δu_s, Δu_a, Δw_s and Δw_a to be constant inside a panel, piecewise integrals can be analytically calculated.

3.2 Application to Japanese SST Project Wing design [1,2]

The wing of a scaled experimental SST called NEXST-1 was designed by the inverse problem with the residual-correction method. They aimed to naturally realize wide laminar flow area on the main wing. Figure 4 shows the outlook of NEXST-1 and the main wing. The design was successfully performed. In Oct. 10, 2005 a flight test succeeded and they obtained fruitful test results. Finally the results confirmed the reliability of the inverse design.

The design was done at M_∞=2.0. In order to realize a wide natural laminar flow region on the wing, the special target Cp distributions were prescribed (see Fig. 7). The inverse design to determine geometry, we used 50 (chord-wise)×82 (span-wise) panels on the half span of a wing and solved the inverse problem with the target Cp. For analytical part, Navier-Stokes simulations were conducted. JAXA's UPACKS code [10] was used to obtain current surface Cp distributions over the wing.

The design results are shown in Figs. 6 and 7. Figure 6 compares the realized Cps of a designed wing with those of the baseline and the target Cps. They are the surface Cp distributions around the wing section at the 50% semi span-station. It is clearly seen that the realized Cps agrees with the target much better than the baseline does. On the upper surface and around leading edge, both of the realized and target Cps are identical. Figure 7 is the comparison of wing sections geometry of the baseline and designed wing. The new type of section airfoil geometry beyond traditional knowledge and experience was theoretically obtained by the numerical inverse design using the mathematical model.

3.3 Other Application of the Mathematical Models

The derived mathematical models in Section 3.1, which are Eqs.(3-4) and (3-7), can be applied to more complicated designs [11,12] and other analysis. In addition, they can be used to solve direct problems. If geometry, Δw_s and Δw_a is given, the surface Cps, Δu_s and Δu_a are simply calculated. The calculated Cps are accurate in potential flow estimation level, but the cost is surprisingly low. The useful application may be that to aerodynamic interaction among multi bodies in a flowfield [11].

The models can also be used to analyze aerodynamic effect of geometry on surface Cp distribution. For example, we can segregate two-dimensional effect from three-dimensional one and then compare the influential coefficient on the Cp value at the point P. Simply speaking, the integral part of each equation indicates the three-dimensional effect and the rest does two-dimensional one.

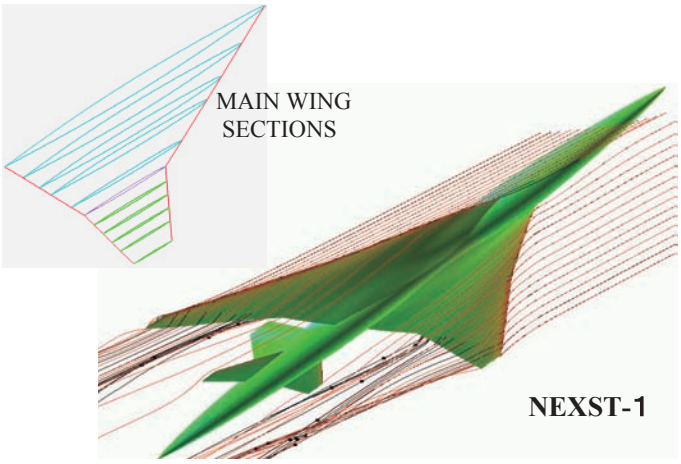

Figure 5 Flowfield around NEXST-1 and wing sections at span-stations of the main wing.

Figure 6 NEXST-1 flight test. (Ref. 4)

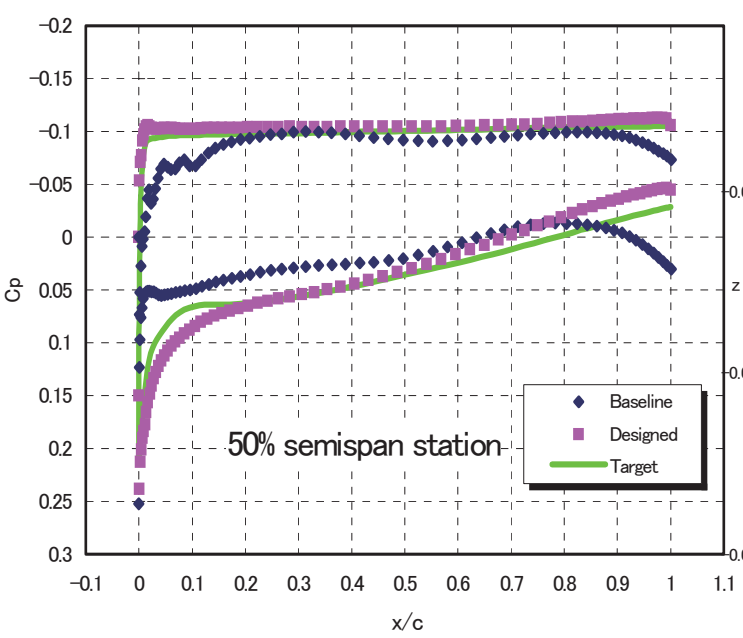

Figure 7 Design results; comparison of surface Cp distributions by computation.

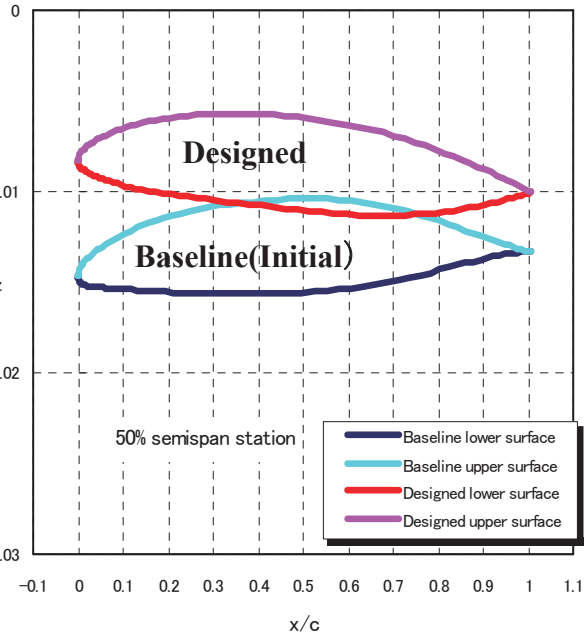

Figure 8 Design results; comparison of a wing section geometry.

4 An Inverse Problem based on Oblique Shock Relation

4.1 Formulation of an Inverse Problem and Derived Mathematical Models

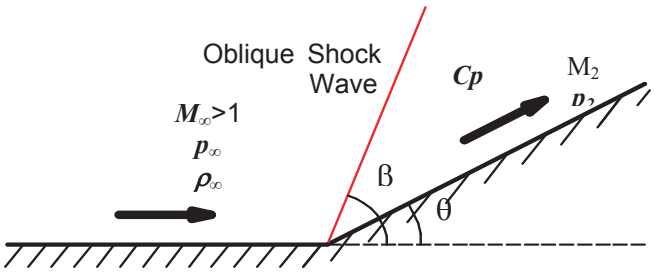

Figure 9 Super sonic flow along a compression corner.

In this formulation, we assume a small flow deflection angle θ is related to Cp values downstream of oblique shock waves by the following local oblique shock relations;

$$Cp = \frac{p_2 - p_\infty}{\frac{1}{2}\rho_\infty M_\infty^2 a_\infty^2} = \frac{4}{(\gamma+1)M_\infty^2}(M_\infty^2 \sin^2\beta - 1) \qquad (4\text{-}1)$$

$$M_\infty^2 \sin^2\beta - 1 = \frac{\gamma+1}{2} M_\infty^2 \frac{\sin\beta\sin\theta}{\cos(\beta-\theta)} \qquad (4\text{-}2)$$

and the asymptotic expansion of $\tan\beta$ when $\sin\mu$ is M_∞^{-1}; β is the oblique shock wave angle to the un-deflected flow direction.

$$\tan\beta = \tan(\mu+\varepsilon) = \tan\mu + \frac{1}{\cos^2\mu}\varepsilon + \frac{\sin\mu}{\cos^3\mu}\varepsilon^2 \qquad (4\text{-}3)$$

Manipulating Eqs. (4-1) to (4-3) and neglecting the more than third order terms of θ, we obtain

$$Cp = c_1\theta + c_2\theta^2 \quad \text{where} \quad c_1 = \frac{2}{\sqrt{M_\infty^2 - 1}}, \quad c_2 = \frac{(M_\infty^2 - 2)^2 + \gamma M_\infty^4}{2(M_\infty^2 - 1)^2} \qquad (4\text{-}4)$$

c_1 and c_2 are Busemann's coefficient[8]. Equation (4-4) holds both of compression and expansion corner. For compression, the flow deflection angle θ is positive, while the angle θ is negative for expansion. This relation is applied to the upper and lower surface of an airfoil. Then we have following equations.

$$Cp_+ = c_1\left(\frac{df_+(x)}{dx} - \alpha\right) + c_2\left(\frac{df_+(x)}{dx} - \alpha\right)^2 \qquad (4\text{-}5)$$

$$Cp_- = -c_1\left(\frac{df_-(x)}{dx} - \alpha\right) + c_2\left(\frac{df_-(x)}{dx} - \alpha\right)^2 \qquad (4\text{-}6)$$

α is the angle of attack of the airfoil. x represents the airfoil-chord direction (see Fig. 10). Subscripts + and – denote the upper and lower surfaces respectively.

Equations (4-5) and (4-6) may be used for design problems. In Ref.13, an SST wing design was performed using the both equations. Here, we adopt the perturbation form (Δ-form) of the equations As demonstrated in Section 2, a design method using a perturbation form extends the applicability of the. Therefore, taking the small perturbation ($C_p \rightarrow C_p + \Delta C_p$ and $f \rightarrow f + \Delta f$) of Eqs.

(4-5) and (4-6), we obtain Δ-form equations. An inverse-problem solves the *x*-derivative of the correction value for the airfoil geometry, $d\Delta f_{\pm}/dx$; this *x*-derivative is related to the difference between the target and the current pressure distributions, denoted as ΔC_p (C_p-residual). Specifically, the geometry correction term Δf (see Fig. 4) comes from ΔC_p, using the small-perturbation forms ($C_p \to C_p + \Delta C_p$ and $f \to f + \Delta f$) of Eq. (4).

$$\Delta Cp_{+} = c_1\left(\frac{d\Delta f_{+}(x)}{dx}\right) + 2c_2\left(\frac{d f_{+}(x)}{dx} - \alpha\right)\left(\frac{d\Delta f_{+}(x)}{dx}\right) + c_2\left(\frac{d\Delta f_{+}(x)}{dx}\right)^2 \tag{4-7}$$

$$\Delta Cp_{-} = -c_1\left(\frac{\mathrm{d}\Delta f_{-}(x)}{\mathrm{d}x}\right) + 2c_2\left(\frac{\mathrm{d} f_{-}(x)}{\mathrm{d}x} - \alpha\right)\left(\frac{\mathrm{d}\Delta f_{-}(x)}{\mathrm{d}x}\right) + c_2\left(\frac{\mathrm{d}\Delta f_{+}(x)}{\mathrm{d}x}\right)^2 \tag{4-8}$$

The airfoil geometry is updated by integrating the geometry correction terms:

$$f_{\pm}^{update}(x) = f_{\pm}(x) + \int_0^x \frac{\mathrm{d}\,\Delta f_{\pm}}{\mathrm{d}\,\xi}(\xi)\,\mathrm{d}\xi \tag{4-9}$$

where the symbol 0 indicates the x coordinate of the airfoil's leading edge. Finally, we have another mathematical model to relate pressure change to airfoil's geometry modification [14].

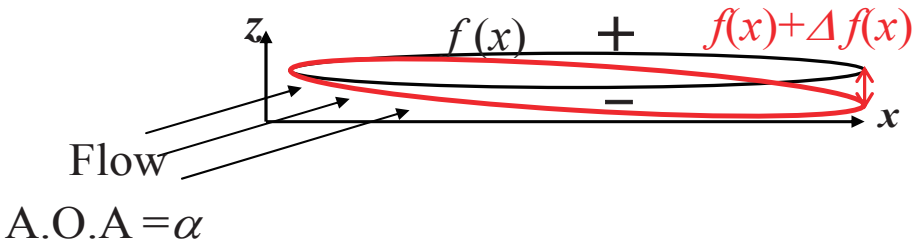

Figure 10. Airfoil geometries based on the current and target pressure distributions.

4.2 Application – Aerodynamic Design of Biplane Airfoils –

The above-mentioned inverse problem design method has been validated. To check its applicability we conducted an airfoil design in a complicated flowfield. The design object is a biplane, where two airfoils strongly interact with each other. Figure 11 is the initial/baseline configuration. We attempted to design the upper element of the biplane by specifying the obtained C_p distribution of an existing biplane by the computation. The design target was a known airfoil, that was the Busemann biplane [15]shown in Fig. 12. During the design process, the shape of the lower element of the biplane remained fixed (see Figs. 11 and 12). This was two dimensional design so the wing of infinite span length was assumed. The design was for the biplane flying at M_∞ = 1.7. In this design, Euler flow simulations were conducted using Tohoku University Aerodynamic Simulation (TAS) code [16]. All the simulations used the same size grid distribution to avoid counting uncertainty error due to the grid size effect during the design process. Through the design, it has been confirmed that the upper element which starts from an arbitrary airfoil geometry converges to the target geometry.

As seen in Fig, 13-(a), the initial geometry of the upper element was a thin flat plate. Figure 13-(b) shows the initial Cp distributions around both of upper and lower airfoils. The target geometry is presented in Fig. 14 with the design result. The pressure distributions around the Busemann biplane (Fig. 12) obtained by analyzing at Mach 1.7 speed are adopted as the target C_p. It is shown in Fig. 15. After 14 times iterations, the realized C_p distribution by the designed airfoil has converged to the target one. In Figs. 14 and 15 the designed geometry and resulted Cp distributions are also presented. Both of geometry and Cp distributions of designed airfoil are identical to those of the target one. Actually, the absolute Root Mean Square (RMS) error between the realized C_p distribution and the target one is 1.4E-4.So the design has been successfully done [17].

The history of the design process is shown in Fig. 16. There, current results from the initial to the 3rd iteration are sequentially displayed. Current airfoil geometry and C_p distribution are presented compared with the target ones. In early stage of the design process, the change in Cp distributions at the airfoil rear part is drastic because of interaction between two elements of the biplane. After the 3rd iteration, the amount of change became smaller as the number of iteration increased; in other words the design converged uniformly to the target geometry. After the 14th iteration, as discussed before and can be seen in Fig. 15 again, the realized C_p by the designed geometry converged to the target one. It has been confirmed that the design method is capable of

performing the aerodynamic design of not only single airfoils but also biplanes where two airfoil elements interfere with each other.

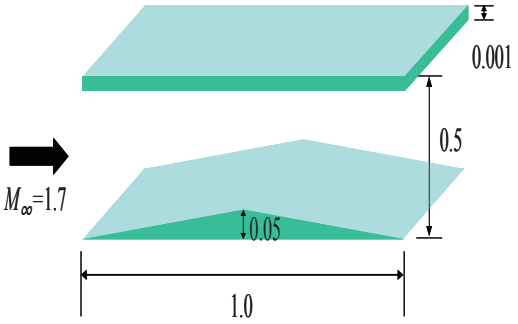

Figure 11 Initial geometry (M_∞=1.7).

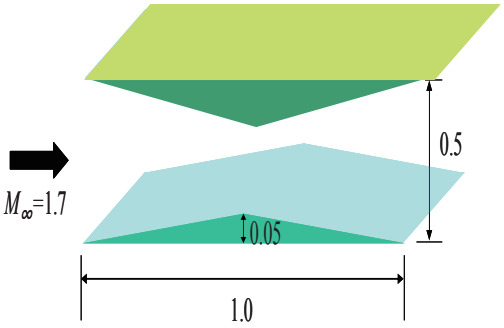

Figure 12 Target geometry (upper element) (M_∞=1.7).

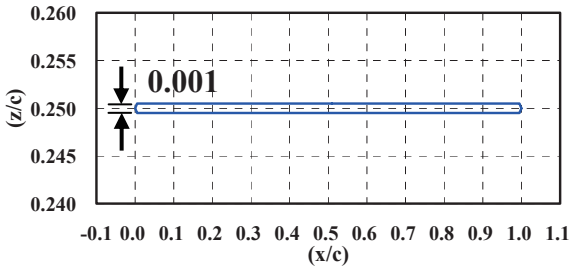

(a) Airfoil geometry of upper element

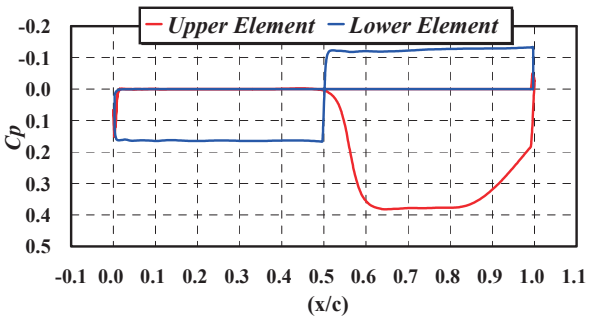

(b) *Cp* distributions

Figure 13 Section airfoil geometry and C_p distributions of initial geometry.

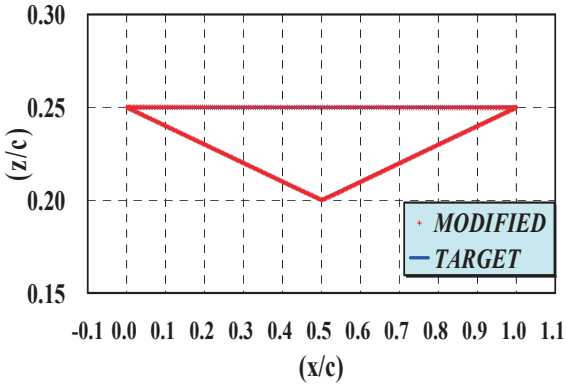

Figure 14 Designed geometry of the upper element.

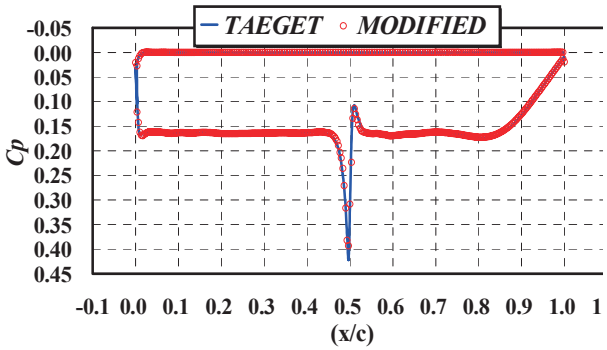

Figure 15 C_p distribution of upper element after 14 time iterations.

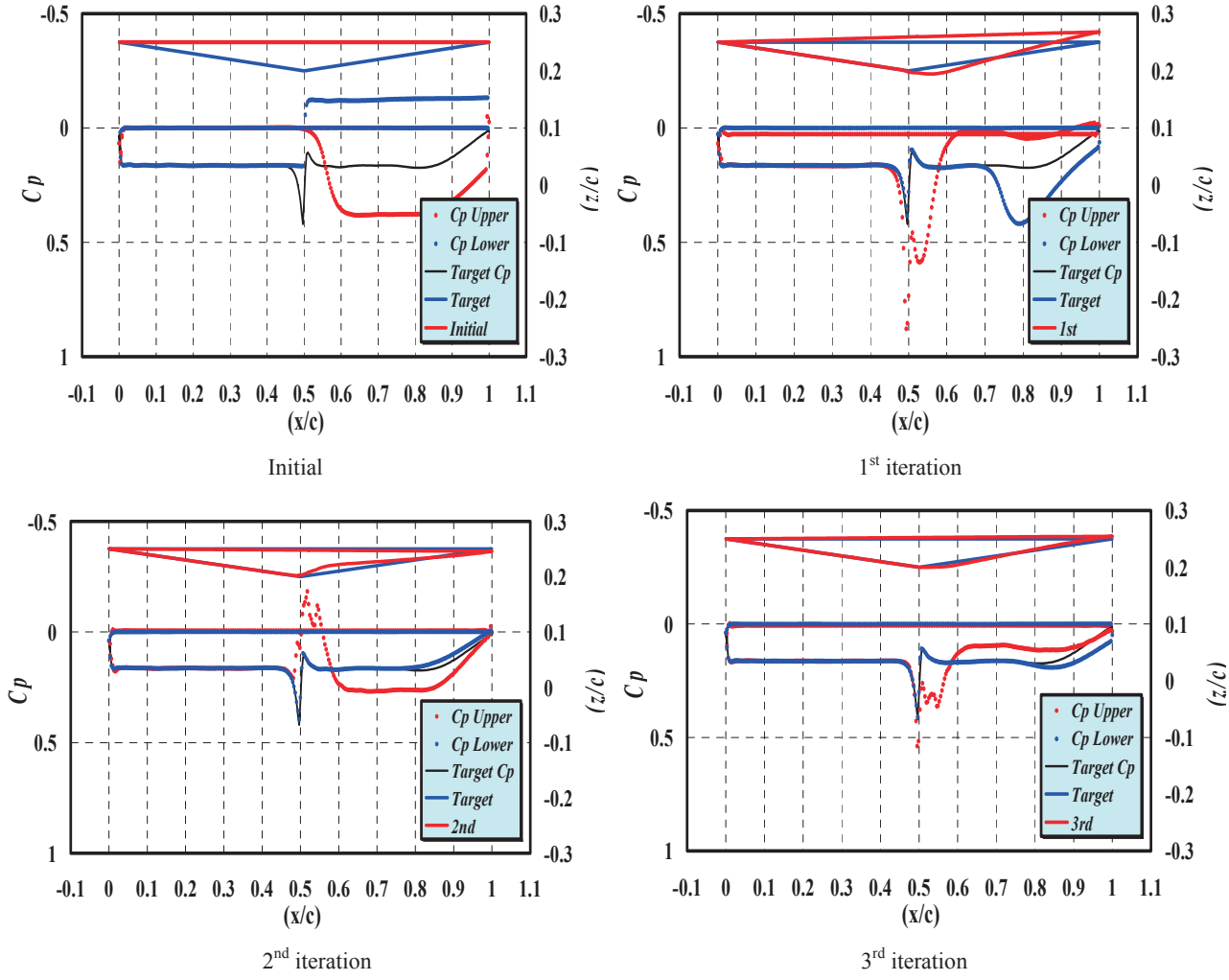

Figure 16 C_p distributions and geometries of modified airfoils during the early stage of design process.

5 Conclusions

For the aerodynamic wing design, the superior points of a inverse problem method are discussed as well as two mathematical models each of which is the core equation of an inverse problem are introduces. One mathematical model comes from three-dimensional potential flow equation and he thin wing theory, while the other is led from Busemann's 2nd order approximation based on the theory of oblique shock wave. The former yields the set of integral-differential equations and the latter does a quadratic equation in the corresponding inverse problem. Combining each inverse problem with residual-correction methodology and modern computational technology enables us to construct a low-cost and high-fidelity design method. To examine its capability and usefulness, several design problems have been done. For the first inverse problem, the design has been performed on a main wing for a scaled SST which realizes wide laminar region on its upper surface. This is a practical design problem in a real production. As for the other one, the biplane airfoil has been designed. The flowfield is complicated so, the design should be hard to converge because two airfoils of the biplane strongly interact with each other. Successful high-fidelity design results have been obtained for all cases. The computational cost is small. The inverse design needs about 20 time flow simulations which is much less than the cost of a general optimization. Consequently, the iterative inverse design methods have been proved efficient and accurate. We are now trying to utilize the mathematical models devised here for other flow analyses.

We would like to conclude this article with an additional advantage of inverse methods. It was indicated in a paper [18] by a famous experienced designer of the Boeing company. The paper stated that an inverse method to use computer could be a new way to revolutionize the design process because it would be not a copy or extension of traditional thought, but complements to human imagination.

References

[1] Matsushima, K., Jeong, S., Takaki, R., Obayashi, S., Nakahashi, K. and Iwamiya, T., "A Supersonic Inverse Wing Design Method and Its Applicaion to Japanese SST," Lecture Note in Physics Vol. 515 Springer, 1998, pp. 79-84.

[2] Matsushima, K. Iwamiya, T., Ishikawa, H., "Supersonic Inverse Design of Wings for the Full Configuration of Japanese SST," ICAS 2000, Proceedings 22nd International Congress of Aeronautical Sciences, 2000 , pp. 213.1-213.8.

[3] Yoshida, K., Makino, Y., "Aerodynamic Design of Unmanned Scaled Supersonic Experimental Airplane in Japan", ECCOMAS 2004, Jyvaskyla, 2004, pp. 24-28.

[4] http://www.apg.jaxa.jp/res/stt/index.html and http://www.apg.jaxa.jp/res/stt/a03.html

[5] Ohnuki, T., Hirako, K., Sakata, K., "National Experimental Supersonic Transport Project," Proceedings of the 25th International Congress of the Aeronautical Sciences, 2006.

[6] Kwak, D., Yoshida, K., Ishikawa, H., Noguchi, M., "Flight Test Measurements of Surface Pressure on Unmanned Scaled Supersonic Experimental Airplane," AIAA Paper 2006-3483, June 2006

[7] Busemann, A., "Aerodynamic lift at supersonic speeds," Luftfahrtforschung, Ed.12, Nr.6, Oct.3, 1935, pp.210-220.

[8] Liepmann, H. W., and Roshko, A., *Elements of Gas Dynamics*, John Wiley & Sons, Inc., New York, 1957, p. 389.

[9] Heaslet, M. A. and Lomax, H.: Supersonic and Transonic Small Perturbation Theory, Vol. 6 of *High-Speed Aerodynamics and Jet Propulsion*, Princeton University Press, 1954, pp. 122-344.

[10] Japan Aerospace eXploration Agency (JAXA), Introduction to UPACS,

[11] Matsushima, K. Iwamiya, T., "An Improved Aerodynamic Inverse Design Method for Complex SST Configuration Combined with 3D NS Solver," Computational Fluid Dynamics 2000, Proceedings of the First International Conference on Computational Fluid Dynamics, ICCFD, 2001 , pp. 679-684.

[12] Matsuhima, K., Iwamiya, T., Nakahashi, K., "Wing design for supersonic transports using integral equation method," Engineering Analysis with Boundary Elements Vol.28, 2004, pp. 247-255.

[13] Ogoshi, H. and Shima E., "Role of CFD in Aeronautical Engineering (15)," Special Publication of National Aerospace Laboratory, SP-37, Proceedings of the 15th NAL Symposium, Tokyo, Japan, June 1997, pp.81-86.

[14] Matsushima, K., Maruyama, D., Nakano, T. and Nakahashi, K., "Aerodynamic Design of Low Boom and Low Drag Supersonic Transport using Favorable Wave Interference," Proceedings of The 36th JSASS Annual Meeting, Tokyo, Japan, April, 2005, pp. 130-133.

[15] Liepmann, H. W., and Roshko, A., *Elements of Gas Dynamics*, John Wiley & Sons, Inc., New York, 1957, pp. 107-123.

[16] Nakahashi, K., Ito, Y., and Togashi, F., "Some Challenge of Realistic Flow Simulations by Unstructured Grid CFD," International Journal for Numerical Methods in Fluids, Vol.43, 2003, pp.769-783.

[17] Maruyama, D., Matsushima, K., Kusunose, K., Nakahashi, K., "Aerodynamic Design of Biplane Airfoils for Low Wave Drag Supersonic Flight," AIAA paper 2006-3323, The 24th AIAA Applied Aerodynamics Conference, June 2006.

[18] McMasters, H. J., and Cummings, M. R.: Airplane Design---Past, Present, and Future, Journal of Aircraft, Vol. 39, No. 1 2002, pp. 10-17.

Inverse design of biplane airfoils for efficient supersonic flight - Preliminary trial to construct biplane airfoil data base -

D. Maruyama* and K. Matsushima.†
Department of Aerospace Engineering, Tohoku University, Sendai, Japan, 980-8579

K. Kusunose‡
Formerly, Institute of Fluid Science, Tohoku University, Sendai, Japan, 980-8577
Currently, Technical Research and Development Institute, Ministry of Defense, Tokyo, Japan, 190-8533

and

K. Nakahashi§
Department of Aerospace Engineering, Tohoku University, Sendai, Japan, 980-8579

There is a biplane concept for an efficient supersonic flight. Busemann biplane is a representative airfoil which has possibility of realizing low-boom and low wave drag. Aerodynamic designs based on the Busemann biplane are demanded for future supersonic transports. In this paper, possibilities of designing supersonic biplanes by utilizing an inverse problem method are discussed based on Computational Fluid Dynamics (CFD). The inverse problem method which has been used in this paper is based on the theory of oblique shock wave. Therefore, it is necessary to examine its usefulness of designing airfoils which causes complicated phenomena such as biplanes where two airfoil elements interfere with each other and 3-dimensional wings. We attempted 2-dimensional cases in our current studies. It was confirmed that a certain biplane which differed from the Busemann biplane converged to the known Busemann biplane in 14 times iterations of design procedure. This knowledge is stated in the previous paper of this one. Then a practical biplane configuration was designed by utilizing the inverse problem method. After 14 times iterations, biplane configuration which has lower wave drag than a zero-thickness single flat plate airfoil at sufficient lift conditions has been successfully designed. Finally, applications to designing 3-dimensional biplane wings are attempted. Target and initial geometries are set to the same ones as the case of 2-dimensional. The above-mentioned inverse problem method was applied to total 10 sections. In 3-dimensional cases which have more complicated phenomena than 2-dimensional cases such as disparity in flow of span direction, convergence after 14 times iterations was confirmed.

Nomenclature

C_d	=	wave drag coefficient
C_l	=	lift coefficient
C_p	=	pressure coefficient
c	=	chord
M_∞	=	free-stream Mach number
t	=	airfoil thickness
D	=	drag
L	=	lift

* Graduate Student, Department of Aerospace Engineering, Tohoku University, Email: daigo@ad.mech.tohoku.ac.jp
† Associate Professor, Department of Aerospace Engineering, Tohoku University.
‡ Senior Research Scientist, Technical Research and Development Institute, Ministry of Defense.
§ Professor, Department of Aerospace Engineering, Tohoku University.

Re = Reynolds number
α = angle of attack
ε = wedge angle

1. Introduction

The objectives of low noise and high fuel efficiency are critical for the next generation supersonic transport. In a word, it is necessary to develop an airplane that has low boom and low drag. Busemann proposed a biplane configuration in a form with the possibility to satisfy these two conditions, which utilizes a favorable interaction between two wing elements[1,2]. The wave drag due to airfoil thickness can be nearly eliminated using a biplane configuration that promotes favorable wave interactions between the two neighboring airfoil elements (here, wave drag being defined as a resistant force on the airfoil due to the generation of shock-waves.). Licher extended the idea to reduce the wave drag due to lift[3]. Recently, a project of a supersonic biplane has been started around Dr. Kusunose for the purpose of a significant reduction in wave drag and sonic boom[4,5]. It is a goal of our study to develop the idea of the supersonic biplane by utilizing modern techniques, including CFD tools, advanced in the last 30 years, and also to propose a practicable biplane wing for low wave drag (therefore, for low boom) in supersonic flight.

We currently focus on designing two-dimensional (2-D) biplane configurations for low drag supersonic flight. For a design method, an inverse problem method[6,7,8] which is based on the theory of oblique shock waves and the concept of small perturbation method is used. Its usefulness of designing airfoils which has complicated phenomena such as biplanes where two airfoil elements interfere with each other was confirmed in our current studies. In this paper, distinguished results of designs for a 2-dimensional biplane airfoil utilizing the inverse problem approach are shown. Finally, we demonstrate its design capability for 3-dimensional biplane wings for the purpose of next future supersonic transport.

2. Biplane Concept for Low Wave Drag Supersonic flight

In our study, low wave drag biplane configurations are studied under the condition that the total maximum thickness ratio (thickness-chord ratios, t/c) is more than 0.10. In supersonic flight of M_∞=1.7, we consider the range of lift coefficient C_l from 0.10 to 0.20. In Fig. 1 wave drag components due to lift and due to thickness are estimated using the supersonic thin airfoil theory for a lifted diamond airfoil of t/c=0.10 at C_l =0.10, with flow condition M_∞=1.7. Here, t/c represents airfoil thickness chord ratio.

Employing the 2-D supersonic thin airfoil theory[2], the lift and wave drag coefficients of a flat plate airfoil at a small angle of attack α are expressed as

$$C_l = \frac{4\alpha}{\sqrt{M_\infty^2 - 1}} \tag{1}$$

$$C_d = \frac{4\alpha^2}{\sqrt{M_\infty^2 - 1}} = \frac{\sqrt{M_\infty^2 - 1}}{4} C_l^2 \tag{2}$$

where, C_l and C_d are defined by L/qc and D/qc, L and D being the airfoil's lift and wave drag, respectively. Symbol M_∞, q, and c represent the free-stream Mach number, dynamic pressure ($0.5\rho_\infty U_\infty^2$) and airfoil chord length. Here, U_∞ represents free stream velocity.

Wave drag of a diamond airfoil is calculated using the thin airfoil theory[2] as

$$C_d = \frac{4}{\sqrt{M_\infty^2 - 1}} \left(\frac{t}{c} \right)^2 \tag{3}$$

Using biplane configurations both wave drag components due to lift and due to thickness can be reduced.

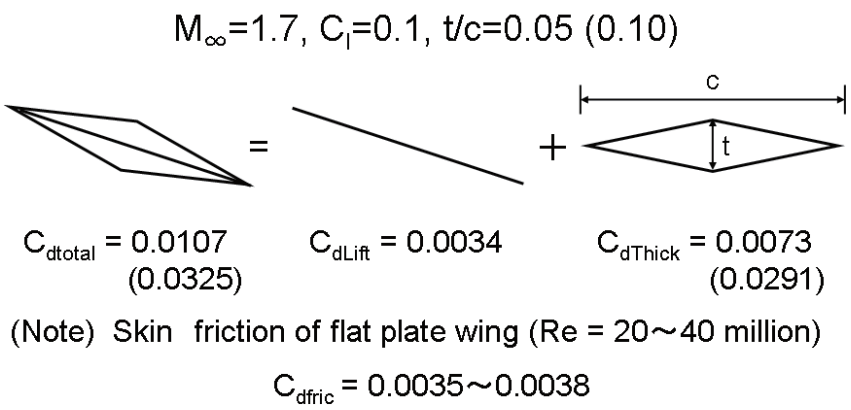

Figure 1. Wave drag components for a diamond airfoil.

2.1 Elimination of Wave Drag due to Airfoil Thickness

As shown in Fig. 1, the majority of the total wave drag of a diamond airfoil is due to its thickness. The biplane configuration can also significantly reduce wave drag due to its airfoil thickness (or volume). Favorable wave interactions between the two airfoil elements can be promoted by choosing their geometries and relative locations carefully. Busemann showed that the wave drag of a zero-lifted diamond airfoil can be completely eliminated by simply splitting the diamond airfoil into two elements and locating them in a way such that the waves generated by those elements cancel each other out[1,2] (see Fig. 2, where ε is wedge angle of a Busemann biplane). Generally, in supersonic flight, wave drag due to an airplane's volume (wing thickness, fuselage, etc.) is large relative to that due to its lift (As shown in Fig. 1). Supersonic aircraft are therefore severely limited in their wing thickness. If the wave cancellation effect can be used effectively, the strong restriction currently imposed on the wing thickness of supersonic aircraft may be relaxed considerably.

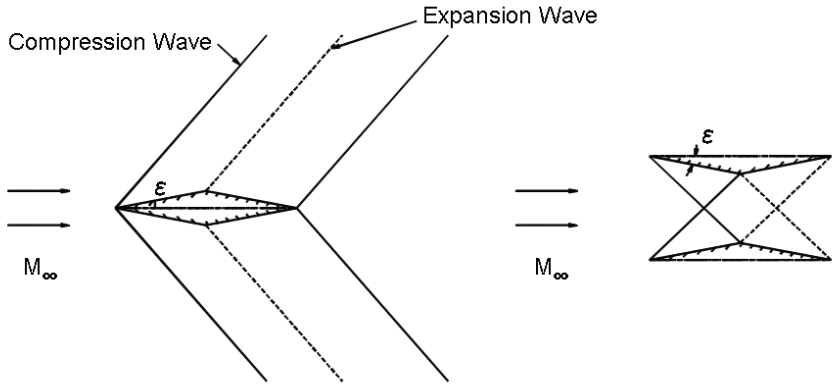

Figure 2. Wave cancellation effect of Busemann biplane.

2.2 Reduction of Wave Drag due to Lift

To achieve minimum wave drag under a given lift condition, we chose the biplane configuration discussed by R. Licher in 1955[3] (see Fig.3, where α is the angle of attack for the lower surface of the lower element) as one of the baseline configurations. This particular biplane configuration exhibits two desirable characteristics: the wave reduction effect due to airfoil lift and the wave cancellation effect due to airfoil thickness. By promoting favorable wave interactions between the upper and lower elements, the wave drag due to lift can be reduced to 2/3 of that of a single flat plate under the same lift condition. Additionally, Busemann's wave-cancellation concept can be applied to the system to reduce wave drag due to airfoil thickness.

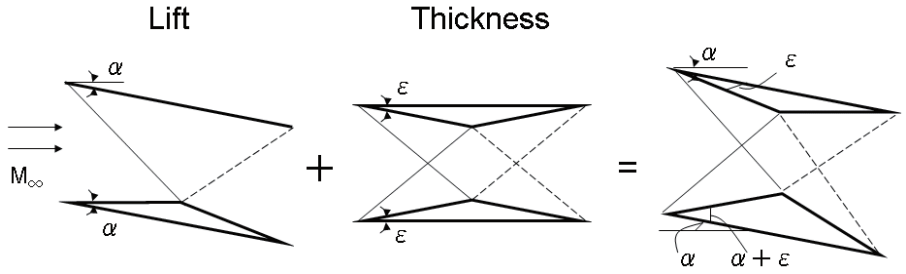

Figure 3. Licher type Biplane including Busemann Biplane.

3. Aerodynamic Design of Practical Biplane Airfoils by Using an Inverse Problem Method

Using the inverse problem method, a 2-dimensional biplane airfoil design has been performed. In this research, a flow solver named TAS code (Tohoku University Aerodynamic Simulation) using a three-dimensional unstructured grid[9,10], was used to evaluate aerodynamic performance. In simulation, the Euler/Navier-Stokes equations are solved by a finite-volume cell-vertex scheme. The lower/upper symmetric Gauss-Seidel (LU-SGS) implicit method for an unstructured grid[11] is used for the time integration. The theory and method and its usefulness for biplane configurations are shown in the previous paper[8]. The design procedure of the inverse deign cycle for biplane airfoils is shown in Fig. 4.

For designing biplane airfoils, a Licher type biplane (see Fig.3) was selected as the initial configuration. As a design condition, free stream Mach number M_∞=1.7, and angle of attack α=1deg. were selected (here, α representing the angle of the lower surface of the lower element against the free stream direction). Here, the total thickness-chord ratio (t/c) is 0.106. Both the target and initial pressure distributions for both the upper and lower elements used for the biplane design were shown in Fig. 5. Our design concept is to meet a demand of C_p distributions, having more lift on the upper surface of the upper element and also generating additional lift, but having lower drag on the lower surface of the upper element, especially near the trailing edge. The obtained C_p distributions (after 14 times iterations) of the upper and lower element, using plots and lines, respectively are shown in Fig. 6. The initial and designed geometry are compared in Fig. 7. The gain of the angle of attack of the lower surface on the lower element against the flow direction is 0.19deg. compared to the initial Licher type biplane. The total maximum thickness ratio (t/c) is 0.102. C_l =0.115, C_d =0.00531 (L/D=21.72). A C_p visualization map at this design point is shown in Fig. 8. Wave drag polar diagrams are shown in Fig. 9. When C_l =0.14, total wave drag is lower than that of the zero-thickness single flat plate airfoil. Thus, by the use of the inverse problem design method, a biplane configuration having a distinguished aerodynamic performance was successfully designed. It may seem surprising to find a biplane configuration that has a lower wave drag than that of a flat plate airfoil, however, this was already predicted by Moeckel more than 50 years ago[12].

Observing the designed shape in detail, the trailing edge of the upper element of the designed biplane configuration was modified to align the concave curve and the shape parallel to the free stream, creating more lift. It should also be noted that the compression waves generated at the leading edge of the elements and the expansion waves generated at the throats of the elements nearly cancelled each other out, thus eliminating the initial pressure peaks at the throat.

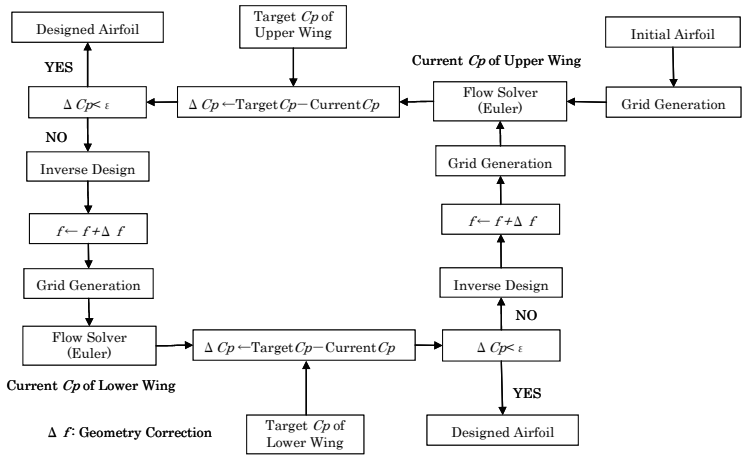

Figure 4. Design cycle.

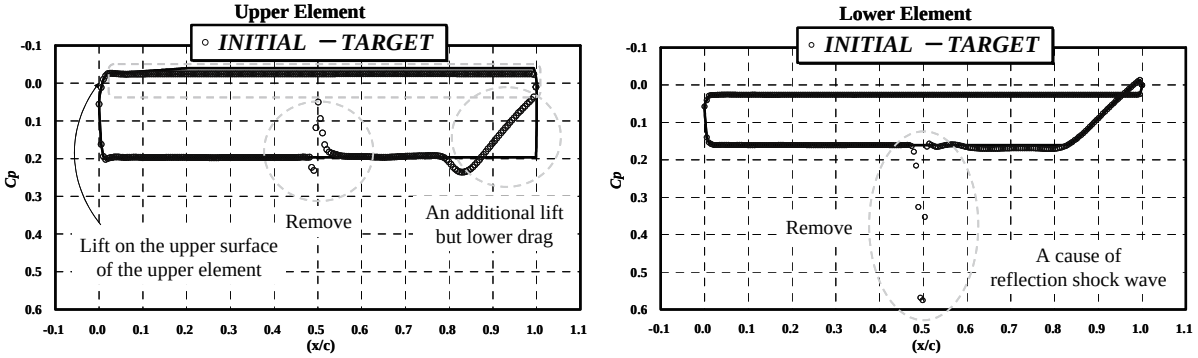

Figure 5. Target C_p distributions.

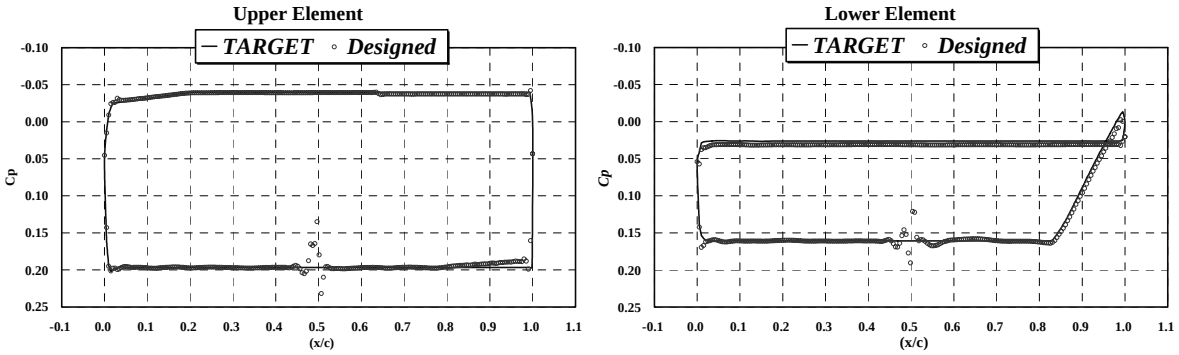

Figure 6. C_p distributions of the designed biplane configuration.

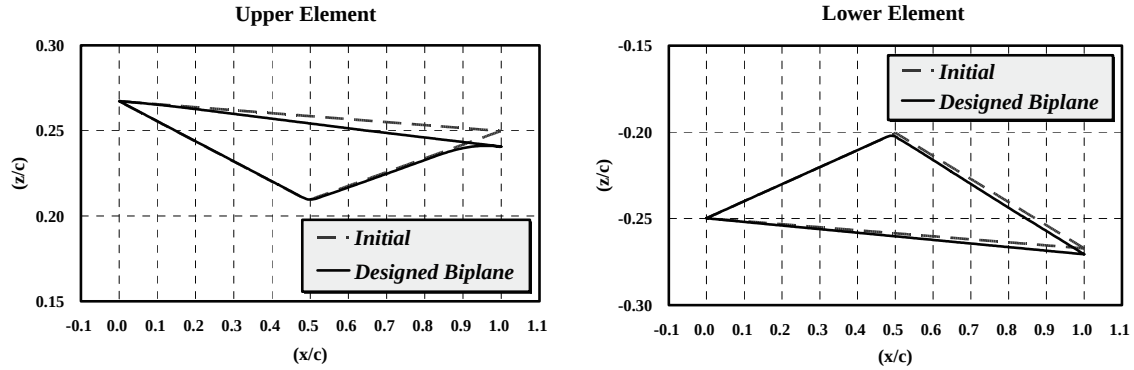

Figure 7. Section airfoil geometries of designed biplane configuration (*t/c*=0.102).

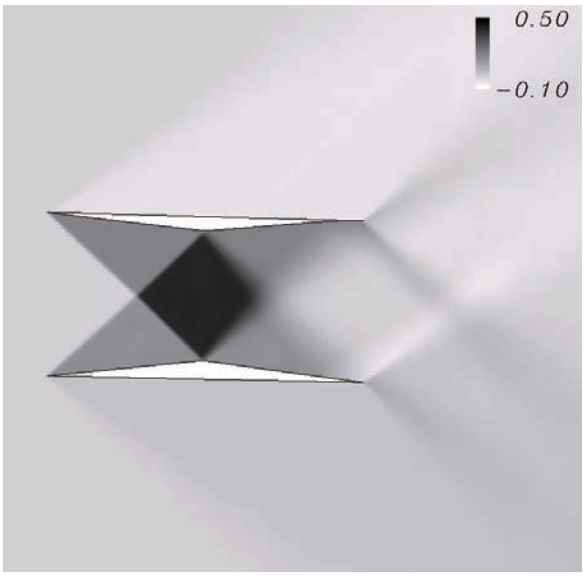

Figure 8. C_p visualization of designed biplane at M_∞=1.7 (α=1.19deg).

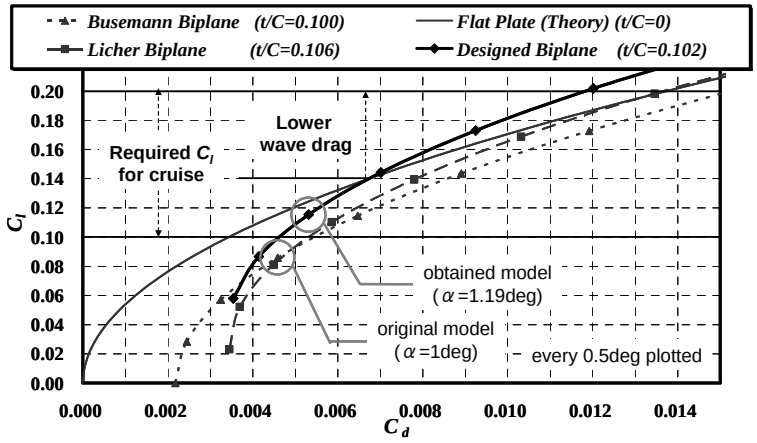

Figure 9. Wave drag polar diagrams of designed biplane at M_∞=1.7.

4. Application to 3-dimensional supersonic biplane

A successful design of 2-dimensional supersonic biplane was shown in the previous paper[8]. Then we are going to challenge to design practical 3-dimensional biplane wings. As a first step of designing practical 3-dimensional biplane wings, we attempted to redesign a known 3-dimensional biplane wing by utilizing the above-mentioned inverse problem method. The residual – correction design strategy utilizing small perturbation form[6,7,8] of the basic equation makes 3-dimensional design possible enables to take the 3-dimensional effects into account, even though the basic equation is for 2-dimensional (a wing of infinit span length). The 3-dimensional effects and interacting effect between the upper and lower wing can be counted by iterations of 3-dimensional flow simulations and the inverse problem solver.

As a design object, the known Busemann biplane whose half-span length is 1 (There is no influence of Mach cones emanuated from wing tips and 2-dimensionality is maintained at the symmetry section) was used as an existing wing shape for target pressure distributions (Fig. 10). The biplane where the upper wing in the Busemann biplane was replaced by a flat plate was used as an initial shape wing (Fig. 11). As the sections for the inverse design, the sections at 10 span stations are located from the symmetry section to the wing tip every 10% span length intervals. The airfoil tip was excluded from designing, and shape on the wing tip is assumed to be the same shape as the shape at 90% span section. The pressure distributions of the Busemann biplane, namely, target pressure distributions appear in Fig. 10. It can be seen that Mach cones influence the C_p distributions at sections from the 30% span station to the wing tip. Detailed pressure visualization of Mach cones and the mesh for CFD analysis are shown in Fig. 12.

Figure. 13 shows obtained geometries and C_p distributions at some sections of the currently designed biplane after 1, 2, 5, 7 times iterations. Equations of the inverse problem method are based on the condition that a flow deflection angle is less than 0.2 radian in supersonic flow. The condition includes the case of thin airfoils. As seen in Fig. 13(a), the obtained geometries agree well with the target ones in the region where there are no influences except for shock waves from the leading edges, that is, in the region from the leading edges to the mid chords at sections within 60 % span (see Fig. 10). According to Fig. 13(b), the obtained geometries after 2 times iterations agree well with the target ones in the region from the leading edges to mid chord sharp apexes at all sections. However, the geometries from the mid chords to the trailing edges are greatly different from target ones and the values of modifications of the geometries among iterations are also very large.

As seen in the obtained shapes after 5 and 7 times iterations (Fig. 13(c) and (d)), the geometries from the leading edges to the mid chords agree well with the target geometries at all sections. Let us see the geometries after 5 times iterations (Fig. 13(c)), the geometry at the 90% span section realizes almost the same shape as the target geometry. This is because influences of Mach cones are primary there and there is little physical interference from the lower wing. Next, let us take a look at the geometries after 7 times iterations (Fig. 13(d)), the geometries at the almost all sections except for the symmetry section are very close to the target geometries. To compare the results after 7 iteration with the geometries after 5 times iterations which have large changes to the span direction, it is confirmed that many iterations are not needed to settle down to the target geometries at many sections. However, the convergence of the obtained geometry at the symmetry section is slow because it is indirectly influenced by other span stations including tip section geometry changes.

The geometries and C_p distributions after 14 times iterations are shown in Figs. 13 and 14. We can observe convergence to the target geometries and C_p distributions at all sections. Table 1 summarizes the absolute RMS (Root Mean Square) errors between the realized C_p distributions and the target ones at all sections. It has been confirmed that the simple inverse problem method is capable of performing the aerodynamic design of 3-dimensional biplane wing shapes where airfoil geometries are changed into a span direction and two airfoil elements interfere with each other. Furthermore, it has been also confirmed that almost the same iteration times are needed to design 3-dimensional wings as the iteration times to 2-mensional airfoil geometry.

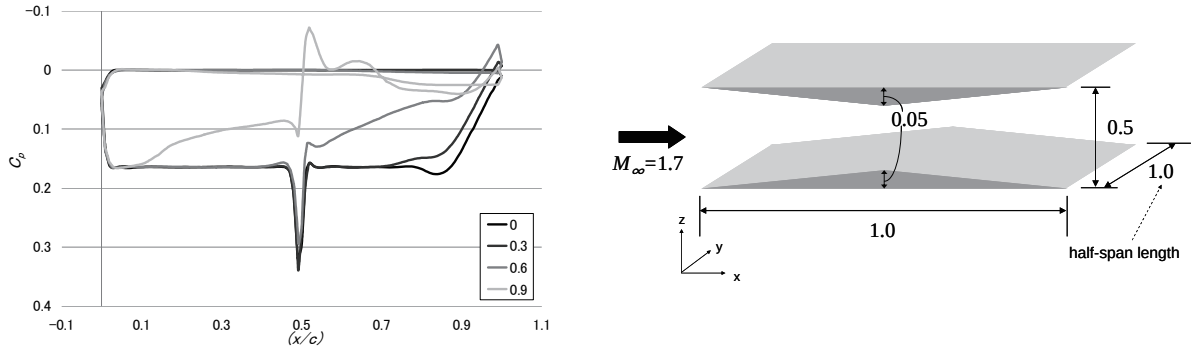

Figure 10. Target C_p distributions at some sections (C_p distributions of the Busemann biplane at each section).

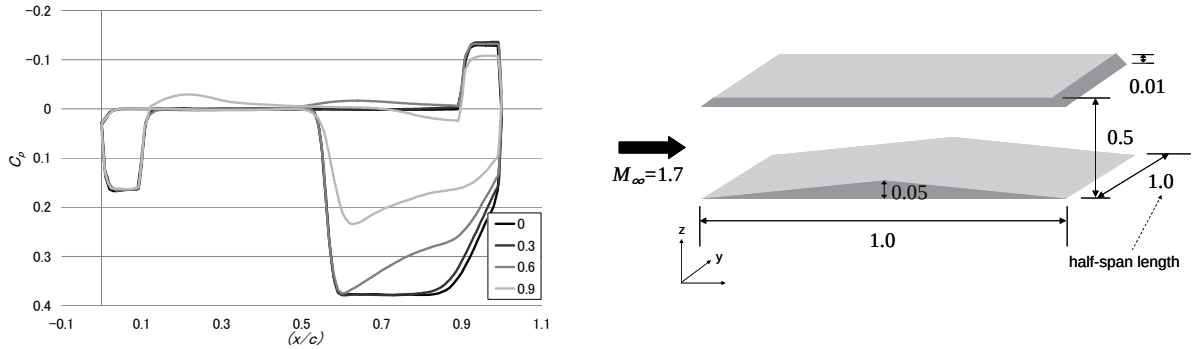

Figure 11. Initial C_p distributions at some sections.

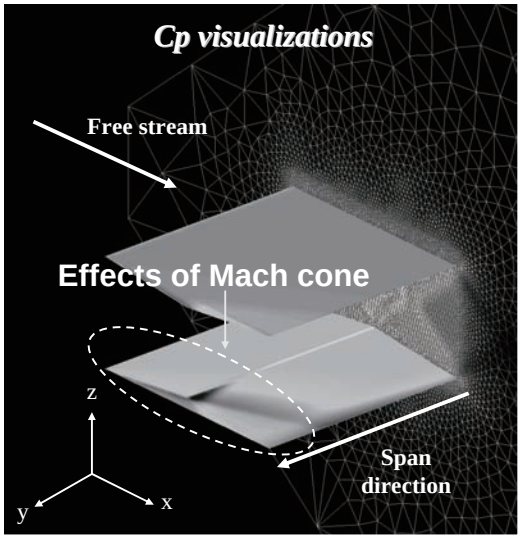

Figure 12. C_p and mesh visualizations around the Busemann biplane at M_∞=1.7 (half-span length 1).

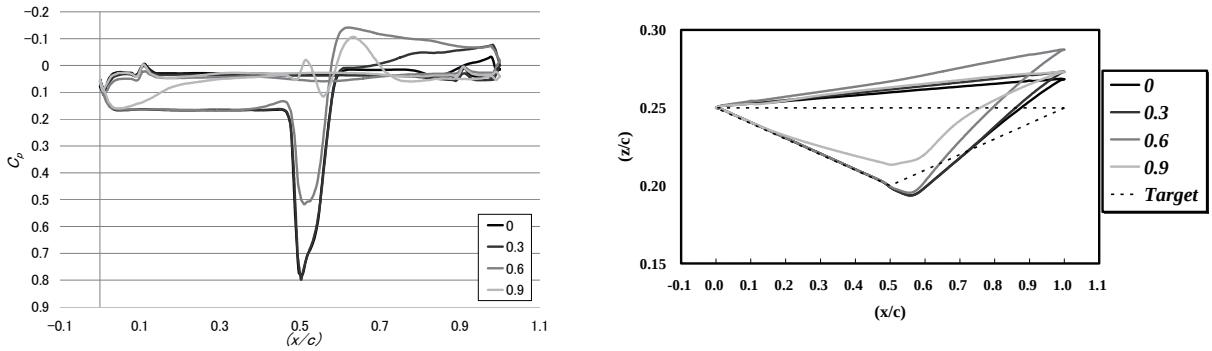

(a) 1st iteration

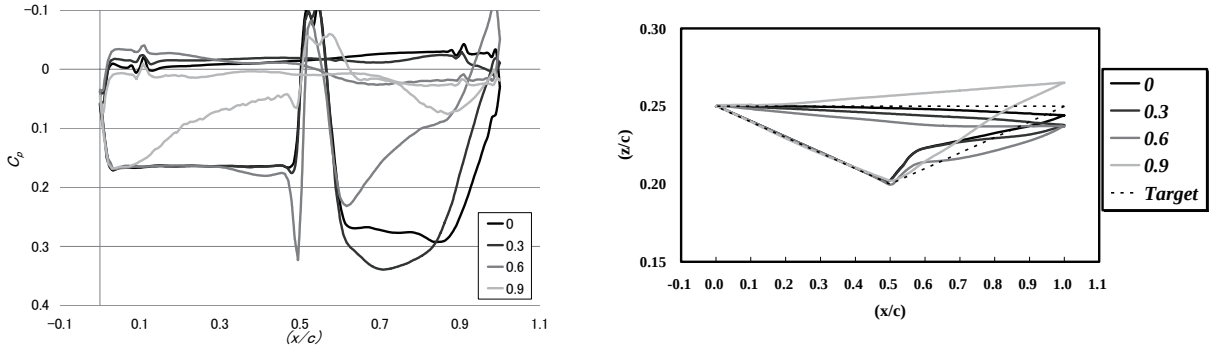

(b) 2nd iteration

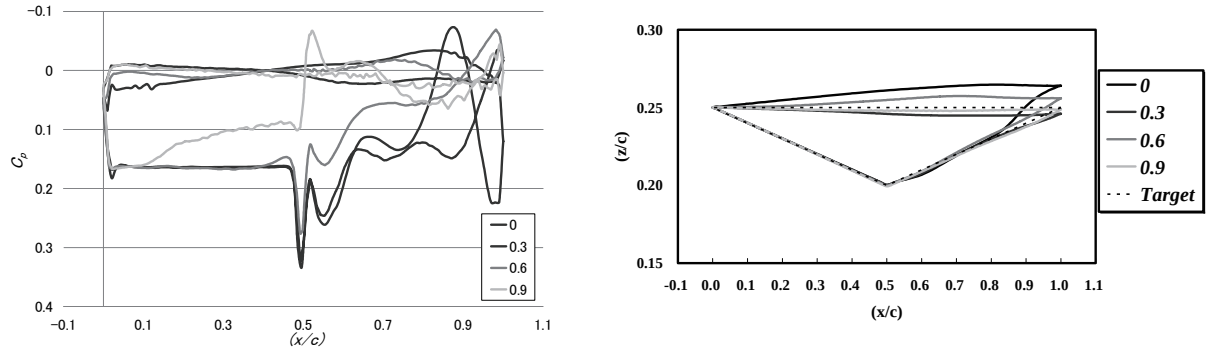

(c) 5th iteration

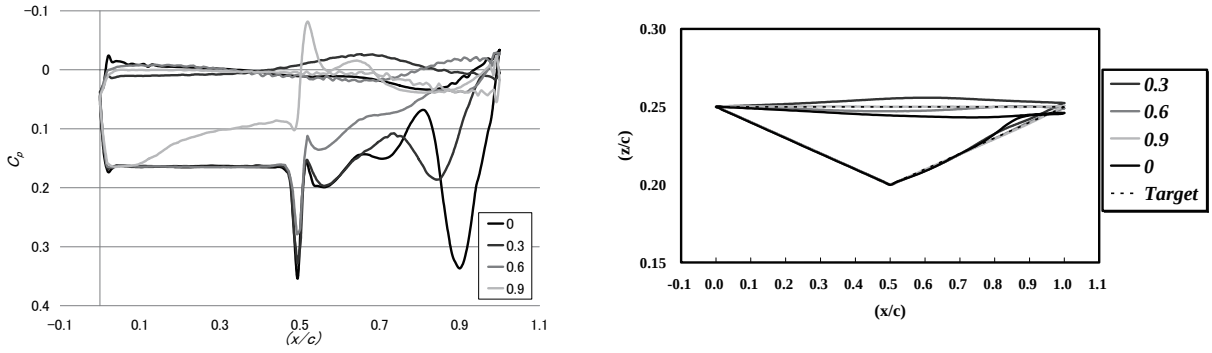

(d) 7th iteration

Figure 13. C_p distributions and geometries of the modified airfoils after certain iterations.

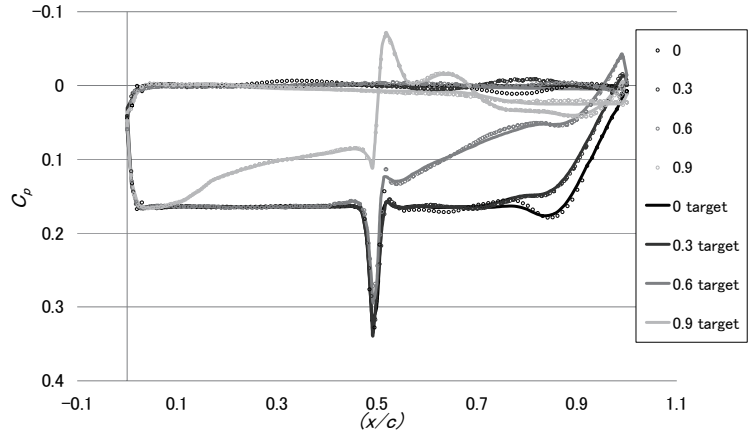

Figure 14. C_p distribution of the upper element of the biplane after 14 times iterations of inverse problem method.

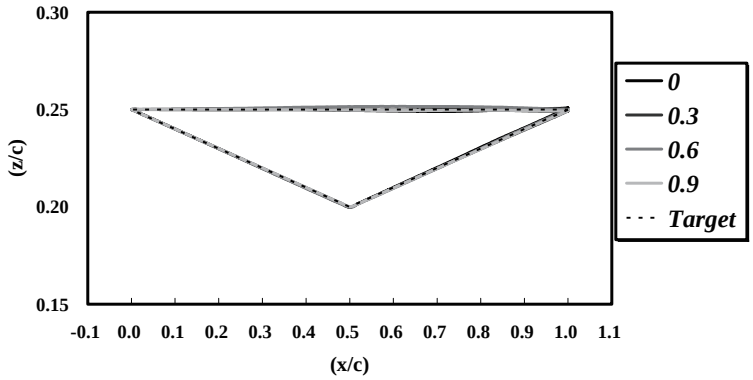

Figure 15. Section airfoil geometries of the upper element after 14 times iterations of inverse problem method.

Table 1. The absolute RMS errors between the realized and initial C_p distrivutions at each section.

(y/c)	0	0.1	0.2	0.3	0.4	0.5	0.6	0.7	0.8	0.9
RMS (*10E-4)	1.99	1.42	2.35	1.53	2.27	1.58	1.74	0.958	1.18	1.09

5. Conclusion

For the purpose of designing a better aerodynamic biplane airfoil than a Busemann biplane and Licher type biplane, an inverse problem method in the previous paper was uded. Concretely, a lower wave drag biplane airfoil than the Licher-type biplane at sufficient lift conditions (C_l>0.1) was aimed under the conditions of a cruise Mach number 1.7 and total thickness-chord ratio about 0.1. Designs are conducted by applying the inverse problem method to the upper element and lower one of the biplane airfoil alternately. Target pressure distributions for the inverse problem method were set to have more lift than the initial airfoil (the Licher-type biplane) with restraining increment of wave drag at chiefly the upper element. We successfully designed a biplane airfoils which achieved lower wave drag compared to both the Busemann biplane and Licher type biplane at C_l>0.07, having a total

maximum thickness ratio 0.102. Especially at C_l >0.14 wave drag was lower than that of a (zero-thickness) single flat plate airfoil which had the lowest wave drag in monoplanes in supersonic flight (for instance, M_∞=1.7).

The inverse problem method was applied to designs of 3-dimesional biplane wing. There are some problems in designs of 3-dimensional biplane such as interference of the upper and lower element, and diversity of span direction flow, and both of them. We set the C_p distributions of the Busemann biplane wing as target ones at 10 sections and a biplane wing whose upper wing is flat plate as an initial geometry. The same design cycle of the 2-dimensinal cases at 10 sections are conducted. It was seen that section geometries which were becoming the target one were becoming away by the influences of changes of span direction flow. After 14 times iteration, all sections converged to the target geometry within around 0.0001 or 0.0002 of the absolute RMS errors between realized C_p distributions and target ones. It can be said that the small perturbation form in the inverse problem method makes possible to design biplane airfoils or wing which has strong interference among other elements. In the future, practical designs of 3-deimensional biplane wings are considered by utilizing this method.

References

[1]Busemann, A., "Aerodynamic lift at supersonic speeds," Luftfahrtforschung, Ed.12, Nr.6, Oct.3, 1935, pp.210-220.

[2]Liepmann, H. W., and Roshko, A., Elements of Gas Dynamics, John Wiley & Sons, Inc., New York, 1957, pp.107-123, pp.389.

[3]Licher, R. M., "Optimum Two-Dimensional Multiplanes in Supersonic Flow," Report No. SM-18688, Douglass Aircraft Co., 1955.

[4]Kusunose, K., Matsushima, K., Goto, Y., Yamashita, H., Yonezawa, M., Maruyama, D. and Nakano, T. "A Fundamental Study for the Development of Boomless Supersonic Transport Aircraft," the 44th AIAA Aerospace Sciences Meeting and Exhibit, AIAA paper, AIAA-2006-0654, January 2006.

[5]Kusunose, K., Matsushima, K., Goto, Y., Maruyama, D., Yamashita, H. and Yonezawa, M., "A Study in the Supersonic Biplane utilizing its Shock Wave Cancellation Effect," Journal of The Japan Society for Aeronautical and Space Sciences, Vol. 55, No. 636, 2007, pp.1-7. (in Japanese)

[6]Matsushima, K., Maruyama, D., Nakano, T. and Nakahashi, K., "Aerodynamic Design of Low Boom and Low Drag Supersonic Transport using Favorable Wave Interference," Proceedings of The 36th JSASS Annual Meeting, Tokyo, Japan, April, 2005, pp. 130-133. (in Japanese)

[7]Maruyama, D., Matsushima, K., Kusunose, K. and Nakahashi, K., "Aerodynamic Design of Biplane Airfoils for Low Wave Drag Supersonic Flight," The 24th AIAA Applied Aerodynamics Conference, AIAA Paper, AIAA-2006-3323, San Francisco, California, June 2006.

[8]Matsushima, K., Maruyama, D., Matsuzawa, T. and Nakahashi, K., "Numerical Modeling for Supersonic Flow Analysis and Inverse Design," Lectures and Workshop International - Recent Advances in Multidisciplinary Technology and Modeling-, Tokyo, Japan, May 2007.

[9]Nakahashi, K., Ito, Y., and Togashi, F., "Some Challenge of Realistic Flow Simulations by Unstructured Grid CFD," International Journal for Numerical Methods in Fluids, Vol.43, 2003, pp.769-783.

[10]Ito, Y., and Nakahashi, K., "Surface Triangulation for Polygonal Models Based on CFD Data," International Journal for Numerical Methods in Fluids, Vol. 39, Issue 1, 2002, pp.75-96.

[11]Sharov, D. and Nakahashi, K.: Reordering of Hybrid Unstructured Grids for Lower-Upper Symmetric Gauss-Seidel Computations, AIAA Journal, Vol.36, No.3, pp.484-486, 1998.

[12]Moeckel, W. E., "Theoretical Aerodynamic Coefficients of Two-dimensional Supersonic Biplanes," NACA TN 1316, 1947.

JAXA Special Publication JAXA-SP-07-008E

Date of Issue : February 29,2008

Edited and Published by : Japan Aerospace Exploration Agency

7-44-1 Jindaiji-higashimach, Chofu-shi,Tokyo 182-8522,Japan

URL:http://www.jaxa.jp/

Printed by : NORTH ISLAND Co.,Ltd

Printed on Recycled Paper